

UNIVERSITY OF CALGARY

Quantitative Cerebrovascular Magnetic Resonance Imaging

by

Matthew Ethan MacDonald

A THESIS

SUBMITTED TO THE FACULTY OF GRADUATE STUDIES
IN PARTIAL FULFILMENT OF THE REQUIREMENTS FOR THE
DEGREE OF DOCTOR OF PHILOSOPHY

DEPARTMENT OF BIOMEDICAL ENGINEERING

CALGARY, ALBERTA

AUGUST 2014

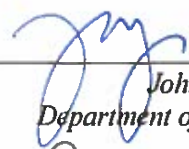
© Matthew Ethan MacDonald, 2014

UNIVERSITY OF CALGARY
FACULTY OF GRADUATE STUDIES

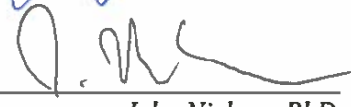
The undersigned certify that they have read, and recommend to the Faculty of Graduate Studies for acceptance, a thesis entitled "Quantitative Cerebrovascular Magnetic Resonance Imaging" submitted by Matthew Ethan MacDonald in partial fulfilment of the requirements of the degree of Doctor of Philosophy.



*Supervisor, Richard Frayne, PhD
Department of Medical Sciences*



*John H Wong, MD
Department of Neuroscience*



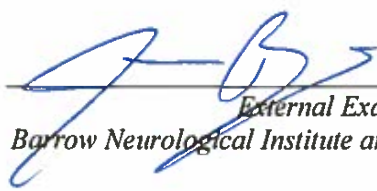
*John Nielsen, PhD
Department of Electrical and Computer Engineering*



*Michael R Smith, PhD
Department of Electrical and Computer Engineering*



*Internal / External Examiner, Robert J Sevick, MD
Department of Neuroscience*



*External Examiner, James G Pipe, PhD
Barrow Neurological Institute and Arizona State University*

11 Sep 2014
Date

Abstract

This thesis explores quantitative cerebrovascular magnetic resonance (MR) imaging, a broad topic, with the aim of providing relevant numerical values associated with blood flow through the brain. Anatomy, pathology and basic angiography methods were reviewed. Several other MR imaging methods for obtaining cerebrovascular measurements are reviewed.

Exploration of the lowest achievable variance with MR imaging was undertaken through simulation using a digital brain phantom. A phantom was constructed from a healthy human brain data set using advanced methodologies to yield volumes of MR parameters (*i.e.*, coil sensitivity, B_0 , B_1 , M_0 , T_1 , T_2 , T_2^* , and χ). The digital brain phantom was then used to simulate the MR acquisition process and generate images, in order to determine the minimal achievable variance as a function of coil profile distortion. It was found that the degree of coil correlation could affect the lowest achievable variance by up to $2\times$ to $3\times$ over practical ranges.

The focus of the experimental chapters is on phase contrast velocity mapping and metrics that can be derived from velocity maps, such as: peak velocity, volume flow rate, and intravascular pressure. Prospective imaging was performed on healthy humans, and eight patients (five cerebral aneurysms and three arteriovenous malformations). A case study of a giant cerebral aneurysm was explored in greater detail, and stent treatment was shown to reduce flow asymmetry. Peak velocity and volume flow rate was determined for vessels in the normal brain. Bootstrapping is performed to assert that group-wise measurements are representative of the broader population and flow laterality is examined. Significant flow asymmetry was found between several paired vessel segments. Flow in the patients was imaged, and derived metrics were compared to the healthy cohort. Patients with aneurysm were found to have significantly lower flow in vessels distal to the aneurysm, while arteriovenous malformation patients were found to have significantly higher flow in vessels supplying the nidus.

Acknowledgements

I would like to thank my supervisor, Dr Richard Frayne, for his time and effort. As well as the supervisory committee members (Drs JH Wong and J Nielsen); and the thesis examination committee (Drs RJ Sevick, MR Smith and JG Pipe). There are several individuals at the University of Calgary that helped with the experiments conducted in this thesis, including folks from the vascular imaging group (Drs CM McCreary, ML Lauzon, LB Andersen), folks from the Division of Neurosurgery (Drs P Dolati, A Mitha), and folks from the Calgary Stroke Team (Drs B Menon, M Essa); These individuals are thanked for fruitful discussion and perspectives on the thesis topics.

I was fortunate enough to receive financial support during the course of this degree allowing me to focus on the projects. I would like to acknowledge the following organizations for financial support: the Natural Sciences and Engineering Research Council (NSERC), Alberta Innovates Health Solutions (AI-HS, formerly AHFMR), and the Dr T Chen Fong Doctoral Scholarship. Operational funding and resources for experiments were provided by: the Canadian Institutes for Health Research, NSERC, the Department of Radiology, University of Calgary and the Seaman Family Magnetic Resonance Research Centre, Foothills Medical Centre, Alberta Health Services.

I would also like to acknowledge my family and friends for their support.

Dedication

This thesis is dedicated to the patients who participated in the imaging trials. These individuals volunteered to participate, giving up their time to further the scientific understanding of their condition. My effort has been focused on developing new scientific knowledge of their diseases, but without their help I would not have been able to. Several of these folks were in poor health yet travelled great distances to be involved in the studies described throughout this thesis, receiving tests in addition to the standard of care without expectation that it would help their condition. I believe that the majority of them did so in the hope that others in the future might not suffer to the same extent that they had. For these reasons, this thesis is dedicated to them.

Table of Contents

Approval Page	ii
Abstract.....	iii
Acknowledgements	iv
Dedication.....	v
Table of Contents	vi
List of Tables.....	ix
List of Figures and Illustrations.....	x
List of Symbols, Abbreviations and Nomenclature	xii
Chapter One: Introduction – The BIG picture.....	1
1.1 Cardiovascular Disease	2
1.2 Imaging.....	4
1.3 Project.....	4
1.4 Scientific Contributions.....	7
Chapter Two: Review of Cerebrovascular Anatomy, Imaging Modalities and MR Imaging.....	8
2.1 Chapter Overview.....	9
2.2 Introduction	9
2.3 The Cerebrovascular System: Structure and Function	10
2.3.1 Arteries.....	10
2.3.2 Capillaries	12
2.3.3 Veins	14
2.3.4 Summary	15
2.4 Common Diseases of the Cerebral Vascular System	15
2.4.1 Atherosclerosis.....	16
2.4.2 Stroke	17
2.4.3 Cerebral Aneurysm	18
2.4.4 Small Vessel Disease and Vascular Dementia.....	19
2.4.5 Arteriovenous Malformation (AVM).....	20
2.4.6 Neoplasm.....	21
2.4.7 Summary	21
2.5 Current Cerebrovascular Imaging Techniques.....	22
2.5.1 X-ray Digital Subtraction Angiography - DSA	22
2.5.2 Computed Tomography - CT	23
2.5.3 Ultrasound - US.....	24
2.5.4 Nuclear Medicine Imaging including PET	24
2.5.5 Non-MR Imaging of the Cerebrovascular System.....	25
2.6 MR Imaging and Contrast Agents.....	26
2.6.1 Basic Principles of MR Imaging.....	26
2.6.2 MR Contrast Agents.....	29
2.7 Chapter Summary	31

Chapter Three: Review of Cerebrovascular MR Imaging Methods.....	32
3.1 Chapter Overview.....	33
3.2 Magnetic Resonance Angiographic Techniques.....	33
3.2.1 Time-of-flight Imaging - TOF.....	34
3.2.2 Phase Contrast Imaging - PC.....	38
3.2.3 Contrast-enhanced MRA - CE MRA.....	43
3.2.4 Arterial Spin Labeling - ASL.....	46
3.2.5 Dynamic Bolus Perfusion Imaging.....	51
3.2.6 T_2^* -weighted Imaging.....	54
3.2.7 Susceptibility-weighted Imaging - SWI.....	58
3.2.8 Quantitative Susceptibility Mapping - QSM.....	61
3.3 Summary of MR Angiographic Techniques.....	64
3.4 Chapter Summary.....	66
 Chapter Four: Establishing the Lower Bound of MRI: Using An Estimation Theory and Statistical Perspective.....	 67
4.1 Chapter Overview.....	68
4.2 Introduction.....	68
4.3 Theory.....	71
4.3.1 Magnetic Resonance Signal.....	71
4.3.2 Noise in the MR System.....	72
4.3.3 Analytic Cramer-Rao Lower Bound.....	75
4.3.4 Machine Distortion.....	78
4.4 Methods.....	80
4.4.1 Digital Anthropomorphic Phantom Design.....	80
4.4.2 Numerical Simulation.....	82
4.5 Results.....	85
4.5.1 Analytical Evaluation of the CRLB.....	85
4.5.2 Digital Anthropomorphic Phantom.....	85
4.5.3 Lower Bound.....	87
4.6 Discussion.....	88
4.7 Chapter Summary.....	89
 Chapter Five: Pressure and Flow Alteration in a Giant Cerebral Aneurysm Treated with a Pipeline Stent.....	 90
5.1 Chapter Overview.....	91
5.2 Objective.....	91
5.3 Methods.....	93
5.3.1 Patient History.....	93
5.3.2 Imaging.....	93
5.3.3 Endovascular Intervention.....	95
5.3.4 Analysis.....	95
5.4 Results.....	99
5.5 Conclusions.....	102
5.6 Chapter Summary.....	103

Chapter Six: Phase Contrast MR Imaging Measurements of Blood Flow in Healthy Human Cerebral Vessel Segments	104
6.1 Chapter Overview.....	105
6.2 Introduction	105
6.3 Methods	108
6.3.1 Subjects	108
6.3.2 MR Acquisition.....	108
6.3.3 Analysis.....	108
6.4 Results	110
6.5 Discussion.....	115
6.6 Chapter Summary.....	117
Chapter Seven: Flow and Pressure Measurements in Aneurysms and Arteriovenous Malformations with Phase Contrast MR Imaging.....	119
7.1 Chapter Overview.....	120
7.2 Introduction	120
7.3 Methods and Materials	123
7.3.1 Patient Cohort.....	123
7.3.2 Imaging Protocol.....	123
7.3.3 Image Processing	125
7.4 Results	127
7.5 Conclusions	133
7.6 Chapter Summary.....	135
Chapter Eight: Is it Okay to Compare Blood Flow on Contralateral Sides of the Brain?	136
8.1 Chapter Overview.....	137
8.2 Introduction	137
8.3 Methods and Materials	139
8.4 Results	142
8.5 Discussion.....	144
Chapter Nine: Discussion and Conclusions	146
9.1 Thesis Review	147
9.2 Reflection on Hypotheses.....	147
9.3 Conclusions	148
9.4 Significance	149
9.5 Future Work and Reflection on Experimental Design	150
9.6 Summary.....	151
Chapter Ten: References	153
Appendix Ethics Approvals.....	180

List of Tables

Table 2.2: List of commonly available gadolinium-containing contrast agents used in MR imaging.	31
Table 4.1: Protocol used for quantification of MR parameters.	81
Table 5.1: Volume flow rate (VFR) measurements in larger cerebral vessels before and after stent deployment.	97
Table 5.2: Comparison of measured and calculated intravascular pressures.	101
Table 6.1: Left-right asymmetry results.	113
Table 7.1: Patient demographics, and aneurysm and AVM size and location.	124
Table 7.2: Image modes acquired. Healthy cohort is from Chapter Six.	129
Table 7.3: Flow velocity and intravascular pressure in and around the aneurysm fundus for each patient.	129
Table 7.4: Nidus size and pressure measurements in AVM patients.	133
Table 8.1: Asymmetry between the left and right sides of the brain.	142

List of Figures and Illustrations

Figure 1.1: Causes of mortality and research funding of disease.....	3
Figure 1.2: Example phase contrast (PC) imaging of the cerebral vasculature.....	5
Figure 2.1: The human cerebral vasculature.....	11
Figure 2.2: Vascular feeding territories.....	13
Figure 2.3: Fundamental MR imaging sequences.....	28
Figure 3.1: Evolution of MR magnetization during time-of-flight (TOF) imaging.....	35
Figure 3.2: Example 3D time-of-flight (TOF) acquisition.....	37
Figure 3.3: Time-of-flight (TOF) image acquisitions with variable flip angle.....	38
Figure 3.4: Phase contrast (PC) sequence diagram.....	40
Figure 3.5: Phase contrast (PC) images.....	42
Figure 3.6: Contrast-enhanced MRA (CE MRA).....	44
Figure 3.7: Non-contrast enhanced (NCE, left) and contrast-enhanced (CE, right) time-of-flight (TOF) maximum-intensity (MIP) images of the circle of Willis (CoW).....	45
Figure 3.8: Optimal arterial contrast agent concentration.....	45
Figure 3.9: Block diagram of arterial spin labeling (ASL) pulse sequence.....	47
Figure 3.10: Pseudo continuous arterial spin labeling (pcASL) images taken at different post labeling delay (PLD) times.....	49
Figure 3.11: An example of bolus passage perfusion imaging during acute ischemic stroke obtained using T2*-weighted dynamic susceptibility contrast (DSC) imaging.....	53
Figure 3.12: Multi-echo gradient recalled echo (GRE) pulse sequence diagram.....	56
Figure 3.13: Comparison of (top) T ₂ * map and (bottom) T ₂ map images.....	57
Figure 3.14: Susceptibility weighted image (SWI) mask filter.....	59
Figure 3.15: Comparing susceptibility weighted image (SWI) echo and filter coefficients.....	60
Figure 3.16: Quantitative susceptibility mapping (QSM) pipeline and example images.....	62
Figure 3.17: Comparison of susceptibility weighted image (SWI) and quantitative susceptibility mapping (QSM) venography.....	63
Figure 4.1: Example of noise on different receiver channels.....	73
Figure 4.2: A plot of the level of correlation e^{-a} against the minimum achievable variance of a fully sampled MR image.....	77
Figure 4.3: Measured B ₀ field, B ₁ fields, and coil sensitivity profiles.....	83
Figure 4.4: Calculated T ₁ , T ₂ , T ₂ *, M ₀ , and susceptibility maps.....	84
Figure 4.5: Pulse sequence used for simulation and evolving magnetization.....	86
Figure 4.6: Comparison of empirical and synthetic images.....	87
Figure 5.1: Pre-operative computed tomography (CT), CT angiography (CTA), X-ray digital subtraction angiography (DSA), non-contrast enhanced time-of-flight (TOF) imaging, and phase-contrast (PC) imaging.....	96
Figure 5.2: Cut planes used for flow volume calculations and temporal series of contrast inflow, and 4D flow velocity and derived fluid force.....	98
Figure 5.3: Post-operative imaging.....	100

Figure 6.1: Diagram illustrating the peak velocity (v_{peak}) and volume flow rate (VFR) calculations.	110
Figure 6.2: Streamline phase contrast (PC) MR angiography image and cut planes derived from one 3D data set.	111
Figure 6.3: Study of the standard deviation change with subjects.	112
Figure 6.4: Peak velocity (v_{peak}) and volume flow rate (VFR) measured in each vessel segment.	112
Figure 7.1: Example cut planes used for measuring volume flow rate in a representative subject with normal flow, an aneurysm patient and an AVM patient (left to right).	126
Figure 7.2: Comparison of angiography methods.	128
Figure 7.3: Volume flow rate measurements in aneurysm patients.	130
Figure 7.4: Volume flow rate measurements in the AVM patients.	131
Figure 8.1: Flow measurement locations.	140
Figure 8.2: Group mean and standard deviation measurements for (top) PC VFR measurements and (bottom) ASL CBF measurements.	141
Figure 8.3: Interdependence between PC VFR and ASL CBF measurements for each vascular territory.	143

List of Symbols, Abbreviations and Nomenclature

Imaging Modalities

ASL	arterial spin labeling
BB	black blood
CE MRA	contrast-enhanced MR angiography
CT	computed tomography
CTA	computed tomography angiography
CTP	CT perfusion
DCE	dynamic contrast-enhanced
DSA	(X-ray) digital subtraction angiography
DSC	dynamic susceptibility contrast
GRE	gradient-recalled echo
MR	magnetic resonance
PC	phase contrast
PET	positron emission tomography
QSM	quantitative susceptibility mapping
SE	spin echo
SPGR	spoiled gradient-recalled echo
SWI	susceptibility-weighted imaging
TCD US	trans-cranial Doppler US
TOF	time-of-flight
US	ultrasound
veASL	vessel encoded ASL

Blood Vessels and Anatomical

F_E	extravascular flow
ACA	anterior cerebral artery
AChA	anterior choroidal artery
ACom	anterior communicating artery
ATD	arterial transit delay time
BA	basilar artery
BBB	blood brain barrier
CBF	cerebral blood flow
CBV	cerebral blood volume
CoW	circle of Willis
ECA	extra cranial artery
GM	gray matter
ICA	internal carotid artery
k-trans	extravascular flow transit time
MCA	middle cerebral artery
MTT	mean transit time
PCA	posterior cerebral arteries

PCom	posterior communicating arteries
PICA, AICA	posterior and anterior inferior cerebral arteries
SCA	superior cerebellar arteries
TTP	time to peak, T_{\max} , and delay (δ)
VA	vertebral artery
WM	white matter

Diseases

AD	Alzheimer's disease
AVM	arteriovenous malformation
A β	amyloid-beta
CAA	cerebral amyloid angiopathy
CHD	coronary heart disease
ICH	intra-cerebral hemorrhage
MCI	mild cognitive impairment
NSF	nephrogenic systemic fibrosis
SVD	small vessel disease
VEGF	vascular endothelial growth factor

Measurement Units

2D, 3D, 4D	two dimensional, three dimensional, four dimensional
A	Amperes
cm	centimeters
g	grams
Hz	Hertz
L	liters
m	meters
min	minute
ml	milliliters
mm	millimeters
mm Hg	millimeters of mercury
mmol	millimolar
ms	milliseconds
s	seconds
T	Tesla

Physical and Technical Terms

\hat{i}	estimated image
M_0	initial magnetization
$M_x(t), M_y(t), M_z(t)$	x, y and z components of \mathbf{M}
\mathbf{Q}_{CORR}	correlation matrix
\mathbf{Q}_{COV}	covariance matrix

T_1, T_2, T_2^*	longitudinal and transverse relaxation times
σ_{iSpace}	variance of image data
σ_{kSpace}	variance of k -space data
ANOVA	analysis of variance
ASPECTS	Alberta Stroke Program early CT score
B	induced magnetic field
BW	bandwidth
C	coil sensitivity
CFD	computational fluid dynamics
CNR	contrast-to-noise ratio
COV	coefficient-of-variation
CRLB	Cramer-Rao lower bound
det	determinant of a matrix
F	force
G	gradient
H	applied magnetic field
i	image
$iDFT$	inverse discrete Fourier transform
ln	natural logarithm
M	magnetization
MIP	maximum intensity projection
p	hydrostatic pressure
$p(_)$	probability density function
$p(_; _)$	likelihood function
$\mathcal{N}(_, _)$	normal distribution
$\mathcal{CN}(_, _)$	circularly normal distribution
r	position
RF	radio frequency
s	MR signal
SNR	signal-to-noise ratio
TE	echo time
TR	repetition time
V	matrix of Eigen vectors
v	velocity
v_{enc}	encoding velocity
VFR	volume flow rate
v_{peak}	peak velocity
α	flip angle
γ	gyromagnetic ratio (42.57 MHz T ⁻¹ for hydrogen)
ε	ASL labeling efficiency or noise distribution
η	noise distribution
θ	estimation parameter, or angle
Λ	matrix of Eigen values
λ	Eigen value
π	Irrational number pi, 3.1415....

e	Euler's number, 2.7182....
ρ	density
ϕ	phase
χ	magnetic susceptibility
ω	Larmor frequency

Chapter One:

Introduction – The BIG picture

1.1 Cardiovascular Disease

Cardiovascular diseases are a devastating set of illnesses that, combined, result in more deaths than any other disease (1) (Figure 1.1, top). Sudden cardiac death from cardiovascular disease can result as a consequence of poor cardiovascular health and can be the first symptom to present. Of cardiovascular mortality, approximately two thirds are cardiac and one third is neurologically related (*i.e.*, stroke or aneurysm). Diseases of the cardiovascular system, particularly the cerebral vasculature, have historically been underfunded relative to other diseases (Figure 1.1, bottom). Compared with other highly prevalent diseases such as cancer, there is an order of magnitude less money spent on vascular research (>10 and >5 times) across Canada, the United States, United Kingdom, Australia and most of Europe (2). Spending is less in spite of the fact that cerebrovascular disease is the leading cause of disability (2). The research that is undertaken to improve prevention, to improve the effectiveness of treatment, and to reduce the cost of current treatments would reduce the burden of vascular disease on society.

Stroke is a common example of a cerebrovascular disease. It refers to a reduction or cessation of blood flow (cerebral ischemia) that may eventually cause brain infarction; this is referred to as ischemic stroke and is the most prevalent form. The second most common form of stroke is haemorrhagic stroke, which has a different pathology whereby bleeding into tissue causes it to become infarcted. Although ischemic stroke is the most prevalent form, there is a wide range of cerebrovascular diseases that can eventually result in these more rudimentary forms, for example, atherosclerotic plaque can fracture from the blood vessel wall, causing ischemic stroke further down in the cerebral watershed, or for another example, an aneurysm may lay dormant for many years and then eventually rupture causing haemorrhagic stroke. It is not fair to lump cerebrovascular diseases as only a clot story, the manifestations are complex and causes of pathology vary greatly.

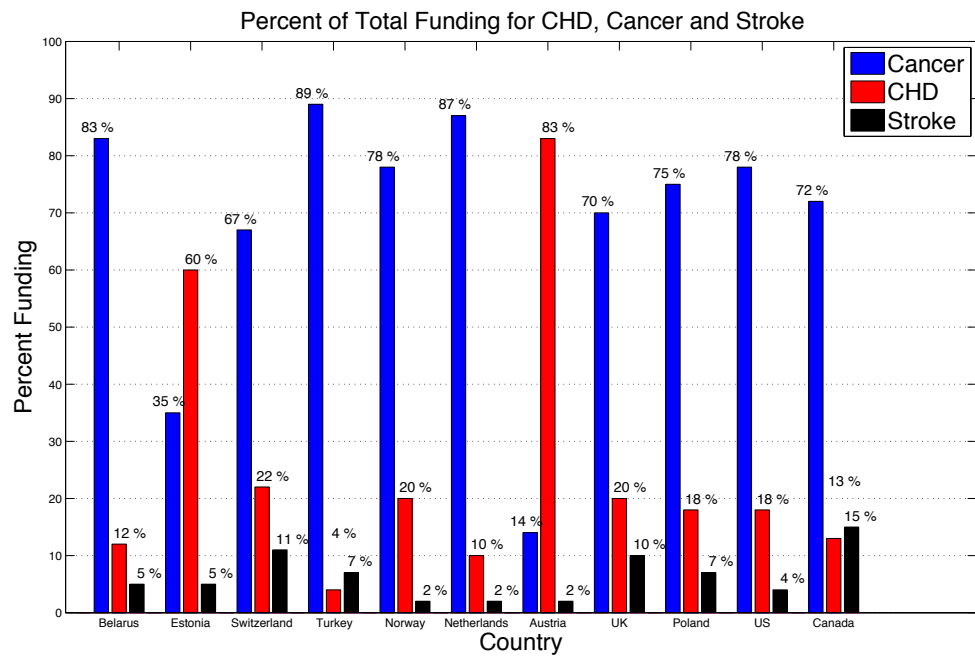
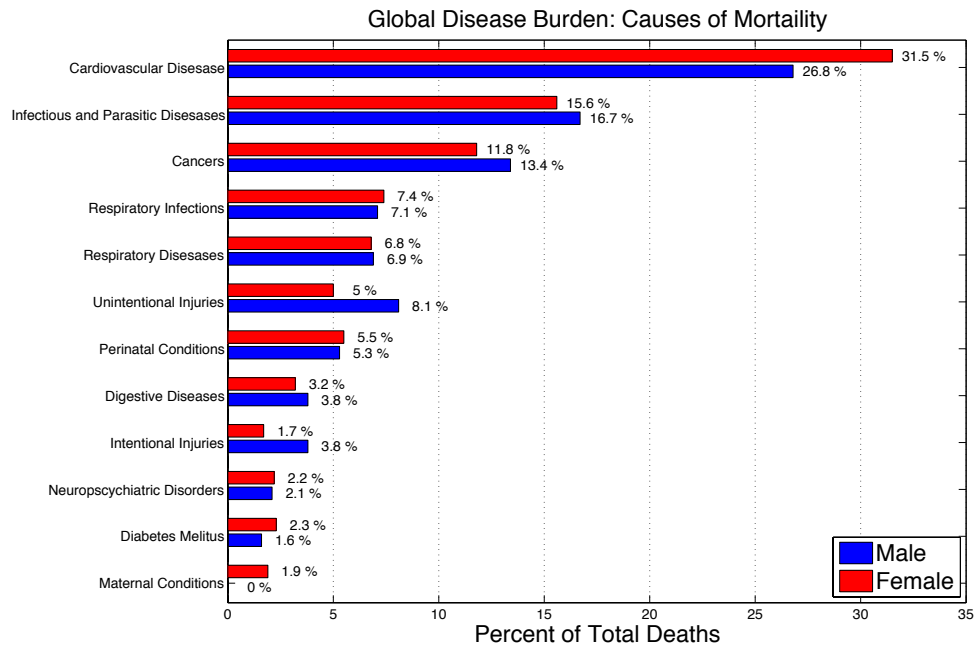


Figure 1.1: Causes of mortality and research funding of disease. Top) Figure from data in the 2004 United Nations report about the global burden of disease (1). The leading cause of mortality for both males and females is cardiovascular disease. Bottom) Spending for cancer, coronary heart disease (CHD) and stroke for several countries, data from ref (2). North American fund allocation follows this trend.

1.2 Imaging

Imaging of cerebrovascular disease has been crucial for the understanding of acute and chronic disease. Computed tomography (CT) imaging is now routine for assessing potential injury, and it is a vital link in the assessment of stroke being either ischemic or haemorrhagic in nature, allowing for medical intervention. CT is inherently a quantitative technique (*i.e.*, it provides measurements in Hounsfield units). Haemorrhaged blood changes the radiographic density (measured in Hounsfield units), such that the detection of these regions is easily observed with CT, however, the ability to distinguish between normal and ischemic tissues with CT does not have the same detection potential. Although CT angiography (CTA) can provide structural information about a cerebral aneurysm, it does not provide quantitative information about the pressure on the aneurysm wall, which intuitively may be a more useful metric in understanding the growth and risk of rupture.

Magnetic resonance (MR) angiography can be performed in many different ways (see an example in Figure 1.2), and thus provides improved information for diagnostic purposes and for the purpose of better understanding disease. MR imaging is one of the most sophisticated engineering feats of our day and the discovery of many new methods, each further advancing the modality, are published each month. This thesis primarily explores the use of advanced quantitative MR imaging methods to obtain new information about the state of the cerebral vasculature.

1.3 Project

This project was motivated by several factors. Blood flow through the brain is vital to human life. Quantitative cerebrovascular MR imaging when explored from a scientific point of view has yielded new knowledge of the cerebral vasculature in previous studies. Cerebrovascular disease is a prevalent form of disease and cause of disability, so having new quantitative methods for assessment will be beneficial. Local expertise in cerebrovascular diseases will facilitate a superior thesis. Impact might be made by focusing on less studied diseases such as cerebral aneurysm and arteriovenous malformation. Understanding of normal cerebral hemodynamics is critical.

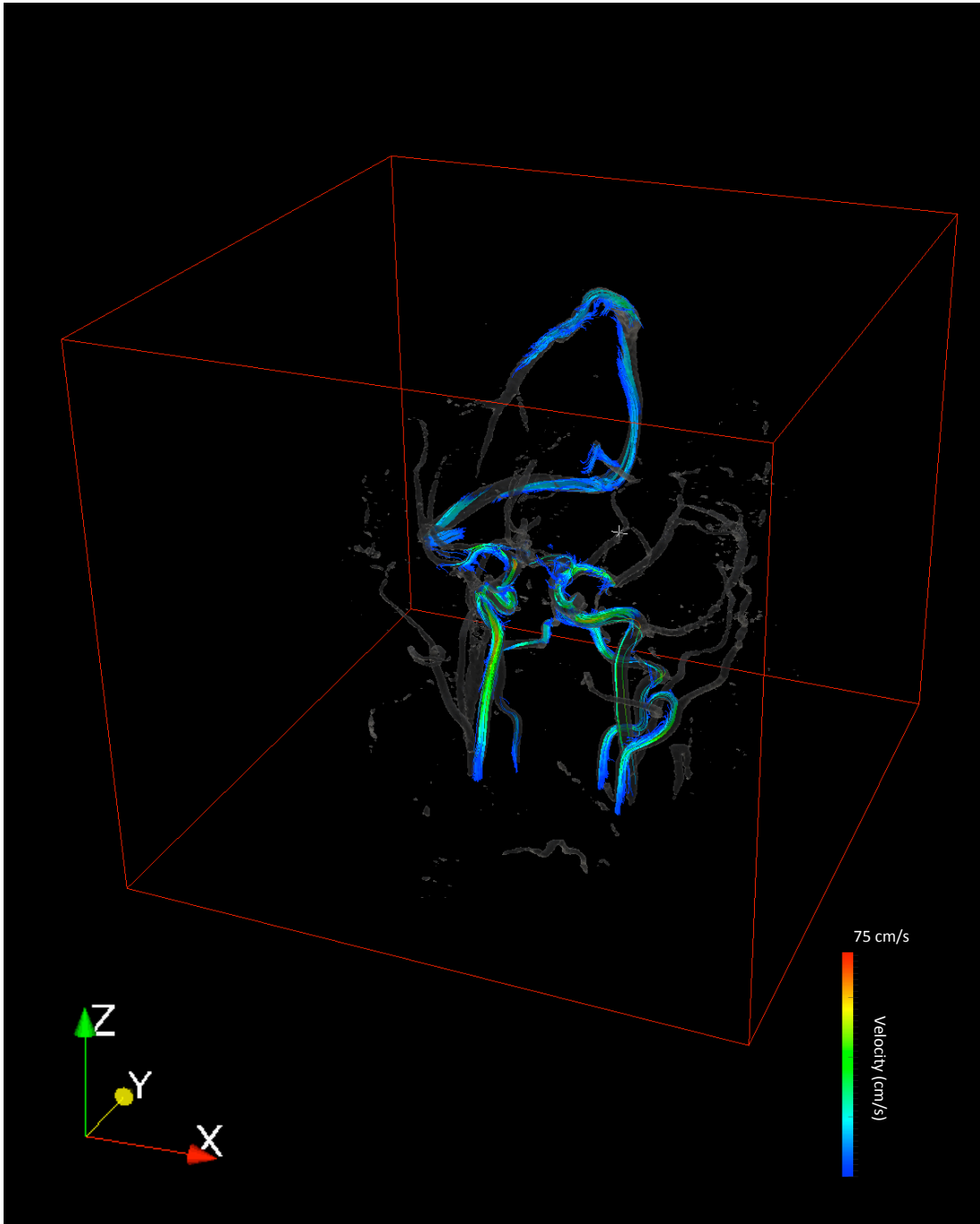


Figure 1.2: Example phase contrast (PC) imaging of the cerebral vasculature. In this visualization, the blood vessels are contoured in gray and seeds are placed to create streamlines, whose color is related to the speed of the flow. This image is intended as an example of quantitative cerebrovascular MR imaging.

The overall hypothesis during this project was that quantitative metrics of the cerebrovascular system would help to improve the understanding of cerebrovascular disease states. Accurate estimation of a wide range of cerebral hemodynamic parameters, including: perfusion, blood flow velocity, and intravascular pressure, could be used to observe the state of the vasculature in the head, and lead to new knowledge on the topic. That advanced acquisition and reconstruction strategies can be used to improve the measurement of these hemodynamic parameters, as they are highly sensitive to implementation methodology. The specific hypotheses tested for each section are introduced in their respective chapters once a solid base is built for understanding their implication. The three specific objectives of the project were to:

- 1) develop a simulation framework for optimizing MR imaging methods and better understand the technology,
- 2) use advanced methodologies to better characterize the flow through the brain, and
- 3) use phase contrast MR imaging to obtain velocity measurements and estimate vessel wall pressure in aneurysm and arteriovenous malformation patients, prospectively.

This thesis is organized into nine chapters. Chapter Two is a literature review covering relevant anatomy and diseases, alternative imaging methods, and it is intended to provide the reader with a background understanding of cerebrovascular anatomy and methodology. Chapter Three reviews modern angiography techniques and image contrast mechanisms. Chapter Four discusses a simulation framework for MR acquisition and reconstruction; this chapter is substantially more technical and should help to develop a much stronger understanding of the MR system. Chapter Four addresses specific objective 1, developing an optimization framework. Chapter Five is a case report with advanced hemodynamic parameters. Chapter Six demonstrates phase contrast MR imaging in a healthy population; this chapter establishes the mean flow rates for a standard healthy group, and addresses specific objective 2. Chapter Seven switches focus to cerebral aneurysm and arteriovenous malformations, and making measurements in these disease states. In Chapter Eight a question is proposed, “is it okay to compare blood flow on contralateral sides of the brain?” Quantitative cerebrovascular metrics are then

used to come to a conclusion. Chapter Nine is a brief chapter of reflection on the project, discussion, and suggested future work; it is the final chapter.

1.4 Scientific Contributions

I was the principal author for all work contained within this dissertation. Others specifically helped with various chapters. Dr R Frayne, my PhD supervisor, aided with all the chapters, providing advice. Chapter Four was influenced by Drs ML Lauzon and J Nielsen. Clinical collaborators, particularly Drs P Dolati, A Mitha, and JH Wong, should be acknowledged for their role in Chapters Five and Seven. Underlying the work presented in this thesis, is a library of custom-written analysis software that allowed for image reconstruction and quantification of MR imaging data into quantitative cerebrovascular parameters, such as velocity, volume flow rate (VFR), and pressure.

With respect to the scientific contributions, an effort was made to share the findings at regional and national symposiums, and via publication in peer-reviewed journals. During the period that work went into this thesis, it was also openly shared at several international scientific meetings, including: 1) one proceeding at the Joint American Association of Medical Physicists and Canadian Organization of Medical Physicists meeting in 2010; 2) ten proceedings at the International Society of Magnetic Resonance in Medicine from 2011 through 2014; 3) five proceedings at the International Magnetic Resonance Angiography Club Working Group from 2011 through 2014. This has resulted in the work being presented in cities around the world, including: Melbourne, Australia; Milan, Italy; Freiburg, Germany; Utrecht, Netherlands; Stockholm, Sweden; and in cities of the United States - New York and Salt Lake City; and in cities across Canada - Halifax, Montreal, Ottawa, Toronto, Edmonton, Calgary/Banff, Vancouver, and Victoria. All the work of this thesis is currently under examination for publication with peer-reviewed journals.

Chapter Two:

**Review of Cerebrovascular Anatomy,
Imaging Modalities and MR Imaging**

2.1 Chapter Overview

Cerebrovascular anatomy and disease, competing imaging methodologies, and basics of MR imaging, are fundamental to understanding the later chapters of this thesis and are reviewed in this chapter. The cerebral circulatory is reviewed; vessels larger than half a millimetre are discussed along with the microcirculation (*e.g.*, at the capillary level, cerebral blood flow and volume). Diseases that afflict and/or are related to the blood flow in the brain are reviewed from a high level point of view to understand their impact and how imaging may play a role in their assessment and/or treatment. Alternative modes of imaging, including: X-ray digital subtraction angiography, computed tomography, ultrasound, and nuclear medicine (particularly positron emission tomography), as they pertain to obtaining measurements about the cerebrovascular system are then reviewed. Finally, the basics of magnetic resonance (MR) imaging, in terms of the Bloch equations are reviewed, including: basic sequence types (gradient recalled echo and spin echo), and basics of MR contrast agents. A relevant understanding of the blood flow and cerebral anatomy, competing imaging methodologies, and the basics of MR imaging should be taken from this chapter.

2.2 Introduction

Modern medical imaging techniques allow unprecedented understanding and visualization of blood flow through the human brain. In the broadest sense of the term, these techniques are angiographic approaches, as they provide structural and functional information about blood flow. Angiography is derived from two Greek words – *angeion* for vessel and *graphein* to record. Often the term is narrowly used as a label for projection images obtained from contrast agent-enhanced radiographic techniques. Partially for convenience but more importantly for completeness, a more inclusive definition of this term is adopted and angiography is referred to more generally as imaging relating to blood and blood flow. In this chapter, the purpose is to provide a structured overview of the current (as of June 2014) state-of-the-art angiographic approaches that use MR imaging to obtain detailed information on the cerebrovascular system. In addition to this objective, the review will provide a summary of the structure

and function of the cerebrovascular system, describing common cerebrovascular pathologies and provide information on other complementary medical imaging methods. Example images produced on a 3 T MR scanner are shown for each method.

2.3 The Cerebrovascular System: Structure and Function

The cerebrovascular system is a complex network of arteries, capillaries and veins that delivers a reliable supply of blood to and from the brain. The brain requires an abundant supply of oxygenated and nutrient rich blood to be delivered from the arteries to the capillaries. At the capillaries, oxygen and other nutrients are provided for tissue function while other waste products, such as carbon dioxide and heat are removed. From the capillary bed the veins cycle blood back toward the heart and pulmonary system. Figure 2.1 shows labeled images of the cerebrovascular system.

2.3.1 Arteries

The ascending aorta originates at the heart and becomes the aortic arch, from which three major arteries branch towards the head. Blood flows through these vessels (the brachiocephalic trunk, the left common carotid artery, and the left subclavian artery) supplying the arms, head and neck. The right subclavian and right common carotid arteries branch from the brachiocephalic trunk. A vertebral artery originates from each subclavian artery. While the subclavian vessels supply blood to the arms, four principal arteries, two carotid and two vertebral arteries (VA), enter the neck to supply the brain (Figure 2.1 left).

Both the left and right carotid arteries bifurcate in the neck, to form the two internal carotid arteries (ICA) and the two external carotid arteries (ECA). The ECAs remain extra-cranial. The ICAs become intra-cranial at the base of the brain. The anterior choroidal arteries (AChA) originate from each ICA and supply parts of the midbrain. The VAs run along the cervical spine, roughly parallel to the brain stem. Toward the top of the brain stem, the two vertebral arteries converge, in a reverse bifurcation, forming the basilar artery (BA). The smaller pontine arteries branch from the BA into the brainstem. The VAs and BA supply blood to the posterior of the brain including the cerebellum via

Human Cerebrovasculature

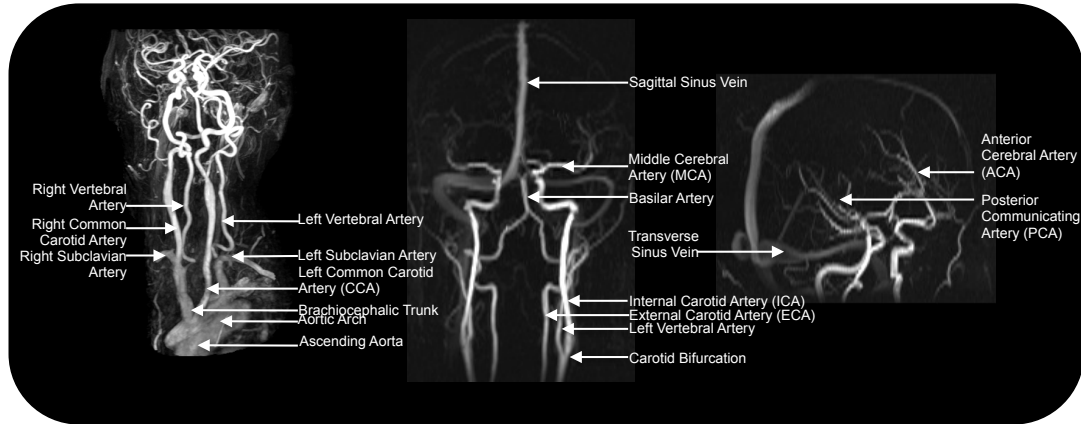


Figure 2.1: The human cerebral vasculature. (left) Contrast-enhanced MR angiogram (CE MRA) showing vessels of the neck and upper aorta. (center) Phase contrast (PC) MRA, from the carotid bifurcation to the top of the head. (right) PC MRA over a smaller field-of-view, focused in on the circle of Willis.

the posterior and anterior inferior cerebral arteries (PICA, AICA), and the superior cerebellar arteries (SCA) (Figure 2.1, middle).

At the base of the brain there exists a looped vascular structure known as the circle of Willis (CoW), which provides a degree of intra-cranial blood flow redundancy. The BA bifurcates into the left and right posterior cerebral arteries (PCA) forming the posterior aspect of the CoW (known as the basilar tip). The PCAs branch towards the posterior of the brain. At approximately the same superior-inferior level, the ICAs both branch into two vessels: the anterior cerebral artery (ACA) and the middle cerebral artery (MCA). The ACAs extend anteriorly along the midline. A smaller vessel, the anterior communicating artery (ACoM) connects the two ACA branches. The CoW is a major source of collateral flow and thus provides circulatory redundancy to the brain, *i.e.*, if one of the ICAs cannot supply blood to the brain then the other ICA can compensate by supplying blood collaterally through the ACoM to the opposite side of the brain (3,4). The MCA branches propagate laterally. Two small arteries, the posterior communicating arteries (PCoM) complete the CoW by connecting each MCA to the adjacent PCA (Figure 2.1, right).

It is, however, possible that even in apparently normal (or healthy) individuals the vascular configurations may not be as described (5,6). Autopsy studies, for example, have

shown that approximately 3.8% of individuals are missing the ACom, while another 3.3% have a duplicate ACom and approximately 2.4% of individuals had no PCom (7). In any of these vascular configurations, the level of redundancy (particularly as provided via the CoW) may be reduced. Although these individuals are otherwise healthy, they may be more susceptible to some vascular diseases, such as ischemic stroke (8,9).

Each MCA has two segments, the M1, which represents the vessel before the MCA bifurcates, and the M2 segments immediately lateral to this bifurcation. The M1 segment has several smaller superior branches, the lenticulostriate (or anterolateral central) arteries (LSA), which supply blood to subcortical structures.

In addition to the blood vessels that perfuse the deep brain from the ICA there is also vessels that branch in from the ECA, and there are small arteries (such as the meningeal arteries) that wrap around the brain and penetrate the brain from its periphery (*i.e.*, from the meninges). These arteries are much smaller than the MCA, ranging in size from 0.03 mm to 0.70 mm in diameter (10). The honeycomb-like blood flow network formed by these vessels provides an important degree of redundancy in cortical blood supply. Vessels, such as the pontine, PCom, lenticulostriate and meningeal arteries, are generally of small caliber and thus have much lower flow, making them difficult to image reliably.

2.3.2 Capillaries

The ACA, MCA, PCA and other smaller intra-cranial arterial vessels penetrate into brain tissue and repeatedly branch to smaller caliber vessels, eventually reaching the capillary bed (typically defined as the network of blood vessels <10 μm in diameter (10)) where nutrient, waste and heat exchange takes place. Territories corresponding to their feeding arteries are shown in Figure 2.2. Capillaries and their immediately adjacent feeding arterioles and collecting venules are not directly visible on MR imaging – however changes in their physiology can be inferred from a variety of imaging techniques. Capillaries in the brain are fundamentally different than those found in other organs, as the inner endothelial cell layer grows much tighter and creates an effective barrier between the blood and the brain tissue (known as the blood brain barrier, or BBB) (11).

Vascular Territories

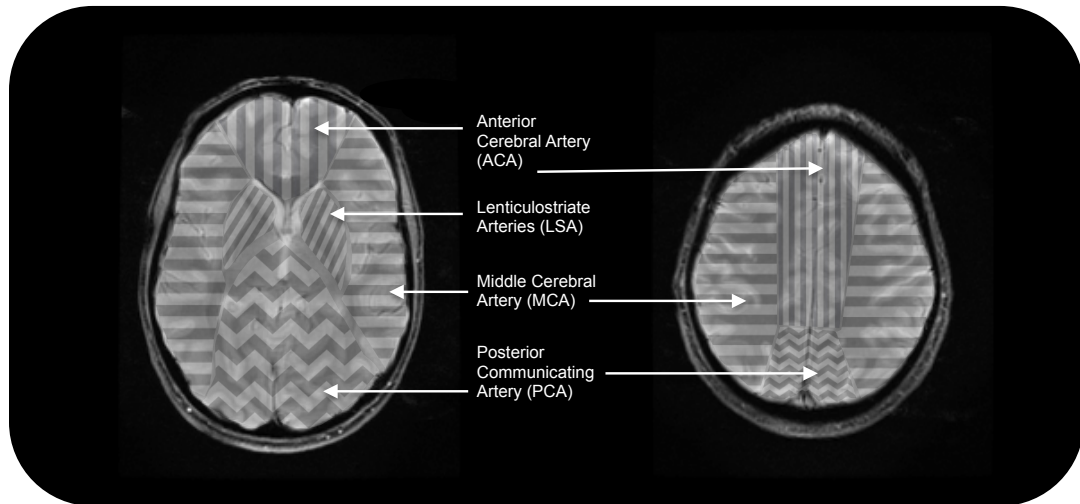


Figure 2.2: Vascular feeding territories. Two slices acquired axially through the brain and textured to classify general territories fed by various arteries. Perfusion territories are generally classified by the name of the feeding artery for the respective territory.

The BBB allows passive passage of small molecules (< 400 to 600 atomic mass units) and active passage of some larger molecules (12), but impedes the exchange of many larger compounds into the extravascular space. Molecular charge and polarity also affect the BBB permeability (13). The fact that the BBB impedes the exchange of larger compounds including most injected medical imaging contrast agents is an important characteristic.

In the healthy brain, perfusion of blood at the tissue level is fairly uniform across both the gray matter (GM) and white matter (WM) components. Commonly, tissue perfusion is assessed with metrics, such as: cerebral blood flow (CBF), cerebral blood volume (CBV), mean transit time (MTT), and arterial transit delay time (ATD). CBF is a measure of the flow per 100 g of tissue mass and has conventional units of $\text{ml } 100 \text{ g}^{-1} \text{ min}^{-1}$, CBV is the volume of blood in 100 g of tissue and is measured in units of $\text{ml } 100 \text{ g}^{-1}$, and MTT is the mean time for a tracer to flow through the tissue and is reported in seconds. ATD is a measure of the delay between the arrival of the contrast agent in a major feeding artery and the arrival time in the tissue reported in seconds, and is closely related to other delay metrics such as: time to peak (TTP), T_{max} , and delay (δ).

Table 2.1: Typical mean perfusion values obtained for a healthy control group. These values are the consensus from published experiments performed with several modalities (positron emission tomography, bolus passage computed tomography perfusion and magnetic resonance perfusion, and arterial spin labeling imaging) (14-23).

* - k -trans and F_E are not well defined in healthy brain tissue, and can only be measured when the BBB permeability increases.

Perfusion Parameter	Tissue Type	
	Gray Matter	White Matter
CBF	60 ml 100 g ⁻¹ min ⁻¹	22 ml 100 g ⁻¹ min ⁻¹
CBV	5.00 ml 100 g ⁻¹	1.75 ml 100 g ⁻¹
MTT	4.0 s	4.8 s
k-trans	~0.0 min ⁻¹	~0.0 min ⁻¹
F_E	~0.0 ml 100 g ⁻¹ min ⁻¹	~0.0 ml 100 g ⁻¹ min ⁻¹

The BBB impedes but does not completely prevent transport of large molecules. The permeability of the BBB can be estimated with careful measurement if a multi-compartmental tissue model is employed. BBB permeability is sometimes characterized by extravascular flow (F_E) measured as flow with the same units as CBF (ml 100 g⁻¹ min⁻¹), or the transit time of that flow exchange (k -trans) measured in min⁻¹. These parameters help to provide metrics of the leakage of the microvasculature into the extravascular space. It should be noted that BBB permeability values are only relevant when there is a tumor or disease type causing the leakage, and normally these metrics are not measurable.

Perfusion can be used to characterize and better understand the functional state of capillary bed performance. For example: if it is anticipated that the vascular bed is leaky, tissue permeability could be measured (14,16). Typical functional values for healthy individuals are found in the literature (14-23) and are summarized in Table 2.1.

2.3.3 Veins

The venous system drains blood from the capillary bed and returns it to the heart. The most prominent vein in the brain is the cerebral sagittal sinus, which runs along the superior and posterior midlines transporting venous blood toward the base of the brain (Figure 2.1, middle). The vein of Galen, another prominent vein, runs along the midline from the ventricles to near where the sagittal sinus meets the base of the brain. The vein

of Galen and the sagittal sinus connect to the right and left transverse sinus veins at the sinus confluence. The transverse sinus vessels run along the side of the skull to a point lateral of where the ICA reaches the brain. The transverse sinus then extends downward in the neck running parallel to the carotid artery and at this point is commonly referred to as the jugular vein (on both left and right sides of the neck). There are both internal and external jugular veins draining the intra- and extra-cranial circulations, respectively. The jugular veins flow into the brachiocephalic veins and eventually into the superior vena cava and venous blood is transferred back to the heart.

2.3.4 Summary

The previous subsections have described the general structure of the cerebral vascular system in humans. Normal arteries, veins and capillaries were described, however, there may be to some degree of variation from this normal configuration in otherwise healthy individuals. In the next section, normal cerebral vascular structure and function will be built upon and the impact of common diseases are discussed.

2.4 Common Diseases of the Cerebral Vascular System

The World Health Organization (1) reported that cardiovascular disease is the number one cause of mortality worldwide (resulting in the death of 26.8% of males and 31.5% of females). Diseases of the cerebral vasculature represent an important subset of all cardiovascular events, as the majority of cardiovascular disease-related morbidity and mortality are caused by events in the heart or brain. A large proportion of the cardiovascular disease spectrum impacts the brain, including diseases like atherosclerosis, hemorrhagic and ischemic stroke, aneurysms, arteriovenous malformations (AVMs), small vessel diseases (vascular dementia, including cerebral amyloid angiopathy) and vascular neoplasms (tumors). In addition, Alzheimer's disease is now viewed as having strong linkages to a number of vascular disease processes (24). This list of common disorders should come as no surprise given the evidence that the vessels of the brain deteriorate with age (25), becoming hardened, lengthened and more tortuous over time. Small hemorrhages (micro-bleeds) are increasingly a common finding near tiny vessels in middle aged (26) as well as more elderly patients (27), and often

asymptomatic suggesting that they may be at least in part a somewhat normal development. In the following sub-sections common diseases of the cerebral vascular system are described, in order to better convey an understanding of how these diseases can be imaged with different MR techniques.

2.4.1 Atherosclerosis

Atherosclerosis is a disease characterized by gradual formation of plaques under the endothelial cell layer in the artery walls. These plaques are generally located in regions where there is disturbed flow, such as near the carotid artery bifurcation. Atherosclerosis affects a large percentage of the adult population, 25.6% of men and 26.4% of women have some carotid atherosclerosis (28). Thickening of the vessel wall from atherosclerosis is found in 9.4% of men and 11.7% of women (28). It can be present in vessels throughout the body and the prevalence has been shown to increase with age (29). Common risk factors associated with developing atherosclerosis include: diabetes, smoking, high cholesterol, age, male gender, and high blood pressure (30,31).

Atherosclerosis that is proximal to the brain is particularly dangerous because if these plaques rupture, the subsequent release of free-floating emboli into the blood can potentially create a sudden vascular incident (often resulting in a transient ischemic attack or, worse, a stroke). Interventions for atherosclerosis include pharmaceutical therapy (*e.g.*, statins) (32,33), endarterectomy (34) and endovascular therapy (35,36).

Endarterectomy is a surgical technique performed by exposing and clamping the vessel above and below the plaque to temporarily stop blood flow. The plaques are then removed and flow restored. Endovascular therapy includes angioplasty and stenting and is performed from within the vessel. The vascular system is entered with devices that are then navigated to the site of disease, making it less invasive. Angioplasty uses balloons to expand the diseased vessel and stents can be deployed from within the vessel to restore the flow and prevent emboli.

Atherosclerosis can also occur in the intracranial vasculature; current MR imaging approaches do not effectively detect lesions in the intracranial vasculature as parent vessels and the resulting plaques are often too small. Historically angioplasty and stenting have been used (37), but more recently the effectiveness of stenting for intracranial

atherosclerosis has been associated with poor outcomes and pharmaceutical therapies are claimed to be more effective (38).

2.4.2 Stroke

Thrombo-embolic cerebral ischemia and primary intra-cerebral hemorrhage (ICH) encompass ~80% and ~20% of all stroke episodes, respectively. Both can present with similar symptoms, but have considerably different etiologies. The former is caused by a partial/full vessel obstruction (typically a blood clot), while a bursting vessel, causing leakage of blood into the surrounding parenchyma, causes the latter.

Ischemic stroke is very prevalent in the adult population, and leads to 5.6% of all deaths in the developed world (39). The risk factors for ischemic stroke include: age, gender, ethnicity, hypertension, atrial fibrillation, diabetes, smoking, heavy alcohol consumption, and carotid atherosclerosis (40). The occlusion of an artery can occur from free-floating emboli in the blood or by thrombus (*i.e.*, coagulation of blood), or some combination of the two. Ischemic stroke is usually an acute event and the re-establishment of flow must be performed as soon as possible (41). Recanalization (removal or reduction of the initial occlusion) and reperfusion (re-establishment of brain perfusion) have been used as surrogate markers of flow re-establishment. However there is increasing evidence suggesting that recanalization may not necessarily lead to reperfusion (42,43). Although most research has focused on the clotting of the blood supply within the arterial vasculature, venous thrombus, where coagulated blood impedes flow in the veins, can also occur and result in ischemia. Several treatments exist for ischemic stroke including intra-venous (IV) thrombolysis or intra-arterial (IA) thrombolysis (delivered during endovascular therapy) (44). Most recently mechanical thrombectomy has been attempted with success using specialized endovascular devices (45).

Knowledge of the degree of cerebral ischemia and infarct is important in determining the most effective management and treatment of ischemic stroke. Tissue that has become infarcted is dead or dying and will not respond to treatment. Tissues that are impaired (*i.e.*, ischemic) but not yet infarcted (*a.k.a.*, penumbra), are the clinical target to be salvaged. These penumbral tissues represent a key target for therapy; the importance

of collateral flow from redundant blood vessels that feed the same tissue region are also now recognized as helping to reduce the damage caused by ischemic stroke (46). Most data suggests that the time window available for intervention during acute ischemic stroke is within the first 3 hours, but treatment with a larger window, up to 4.5 h post onset, has been recently stated as being beneficial (47).

Primary ICH occurs when vessels bleed into the surrounding extravascular tissue. Risk factors for ICH are similar to AIS. The primary injury occurs within minutes of bleeding and is largely a result of mechanical damage associated with edema and subsequent mass effect. After the initial rupture the hematoma can expand for several hours through the primary leakage or injured surrounding vessels. There is an exponential increase in mortality when the hematoma volume exceeds 30 ml (48).

The treatments for hemorrhagic stroke include blood pressure reduction, drug therapy and surgical intervention to relieve intracranial pressure and reduce hematoma expansion (49). Factor VII, a protein which causes blood clotting, has been shown to reduce hematoma growth in acute hemorrhage patients (50), but carries the increased risk of ischemic stroke.

Imaging plays a key role determining if a stroke is ischemic or hemorrhagic. Identification of the stroke subtype is essential for treatment decisions. For example, giving IV thrombolysis treatment to a patient with hemorrhagic stroke will likely worsen their condition (51). Deposited blood in tissue from hemorrhage has a high concentration of iron and results in susceptibility changes in tissue, of significance for MR imaging.

2.4.3 Cerebral Aneurysm

Aneurysms are formed when a blood vessel wall expands outward, resulting in a vascular sac. The prevalence of intracranial aneurysms is estimated to be ~2.3% in adults and tends to increase with age (52). Aneurysm etiology is unclear but is thought to be caused by abnormal pressure on a vessel wall (53), focal wall weakness, or previous trauma. Aneurysms that form near bifurcations due to high pressure are called berry or saccular aneurysms and ones that protrude outward due to a weakened vessel wall are called fusiform aneurysms. When a cerebral aneurysm expands, it can infringe on structures such as the optic nerve (*a.k.a.*, mass effect). Cerebral aneurysms are of high risk to

rupture creating hemorrhagic stroke, but exact risk varies depending on the location and size of the aneurysm (52,54). Treatment for cerebral aneurysms includes neurosurgical clipping (55) or endovascular coiling/stenting (56). During aneurysm clipping, the aneurysm is surgically exposed and a clip is placed at the aneurysm neck. In coiling/stenting treatment, endovascular devices are used to deploy a coiled wire into the aneurysm. The wire packs the aneurysm causing embolization. An optional stent may be also placed over the aneurysm neck to prevent the coil from subsequently moving and divert the flow (57).

2.4.4 Small Vessel Disease and Vascular Dementia

Small vessel disease (SVD) is an umbrella term that refers to a progressive, often age-related, cognitive decline associated with mixed pathologies of the cerebral vascular system. More standardized terminology and assessment methods surrounding SVD have been recently established for neuroimaging markers, such as: subcortical infarcts, white matter hyperintensities, lacunes, perivascular spaces, and cerebral microbleeds (58). Vascular changes are also implicated in advancing Alzheimer's disease (AD) (25). Dementia is highly prevalent amongst the elderly population (59). Autopsy studies have demonstrated pure vascular dementia in about 11% of a large demented cohort (60). In the same study, strokes were present in 75% of the mixed dementia cohort (60). Vascular risk factors such as hypertension and diabetes have been found to contribute to the risk of dementia (61,62). Furthermore, reduced CBF has been found in the frontal and parietal cortices of some dementias including AD (63). Small bleeds into tissues or regions of focal ischemia in the brain may bring about vascular dementia. Disentangling the exact contribution of vascular disease in dementia is difficult (24,60,63,64). The prevalence of vascular dementia may be underestimated as patients that suffer primarily from vascular forms are often diagnosed with another form of dementia. Treatments for vascular dementia are somewhat limited, and are mainly restricted to appropriate management of risk factors (65).

Cerebral amyloid angiopathy (CAA) is a specific small-vessel disease involving the deposition of amyloid-beta ($A\beta$) protein in or near the vessel wall (11). CAA can be either sporadic or hereditary (several genes have been isolated as risk factors for the

disease (66)). Population prevalence of CAA increases with age and is 2.3% for those 65 to 74 years, 8.0% for those 75 to 84 years, and 12.1% in those over 85 years (67). Half of individuals over 80 years show some markers of CAA pathophysiology on imaging and CAA is considered responsible for between 5% and 20% of all spontaneous intra-cerebral hemorrhages. CAA has many commonalities with AD and was found in 89% of brain autopsies in an AD cohort of 1110 subjects (60). CAA generally presents near the small arterioles of the brain and is most commonly found in the occipital lobe. Microbleeds, fibrosis and micro-aneurysms are all commonly found in the affected blood vessels (11). The treatment options for CAA are limited. CAA has been considered a risk factor for bleeding during thrombolysis therapies (68).

2.4.5 Arteriovenous Malformation (AVM)

An AVM is an abnormality where the arterial system directly connects to the venous system, bypassing the capillary bed. AVMs inherently have fast flow and low resistance. They effectively shunt blood between the arterial and venous systems, which often creates abnormal and tortuous flow patterns. Blood from the arterial system is shunted directly through to the venous system, which is not designed to handle higher arterial blood pressures. AVMs have a relatively low prevalence (ranging from 0.018% to 0.1% (69,70)) in the adult population. The risks of AVM include: backflow from the venous system to the arterial system, increased venous pressure, venous stenosis and aneurysms, thrombus, high wall shear stress, and hemorrhage. The risk of bleeding from an AVM is high: 2% per year for AVMs without evidence of bleeding and 18% in the first year post-rupture (70). AVMs are responsible for 9% of all subarachnoid hemorrhages and 1% to 2% of strokes. Since AVMs tend to occur in young adults it contributes greatly to strokes in this population. The alterations of blood supply can also increase the risk of patients developing *de novo* seizures (~1% risk of seizures per year (70)). The cause of these malformations is due to expression of vascular endothelial growth factor (VEGF), and has been associated with genetic mutation and angiogenic stimulation in murine models (71). Treatment of AVMs includes medication and embolization of the vascular shunts linking the arterial and venous systems. Embolization is generally performed with

stereotactic radiosurgery or by endovascular therapy (endovascular therapy is preferred for larger AVMs (72)).

2.4.6 Neoplasm

Several types of brain tumors can become vascularized and/or develop associated malformations of the vascular system. MR imaging can be exploited to obtain knowledge of tumors for management or therapy. Tumors in the brain tend to be angiogenic with new vessels growing in patterns differing from the previously described healthy case. The vasculature changes also cause regions of tissue within the tumor to receive inadequate blood flow and become necrotic. In many cases the vessel wall remains intact but some cells are replaced by cancerous cells. This infiltration weakens the vessel wall, increasing BBB permeability and thus increasing the risk of hemorrhage. Viscosity of the blood is known to change in brain tumors due to changes in hematocrit, primarily resulting from the presence of cancer cells in the blood (73). Changing viscosity can alter several hemodynamic parameters, such as flow resistance and wall stress. Vessel wall structure may become altered within the brain tumor (74). The velocity of blood within the tumor has also been shown to change so that cell velocities in arteries and veins become indiscernible, unlike in normal brain tissue (74). It has been known for some time that the vessel diameter of the microstructure in tumors will be larger than the vessel diameter in normal tissue (75), potentially leading to increased CBV. The treatments for tumors include medical and radiation therapy, and surgical removal. Treatments with radiation therapy are known to alter flow characteristics (76) and can be monitored with angiography. Anti-angiogenic pharmaceutical therapies may also be effective at tumor reduction (77).

2.4.7 Summary

Numerous diseases affect the cerebral vascular system. In this section, some of the more common conditions were described with a brief synopsis to better understand how MR imaging can be useful in the assessment of each disease was provided. The next section compares the angiography methodologies that do not utilize MR.

2.5 Current Cerebrovascular Imaging Techniques

Routine medical imaging of the cerebrovascular system is performed with different methods, including: x-ray digital subtraction angiography (DSA), computed tomography (CT), ultrasound (US), nuclear medicine (primarily with positron emission tomography, PET), and MR imaging. This section discusses the first four of these methods to provide perspective on the relative strengths and weaknesses of each modality for imaging the cerebral vasculature. It concludes with a general comparison of x-ray DSA, CT, US and PET versus MR imaging for assessment of common cerebral vascular diseases. In the following section, specific applications of a variety of MR approaches are overviewed.

2.5.1 X-ray Digital Subtraction Angiography - DSA

X-ray DSA imaging is often seen as the gold standard method for performing cerebrovascular angiography studies (78-80). DSA imaging works by collecting an image with no contrast agent in the blood, and then subtracting it from subsequent images while an iodine-based contrast agent is injected. The resulting difference of the two images shows only the passage of the contrast agent in the vascular system, rendering a good depiction of the filling and washout in the vessel lumen. DSA benefits from the high temporal and spatial resolutions obtainable with x-ray imaging systems. Although modern systems can collect images faster and with higher resolution, acquired pixels are usually 0.1 mm^2 and images are typically collected at 4 to 15 frames per second (Hz). Higher spatial and temporal resolutions are possible but their acquisition is practically limited by minimizing radiation exposure. Intra-arterial (IA) administration of the iodinated contrast agents through endovascular catheters is preferred (over IV) as it maximizes vascular image contrast and allows the flow in different vessels to be evaluated independently. DSA uses a catheter to administer a forced injection of contrast agent, affecting the hemodynamics. Modern x-ray fluoroscopy suites used for DSA are often equipped with bi-planar imaging systems that allow two projection images at different angles to be collected during a single contrast agent injection. On some systems, these detectors can rotate during the injection to collect 3D tomographic images (79), but this reduces temporal resolution and increases radiation dose.

2.5.2 Computed Tomography - CT

Modern computed tomography (CT) systems are widely available and can perform a variety of cerebrovascular imaging examinations. A non-contrast examination can cover the whole brain in ~165 ms using a multi-slice scanner (81,82). CT allows for detection of hemorrhage and for this reason has a major role in identifying ischemic stroke patients for IV thrombolysis therapy (83).

CT angiography (CTA) is based on the same principle as x-ray imaging, and acquires data during the passage of an iodine-based contrast agent through the vasculature. CTA studies can utilize an IV injection (rather than IA injection) and time the data acquisition to when the contrast agent passes through the arteries under study. CTA can be performed with or without subtracting a previously acquired unenhanced image. Typical CTA examinations provide images with high spatial resolution (0.4 mm³ pixels) (82). As was the case with x-ray DSA imaging, higher resolutions can be achieved but at the cost of increased radiation dose.

In the late 1970s, CT perfusion (CTP) was first proposed in humans by using xenon-133 as a tracer (84). Xenon-133 is non-radioactive and readily crosses the BBB, resulting in a change in the x-ray attenuation of brain tissue. Xenon uptake in GM has been shown to relate to CBF (84,85). Xenon-based CTP examinations take approximately 5 minutes and due to quick washout of xenon from the tissue can be repeated after 15 min to 20 min. Limitations of xenon CTP include headache, nausea, reduced respiratory rate and hallucinations. Xenon also has anesthetic effects which can confound its use in some studies (86). A second and now more common way to measure perfusion with CT is by rapidly imaging an iodine-based contrast agent as it passes through the brain tissue (87,88). Bolus-passage CTP has now been implemented on many commercial systems and has proven useful in measuring key perfusion parameters, including: CBF, CBV, MTT, TTP (21) and, more recently, BBB permeability (89). Radiation exposure during bolus passage CTP examinations is higher than conventional CT imaging, as the images need to be repeatedly acquired during the contrast agent passage.

Radiation exposure is a principle limitation to CT-based imaging of the cerebrovascular system. Typical exposures for CT, CTA and bolus passage CTP are 1.7

mSv, 1.9 mSv, and 5.0 mSv respectively (90). A full stroke CT imaging work-up is estimated to result in an exposure of 9.5 mSv and a local radiation dose of up to 444 mGy (90). Accumulated dose from x-ray and CT examinations is a great limitation to their repeated use. While the diagnostic benefit of CT imaging is clear, the overall benefit of using CT, particularly CTP, requires additional scrutiny due to risks associated of radiation exposure (91).

2.5.3 Ultrasound - US

Imaging in the brain with ultrasound (US) is difficult because of the large reflection from tissue-bone interfaces and attenuation of ultrasound waves by the cranium (skull). Transcranial Doppler US (TCD US) represents a specialized technique (92) and an exception to this general statement. TCD US exploits specific areas of the cranium that are relatively thin and can acquire images of some of the major intracranial vessels including the distal ICA, PCA, CoW and MCA. TCD US fails in some subjects who do not have appropriately thin bone. In general, it is not effective at examining other vessels in the brain. Extra-cranially, US imaging of the carotid artery is not limited by the skull and is an effective, commonly used approach, to study the carotid arteries. In particular, US is used to determine the presence and severity of atherosclerotic plaques in carotid arteries (93,94). An important variant, based on the Doppler principle, is used to provide blood velocity in the carotid arteries (95). Perfusion measurements in the vessel wall and plaque have recently been demonstrated using micro-bubble enhanced ultrasound (96). The reactivity of the vasculature can be assessed with TCD while the patient performs a carbon dioxide inhalation challenge (97,98).

2.5.4 Nuclear Medicine Imaging including PET

Nuclear medicine-based approaches can be used when functional cerebrovascular metrics are desired (99). All nuclear medicine-based approaches use an injected radioactive agent and produce activity maps of the uptake of this agent in tissue. Typically parametric images of function are generated. These parametric maps are often superimposed on anatomical maps that are acquired with CT or MR. Most nuclear medicine approaches use gamma-emitting radioisotopes and are generally capable of making only semi-

quantitative measurements. Positron emission tomography (PET) is an exception; it uses co-incidence detection of co-linear photons. With appropriate kinetic modeling, PET can generate quantitative images. In general, nuclear medicine approaches are slow and have lower temporal and spatial resolution and their application is primarily limited to imaging the chronic phase of cerebrovascular disease.

PET imaging is often considered to be the gold standard (100) for measuring perfusion metrics, and provides estimates of glucose uptake, CBF, and CBV (101). Most PET scans employ 18-fluorine fluorodeoxyglucose to study the uptake of glucose. The half-life of 18-fluorine is 110 minutes, which is sufficiently long to allow shipping from production to imaging facilities. It has been recently shown that fluorodeoxyglucose can also be effective for imaging metabolically active carotid artery atherosclerotic disease, with IV-administered radiopharmaceuticals (102,103). PET imaging has some disadvantage: it has a lower spatial and temporal resolution than the other described imaging modes and is thus not effective at generating images of the macroscopic vasculature.

PET brain perfusion experiments can be performed either statically or dynamically by inhalation of 15-oxygen gas. Due to the short half-life of 15-oxygen (2 min) this isotope must be produced using an onsite cyclotron. Measurement of the arterial input function activity is required with invasive arterial blood sampling. In dynamic studies, a model fitting or a convolution model relationship between the arterial function and the tissue activity is used to estimate CBF (104). Measures of CBF derived from PET and MR have been compared during sub-acute ischemic stroke giving comparable results (105). Although PET is considered the gold standard for brain perfusion imaging, its cost is high relative to other imaging modes, it is more invasive, and thus is often less preferred.

2.5.5 Non-MR Imaging of the Cerebrovascular System

MR is considered to be a safe modality, particularly when comparing to alternatives that require ionizing radiation such as x-ray, CT and PET. The perceived weaknesses of MR imaging are generally thought to be the higher cost of the equipment and its operation, and the longer scan times required for examinations. Compatibility of some patients with

MR is also a concern, *i.e.*, the challenges of ensuring MR-compatibility of an aphasic and unaccompanied ischemic stroke patient. Contradictions to MR, such as a medical implants, suggests that CT imaging should sometimes be preferred. Although here the use of MR-based angiographic approaches is advocated, it is important to recognize that MR is not always the primary cerebrovascular imaging method for some patients.

2.6 MR Imaging and Contrast Agents

2.6.1 Basic Principles of MR Imaging

Clinical MR imaging typically measures the magnetic flux from 1-hydrogen nuclei in an externally applied magnetic field. Other nuclei (including 13-carbon, 23-sodium, 31-phosphorous) can produce a measureable, albeit much smaller MR signal, however, these and other isotopes are rarely used in clinical MR imaging. When in a magnetic field, \mathbf{B} , the 1-hydrogen nuclei precess (or spin) at the Larmor frequency, $|\omega| = \gamma\mathbf{B}$, where $\gamma = 42.57 \text{ MHz T}^{-1}$ for 1-hydrogen. A net magnetization results from an ensemble of 1-hydrogen nuclei. The precessing net magnetization results in a measured MR signal that is complex valued, *i.e.*, having both real and imaginary components (or equivalently described by magnitude and phase components). Normally the magnitude of this signal is used to create images. However some cerebrovascular imaging techniques also use information from the phase of the signal as well.

Excitation of the 1-hydrogen nuclei is achieved by application of radio frequency (RF) pulses applied to the subject. Spatial localization of the resulting emitted signal is achieved by application of three orthogonal magnetic gradients that are varied in time. The time course of the applied RF pulse and gradient fields determines the characteristic of the MR images and is referred to as a pulse sequence. In MR imaging the RF excitation and measurement of resulting echoes is repeated many times, each time with a different spatial encoding. The time required to acquire an image can vary from a few seconds to many minutes. When the sampling is completed, the acquired MR data is processed (typically by applying an inverse Fourier transform) to obtain an image. The time between successive RF excitations is known as the repetition time (TR) and the time between RF excitation and the echo formation is known as the echo time (TE). The

amount of RF excitation is another important parameter and is denoted by the flip angle (α).

A phenomenological equation, the Bloch equation (106-109), governs the evolution of MR magnetization over time,

$$\frac{d\mathbf{M}(t)}{dt} = \gamma(\mathbf{M}(t) \times \mathbf{B}(t)) - \frac{M_x(t) + M_y(t)}{T_2} - \frac{M_z(t) - M_0}{T_1} \quad \text{Eq 2.1}$$

where $\mathbf{M}(t)$ is the magnetization; $M_x(t)$, $M_y(t)$, and $M_z(t)$ are the x , y and z components of $\mathbf{M}(t)$; γ is the gyromagnetic ratio; and $\mathbf{B}(t)$ is the time varying total applied magnetic field. T_1 and T_2 are the longitudinal and transverse relaxation times, respectively, and are both intrinsic properties of the tissue being imaged.

Examples of the two primary classes of MR imaging pulse sequences are shown in Figure 2.3. The two sequence classes are spin echo (SE) and gradient-recalled echo (GRE). Each sequence uses a combination of RF and gradient pulses to form a measurable echo. With SE a second RF pulse is combined with gradients to form an echo, which is then sampled. In GRE, only gradients are used to form the echo. SE sequences produce higher signal-to-noise ratio (SNR) images and are often less susceptible to image artifacts. However, they are slower and, as a result, the majority of MR angiographic sequences are derived from the faster GRE sequences. Eq 2.1 predicts the signal evolution for SE sequences. Typically, $\alpha = 90^\circ$ with SE imaging. For GRE sequences α can vary, however, the shorter T_2^* relaxation time must be used instead of T_2 in Eq 2.1. Sequences with short TR and TE are said to have predominantly T_1 -weighting. When TR and TE are long, the images are predominantly T_2 - (SE) or T_2^* - (GRE) weighted. T_1 -weighted sequences are commonly used to see vessels (described later in the time-of-flight and contrast-enhanced imaging subsections); whereas, T_2^* -weighted images are used in susceptibility imaging approaches.

MR can be used to acquire two- or three-dimensional (2D or 3D, respectively) images. In 2D imaging a set of slabs are excited and spatial information is separately encoded by the gradients in the other two dimensions. The excited slabs can be contiguous or be separated in space. With 3D imaging, a single, thicker slab is excited and spatial information is encoded in all three dimensions. Three-dimensional MR

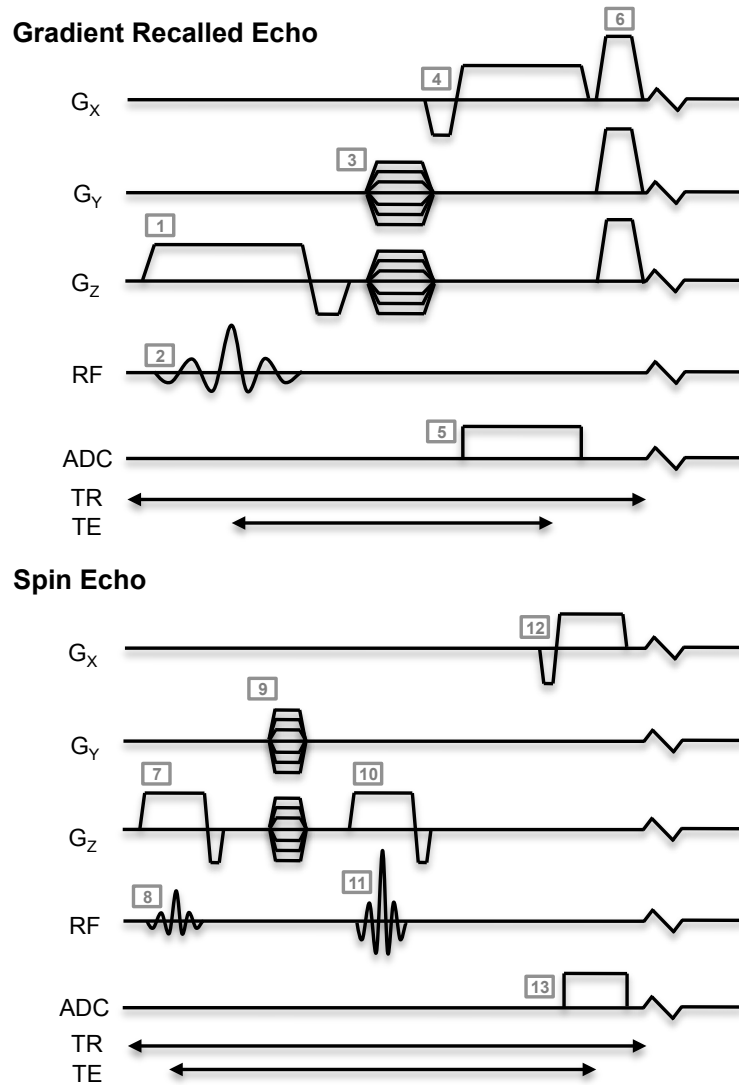


Figure 2.3: Fundamental MR imaging sequences. Most imaging sequences can be classified as either gradient-recalled echo (GRE, top) or spin echo (SE, bottom). The G_x , G_y , and G_z curves represent the strength of the gradient magnetic field time along the x-, y- and z-directions, respectively. The RF curve labels the radio frequency signal and the analog-to-digital converter (ADC) indicates when the MR signal (or the echo) is sampled. TR and TE are the sequence repetition time and echo time, respectively. The gradient, RF and ADC pulses are labeled 1 through 13. Pulses 1, 2, 7 and 8 form the slab-selective (along the z-direction) excitation. Pulses 3 and 9 are the phase encoding gradients for spatial encoding along the y-direction. Pulses 4 and 12 are the readout gradients, which are on when the ADC is turned on (pulses 5 and 13) in order to spatially localize along the x-direction. Pulses 10 and 11 form the slice-selective SE refocusing pulse.

acquisitions have better spatial resolution in the slab-encode direction and improved SNR compared to 2D approaches, but typically take longer to acquire and therefore are more susceptible to image artifact from patient motion. In many angiographic applications of the neck and brain, 3D imaging is preferred to better visualize complex vascular structures. Frequently, maximum intensity projection (MIP) angiographic images are formed by post-processing the acquired 3D data (110,111).

Over the last 15 years several methods have been proposed to reduce the acquisition time of MR imaging. All of these methods incur some penalty in image quality, such as decreased SNR, or are more susceptible to image artifacts. Accelerating MR angiography has proven to be very useful as the SNR is generally high, and an increase in imaging rate allows better capture of dynamic processes. Some of the key acceleration techniques include: time-resolved imaging of contrast kinetics (TRICKS) (112), simultaneous acquisition of spatial harmonics (SMASH) (113), sensitivity encoding (SENSE) (114), partially parallel imaging with localized sensitivities (PILS) (115), generalized autocalibrating partially parallel acquisitions (GRAPPA) (116), compressed sensing (CS) (117), and iterative self consistent parallel imaging reconstruction from arbitrary k-space (SPIRiT) (118). In addition to high SNR, the sparsity of MRA is also important for the CS-related methods. There are many acceleration methods in addition to those mentioned here. Accelerating MR imaging has and continues to be a focus of research for many, the benefits of which are observed when collecting a variety of MR angiograms.

Subsequently, when discussing specific MR techniques, the pulse sequence and image reconstruction processes used by that method are briefly reviewed. For a more thorough discussion of MR imaging and systems please refer to the following sources, Refs (119-126).

2.6.2 MR Contrast Agents

Contrast agents are an important part of many cerebral vascular examinations and a brief summary and their effects are warranted prior to fully describing the MR angiographic imaging techniques. Many contrast agents have been proposed based primarily around the magnetic properties of small iron particles or gadolinium ions (127-131). Iron-based

contrast agents also shorten relaxation times but can cause undesired susceptibility, require larger volume injections, and have only been approved in a few jurisdictions. Gadolinium-based MR contrast agents are more widely used. Gadolinium ions cause local perturbations to the magnetic field and are thus efficient modifiers of the measured MR signal. Table 2.2 summarizes the most commonly used gadolinium-containing contrast agents.

A key property of gadolinium-containing contrast agents is the relaxivity. They change the relaxation properties with changing concentrations in the blood. The change in T_1 or T_2^* can be estimated analytically in solutions. Although the relaxivities are not perfectly linear with concentration (132), a linear approximation for the relationships $T_1 = 1/R_1$ and $T_2^* = 1/R_2^*$ provides guidance,

$$\begin{aligned} R_1 &= R_1|_0 + \kappa_1 \cdot [Gd^{3+}] \\ R_2^* &= R_2^*|_0 + \kappa_2^* \cdot [Gd^{3+}] \end{aligned} \tag{Eq 2.2}$$

where $R_1|_0$ and $R_2^*|_0$ are the contrast-agent-free relaxivities of blood, $[Gd^{3+}]$ is the concentration of gadolinium in the blood, and κ_1 and κ_2^* are the linear relaxivity constants. The relaxivity constants vary across contrast agents but are generally in the range of $4.4 \text{ L mmol}^{-1} \text{ s}^{-1}$ and $30 \text{ L mmol}^{-1} \text{ s}^{-1}$ for κ_1 and κ_2^* , respectively at 3 T (133-135). The relaxivities of contrast agents are known to change with field strength (136).

Gadolinium ions (Gd^{3+}) are toxic and if directly administered can bond to and otherwise interfere with the function of a number of biological molecules. To ensure safety, gadolinium-containing contrast agents are chelated to prevent the ion from interacting with other molecules. Chelation results in a more stable compound and improves solubility. However, there still exists a potential for undesired biological effects. Reports have been made of acute hypersensitivity (*e.g.*, headaches, nausea, dizziness, vomiting, and allergic reactions in a small number of subjects (137)) and, more recently, gadolinium-containing agents have been implicated in nephrogenic systemic fibrosis (NSF) in a small group of patients (138,139). There is emerging evidence to support the hypothesis that subjects with renal insufficiency may be at higher risk for NSF because their biological clearance time for contrast agents is increased (138-140), and that adjusting hospital policy may mitigate this risk (141,142).

Table 2.2: List of commonly available gadolinium-containing contrast agents used in MR imaging. Table derived from references in the table and the European Medicines Agency and Food and Drug Administration web sites accessed 1 June 2014. Note that the listed agents may not be marketed in all jurisdictions.

Agent		Approval		References
Trade Name Abbreviation	Marketed Name (Manufacturer)	EU	US	
Gadobenate Gd-BOPTA	MultiHance® (Bracco Imaging SpA, Milan, Italy)	✓	✓	(143-146)
Gadobutrol Gd-DO3A-butrol	Gadovist® (Bayer Schering Pharma AG, Berlin, Germany)	✓	✓	(147-149)
Gadodiamide Gd-DTPA-BMA	Omniscan® (General Electric Healthcare Inc., Princeton, NJ, USA)	✓	✓	(150-152)
Gadofosveset trisodium MS-325	Ablavar®/Vasovist® (Bayer Schering Pharma AG, Berlin, Germany)		✓	(153-156)
Gadopentetate dimeglumine (Gd- DTPA)	Magnevist® (Bayer Schering Pharma AG, Berlin, Germany)	✓	✓	(143,157-161)
Gadoterate meglumine Gd-DOTA	Dotarem® (Guerbet GmbH Sulzbach, Germany)	✓		(158,159,162- 164)
Gadoteridol Gd-HP-DO3A	ProHance® (Bracco Imaging SpA, Milan, Italy)	✓	✓	(165-168)
Gadoversetamide Gd-DTPA-BMEA	OptiMARK® (Mallinckrodt Inc., Hazelwood, MO, USA)	✓	✓	(169-171)
Gadoxetate disodium Gd-EOB-DTPA	Eovist® (USA)/Primovist® (EU) (Bayer Schering Pharma AG, Berlin, Germany)	✓	✓	(172,173)

EU = European Union, US = United States of America

2.7 Chapter Summary

In this chapter, cerebrovascular anatomy and common pathologies, alternative modes of cerebrovascular imaging, and the basics of MR imaging and contrast agents are reviewed. The content discussed in this chapter will be built upon in later chapters. In the next chapter the focus will be set upon different types of cerebrovascular MR imaging, such as phase contrast.

Chapter Three:

**Review of Cerebrovascular MR
Imaging Methods**

3.1 Chapter Overview

There are a host of available MR acquisition schemes for obtaining images and quantifying different aspects of the cerebrovascular system. Cerebrovascular imaging is of great interest in understanding neurological disease. Magnetic resonance (MR) imaging is one technology that can non-invasively visualize and provide information about: 1) the structure of major blood vessels, 2) the blood flow velocity in these vessels, and 3) the microcirculation, including assessment of perfusion. While other medical imaging modalities can also interrogate the cerebrovascular system, MR provides the most comprehensive assessment as it can acquire many different structural and functional image contrasts while maintaining a high level of patient comfort and acceptance. The extent of the examination is only limited by the practicalities of patient tolerance or clinical scheduling limitations. Currently, MR imaging methods can provide a range of metrics related to the cerebral vasculature, including: 1) major vessel anatomy, via time-of-flight and contrast-enhanced imaging, 2) blood flow velocity, via phase-contrast imaging, 3) major vessel anatomy and tissue perfusion, via arterial spin labeling and dynamic bolus-passage approaches, and 4) venography, via susceptibility-based imaging. When designing an MR imaging protocol for patients with suspected cerebral vascular abnormalities, it is appropriate to have a complete understanding of when to use each of the available techniques in the “MR angiography toolkit”.

3.2 Magnetic Resonance Angiographic Techniques

MR angiographic imaging draws upon a wealth of available contrast mechanisms, many of which can be used to provide high-quality diagnostic images of the blood and blood vessels. Depending on the method chosen, information can be obtained about the arterial system, the venous system, the capillary bed, or a combination. Several available MR methods exist to investigate the cerebrovascular system and new methods are continually being proposed, developed and evaluated. The principle established and emerging methods presented in this review include: 1) time-of-flight (TOF) imaging, 2) phase contrast (PC) imaging, 3) contrast-enhanced (CE) imaging, 3) arterial spin labeling (ASL), 4) dynamic bolus passage imaging, and 5) T_2^* -weighted imaging (including:

susceptibility-weighted imaging (SWI) and quantitative susceptibility mapping (QSM)). In the following subsections each of these MR methods is described by contrast mechanisms, pulse sequence implementations, key features and sensitivity to important cerebrovascular parameters, and provide examples (obtained at 3 T) of where their application may be useful in diagnosis of cerebrovascular disease.

3.2.1 Time-of-flight Imaging - TOF

TOF imaging is one of the most popular and perhaps the oldest technique for cerebrovascular MR. TOF imaging relies on the differential effects between stationary background tissues and flowing blood to provide images with bright blood and low tissue signal. The term TOF is actually a misnomer, since the blood-to-background contrast is derived from the static tissue being repeatedly excited by the applied RF pulses, causing the steady-state magnetization signal to be reduced. This effect is more correctly described as signal saturation. Blood that flows into the excited volume has not yet been affected by these pulses and is thus unsaturated, resulting in considerably more MR signal from the blood than from the background tissue (174,175). TOF imaging uses a GRE sequence, which has a short TR and is inherently T_1 -weighted. TOF imaging has also been shown to improve with increased magnetic field strength, not only because there is an increase in the bulk magnetization, but there is also an increase in background tissue T_1 with increased field strength, which improves the contrast between the blood and background tissues. Adding gadolinium-containing contrast agents to the blood will further decrease T_1 and enhance the blood-to-background signal difference but at the cost of preventing venous suppression (described below) (176).

Figure 3.1 shows a conceptual explanation of the TOF inflow effect and the expected signal difference for several T_1 values. The measured signal of background brain tissue is easy to establish as it can be assumed to be at the steady state. The expected steady state signal value of a spoiled gradient-recalled echo (SPGR) TOF image can be derived from Eq 2.1 and can be expressed mathematically by,

$$S_{MR} = M_0 e^{-TE/T_2^*} \frac{1 - e^{-TR/T_1}}{1 - e^{-TR/T_1} \cos \alpha} \sin \alpha \quad \text{Eq 3.1}$$

where S_{MR} is the steady-state MR signal intensity, and α is the flip angle. Spoiling refers

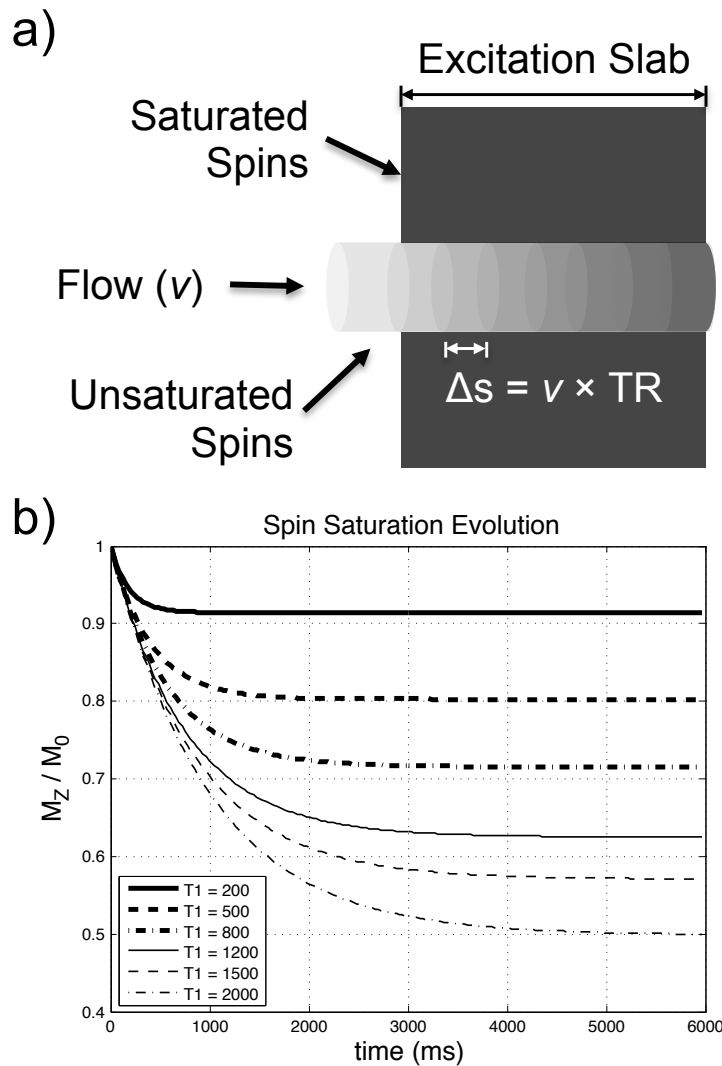


Figure 3.1: Evolution of MR magnetization during time-of-flight (TOF) imaging. (a) Blood-to-background contrast in TOF is due to the saturation of the signal from repeated RF excitations. Blood moving with a velocity, v , and has large initial magnetization prior to entering the excitation slab. Once within the excitation slab the blood experiences more excitation pulses, becomes saturated and the measurable signal is decreased. However, prior to each excitation, new unsaturated blood enters the excitation slab. The signal from blood is therefore a function of the T_1 of arterial blood (2100 ms at 3 T), the blood velocity, the TR and the slab thickness (Δz). (b) Signal saturation as a function of the time that the blood has been in the imaging plane, shown for different values of T_1 . Background tissue T_1 in the brain is approximately 1,500 ms at 3 T. Blood and tissue with shorter T_1 values recover faster and are less suppressed. Adding gadolinium-containing contrast agent to the blood shortens the T_1 resulting in higher signal in TOF and CE MRA images. The parameters used for the simulation in b were TR = 30 ms, TE = 2.6 ms, and $\alpha = 10^\circ$.

to destroying any coherent transverse magnetization (M_x and M_y) at the end of each TR interval. The signal of the blood is more difficult to establish as it is a function of both signal saturation and the flow velocity (as illustrated in Figure 3.1a). For thicker excitation slabs, the blood in the more distal vessels will have seen many RF pulses and thus this signal will be lower compared to unsaturated blood just entering the volume. It is for this reason that TOF imaging is generally performed with either a series of 2D slices or with several thin 3D slabs. Figure 3.2 compares two TOF acquisitions acquired with a series of thick and thin 3D slabs. The loss of blood-to-background contrast is readily apparent in the superior portions of the thick slab data, leading to the ‘venetian blind’ artifact.

Suppression of the venous vessels in TOF can be achieved by application of saturation pulses to regions superior to the imaging slab(s) (177,178). The effect of flip angle on arterial and venous blood-tissue contrast is also worth understanding (177,179,180). Increasing the flip angle increases the level of saturation in both tissue and blood. Slower flowing venous blood will also become more saturated, thus higher flip angles are effective at visualizing the faster moving blood in the arterial system while lower flip angles can be used to visualize both veins and arteries (Figure 3.3).

Ramped RF pulses can be applied to change the flip angle across the slab (and thus attempt to compensate for differential saturation of blood across the imaging slab) with the objective of keeping the contrast between blood and tissue high even in the more superior vessels (181). Commonly a linear ramp pulse reduces the flip angle linearly in the inferior-superior direction across the slab in order to limit the saturation of inflowing blood. With the onset of acceleration techniques and higher field magnets TOF imaging has continued to improve (177,182-185). Higher spatial resolutions permit visualization of the smaller vessels, such as the lenticulostriate arteries (183). Imaging at field strengths greater than 3 T also provides for improved SNR in TOF imaging (186).

A somewhat analogous TOF effect can also be employed with SE imaging. TOF effect for producing high blood-background contrast (with bright blood signal) with GRE sequences has been described. Conversely, by using SE sequences and longer echo times, black-blood (BB) contrast can be obtained (187,188). In BB imaging, the blood

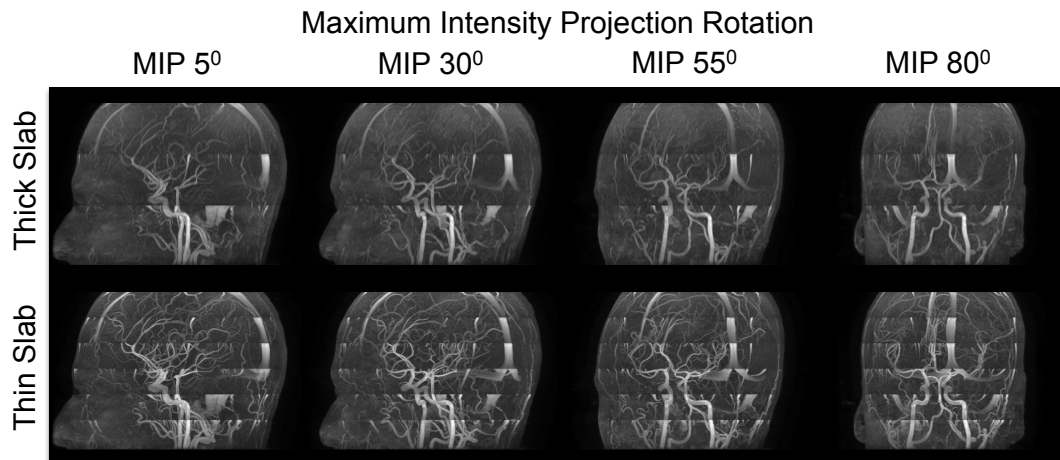


Figure 3.2: Example 3D time-of-flight (TOF) acquisition. (Top) 32-mm thick slabs and (bottom) thinner 16-mm thick slabs. Each row presents a maximum-intensity projection (MIP) image from several angles about the superior-inferior axis. A more subtle effect is the loss of arterial conspicuity in superior segments for small vessel where the blood is slower moving. Overlapping of the slabs is performed to reduce the apparent seams. 3D TOF sequence acquisition parameters were: TR/TE/ α of 22 ms/2.6 ms/15°, FOV of 24 cm \times 24 cm, 320 \times 224 acquisition matrix, receiver BW of \pm 31.25 kHz, and sensitivity encoding acceleration of 2. The excitation parameters were (top) 3 slabs of eight 2-mm slices with an overlap of 2 slices or (bottom) 6 slabs of 16 1-mm slices with an overlap of 4 slices.

appears dark (relative to the stationary tissue) because the blood that was initially excited, moves away from the acquisition volume before the signal is refocused by the SE refocusing RF pulse. Typically BB imaging uses a SE derivative, known as fast spin echo (FSE), that more efficiently collects a train of echoes per excitation. In principle, BB imaging should provide images of the blood vessel wall without flow artifacts from the blood (187).

TOF imaging is useful for the assessment of a wide range of cerebrovascular diseases, including ischemic stroke, carotid atherosclerosis, and vessel malformations such as AVMs or vascular tumors. With the potential to visualize the lenticulostriate arteries, it has been suggested that high-resolution TOF imaging eventually may be useful for evaluating small vessel disease (183). Nonetheless, current TOF techniques are inherently good for imaging the macroscopic arteries and veins. For ischemic stroke, occlusion in the ACA, MCA and PCA can be typically observed with TOF imaging, and

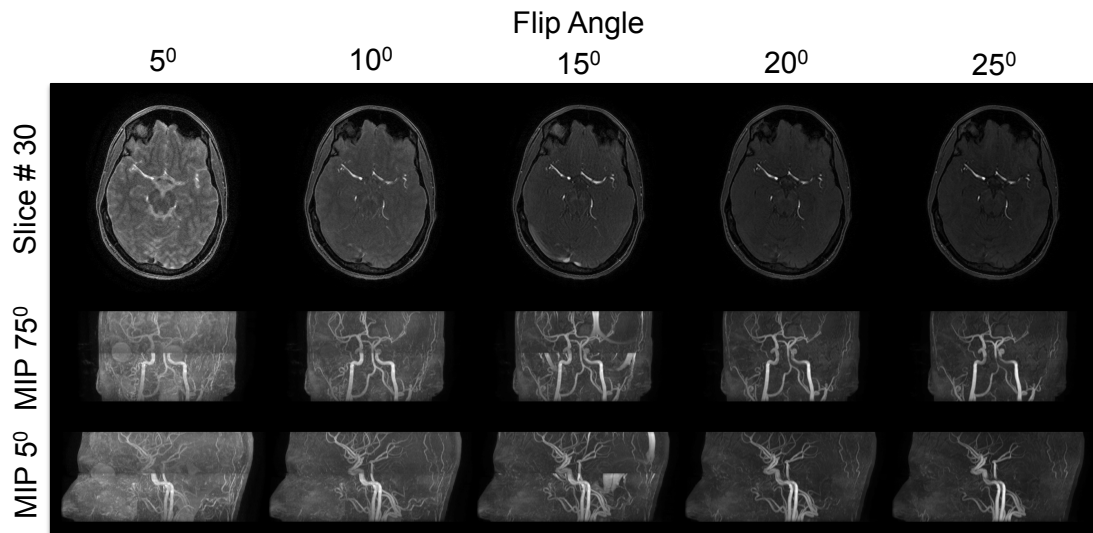


Figure 3.3: Time-of-flight (TOF) image acquisitions with variable flip angle. Shown are a central slice from the acquired volume and MIP images at 5° and 75° rotation about the superior-inferior axis relative to the anterior-posterior axis (0°). As apparent from Eq 3.1 an increased flip angle results in lower steady-state magnetization. This results in lower signal of the background tissue, but also reduces the signal from distal vessels. The effect of flip angle on TOF images is to reduce signal of the tissue and venous blood, while fast flowing blood in the arterial system, which does not see the same level of saturation, remains comparatively brighter. For the 3D TOF acquisition TR/TE were 22 ms/2.6 ms, 2 slabs were acquired each with twenty-two 2-mm thick slices.

for carotid atherosclerosis, both partial or complete occlusions, can be visualized. BB FSE imaging is effective for imaging the vessel wall (189,190), atherosclerosis (191,192), and for measuring vessel distensibility (193,194).

3.2.2 Phase Contrast Imaging - PC

PC imaging is based on the observation that a gradient magnetic field will affect the phase of the MR signal from moving blood differently than static tissue. PC imaging is typically developed from a GRE sequence by adding a bipolar velocity-encoding gradient pulse to encode blood velocity. This encoding process can be applied in three orthogonal directions to measure the velocity vector. Often in practice only the velocity magnitude (or speed image) is displayed, as analysis or rendering of vector fields can be time consuming. The generated speed image is used to form projection MR angiograms due to the absence of background tissue signal.

PC imaging uses two or more volume acquisitions to encode velocity. For the case of measuring velocity in one direction, two image data sets are acquired (with differing velocity encode settings) and the resulting image is derived from the difference in the measured phase of the MR signal. When the object is not static the first and potentially higher moments must be taken into consideration in developing an expression for phase,

$$\phi(\mathbf{r}, TE) = \gamma r_0 \int_0^{TE} G(t) dt + \gamma v_0 \int_0^{TE} tG(t) dt + \dots \quad \text{Eq 3.2}$$

where ϕ is the measured phase, \mathbf{r} is the spatial position, TE is the echo time, γ is the gyromagnetic ratio, $\mathbf{G}(t)$ is the time varying gradient in a direction, and \mathbf{v} is the velocity.

A typical pulse sequence diagram for PC imaging is shown in Figure 3.4. The acquisition is commonly performed with a velocity-sensitizing bipolar gradient. The measured phase difference ($\Delta\phi$) between the two acquisitions is linearly proportional to the velocity and difference in first moment of the bipolar gradients (195,196),

$$\phi_1 - \phi_2 = \Delta\phi = \gamma v \Delta M_G \text{ and} \quad \text{Eq 3.3}$$

$$v = \frac{\Delta\phi}{\gamma \Delta M_G} = \frac{\Delta\phi}{\pi} v_{enc},$$

where $\Delta M_G = \int_0^{TE} t\mathbf{G}(t) dt$ is the difference in first moments between the bipolar gradients, and v_{enc} is the operator-prescribed velocity encoding value ($v_{enc} = \pi/(\gamma \Delta M_G)$). If the blood velocity exceeds v_{enc} then velocity aliasing occurs and velocities within a vessel can appear as if they were moving in the opposite direction. This artifact occurs when measuring vessels with high velocity. For example, if v_{enc} is set to be 100 cm s^{-1} and the true blood velocity is 120 cm s^{-1} then the MR PC measurement will be 80 cm s^{-1} in the opposite direction. In normal practice to avoid velocity aliasing, v_{enc} is generally set to a value higher than the expected maximum blood velocity in the vessels under investigation. There are several encoding schemes, the one described here is a two-point method, though four- and six-point methods are required to encode in different directions (197). The popular four-point method typically uses a Hadamard encoding scheme. Non-linear gradient effects can contribute error to velocity measurements (198).

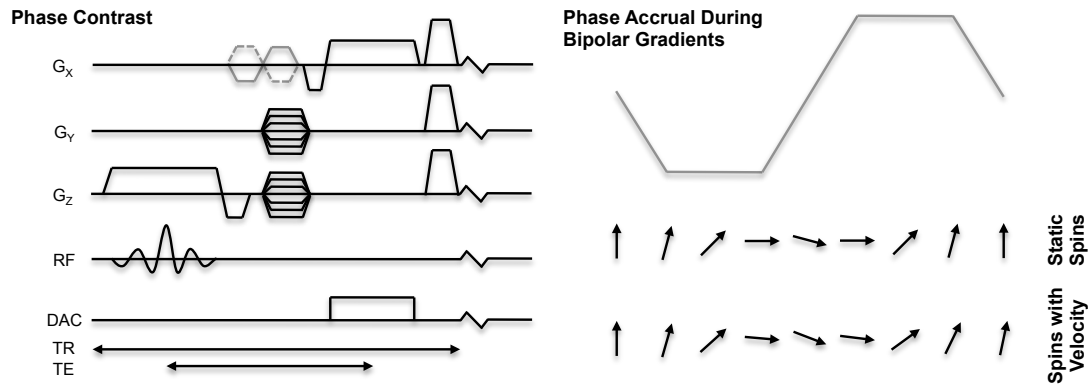


Figure 3.4: Phase contrast (PC) sequence diagram. This imaging sequence adds bipolar gradients (indicated in gray) to a GRE sequence. Velocity encoding along in the x-direction is shown. The image data is acquired twice to encode the velocity, once with the gradient using the solid gray line and once with the dashed gray line. Subtraction of the reconstructed phase images generates velocity measurements. The bipolar gradients can also be applied in the y- and z-directions to encode velocity in those directions.

PC imaging can be performed with cardiac gating to allow for an assessment of the blood velocities at various phases throughout the cardiac cycle. Both prospectively and retrospectively gated approaches can be used, but may result in undesirable temporal filtering of the cardiac waveform (199,200). Other useful functional parameters can also be derived from PC velocity measurements, including: volume-flow rate (VFR) (201,202), wall shear stress (WSS) (203), and vessel wall pressure (204). Knowing the pressure on the wall of a blood vessel or aneurysm has valuable prognostic implications. VFR can be calculated by taking the blood velocity and performing a surface integral across the vessel lumen. VFR is sometimes a more preferable functional metric than velocity, as the velocity can vary across the lumen and the flow volume better estimates blood supply through a vessel. Care needs to be taken to understand partial-volume errors (PVE) when integrating pixels that include wall and slowly moving blood (205).

Wall shear stress (τ_w) is a parameter of note when discussing atherosclerosis initiation and progression (206,207) and can be estimated with steady state Newtonian or

laminar flow models from PC velocity measurements. In many reports (203,208-212), wall shear stress is calculated as,

$$\tau_w = \mu \left. \frac{\delta v}{\delta \hat{r}} \right|_{r=wall} \quad \text{Eq 3.4}$$

where τ_w is the wall shear stress, μ is the dynamic fluid viscosity, \mathbf{v} is the fluid velocity, and \hat{r} is the radial direction of the vessel. Eq 3.4, although widely used for cerebrovascular fluid dynamic simulations, is somewhat limited; the equation only solves for wall shear stress in the steady state. Eq 3.4 also assumes the flow is Newtonian and does not provide information about the other stress tensor components. These assumptions may not always hold true due to vessel configuration or disease state (213). More advanced estimation using the Navier-Stokes equation can be employed (196,214-219),

$$\rho \left(\frac{d\mathbf{v}}{dt} + \mathbf{v} \cdot \nabla \mathbf{v} \right) = -\nabla \mathbf{p} + \nabla \cdot \mathbf{T} + \mathbf{F} \quad \text{Eq 3.5}$$

where ρ is the fluid density, \mathbf{p} is the driving hydrostatic pressure, \mathbf{T} is the total stress tensor, and \mathbf{F} represents the other forces acting upon the fluid. Accurately quantifying stress for pulsatile blood flow requires sophisticated computational fluid dynamics (CFD) analysis to properly model the flow in realistic geometries (203). In addition, the non-rigid nature of the vessel wall should also be modeled (220).

Example PC images are shown in Figure 3.5. Both images are derived from the same PC acquisition: one image is a projection angiogram calculated from the speed image and the other image is a streamline rendering depicting the steady-state velocity field. To generate the streamline image, a computational fluid dynamics simulation was performed with an open source software package (OpenFOAM; OpenCFD Ltd., Bracknell, UK). The velocity streamlines were rendered with a visualization tool (Paraview; Kitware Inc., Clifton Park, NY, USA). Other programs for computational fluid dynamics analysis that are capable of rendering such images include Enight (CEI Software, Apex, NC, USA), and Palabos (FlowKit CFD Solutions, Lausanne, Switzerland).

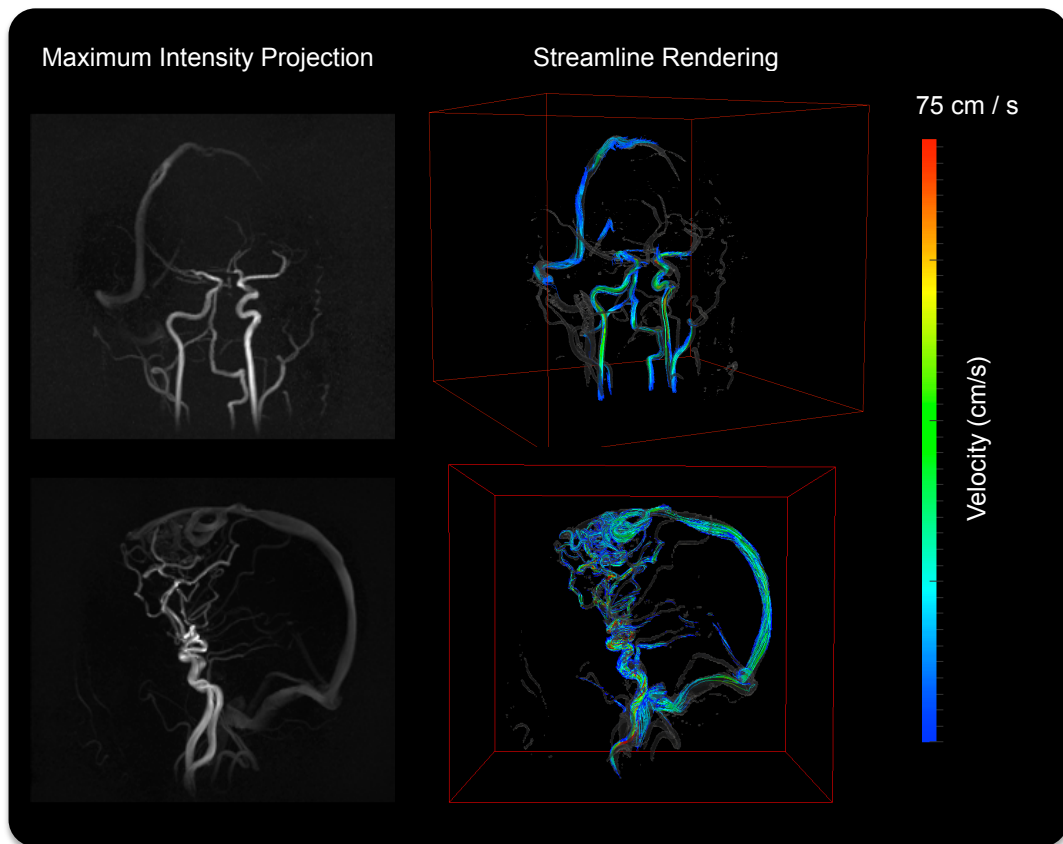


Figure 3.5: Phase contrast (PC) images. Showing (left) a maximum intensity projection (MIP) image through the speed data (velocity magnitude), and (right) isosurface (thresholded at 7 cm s^{-1}) and velocity streamline rendering. Color in the rendering shows the magnitude of the velocity (speed). The top row of the images shows normal vascular configuration, while the bottom row shows an example AVM patient. The acquisition parameters used to collect these images were TR/TE/ α /venc of 8.2 ms/3.83 ms/ 10° /150 cm s^{-1} . Spatial resolution was 1 mm isotropic and the total acquisition time was 8 min.

PC imaging is useful when assessing many diseases that alter blood velocity in the macroscopic vessels as the technique can provide high-resolution structural and functional information. Volume flow rate provides an important measure of the physiology. Hemodynamic information, such as pressure and wall shear stress, provided from PC data can be useful in assessing AVMs, carotid stenosis, and aneurysms.

3.2.3 Contrast-enhanced MRA - CE MRA

CE imaging is performed by injecting gadolinium-containing contrast agents (described previously) into the blood in a fashion similar to x-ray DSA and CTA imaging. Nearly always this injection is into a vein, with the exception that an IV injection is used and volumetric data is acquired, CE MRA is conceptually very similar to the way that x-ray DSA images are acquired. A fast 3D T_1 -weighted GRE image is collected before the contrast agent is injected and then another volume acquisition is collected when the contrast agent is in the blood vessels of interest. Normally the acquisition of the second volume is timed so that the arteries are enhanced but not the veins. If a venogram is desired, then the second volume is timed to coincide with venous enhancement. Subtraction of the pre- and post-contrast injection images leaves only the enhanced signals from the desired vessels. Example CE MR projection angiograms in the neck and brain are shown in Figure 3.6.

During a CE-MRA procedure, the acquisition sequence always utilizes the reduction in T_1 provided by the contrast agent to provide positive vascular contrast (*i.e.*, bright vessels). A fast GRE technique, such as a T_1 -weighted 3D SPGR, is usually used for CE MRA. Since they both use T_1 -weighted SPGR sequences, the previously described TOF effects can add to the CE effects (175). TOF images before and after contrast agent administration are shown in Figure 3.7. The TOF enhancement in the inferior vessels is clearly seen in the image without contrast. This TOF effect is combined with CE vascular enhancement in the post-contrast image. Post-contrast CE MRA is another variant that is used clinically, however, the simultaneous enhancement of both arterial and venous structures and of extra-cranial enhancing tissues is often undesired.

Because CE MR imaging uses a high SNR 3D acquisition, imaging speed can be accelerated significantly with methods such as time resolved imaging (221-224), constrained reconstruction (117,118,221,225,226) and parallel imaging (227-229). Imaging acceleration rates of up to 36 \times have recently been demonstrated (230). Image acceleration methods have the effect of reducing the SNR, but since CE imaging has inherently high SNR (compared to some other MRA methods) the visual quality of the images is generally acceptable.

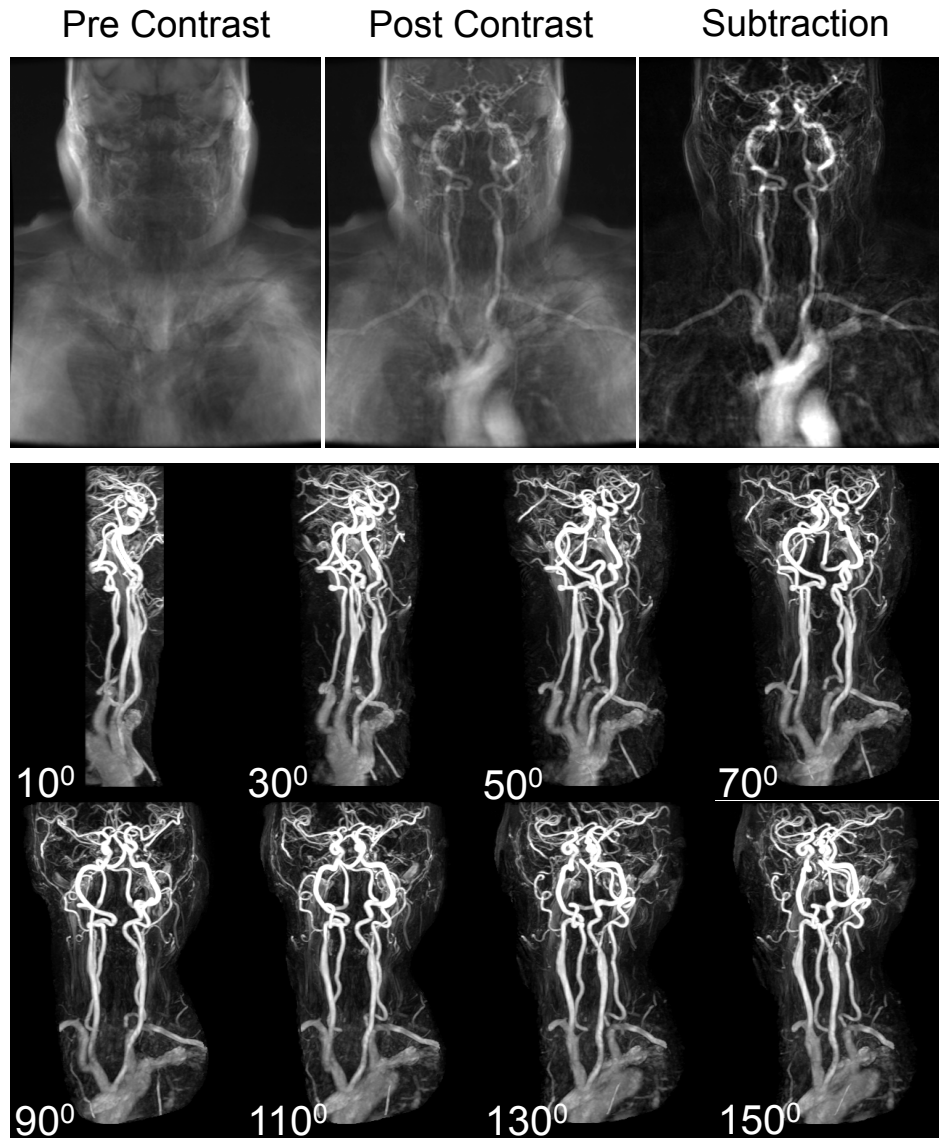


Figure 3.6: Contrast-enhanced MRA (CE MRA). Shown are maximum-intensity projection (MIP) images (top row) of the acquired 3D SPGR images before contrast agent injection, as the contrast enters the arterial system, and through a subtracted data set. Images have high signal-to-noise ratio (SNR) even in areas of high motion, i.e., the aorta and near the heart. Subtracted CE MIP images (bottom two rows) cropped and at multiple angles about the superior-inferior axis show the advantages of collecting a 3D data set. The 3D CE MRA parameters used for acquisition were $TR/TE/\alpha$ of $5.6\text{ ms}/1.7\text{ ms}/20^\circ$, a 3D acquisition matrix of $384 \times 256 \times 76$ over a $32\text{ cm} \times 32\text{ cm} \times 13.7\text{ cm}$ volume. This acquisition was fluoroscopically triggered such that the 3D acquisition began when the contrast was observed in the heart. This timing acquired an image that has the majority of the contrast agent in the arterial system.

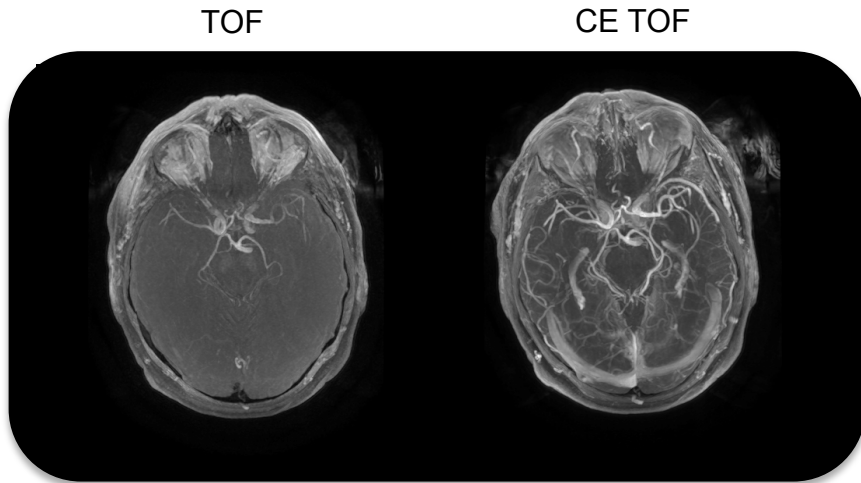


Figure 3.7: Non-contrast enhanced (NCE, left) and contrast-enhanced (CE, right) time-of-flight (TOF) maximum-intensity (MIP) images of the circle of Willis (CoW). The NCE image shows fewer vessels and only vessels with high through-slab velocities. The CE image shows more vessels, including those with slower and/or in-slab flow. Both acquisitions were acquired with TR/TE/ α of 22 ms/2.6 ms/15°, an acquisition matrix of 320 × 224 × 8 acquired over a 24 cm × 24 cm × 1.6 cm field-of-view.

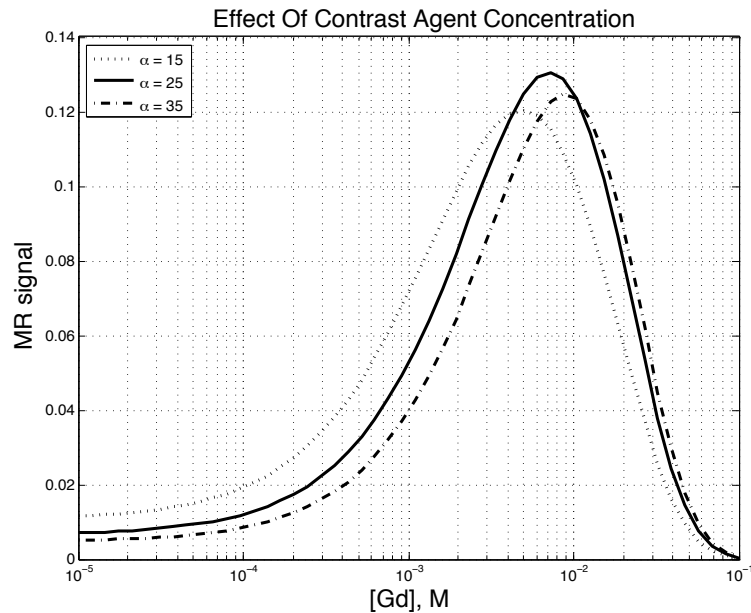


Figure 3.8: Optimal arterial contrast agent concentration. This plot was generated with the SPGR signal equation (Eq 3.1), with TR/TE of 3.0 ms/2.3 ms. For the simulation, the T1 and T2* of blood were assumed to be 2,000 ms and 200 ms, and relativities (κ_1 and κ_2^*) of 4.4 L mmol⁻¹ s⁻¹ and 30 L mmol⁻¹ s⁻¹ respectively.

Signal in CE images cannot be increased indefinitely, there exists an optimal contrast agent concentration for a given set of SPGR acquisition parameters (133). The values selected for image acquisition are chosen to maximize contrast between the blood and non-blood tissues. Figure 3.8 shows an example of this optima: as the T_1 is shortened the images become enhanced, but as the contrast agent concentration becomes high the signal eventually decreases due to the shortened T_2^* effect becoming dominant.

CE-MRA acquisition can also be timed to acquire images during early phase, mid phase or late phase. Early phase CE imaging is performed by acquiring image data early after contrast agent injection (while the contrast agent is still in the arterial system), mid phase is collected when the contrast agent is in both the arteries and veins, and late phase is collected when the contrast agent is in the veins. Depending on the acquisition delay, the CE images can visualize the arterial system, the venous system or both. Rapid thick slab imaging has also been demonstrated to visualize the contrast agent passage (230).

Injection of contrast agent in MR applications is limited mainly to IV administration, often followed by a large saline bolus. IA injection of contrast agents are rarely performed in humans, although similar to DSA x-ray, they allow highly selective angiographic visualization. There have been demonstrations of IA contrast enhancement in animals (133,231-233) and humans (234,235).

CE MR imaging can be useful in obtaining higher SNR and, when rapid structural images are required. CE MR can be used to visualize the passage of a contrast agent through the blood to obtain different information than the previously described methods. CE MR imaging is used for clinical evaluation of structural vascular diseases.

3.2.4 Arterial Spin Labeling - ASL

ASL is an important method for obtaining images of function at the level of the capillaries, such as cerebral blood flow (CBF). ASL is a subtractive technique and forms an image from the difference between two images. Of the two volumes acquired: one has a magnetic tag applied (achieved by inversion pulses) and one without (236,237). In both images, the labeled blood is allowed a specified time, referred to as the post-labeling delay (PLD) time (Figure 3.9), to flow into the imaging volume (placed over the brain) before the image is acquired. With shorter PLD times (0.1 s to 0.6 s) visualization of the

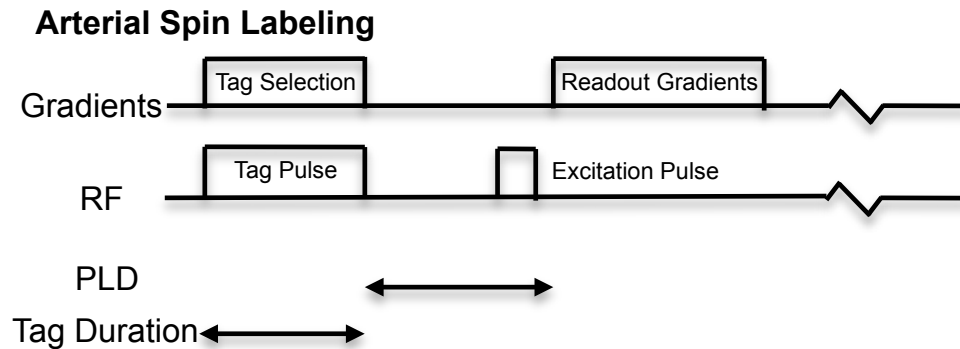


Figure 3.9: Block diagram of arterial spin labeling (ASL) pulse sequence. As there are many variations of ASL, generalized diagram of the ASL pulse sequence has been drawn, with an inversion process followed by image acquisition. With respect to the timing of ASL sequences, two parameters of note include the post labeling delay (PLD) time, and the Tag Duration, the time over which the tag is on.

macroscopic vessels in the head can be achieved (238,239); but, measurement of brain tissue perfusion generally requires longer PLD times (of 1.0 s to 3.0 s) so that the labeled blood can flow into the capillary bed and across the BBB (240). ASL is not effective at imaging the venous system because the decay of the longitudinal magnetization is short relative to the arterial-venous transit time (*e.g.*, the T_1 relaxation causes the label to disappear before blood can flow into the veins). Use of higher field strengths (>1.5 T) has also been demonstrated to improve ASL as the longer T_1 times allow labeling to persist longer (241-243).

A large number of ASL variations exist (239,241,242,244-253) making it challenging to make recommendations for a generalized methodology. A recent publication of several authors in the field attempts to tackle this issue (254). Figure 3.9 shows a conceptual block diagram sequence used to obtain ASL images. A variety of schemes are possible for the image acquisition (*i.e.*, data readout) – ASL has been implemented with rectilinear (239,250,255), spiral (256,257), propeller (247), and 3D radial trajectories (244). ASL sequences are generally classified into two groups: 1) pulsed ASL (pASL) and 2) continuous ASL (cASL). The main difference between these acquisition types is in how the label is applied. The pASL sequence uses a much shorter labeling pulse on the order of 15 ms, while cASL uses a longer label duration with a

continuous series of pulses lasting between 0.75 and 2.0 s. A popular variant of cASL is pseudo-continuous ASL (pcASL), where a series of discrete pulses are applied. This method has become one of the more widely adopted techniques.

The perfusion study group has recently come to some consensus about the methodologies that should be used for ASL imaging (254). The summary of the most recent guidelines makes recommendations for hardware considerations, ASL approaches, time delay between labeling and imaging, background suppression, readout approaches, post processing methods, and clinical implementations. They recommend field strength of 3 T with an 8-channel head coil. They recommend a pcASL implementation, with background suppression and 3D multi-echo readout. Simple, but quantitative, methods for providing CBF measurements are suggested (see below). These guidelines are expected to be updated every three to five years.

The quantification of ASL is derived with a model based on a number of factors: the acquired difference image, selected sequence parameters, and other magnetic parameters (including T_1 of blood, and both blood and tissue magnetization, M_0). The Bloch equation for the longitudinal magnetization can be rewritten to consider inflowing blood (237):

$$\frac{dM_{Blood}}{dt} = \frac{M_{Blood}|_0 - M_{Blood}}{T_1} + CBF \left(M_{Arterial} - \frac{M_{Blood}}{\lambda} \right) \quad \text{Eq 3.6}$$

where λ is the blood-brain partial volume coefficient (defined by [quantity of tracer/mass of brain]/[quantity of tracer/volume of blood]), M_{Blood} is the longitudinal magnetization of the blood water, $M_{Blood}|_0$ is the fully relaxed M_{Blood} , and $M_{Arterial}$ is the longitudinal magnetization of the inflowing arterial blood. This model was expanded upon by Buxton, *et al.*, (258) with a generalized kinetics model incorporating the tissue residue function (*i.e.*, the function of the inflowing blood). The formula to calculate CBF varies with the acquisition technique. In general it is derived from the difference in magnetization

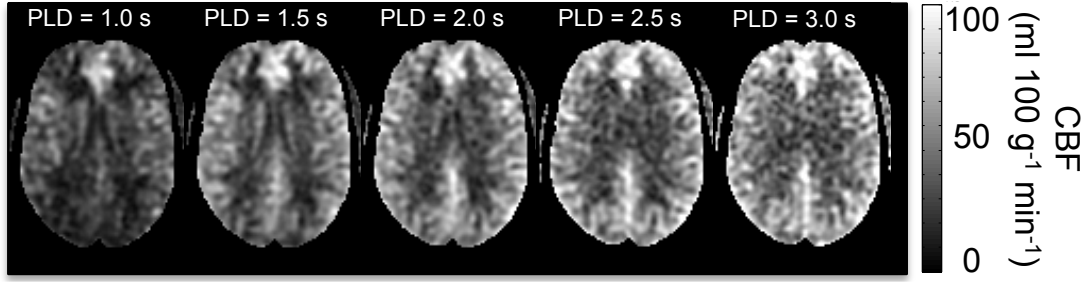


Figure 3.10: Pseudo continuous arterial spin labeling (pcASL) images taken at different post labeling delay (PLD) times. For PLD = 1.0 s, perfusion is reduced in the anterior brain but is even more reduced in the posterior regions because the labeled blood has not had sufficient time to enter these brain regions. Between PLD = 1.5 s and 2.0 s the filling appears to be more uniform across the brain, however, these images suggest that the posterior regions of the brain may require a longer PLD. The acquisitions at PLD = 2.5 s and 3.0 s as expected have more accurate measures, but diminished signal to noise ratio (SNR). The pcASL sequence used to collect these images obtains a stack of spirals readout trajectory with 1024 points per arm, 4 arms, and 3 signal averages, TR/TE/ α of 4,645 ms/10.8 ms/111°, thirty-six 4-mm thick slices were acquired over a 22 cm \times 22 cm acquisition matrix. This acquisition used a labeling duration of 1.0 s. Total acquisition time ranged between 2.5 min and 2.7 min to acquire a brain volume of the PLD time.

between the two imaged volumes (241,258-261), an example is:

$$\begin{aligned} \text{CASL: CBF} &= 6000 \frac{\lambda(\text{SI}_{\text{control}} - \text{SI}_{\text{label}})e^{PLD/T_{1B}}}{2T_{1B}\text{SI}_{\text{PD}}(1 - e^{LT/T_{1B}})\epsilon} \\ \text{PASL: CBF} &= 6000 \frac{\lambda(\text{SI}_{\text{control}} - \text{SI}_{\text{label}})e^{PLD/T_{1B}}}{2T_1\text{SI}_{\text{PD}}\epsilon} \end{aligned} \quad \text{Eq 3.7}$$

where, T_{1B} is the T_1 of blood; ϵ is the labeling efficiency; PLD is the post labeling delay time; ST is the saturation time; LT is the duration of the labeling pulse; $\text{SI}_{\text{control}}$, SI_{label} and SI_{PD} , are the signal intensities of the control, label and proton density images, respectively; T_1 is the inversion time used by the PASL sequence. 6000 is a scaling factor for unit conversion. Several pcASL acquisitions utilizing a spiral readout trajectory are shown in Figure 3.10. The effect of changing the PLD time on the SNR can be seen as well as the blood pool filling between the anterior and posterior regions of the brain. There are sources of error that can arise during the ASL tagging process, such as having off resonance effects near where the labelling takes place (e.g., stent), or faster blood flow may reduce tagging efficiency as the blood does is not in the labelling plane as long.

Vessel encoded ASL (veASL) (250,251,255,262,263) is another variation, whereby blood is selectively labeled in vessels allowing for the assessment of perfusion arising from specific arteries. Regional perfusion information provided by veASL is not available from other perfusion imaging methods. The veASL sequence applies additional gradient pulses while the label is being applied (251). Gradients are applied orthogonally to the slice encode plane and applied at various angles with each repetition. Images of the corresponding vascular territories are revealed, produced by decoding the effect of these gradients as described in Refs (251,255). The veASL sequence is most commonly used with labels applied to vessels below the CoW (251,264), but recently there have been demonstrations of labels applied intra-cranially (239,263,265). When tagging above the CoW, more than eight independent vessels can potentially be labeled.

Velocity selective ASL (vsASL) is another emerging variant, where the label is such that it only excites blood with a specific velocity (252). In pASL and cASL methods the label is generally placed inferiorly to the image volume, while vsASL excites blood in the vasculature proximal to the capillary bed with a narrow velocity range. This ASL variation is desirable as it can excite blood closer to the capillary bed making it less sensitive to the transit from the labeling plane and longitudinal magnetization decay. This thus allows perfusion measurements in regions that might have longer delays, such as stroke cases. There are a host of challenges with this implementation and it is not currently recommended in the most recent version of the study group consensus.

ASL is well suited for perfusion imaging in the brain in healthy subjects. Physiologic and pathologic variations have been documented to affect ASL measurements (266,267). ASL can provide fast measurements of the perfusion during acute ischemic stroke (267,268). ASL studies have correlated decreased perfusion during Alzheimer's disease and mild cognitive impairment (MCI) (63,269,270). Cerebral perfusion has also been measured during healthy aging and found to decrease through life (271). veASL has the potential for understanding collateral flow during disease states. For example veASL was demonstrated recently in an AVM, showing which vessel contributed to regions of the AVM using vessel selectivity above the CoW (272). ASL competes with PET, and both CT and MR contrast bolus passage imaging (discussed

subsequently) in providing CBF measurements. ASL is considered the least invasive perfusion imaging method because there is no ionizing radiation and no need for contrast agent injection. ASL may be useful in understanding a large variety of other cerebrovascular diseases by providing CBF measurements.

3.2.5 Dynamic Bolus Perfusion Imaging

MR dynamic bolus perfusion imaging is another class of techniques that estimates parameters related to blood flow in tissue. They are conceptually similar to the dynamic bolus perfusion imaging available with CT (21,87) in that the contrast agent is injected into the blood while rapid imaging of the brain is performed. The result is a time course of images showing the contrast agent passage through the arteries, capillaries and veins. Analysis of the image data can estimate several important vascular parameters: TTP, CBF, CBV, ATD, BBB permeability and k^{trans} . Bolus passage perfusion imaging can be performed using one of two MR techniques, either: 1) dynamic susceptibility contrast (DSC) imaging (18,19), which is T_2^* -weighted and the contrast agent causes signal loss, or 2) dynamic contrast-enhanced (DCE) imaging (18,19), which is T_1 -weighted where the contrast agent causes signal enhancement. Except for investigating neoplasms, DSC perfusion imaging is the more widely used of the two approaches for cerebrovascular imaging. DCE is more frequently used in tumors where the BBB may be compromised.

With either DSC or DCE acquisition methods, the measured signal intensities versus time are first converted to contrast agent concentration curves ($C(t)$) using either of the following relationships (18,19,87):

$$\begin{aligned} \text{DSC: } S(t) &= S_0 e^{-TE \cdot C(t) / \kappa_2} \\ \text{DCE: } S(t) &= S_0 + \frac{\kappa_1 C(t)}{R_1} \end{aligned} \tag{Eq 3.8}$$

where $S(t)$ is the signal intensity function, S_0 is the baseline signal intensity, TE is the echo time, R_1 is the original longitudinal relaxation time, and κ_1 and κ_2 are the contrast agent relaxivities. The DCE signal intensity-to-contrast concentration function (Eq 3.8) is the most common in literature, however, this analytical derivation makes several assumptions and so, newer (and more complex) analytical and numerical relationships of

contrast agent concentration to signal intensity functions have been proposed to more accurately estimate concentration from the MR signal (273,274).

There are models that can be fit to the concentration functions to estimate perfusion parameters, such as the Tofts model (87,275) or extended Tofts model (276,277). These models can generally be shown to approximate specific cases of the more broadly used impulse response formulation described below, such as weakly vascularized or heavily perfused tissue (278).

For quantification of CBF, a concentration signal from a feeding artery ($C_a(t)$) is used to deconvolve the arterial blood flow effects from the signals obtained in the brain tissue ($C_T(t)$). The flow-scaled tissue residue function ($CBF \cdot R(t)$) is related to the tissue and arterial contrast agent function by:

$$C_T(t) = CBF \cdot R(t) \otimes C_a(t) \quad \text{Eq 3.9}$$

where \otimes is the convolution operator. The residue function is most often modeled as an exponential decay function,

$$R(t) = \begin{cases} 0 & , \quad t < ATD \\ e^{-\frac{t-ATD}{MTT}} & , \quad t > ATD \end{cases} \quad \text{Eq 3.10}$$

by assuming a single compartment model. More sophisticated models have been proposed for the residue function, such as a dual compartment model that also models the permeability between blood vessels and extracellular space (14,21,278),

$$R(t) = \begin{cases} 0 & , \quad t < ATD \\ e^{-\frac{t-ATD}{MTT}} + \frac{F_E}{F_E + F_P} \left(1 - e^{-\frac{t-ATD}{MTT}}\right) & , \quad t > ATD \end{cases} \quad \text{Eq 3.11}$$

where F_E and F_P represent the flow in the extracellular space and the plasma, respectively. This enhanced model can provide estimates of the BBB permeability (14,87,279). Figure 3.11 illustrates the process of deriving perfusion parameters from DSC bolus passage images in an acute ischemic stroke patient.

There are several limitations to MR perfusion imaging with bolus passage techniques, including: 1) the complexity of signal processing (due to the need for signal deconvolution) (17), 2) the implicit tradeoff between temporal sampling rate and spatial resolution, and 3) the challenges of selection of the arterial input function (280,281).

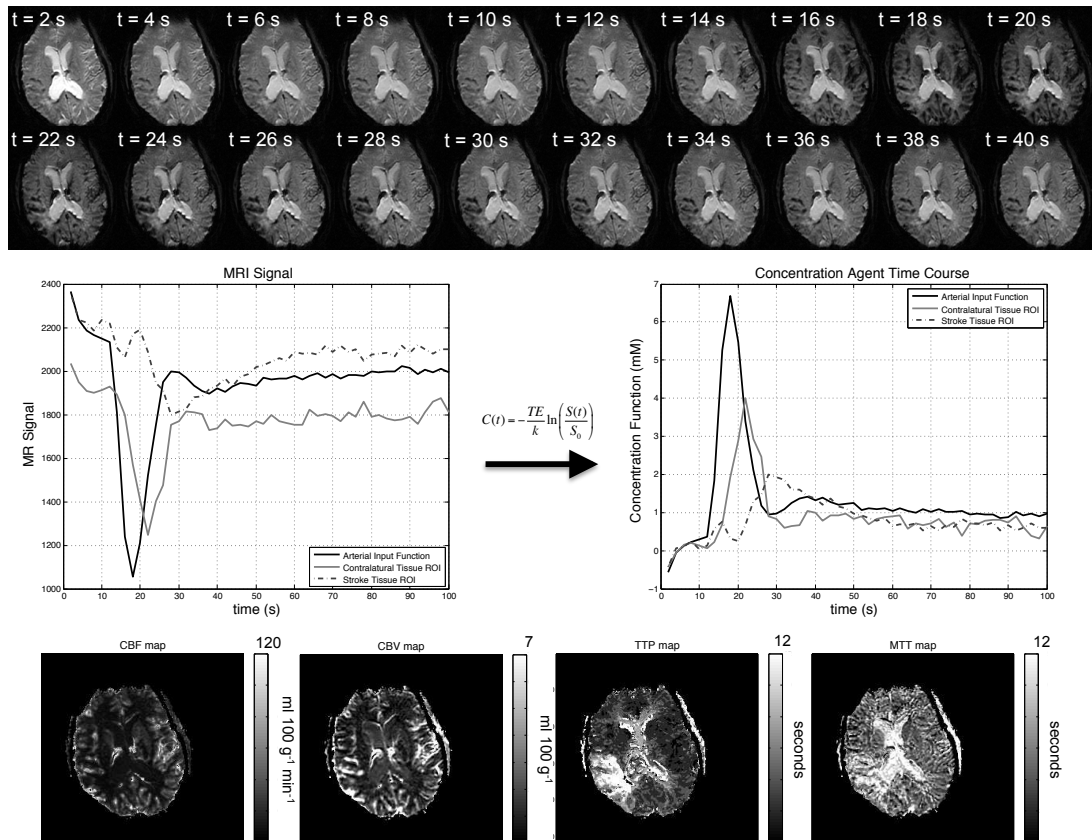


Figure 3.11: An example of bolus passage perfusion imaging during acute ischemic stroke obtained using $T2^*$ -weighted dynamic susceptibility contrast (DSC) imaging. On the Top is a subset of the temporal series of contrast agent passage. Times series are extracted for the delayed ischemic tissue, contralateral ‘normal’ tissue, and the arterial input function (graph on left). The MR signal intensity was converted to contrast agent concentration using Eq 3.8 (graph on right). The derived quantitative cerebral blood flow (CBF), cerebral blood volume (CBV), time to peak (TTP) and mean transit time (MTT) maps (bottom row) show an ischemic region with decreased CBF, and increased TTP and MTT. The MR acquisition parameters were $TR/TE/\alpha$ of 2000 ms/30 ms/45°, an acquisition matrix of 144×144 over a 24 cm \times 24 cm field-of-view with seventeen 5-mm thick slices prescribed to provide whole brain coverage. The TR described here was for the whole volume to be acquired.

Signal deconvolution is inherently an ill-posed mathematical problem and biases have been observed with several available regularization techniques (17-19,282-286). The Nyquist criterion required to accurately sample inflowing contrast agent is found empirically to be 2 s or faster, which puts constraints on the acquired matrix size and thus

the spatial resolution and voxel size. Selection of the arterial input function may be biased from PVE (287-289) and non-linear contrast-agent-induced susceptibility effects (290), these biases propagate through the quantification process and ultimately result in inaccuracies of perfusion maps. The arterial input function errors are greater for DSC methods than for DCE approaches because the PVE has a greater contribution.

Acceleration of dynamic bolus passage MR imaging has also been demonstrated with parallel imaging (291) and more recently with constrained reconstruction (230). Faster volume acquisition is not necessarily advantageous, since it may be preferred to have longer TR times or higher spatial resolution while maintaining temporal sampling times at ~ 2 s. Acceleration strategies have allowed for an improvement in image contrast (292) or spatial resolution (230)..

DSC, DCE, ASL and PET-derived CBF estimates have been compared in several studies that have demonstrated similar measurements in both healthy and diseased subjects (268,293-296). This is reassuring considering the vastly different acquisition methodologies and suggests that CBF is a reliable cross-modality metric. The role of perfusion parameters in cerebrovascular disease was discussed in the ASL subsection. The advantage of using MR dynamic bolus perfusion imaging instead of ASL include: 1) the ability to derive CBV and, potentially, BBB permeability, 2) the ability to more accurately measure perfusion in tissues that have longer transit delays (*i.e.*, tissues with transit times greater than 4 s which is of particular interest in ischemic stroke where the delay can be as long as 12 s), and 3) overall shorter acquisition time.

3.2.6 T_2^* -weighted Imaging

A GRE sequence (Figure 2.3) is inherently sensitive to changes in tissue T_2^* . For long TE, GRE images are dominated by the T_2^* contrast mechanism, which can be exploited for the detection of hemorrhage or veins. The Bloch equations (Eq 2.1) for magnetization evolution with GRE imaging becomes (106-109),

$$\frac{d\mathbf{M}(t)}{dt} = \gamma(\mathbf{M}(t) \times \mathbf{B}(t)) - \frac{M_x(t) + M_y(t)}{T_2^*} - \frac{M_z(t) - M_0}{T_1} \quad \text{Eq 3.12}$$

where T_2 is replaced by T_2^* . The signal equation was described previously (Eq [3]). T_2^* signal decay is very similar to T_2 decay and is often approximated as a decaying

exponential with $T_2^* < T_2$. T_2^* signal decay is a result of more rapid dephasing of the MR signal (leading to more signal attenuation) because this relaxation term includes additional factors that include the magnetic susceptibility effects (Figure 3.13).

Although magnetic susceptibility is often referred to as a source of unwanted image artifact (290,297,298) – the classic example being the signal attenuation in brain immediately superior to the nasal sinus and auditory canals – susceptibility can also be a powerful additional source of MR image contrast (299-301). T_2^* -weighted contrast is effective for imaging structures of higher iron or calcium content as these introduce large, local susceptibility changes. For functional applications T_2^* -weighted imaging is effective at detecting deoxygenated hemoglobin and hemosiderin, and it has been demonstrated to have utility for detecting both microbleeds and hemorrhage (302,303).

The main disadvantage with imaging using T_2^* -weighted contrast is the high level of blooming in the image. Secondly, the dependence of T_2^* signal loss on field strength, magnetic field homogeneity, pulse sequence acquisition, and orientation, is undesirable. Blooming refers to the amount of spatial distortion that extends around susceptibility inhomogeneities. The extent of distortion is dependent on shape and acquisition parameters, particularly TE. Although susceptibility-sensitive sequences have a higher rate of hemorrhage detection than CT imaging (viewed as the current gold standard) (303), volume of hematoma is not easily quantified with T_2^* -weighted GRE images due to blooming effects. The change of shape with acquisition and orientation parameters makes the quantification of hemorrhage volumes more variable and potentially less accurate.

The following subsections on susceptibility-weighted imaging (SWI), and quantitative-susceptibility mapping (QSM) are all important derivatives of the basic T_2^* -weighted sequence and exploit other aspects of the MR susceptibility contrast mechanism.

Multi Echo Gradient Recalled Echo

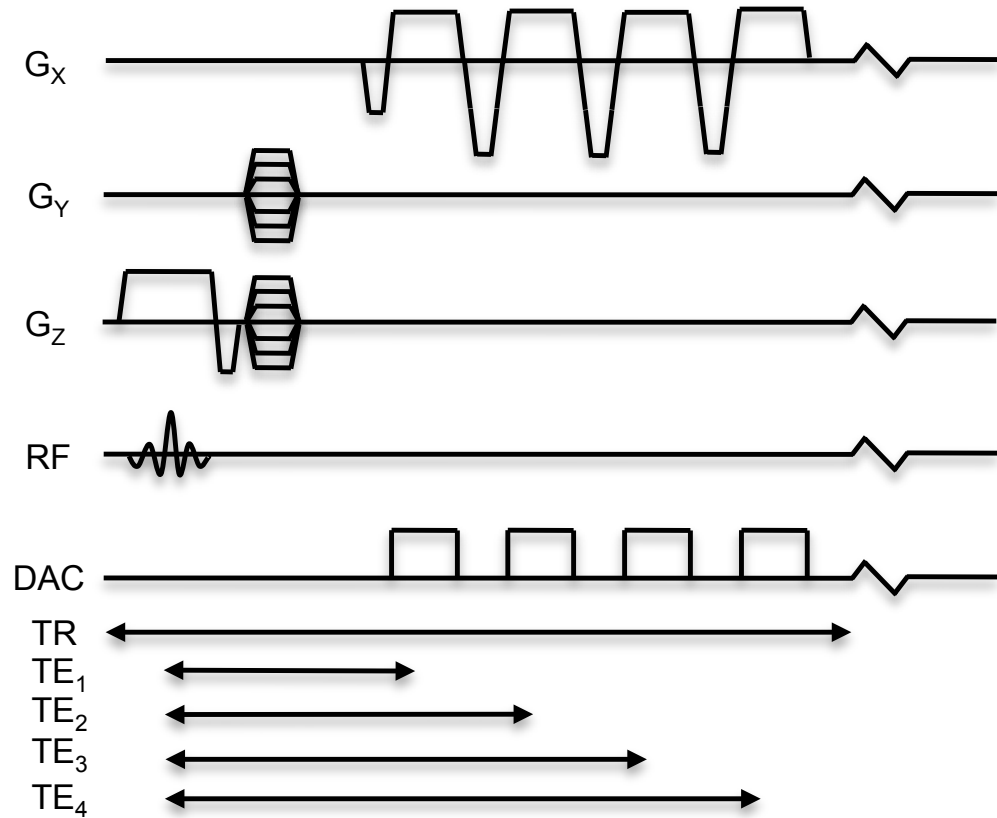


Figure 3.12: Multi-echo gradient recalled echo (GRE) pulse sequence diagram. The G_x gradient allows the acquisition of four echoes for improved calculation of magnetic field through fitting.

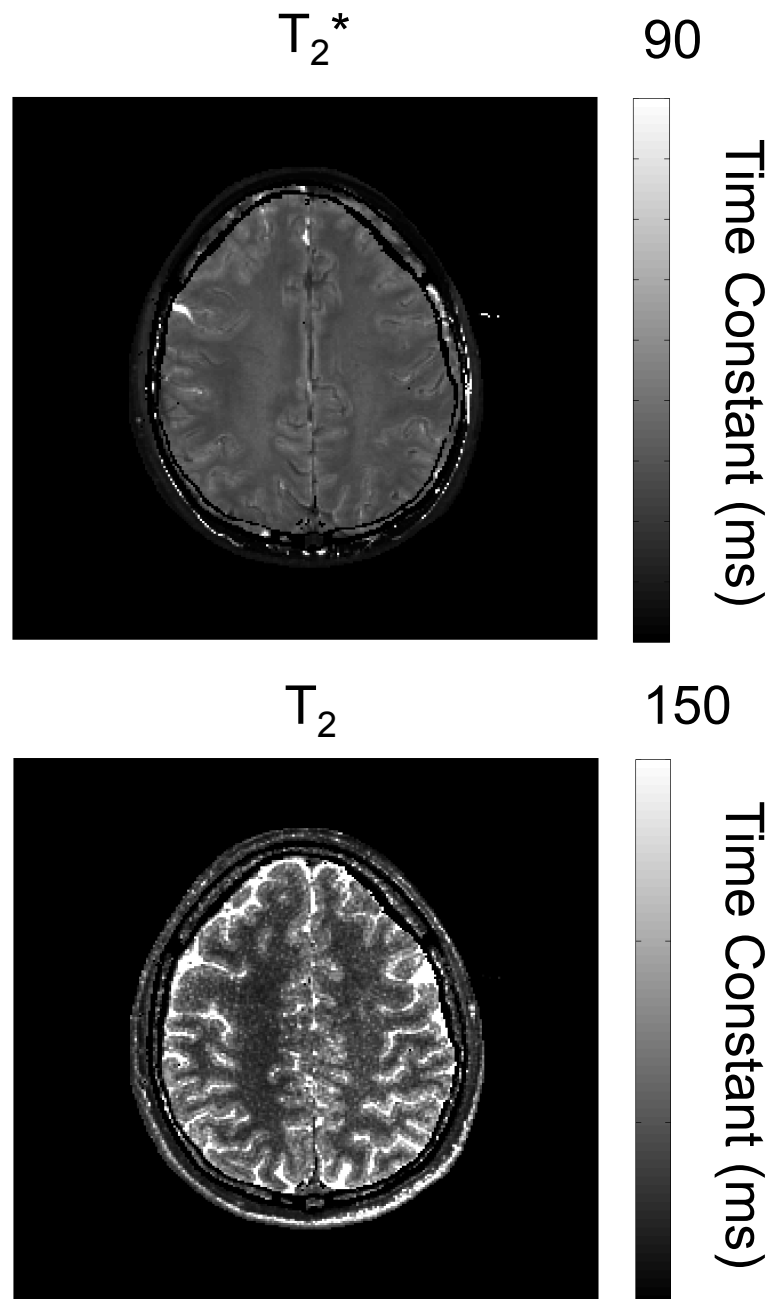


Figure 3.13: Comparison of (top) T_2^ map and (bottom) T_2 map images. In this example, the T_2^* decay is approximately one tenth of the T_2 . Over practical range changes in oxygenation extraction fraction (OEF), T_2^* decay can change by up to 30% with physiological variation, T_2 measurements are less sensitive, changing ~20% with this physiological variation (304,305).*

3.2.7 Susceptibility-weighted Imaging - SWI

SWI can be used to provide images of the venous system or to provide images of hemorrhage and cerebral microbleeds. Like T_2^* -weighted imaging, SWI is sensitive to susceptibility differences. Both deoxygenated hemoglobin in the venous system and hemorrhagic tissue have high susceptibility and are emphasized on SWI. SWI is also used to create images where deoxygenated hemoglobin and hemosiderin are hypointense (*i.e.*, has lower signal intensity) (299).

Magnetic susceptibility, χ , is a tissue material property and is directly related to the relative magnetic permeability, μ_r , by:

$$\chi = \mu_r - 1 \quad \text{Eq 3.13}$$

Magnetic susceptibility is often reported in parts per million (ppm) and ranges between -0.2 ppm and 0.1 ppm in the healthy human brain. Most properly described, susceptibility is a tensor measure that indicates how magnetized a material will become when a magnetic field is applied. The largest component of this tensor, χ_{33} , is the magnetism generated in the direction of the main field.

Magnetic susceptibility can also be related to the applied field, \mathbf{H} , and induced magnetization, \mathbf{M} , as $\chi = \mathbf{M}/\mathbf{H}$. Strictly defined, susceptibility is a tensor quantity that is used to relate the \mathbf{B} and \mathbf{H} fields. Magnetic susceptibility is related to the applied and induced fields as,

$$\mathbf{B} = \mu_r \mu_0 \mathbf{H} = (1 + \chi) \mu_0 \mathbf{H}, \quad \text{Eq 3.14}$$

where \mathbf{B} is the induced magnetic field (*i.e.*, $\mathbf{B} = \mu_0(\mathbf{M} + \mathbf{H})$), and $\mu_0 = 4\pi \times 10^{-7}$ H A m⁻² is the magnetic permeability of free space. Although the problem of estimating susceptibility appears to have a relatively straightforward solution to Eq 3.14, in reality the effects of susceptibility inhomogeneity require a more sophisticated solution.

In most MR imaging applications, the image volume is heterogeneous (and for example, would include tissues with various susceptibilities, such as air and tissue). Susceptibility can also vary extensively across tissue. Regions of higher magnetic susceptibility result in greater induced magnetism and this locally induced field change induces more magnetization in the directly adjacent tissue in a dipole (or blooming)

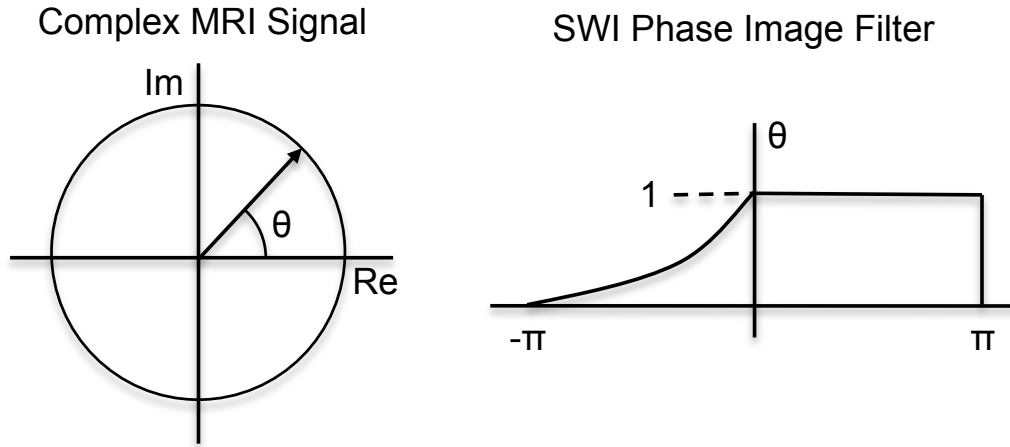


Figure 3.14: Susceptibility weighted image (SWI) mask filter. (left) Complex MR imaging data has a phase angle (θ). (right) general form of the SWI image mask filter as described by Eq 3.15. Attenuation of the magnitude of the signal is determined and multiplied by the SWI image mask filter.

fashion. The changes in local induced field also cause small but appreciable changes in the local resonance frequency of the signal measured by MR. GRE sequences can collect either one echo as in Figure 2.3, or multiple echoes as in Figure 3.12 (306).

There are many variations of SWI. Fundamentally, these methods use GRE sequences and collect and combine both the magnitude (affected by T_2^* signal loss and TE) and phase images (affected by local frequency changes and TE). As TE is lengthened the magnitude signal is attenuated where there is higher susceptibility, and the phase images show greater dephasing. To create a susceptibility-weighted image, magnitude images are multiplied in a pixel-by-pixel fashion with a filter calculated from the phase image. The phase-image mask is designed to attenuate the signal in regions that have phase characteristics indicative of high susceptibility, enhancing the contrast on susceptibility-weighted images between tissues of differing susceptibility. The mask, $g(\mathbf{r})$, commonly used for SWI filtering is (299),

$$g(\mathbf{r}) = \begin{cases} \left[\frac{(\pi - \phi(\mathbf{r}))}{\pi} \right]^m & , \quad \phi(\mathbf{r}) > 0 \\ 1 & , \quad \phi(\mathbf{r}) < 0 \end{cases} \quad \text{Eq 3.15}$$

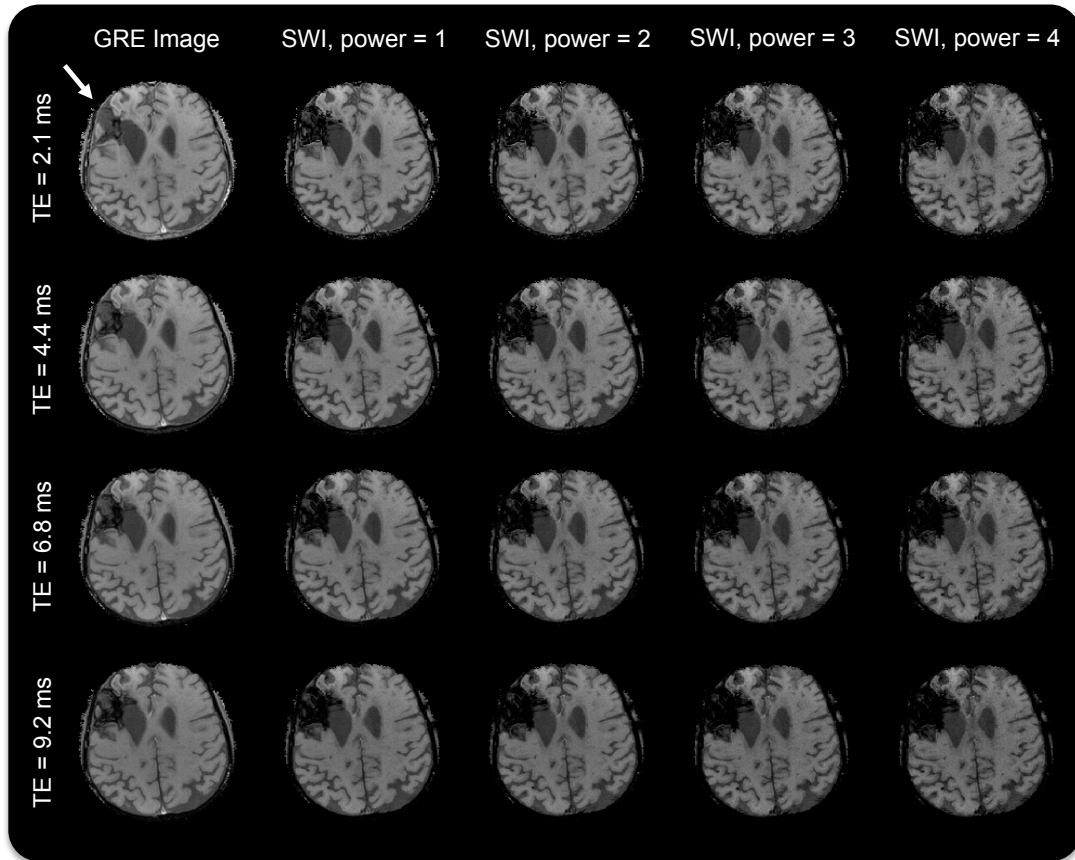


Figure 3.15: Comparing susceptibility weighted image (SWI) echo and filter coefficients. (left most column) T_2^ -weighted GRE and (right four columns) susceptibility-weighted images (SWI) of a intra-cerebral hemorrhage (arrow) at multiple echo times and masking filter powers (m in Eq 3.15). There is an apparent increase in the hemorrhage size with increased echo time and filtering coefficient.*

where \mathbf{r} is the spatial location, m is a constant chosen for reconstruction, and $\phi(\mathbf{r})$ is the phase image. A graphical representation of this SWI phase image mask filter is shown in Figure 3.14 (299). Materials that have higher susceptibility have phase image mask values that cause more attenuation. Eq 3.15 is described as a positive phase mask, which is sensitive to paramagnetic materials. The filter expression could be altered to modify negative phase values to create a negative phase mask filter that would be sensitive to diamagnetic materials. Eq 3.15 modified to be sensitive to both types of susceptibility would replace the $\phi(\mathbf{r}) < 0$ condition to match the $\phi(\mathbf{r}) > 0$ case.

As expected, improving the sensitivity of GRE sequences to susceptibility changes impacts the rates of pathologic detection. For example, SWI in comparison to T_2^* -weighted GRE imaging in a CAA patient showed 201 versus 71 microbleeds over the same volume (307). In another report, SWI was compared against T_2 -weighted SE imaging and was found to detect hemorrhage in more than twice as many subjects (303).

An example of SWI is shown in Figure 3.15 for a range of echo times and filtering constants (m). This image shows an elderly subject with CAA who had an ICH. On both the SWI and T_2^* -weighted GRE imaging, the ICH appears larger than the actual size due to T_2^* -induced blooming, the degree of blooming can be emphasized to varying degree, depending on the echo time used for the magnitude image and the SWI filtering constants.

3.2.8 Quantitative Susceptibility Mapping - QSM

QSM is a new approach that attempts to quantify tissue susceptibility. Of the described techniques, QSM is the newest and least developed. It adopts an alternative approach to imaging susceptibility than the previously described SWI: rather than attenuating magnitude measurements with a phase image mask, QSM attempts to assign a quantitative value for the magnetic susceptibility to each pixel in the image. QSM also uses a GRE imaging sequence and benefits from a multi-echo implementation, as multiple echoes improve calculation of the magnetic field changes underlying the image.

The quantification methods used to estimate susceptibility vary greatly (301,308-312). In this section, a generalized formulation for QSM processing is discussed along with some of the differences between the principally proposed quantification methods. Eq 3.13 illustrates the relationship between magnetic permeability and susceptibility and Eq 3.14 describes the relationship between the applied-field, induced-magnetism, and tissue permeability. In both of these equations it appears as though magnetic susceptibility is a constant, however, as \mathbf{B} and \mathbf{H} are both vector fields that are governed by Maxwell's equations (313), susceptibility therefore has a non-local effect on heterogeneous objects. Unfortunately, the analytic relationship used to relate the magnetic field outside a region of varied susceptibility changes greatly with the shape and the orientation to the magnetic field (297).

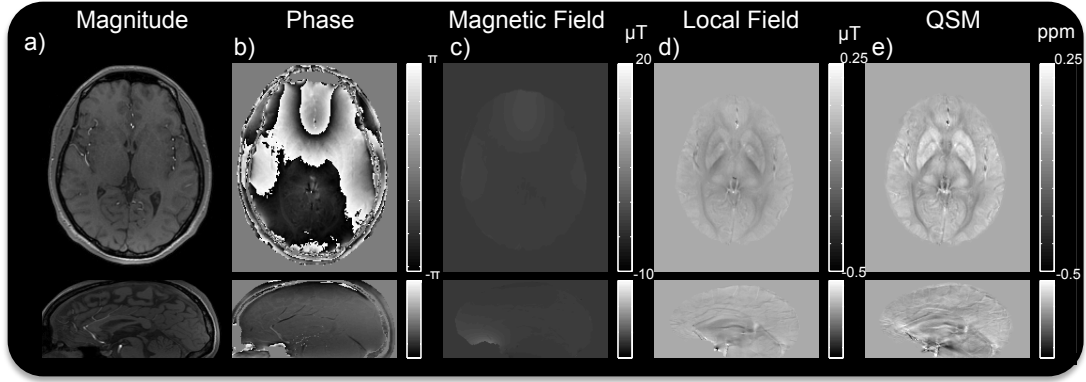


Figure 3.16: *Quantitative susceptibility mapping (QSM) pipeline and example images. Images from steps used to calculate QSM images. Magnitude and phase images are shown, the magnetic field is then calculated, and the background field is removed to calculate the local magnetic field. Dipole inversion is applied to the local field to remove the non-local effect and obtain the QSM measurements. The voxel size was 1 mm^3 , over a $256 \times 256 \times 128$ acquisition matrix. RESHARP background removal was used to remove the background field and L_1 weighted constrained dipole inversion was used to calculate the QSM image.*

Most proposed QSM methods rely on the MR phase images instead of the magnitude images. Multi-echo GRE images are preferred over single-echo variants for estimating the \mathbf{B} field. The induced field can be calculated from two or more phase images acquired at different echo times by modifying the Larmor equation to:

$$\mathbf{B} = \frac{1}{2\pi\gamma} \frac{\boldsymbol{\phi}}{\mathbf{TE}} \quad \text{Eq 3.16}$$

where $\boldsymbol{\phi}$ is a vector of the phase images corresponding to a vector of echo times, \mathbf{TE} . In general, wrapping is present in the phase images, and images must therefore be unwrapped (314). The calculated \mathbf{B} field across the brain is also affected by distortion near the air-tissue and other susceptibility interfaces. To remove this bulk effect, high-pass spatial filtering or more advanced background field-removal techniques have been proposed (309,310,315). After the background magnetic field removal (Figure 3.16d), only the local changes resulting from local difference in tissues

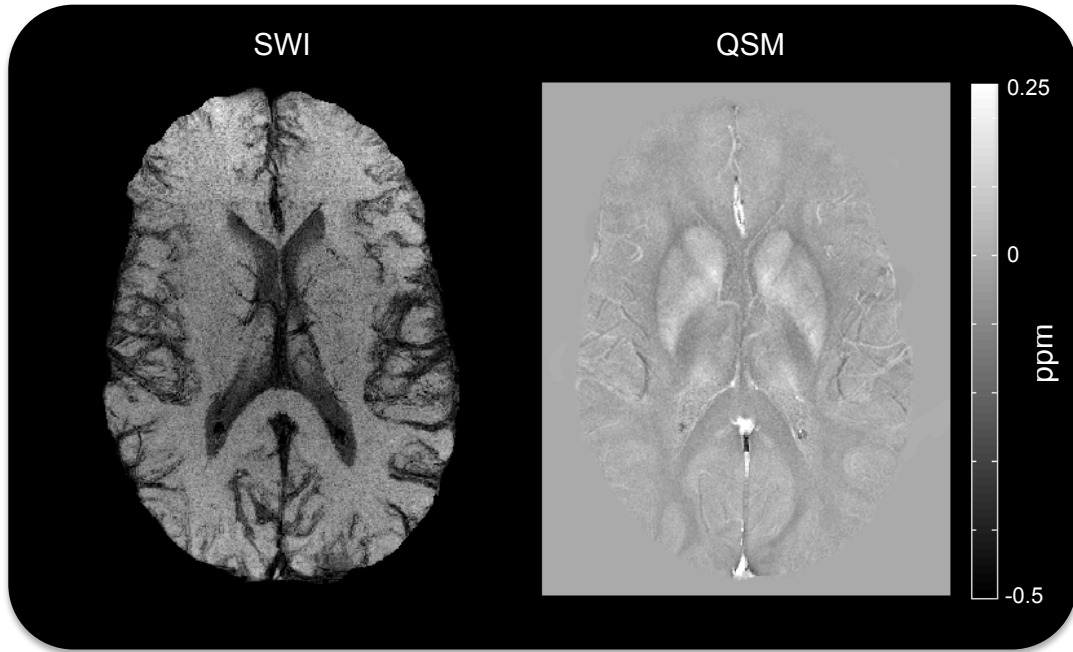


Figure 3.17: Comparison of susceptibility weighted image (SWI) and quantitative susceptibility mapping (QSM) venography. Images were reconstructed from data in the same acquisition with the same spatial location. The acquisition voxel size was 0.5 mm^3 , over a $512 \times 512 \times 64$ acquisition matrix. The SWI image was calculated with a minimum intensity projection and the QSM image was calculated with a mean intensity projection, both over 4 mm to improve the SNR and be able to see some of the viens running parallel to the slice.

susceptibility remain. The effects of blooming can be then removed through deconvolution and inverting,

$$\frac{\delta B}{B} = d(\mathbf{r}) \otimes \chi \quad \text{Eq 3.17}$$

to solve for χ , where the dipole kernel, $d(\mathbf{r})$ is,

$$d(\mathbf{r}) = \frac{3\cos^2\theta - 1}{4\pi|\mathbf{r}|^3} \quad \text{Eq 3.18}$$

where \mathbf{r} is the position vector, θ is the angle between \mathbf{r} and the \mathbf{B} field. Dipole deconvolution removes the unwanted spatial distortion in MR imaging associated with susceptibility. An example of a deconvolved quantitative susceptibility map is shown in Figure 3.16e.

Other methods can be used to quantify susceptibility with images at multiple orientations, where use of this additional information can yield a solution to this ill-posed problem with using a least squares formulation (316,317). Efforts have also been made to calculate the individual tensor components of the magnetic susceptibility (317,318). QSM has also been proposed for imaging contrast agent dynamics, hopefully, resulting in more localized and accurate assessment of contrast passage.

QSM imaging is useful in assessing several disease states such as hemorrhage and microbleeds (300,301). It can be used for venography (319,320), as demonstrated in Figure 3.17 which compares QSM and SWI venography. QSM could be used for the assessment of calcified atherosclerotic plaques.

3.3 Summary of MR Angiographic Techniques

This review has described and shown examples of the full range of available MR angiography methods for investigating aspects of the cerebrovascular system. Depending on the specific application or clinical question, the utilization of several different methods for obtaining diagnostic information about the cerebrovascular state may be appropriate. When selecting an angiography method for a given imaging task, the total scan time, overall image quality and relevance of the provided diagnostic information are key factors. For example, at 3 T even with matched isotropic 0.5 mm spatial resolution, the findings from TOF and PC imaging approaches can vary greatly. On the PC images the PCom is less likely to be seen than on TOF images. TOF imaging will show thrombus with hyperintense signal while phase contrast will not show it at all. These two observations suggest that TOF imaging is better for assessing changes expected in acute ischemic stroke. The added value in providing quantitative velocity information (from PC) is small when assessing stroke. On the other hand, PC imaging is much more appropriate and useful (compared to TOF) when assessing complex flow dynamics in cerebral aneurysms.

When selecting a method for perfusion imaging, ASL may appear to be the preferred technique, as it does not require contrast agent injection and can produce images that are vessel selective. However, ASL has been demonstrated to underestimate

the CBF in ischemic tissues with $ATD > 4$ s. This underestimation occurs because the ASL label is a function of T_1 and only persists for a relatively short period. In the case of ischemic stroke, arterial delays may be 12 s or longer (17). Bolus passage imaging may be expected to more accurately assess perfusion of ischemic regions during stroke (268). Further, in brain tumors, DCE bolus passage MR imaging might be selected, over DSC or ASL perfusion imaging, for superior information about the BBB permeability. In addition, neither DSC nor ASL MR images have limited spatial resolution due to susceptibility-induced spatial distortion.

In the presence of occlusion, collateral blood flow where blood takes an alternative route to the tissue may be a lifesaving phenomenon. The CoW is a source of redundancy in the vascular tree and can aid in collateral blood flow, for example if there was an occlusion in the left ICA due to stenosis, blood could pass up through the right ICA, through the ACom and supply brain tissue on the left side of the brain. The honeycomb like structure of the meningeal arteries and pial arteries are also a major source of collateralization. When imaging disease it may be of interest to assess the collateral flow dynamics as well. Collateral flow may present differently with each of the available angiography methods. With TOF, if the blood takes a longer (and usually slower) path it will have reduced signal in the images. With phase contrast, it may be hard to detect collateral flow if it is slower, though the direction of the flow is measurable providing information about the collateralization. ASL images may have bright vessels where flow is slowed (254,321), providing information about the collateral flow. Vessel encoded ASL is particularly useful at assessing collateralization (322,323). DSC and DCE will tend to show longer delays in regions supplied through collateralization (324,325).

PET, ASL, DSC and DCE all provide estimates of cerebral perfusion parameters, though the underlying physics and respective tracer kinetics are different. In the case of PET and ASL, the tracers are oxygen and water, respectively. Both oxygen and water can freely pass through the BBB, while the most contrast agents used in DSC and DCE are larger molecules that do not pass through an intact BBB. That being said, there are some applications where contrast agents can be used that do pass through the BBB (326).

Understanding that perfusion parameters derived from different methods have different underlying physics is important in interpreting the measurements.

With respect to the susceptibility imaging methods it can be challenging to determine whether to use T_2^* -weighted GRE imaging, SWI, or QSM for venography. T_2^* -weighted GRE imaging has existed for the longest time and is operationally quite robust, however, detection rates for some abnormalities have been shown to be much higher with SWI. Both T_2^* -weighted GRE imaging and SWI will over-estimate the width of the veins due to blooming effects and the vessel width will also vary with orientation. QSM is might be avoided due to the complexity of implementation with respect to the competing methods. Using QSM has lower detectable differences between veins and tissues, but QSM can more accurately measure the vessel diameter. For hemorrhage detection, the magnitude GRE and SWI images will quantify the hemorrhage volume differently at different echo times, so again QSM is preferred.

Imaging the cerebral vasculature is of great interest and is a high yield application for most large hospitals due to the prevalence of cerebrovascular diseases. The large number of innovative techniques for imaging blood has grown vastly in the past thirty years providing a variety of image contrasts and vascular metrics.

3.4 Chapter Summary

In this chapter, different methodologies available for performing cerebrovascular MR evaluations were discussed. This review is intended to be an all encompassing summary of the currently available methods. Later sections of the thesis (Chapters Five through Eight) discuss mostly PC imaging, as these are the most fruitful of the experiments I performed during my PhD research. As this thesis has a strong methodological focus, understanding the state of the art methodology is critical. It is key to understand however, why there may be a preference to using PC rather than TOF, or ASL instead of DSC; from the point of view of the underlying physics. In the next chapter, simulation is used to better understand MR technology.

Chapter Four:

Establishing the Lower Bound of MRI: Using An Estimation Theory and Statistical Perspective

4.1 Chapter Overview

The purpose of this chapter is to characterize the lower bound of magnetic resonance (MR) image variance with and without machine and physiological distortions. The analytic formulation and conceptual framework of the Cramer-Rao lower bound (CRLB) to model the collection and reconstruction of MR images is presented, and these are compared to experimental values. For numerical CRLB evaluation, a digital brain phantom was first generated by using fast quantification techniques to parameterize brain T_1 , T_2 , T_2^* , proton density, and magnetic susceptibility. Machine distortion parameters were then incorporated, namely: noise correlations, spatial gradient warping, coil sensitivity, and both B_0 and B_1 inhomogeneities. Images via a Bloch equation simulation on the digital brain phantom for an arbitrary MR sequence was then synthesized. The histograms of these synthetic images were compared with experimentally acquired brain images: their first and second moments from the histograms differed by 1.9% and 25.2%, respectively. This result demonstrates a high degree of similarity between the simulations and experimental data. The lower bound for noise was characterized analytically and shown to be greater (by a factor of $4\times$ to $5\times$) in the presence of distortion. This increase was verified with the finding that the variance was $4.49\times$ greater when the channels were fully correlated. The results indicate that using synthetic MR images to characterize image quality offers an alternative, powerful and robust methodology to optimize acquisition parameters for MR sequences.

4.2 Introduction

Magnetic resonance (MR) imaging is a popular modality for conducting medical imaging examinations; it yields excellent soft tissue contrast and poses few safety issues (*i.e.*, no radiation dose) (121). With MR imaging the goal is to have simultaneously high signal-to-noise ratio (SNR) and contrast-to-noise ratio (CNR), as this provides improved detection of pathology. The goal can be achieved by minimizing the MR signal variance (*i.e.*, decreasing noise). The noise variance in the final MR images is, in general, related to the time spent acquiring the data (*e.g.*, the longer the scan time, the better the final image) (327). Nevertheless, by more accurately defining and understanding the sources

that lead to MR image variance, a practical and viable methodology to improve and/or optimize MR acquisitions subject to machine design, image quality and timing constraints is provided.

The Cramer-Rao lower bound (CRLB) represents the minimum achievable variance with an unbiased image estimator (328). Minimum variance unbiased estimation is often the preferred estimator for MR imaging and is implemented as a Fourier transform of the acquired k -space data; its derivation is much simpler than more sophisticated reconstruction techniques (121,328,329). In practice, biased image estimators, such as Bayesian estimators like compressed sensing (117), can achieve a lower mean squared error (328). Bayesian estimators will be omitted here to focus on the CRLB.

Optimization with the CLRb is performed in a broad range of engineering applications, particularly in the fields of telecommunication and localization (330-332). In medical imaging, the CRLB has been used as a method of optimization, but these studies are limited in their general applicability. For example, Alexander *et al.* (330) described a method for optimizing an estimator to meet the CRLB with respect to diffusion tensor imaging. Although the methodology was well described, their analysis did not extend past the specific diffusion model.

Often the CRLB is a function of many factors and cannot be determined analytically. Still, for most complex systems, the CRLB can be found (or at least approximated) via numerical simulation to find the maximum likelihood estimator (333-335), the numerically derived equivalent to the analytically derived minimum variance unbiased estimator. MR imaging falls within this realm, and a solution for its lower bound can be found using Monte Carlo simulation (336,337). By whatever means available, be they analytical or Monte Carlo measurements, if one can approximate the probability density function of the estimator, then one can infer the variance. Briefly stated, one takes the natural logarithm of the probability density function to get the log-likelihood function, whose maximum can be calculated; this is termed the 'score'. The variance of the score is also the minimum variance of the estimator, the inverse of which is the Fisher information (328).

MR systems today are efficiently shielded from external electromagnetic radiation, thereby reducing noise effects. The dominant noise source in human imaging is caused by thermal noise in the sample being imaged (338-340), whose distribution is normally distributed (341). MR data is collected in k -space (*i.e.*, Fourier space) from several channels simultaneously, and the noise on the separate channels is correlated (114,339,340). Ideally, to maximize image information the channels should be uncorrelated, but in practice this is not always achievable as different channels are often coupled due to imaging coil overlap (*i.e.*, coil coupling). MR receiver coils operate in the radio frequency band, and the acquired noise is effectively temporally uncorrelated (342). Decorrelation of the channels has been performed with a Wiener type decorrelation filter (*a.k.a.* a matched filter, or noise whitening filter), where the array of points collected at each point in time is multiplied by a Cholesky matrix (328,343,344).

There are several forms of distortion that exist in MR imaging which can change signal and noise properties, including: 1) non-uniform static field (B_0 inhomogeneity), 2) non-uniform excitation field (B_1 inhomogeneity), 3) non-uniform coil sensitivity profiles, and 4) non-linearity of gradients. These distortions affect the SNR differently throughout the image, thereby making an overall (or average) estimate of the SNR difficult to correctly quantify. In many situations, it is often unsuitable to use an average SNR, since this may have little relevance in specific regions of the image.

The purpose of this chapter is to establish (using theory and numerical simulation) the lower bound of uncertainty for MR data acquisition and confirm the limit experimentally. The specific objectives of the chapter are to first analytically define the CRLB to a reasonable extent, and then to expand upon it using appropriate numerical simulations. Further understanding of the minimum achievable variance will lead to new appreciation about the significance of machine and physiological distortions. More specifically, since the CRLB is closely related to the SNR, its investigation will lead to improved insight about the MR system. This work also demonstrates positive evidence for the use of synthetic images. A concise theoretical overview of the MR signal and its noise propagation is provided. The CRLB is derived analytically, including coil sensitivity and correlated noise, after which distortions are considered. Thereafter, the

numerical/simulation methodology is described, including the generation of a digital brain phantom with valid physiologic parameters, synthesizing MR images by using a Bloch equation simulator, and then comparing the synthetic results to experimental images obtained in healthy volunteer with histogram analysis.

4.3 Theory

4.3.1 Magnetic Resonance Signal

Nuclear MR signal generation has been well documented and explained over the last 70 years. There is, in fact, a great deal of literature describing the underlying quantum mechanical model (345). However, for the purposes of this manuscript, only the classical and phenomenological model, known as the Bloch equations, is necessary to describe the MR signal. Magnetization (\mathbf{M}) is simply represented as a vector with three orthogonal components, and the net signal (s) is generated by the sample being imaged.

Magnetization evolution is dependent on several physiological properties, including proton density (M_0), relaxation times (*e.g.*, T_1 , T_2 , T_2^*), and magnetic susceptibility (χ).

The MR signal can be calculated with a Bloch simulation similar to that described by Kwan *et al.* (346). Kwan uses an intuitive summation of spin vectors approach, originally credited to Hahn (347). Initially, the values of M_x and M_y are zero and all the magnetization is stored in the M_z component. After excitation, the evolution of M_x , M_y , and M_z components of \mathbf{M} are calculated as they progress to equilibrium via the Bloch equation,

$$\frac{d\mathbf{M}}{dt} = \gamma(\mathbf{M} \times \mathbf{B}) - \frac{M_x}{T_2} \hat{x} - \frac{M_y}{T_2} \hat{y} + \frac{M_0 - M_z}{T_1} \hat{z}, \quad \text{Eq 4.1}$$

Magnetic susceptibility is introduced by relating the induced field (\mathbf{B}), \mathbf{M} components, and the applied field \mathbf{H} , as $\mathbf{B} = \mu_0(1 + \chi)\mathbf{H} = \mu_0(\mathbf{H} + \mathbf{M})$. The imaged volume is made up of many magnetization vectors (*i.e.*, isochromats), sufficient to avoid discretization artifacts (346); conventional MR scanning gradient fields are applied to the image volume for spatial localization, whereby gradients alter the magnetic vector (\mathbf{B}) spatially and temporally. The measurable transverse magnetization can then be found for each coil

by weighting the volume by the coil sensitivity profile, C , and integrating over all spin vectors:

$$s_n(t) = \sum_{\mathbf{r}} C_n(\mathbf{r}) \mathbf{M}_t(\mathbf{r}) \quad \text{Eq 4.2}$$

where \mathbf{r} is the spatial dimension ($\mathbf{r} = [x, y, z]$), s_n is the (k -space) signal measured on the n -th channel and \mathbf{M}_t is the magnetization projected onto the x - y plane. The acquired k -space signal can then be collected and reconstructed as desired.

4.3.2 Noise in the MR System

The noise in acquired MR images is caused both by thermal inductive losses in the patient and thermal noise introduced by electronics (339). Typically, with human MR imaging, the dominating form of noise is thermal noise introduced by the patient, which is,

$$\langle V^2 \rangle = 4k_B T R \Delta f \quad \text{Eq 4.3}$$

where V is the induced voltage, k_B is Boltzmann's constant ($8.31 \text{ J K}^{-1} \text{ mol}^{-1}$), T is the temperature (in K), R is the resistance of the subject, and Δf is the frequency band. The sample resistance can be found by observing a ratio of the coil Q -factors loaded and unloaded (339). Conversely, the thermal noise can be estimated from the variance in the final image if all other parameters are known.

Since the coil sensitivity profiles from phased array coils are not uniform, the noise produced in the sample is not the same on each of the channels. Furthermore, the noise on each channel is a function of the coil coverage (*i.e.*, the greater the coverage over the sample, the more noise). The covariance between the channels can be approximated by the spatial overlap of the coils (*i.e.*, coil overlap implies that the same thermal noise is acquired by two separate channels, so the noise is correlated). In order to fully derive the covariance matrix from coil sensitivity profiles, the noise contribution from each portion of the sample should be known. Since this is impractical, one generally assumes that each portion of the sample contributes an equal amount of noise. The

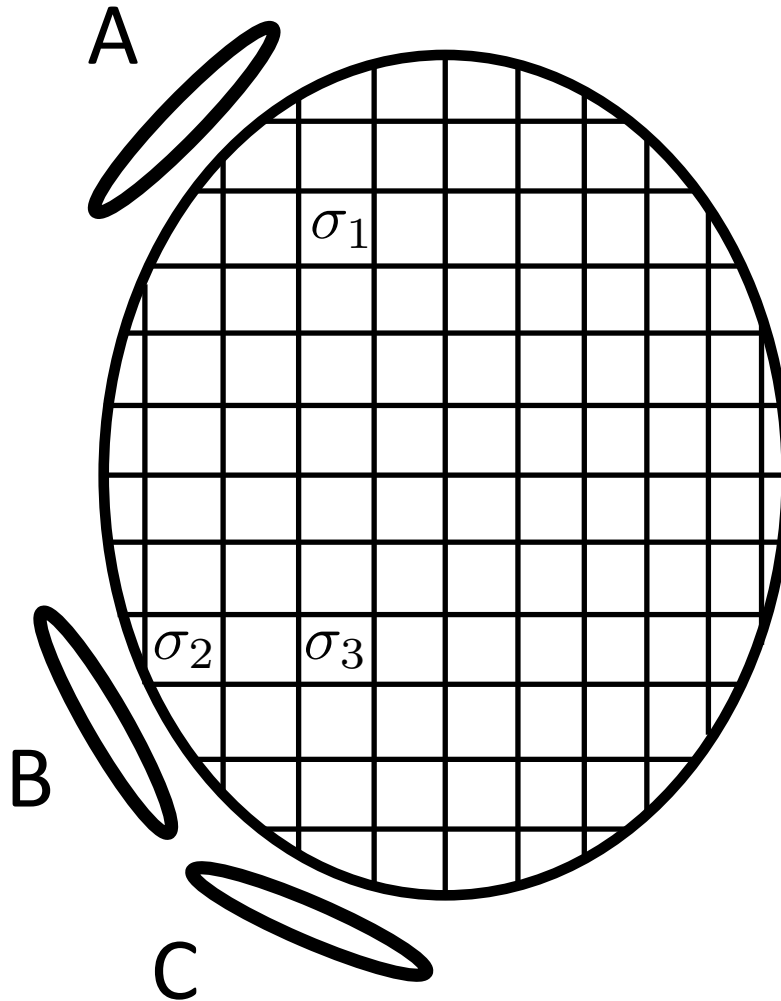


Figure 4.1: Example of noise on different receiver channels. Here, three receiver coils are shown (A, B and C) around an object being imaged. The object is the source of noise and split up with the grid to many smaller noise sources. For reference, three noise sources are shown (σ_1 , σ_2 and σ_3). The degree to which each noise source propagates to each coil depends on the coil sensitivity profiles. Noise source σ_1 propagates mostly to coil A and very little to B and C, it would not be a source contributing greatly to correlation. Noise source σ_2 being closer to coil B would primarily result in noise on B, but would result in some noise on channel C as well, causing some correlation. Noise source σ_3 would be picked up equally by coils B and C, resulting in correlation between these channels, though as it is far from coil A, it would not cause much correlation of coil A with either coil B or C.

covariance matrix between the channels is then:

$$\mathbf{Q}_{COV} = \begin{bmatrix} \sum_r C_1(\mathbf{r})C_1(\mathbf{r}) & \sum_r C_2(\mathbf{r})C_1(\mathbf{r}) & \dots & \sum_r C_N(\mathbf{r})C_1(\mathbf{r}) \\ \sum_r C_1(\mathbf{r})C_2(\mathbf{r}) & \sum_r C_2(\mathbf{r})C_2(\mathbf{r}) & \dots & \sum_r C_N(\mathbf{r})C_2(\mathbf{r}) \\ \vdots & \vdots & \ddots & \vdots \\ \sum_r C_1(\mathbf{r})C_N(\mathbf{r}) & \sum_r C_2(\mathbf{r})C_N(\mathbf{r}) & \dots & \sum_r C_N(\mathbf{r})C_N(\mathbf{r}) \end{bmatrix} \quad \text{Eq 4.4}$$

where \mathbf{Q}_{COV} is the covariance matrix, N represents the maximum number of receiver channels, and superscript H represents the Hermitian operator (complex conjugate transpose). The correlation matrix, \mathbf{Q}_{CORR} , can then be found by normalizing the covariance matrix, where σ_{kSpace}^2 is the variance data vector,

$$\begin{aligned} \mathbf{Q}_{COV} &= \sigma_{kSpace}^2 \mathbf{Q}_{CORR} \\ \mathbf{Q}_{COV} &= \end{aligned} \quad \sigma_{kSpace}^2 \begin{bmatrix} 1 & \frac{\sum_r C_2(\mathbf{r})C_1(\mathbf{r})}{\sqrt{\sum_r C_2(\mathbf{r})}\sqrt{\sum_r C_1(\mathbf{r})}} & \dots & \frac{\sum_r C_N(\mathbf{r})C_1(\mathbf{r})}{\sqrt{\sum_r C_N(\mathbf{r})}\sqrt{\sum_r C_1(\mathbf{r})}} \\ \frac{\sum_r C_1(\mathbf{r})C_2(\mathbf{r})}{\sqrt{\sum_r C_1(\mathbf{r})}\sqrt{\sum_r C_2(\mathbf{r})}} & 1 & \dots & \frac{\sum_r C_N(\mathbf{r})C_2(\mathbf{r})}{\sqrt{\sum_r C_N(\mathbf{r})}\sqrt{\sum_r C_2(\mathbf{r})}} \\ \vdots & \vdots & \ddots & \vdots \\ \frac{\sum_r C_1(\mathbf{r})C_N(\mathbf{r})}{\sqrt{\sum_r C_1(\mathbf{r})}\sqrt{\sum_r C_N(\mathbf{r})}} & \frac{\sum_r C_2(\mathbf{r})C_N(\mathbf{r})}{\sqrt{\sum_r C_2(\mathbf{r})}\sqrt{\sum_r C_N(\mathbf{r})}} & \dots & 1 \end{bmatrix} \quad \text{Eq 4.5}$$

It is at this stage where noise can be established as a circularly normal distribution, having a mean of zero and a covariance of $\sigma_{kSpace}^2 \mathbf{Q}_{CORR}$.

$$k(t_n, m) = s_{S,m}(t_n) + \eta ; \eta \sim \mathcal{CN}(0, \sigma_{kSpace}^2 \mathbf{Q}_{CORR}) \quad \text{Eq 4.6}$$

In practical circumstances it is not always true that noise will have zero mean. Still, in this simplified model the noise statistical parameters are assumed to be measurable such that a noise bias could effectively be removed. The likelihood function of the k -space data in the presence of this circularly normal distribution is,

$$p(\mathbf{k}; \mathbf{S}) = \frac{1}{2\pi \sigma_{kSpace}^2 \det(\mathbf{Q}_{CORR})} e^{-\frac{1}{2\sigma_{kSpace}^2} (\mathbf{k}-\mathbf{S})^H \mathbf{Q}_{CORR}^{-1} (\mathbf{k}-\mathbf{S})} \quad \text{Eq 4.7}$$

where, \mathbf{k} is a vector of k -space values from the channels for a given point in time, and \mathbf{S} is a vector of the measured magnetization for the channels.

4.3.3 Analytic Cramer-Rao Lower Bound

The CRLB in MR imaging can be determined analytically when there is no distortion. When there is sufficient SNR, a normal distribution can be assumed to simplify the problem. MR image generation is involved and complicated; several correction schemes are performed during image reconstruction to improve image quality. However, for derivation purposes, these complexities are avoided to present a simplified scenario, including correlated noise.

Using the inverse discrete Fourier transform, and combining the coil images with a sum-of-squares operation, the image noise follows a chi-distribution,

$$\hat{i}(\mathbf{r}) = \sum_m \text{abs}[iDFT_N(k(\mathbf{r}) + \eta)] = i(\mathbf{r}) + \varepsilon ; \varepsilon \sim Chi_{2Ncoil} \quad \text{Eq 4.8}$$

where $i(\mathbf{r})$ is the image volume data, $\hat{i}(\mathbf{r})$ is the estimated image volume in the presence of noise; and ε is the chi-distributed noise present in the estimated image data. Note that as the mean of the image becomes much larger than its noise (*i.e.*, as the SNR increases), the chi-distributed noise tends to a normal distribution. In effect, the noise distribution can be simplified into its first and second moments, whereby the signal estimation function becomes,

$$\begin{aligned} \hat{i}(\mathbf{r}) &= i(\mathbf{r}) + \langle \mathcal{N}(m, \sigma_{iSpace}^2) \rangle + \mathcal{N}(0, \sigma_{iSpace}^2) \\ &= i(\mathbf{r}) + \mu_{iSpace} + \mathcal{N}(0, \sigma_{iSpace}^2) \end{aligned} \quad \text{Eq 4.9}$$

In Eq 4.9, μ_i is a bias in the image due to noise, and σ_{iSpace}^2 is the variance of the image ($\sigma_{iSpace}^2 = \sigma_{kSpace}^2/N$) for the case where the channels are completely uncorrelated). If the k -space signal noise level is measured then this bias, μ_{iSpace} , can be determined and removed, but in practice this is rarely done.

Letting $\theta = i + \mu_i$ the likelihood function of the estimated image can be expressed as a specific normal (*a.k.a.* Gaussian) case,

$$p(\hat{i}; \theta) = \frac{1}{\sqrt{2\pi\sigma_{iSpace}^2}} e^{-\frac{(\hat{i}-\theta)^2}{2\sigma_{iSpace}^2}} \quad \text{Eq 4.10}$$

The score (*i.e.*, derivative of the log-likelihood function) and the expectation of the

second derivative can then be found as:

$$\frac{d \ln p(\hat{i}; \theta)}{d\theta} = \frac{1}{\sigma_{iSpace}^2} (\hat{i} - \theta) \quad \text{Eq 4.11}$$

$$\sigma_{iSpace}^2 = - \frac{1}{\left\langle \frac{d^2 \ln p(\hat{i}; \theta)}{d^2 \theta} \right\rangle} \quad \text{Eq 4.12}$$

The Fisher information and CRLB are thus analytically found to be $1/\sigma_{iSpace}^2$ and σ_{iSpace}^2 , respectively. It should be noted that this expression is the same as the classical CRLB for a normally-distributed random variable (328).

This section has thus far demonstrated the derivation of the CRLB when there is no distortion. This represents the lowest achievable variance with MR imaging. Next, correlated noise is introduced and shown to reduce the information content of the acquired data by raising the CRLB. Correlated noise arises when the noise on individual receiver channels are not independent. Correlation between channels can be expressed with a correlation matrix (\mathbf{Q}_{CORR}), and if the channels are related by spatial position as in MR imaging, then the elements of \mathbf{Q}_{CORR} can be approximated by,

$$q_{ij} = e^{-a|j-i|} \quad \text{Eq 4.13}$$

Where q_{ij} is the i^{th} row and j^{th} column term in the matrix \mathbf{Q}_{CORR} , and ‘ a ’ scales the off diagonal components of the matrix (bounded between 0 and 1). Eq 4.13 is a convenient way to vary the level of correlation by adjusting a single parameter. A decreased value of ‘ a ’ results in increased correlation between channels. Typically, e^{-a} is expected to range between 0.4 and 0.6 for most modernly designed coil arrays.

Since a correlation matrix is semi-positive definite, it can be expressed as $\mathbf{Q}_{CORR} = \mathbf{V}\mathbf{\Lambda}\mathbf{V}^H$, where \mathbf{V} is the matrix of eigenvectors and $\mathbf{\Lambda}$ is the diagonal matrix of eigenvalues. The probability density function of the correlated normal noise case is,

$$p(\mathbf{k}; \mathbf{S}) = \frac{1}{2\pi\sigma_{kSpace}^2 \prod_n \lambda_n} e^{-\frac{1}{2\sigma_{kSpace}^2} (\mathbf{k}-\mathbf{S})\mathbf{V}^H\mathbf{\Lambda}^{-1}\mathbf{V}(\mathbf{k}-\mathbf{S})} \quad \text{Eq 4.14}$$

where the λ_n terms are the eigenvalues, and $\prod_n \lambda_n$ is the multiplicative sum of those eigenvalues. Eq 4.14 can be further analyzed by taking the derivative of the natural

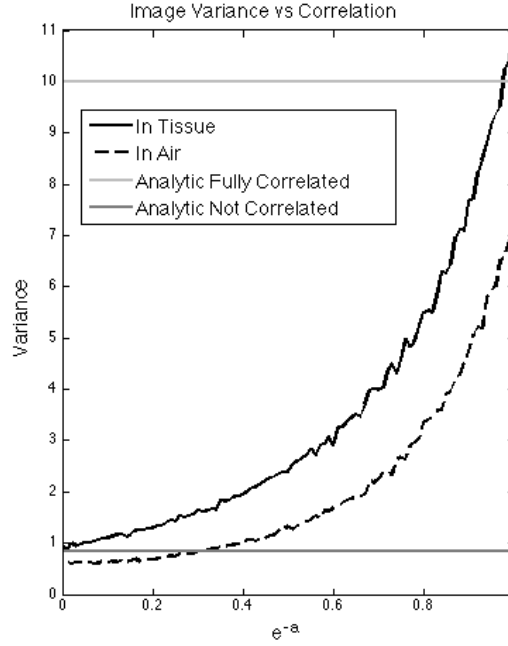


Figure 4.2: A plot of the level of correlation $e^{-\alpha}$ against the minimum achievable variance of a fully sampled MR image. This graph demonstrates the relationship between the degree of correlation between receiver channels and the variance in the final images.

logarithm, and finding the CRLB of the k -space noise.

$$\frac{d \ln p(\mathbf{k}; \mathbf{S})}{d\mathbf{S}} = -\frac{1}{\sigma_{kSpace}^2} \sqrt{\Lambda^{-1} \mathbf{V}} (\mathbf{k} - \mathbf{S}) \quad \text{Eq 4.15}$$

Eq 4.15 shows that the Fisher information of the k -space data is dependent on the eigenvalues and eigenvectors of the correlation matrix. This increases the CRLB as the channels become more correlated. The matrix \mathbf{Q}_{CORR} can be estimated by averaging any noise points in k -space or observing the relation between samples as in Eq 4.5. Data can be de-correlated by multiplying the sample vector by the matched filter,

$$\mathbf{k}_{DeCorrelated} = \frac{\sqrt{\Lambda^{-1} \mathbf{V}}}{\sigma_{kSpace}^2} \mathbf{k}_{Correlated} \quad \text{Eq 4.16}$$

where $\mathbf{k}_{Correlated}$ is a vector of each of correlated samples at a given point in time, and $\mathbf{k}_{DeCorrelated}$ is the decorrelated vector. As the CRLB increases for the k -space data, it in turn increases for the image data as well, $\sigma_{iSpace}^2 = \sigma_{kSpace}^2 / (M \sqrt{\Lambda^{-1} \mathbf{V}})$. In the case

where the channels are fully uncorrelated and there is no independence of the noise, the image variance can be found as $\sigma_{iSpace}^2 = \sigma_{kSpace}^2/M$, and there is no improvement in adding imaging coils. In Figure 4.2 there is a plot of the term ‘ a ’ used in Eq 4.13 vs. the lower bound in simulation. As the correlation increases between the MR receiver channels there is an increase in the minimum achievable lower bound. The lower bound in this case matches the analytic CRLB derived above.

4.3.4 Machine Distortion

There are several sources of distortion in MR images, including B_0 and B_1 inhomogeneity, coil sensitivity, non-linear gradient warp correction, subject motion and eddy currents, to name a few. B_0 inhomogeneity arises when the static magnetic field is not uniform. It can arise from imperfections in magnet construction or the spatially varying magnetic susceptibility of the subject. If there is rapidly changing spatial susceptibility from the patient being imaged, this can result in B_0 distortion (290,348). Different MR pulse sequences have varied sensitivity to static field inhomogeneity; gradient-recalled echo planar imaging (EPI) is very sensitive (290), while spoiled gradient-recalled echo (SPGR) is less sensitive. Mathematically, B_0 distortion can be described with a spatial function,

$$B_{0,eff}(\mathbf{r}) = B_{0,ideal}(\mathbf{r}) + B_{0,dis}(\mathbf{r}) \quad \text{Eq 4.17}$$

where $B_{0,ideal}(\mathbf{r})$ is the ideal static field, $B_{0,dis}(\mathbf{r})$ is distortion in the field, and $B_{0,eff}(\mathbf{r})$ is the effective field which varies as a function of space. In practice, the B_0 field can be measured by collecting a series of MR image volumes with different echo times (TE), fitting to the phase difference between them, then dividing by the TE to estimate the local Larmor frequency and thus the $B_{0,eff}(\mathbf{r})$. When correcting for bias due to B_0 it is almost always desired to measure the field, as it is object-dependent.

B_1 field inhomogeneity arises from non-uniform excitation (349). Ideally, if a flip angle of, say, 60 degrees was prescribed then all magnetization in the volume would be nutated by this amount. However, in practice, this is not the case; the flip angle can vary throughout the image volume. Generally, the variation of flip angle is within $\pm 30\%$ or so.

Again this distortion is spatially varying and can be described as,

$$B_{1,eff}(\mathbf{r}) = B_{1,ideal}(\mathbf{r}) \times B_{1,dis}(\mathbf{r}) \quad \text{Eq 4.18}$$

where $B_{1,eff}$ is the measured flip angle, $B_{1,ideal}$ is the ideal or prescribed flip angle, and $B_{1,dis}$ is the distortion scaling the flip angle.

Coil sensitivity artifacts arise due to the spatial sensitivity of receiver coils and were addressed by Eq 4.2. If magnetization is located closer to the receiver coil then it will have a higher weighting than magnetization that is further away,

$$i_{eff}(\mathbf{r}) = \sum_m C_m(\mathbf{r})i(\mathbf{r}) \quad \text{Eq 4.19}$$

where i is the image volume with no sensitivity coil artifact, i_{eff} is the measured signal, and C_m is the spatially varying coil profile. Coil sensitivity profiles are routinely measured since they are used for sensitivity encoding (SENSE) algorithms that accelerate image acquisition via parallel imaging (114,350). If coil sensitivity profiles are not corrected for there is a reduction of signal in the center of the object and an increase of the signal towards the edges of the object. The coil sensitivity profiles can be estimated by reconstructing images from each of the channels and then dividing these images by either a sum of squares or a body coil image with a more uniform profile (114). Although the coil sensitivity profiles can, in principle, be generated through simulation with accurate knowledge of the physical coil construction, in practice coil sensitivity profile estimates are almost always measured.

It is desirable to have linear gradient coils but non-linearity usually exists to some degree and causes spatial shifting of the image,

$$i_{warped} = i_{eff}(\mathbf{r} + \mathbf{d}(\mathbf{r})) \quad \text{Eq 4.20}$$

where i_{warped} is the warped signal i_{eff} is the acquired signal and \mathbf{d} is a vector field that distorts the position of the acquired signal. Although gradient coils can be constructed that are very linear, these components are generally optimized for switching speed and to reduce peripheral nerve stimulation (351,352). A vector field of the resulting distortion can be calculated from spherical harmonic coefficients (353-355).

4.4 Methods

4.4.1 Digital Anthropomorphic Phantom Design

To perform simulations a brain volume was developed. One healthy human volunteer was recruited (26 year old female) and consented to having data acquired and used for this study. Imaging was performed with a 3 T MR scanner (Discovery MR 750, General Electric Healthcare, Waukesha, WI). A protocol was developed which calculated a broad range of imaging metrics; biological measurements of the tissue including T_1 , T_2 , T_2^* , χ and M_0 were collected, and in addition machine specific metrics including the noise correlation, gradient warping, B_0 field, B_1 field, and coil sensitivity profiles were measured.

The protocol used for image acquisition took a total of 26 minutes. The imaging sequences and prescribed parameters are outlined in Table 1. From sequence 1, the B_0 field was calculated by line fitting the phase evolution with respect to TE . Phase correction was performed on the phase maps used to calculate the B_0 fields as described by Jezzard *et al.* (290). From sequence 2, the B_1 estimate is obtained; this sequence acquires the data with interleaved TRs and then estimates the B_1 map with the methods described by Voigt *et al.* (349). The coil sensitivity profiles were measured from the magnitude coil images, divided by a sum-of-squares coil sensitivity maps (114); values in air, where the coil sensitivity could not be measured, were set to zero. Maps of T_2^* were calculated from sequence 1 with an exponential fitting process. Using sequences 3-6, maps of the T_1 and T_2 were calculated from the DESPOT1 and DESPOT2 methods (356,357). Magnetic susceptibility (χ) was calculated from the magnetic field (Sequence 1) using background field removal and dipole fitting, M_0 was estimated by the direct relationship between susceptibility and applied field, $M_0 = \chi \mathbf{H}$. Brain extraction (skull stripping) was performed for all the maps.

The noise covariance matrix was calculated using Eq 4.5 and the measured coil sensitivity profiles; the correlation matrix and noise variance (σ_{kSpace}^2) were determined by normalizing the maximum of the covariance matrix to one.

Table 4.1: Protocol used for quantification of MR parameters.

Sequence #	Parameters									
	FOV (cm)	TR (ms)	TE (ms)	Flip (degrees)	BW (\pm kHz)	Slice Thickness (mm)	Matrix Size	Aqu Time	Num Echoes	PI Acceleration Factor
1 multi echo SPGR	25.6 × 25.6 × 12.8	2000	2.2-21.7	15	62.5	2	256 × 256 × 128	4:12	8	2
2 B1 mapping	25.6 × 25.6 × 12.8	16-60	1.7	60	62.5	4	128 × 128 × 32	5:53	1	1
3 SPGR 1	25.6 × 25.6 × 12.8	6.9	3.1	4	31.25	1	256 × 256 × 128	3:58	1	1
4 SPGR 2	25.6 × 25.6 × 12.8	6.9	3.1	18	31.25	1	256 × 256 × 128	3:58	1	1
5 bSSFP 1	25.6 × 25.6 × 12.8	6.7	3.3	4	125	1	256 × 256 × 128	3:47	1	1
6 bSSFP 2	25.6 × 25.6 × 12.8	6.7	3.3	18	125	1	256 × 256 × 128	3:47	1	1

SPGR – Spoiled Gradient Recalled Echo, bSSFP – balanced steady-state free precession

4.4.2 Numerical Simulation

Numerical simulations were performed to quantify the lower bound. A k -space signal model was created from the image space signal generated from the anthropomorphic phantom. Monte Carlo style simulations were performed to observe how the noise in k -space would propagate through to the final images. Different distortion effects could be incorporated or removed from the simulation to understand how these effects change the final image. Numerical simulations were performed on a Unix computer (OpenSUSE 12.3, 64-bit edition, Cambridge, MA). Software was written in MATLAB (R2013a, Natick, MA) as it provided for simple visualization of the data. Since the overall computational demand was high, C/C++ functions were written in MEX format to decrease overall simulation runtime.

MR signal values were calculated with the Bloch equation as described in the theory section. Maximum gradient strength and slew rate were set to match that configured for our magnet, 50 mT m^{-1} and $200 \text{ mT m}^{-1} \text{ ms}^{-1}$, respectively. Empirical parameters matching Table 1 Sequence 3, $TR = 6.9 \text{ ms}$ and $TE = 3.1 \text{ ms}$, were used in the Bloch equations and compared against images from that sequence. RF spoiling and spoiler gradients were utilized. Pulse sequences were set to match those used on the scanner. The pulse sequence shown in this study was the spoiled gradient recalled echo (SPGR), as SPGR challenges the simulation with saturation and phase dispersion effects.

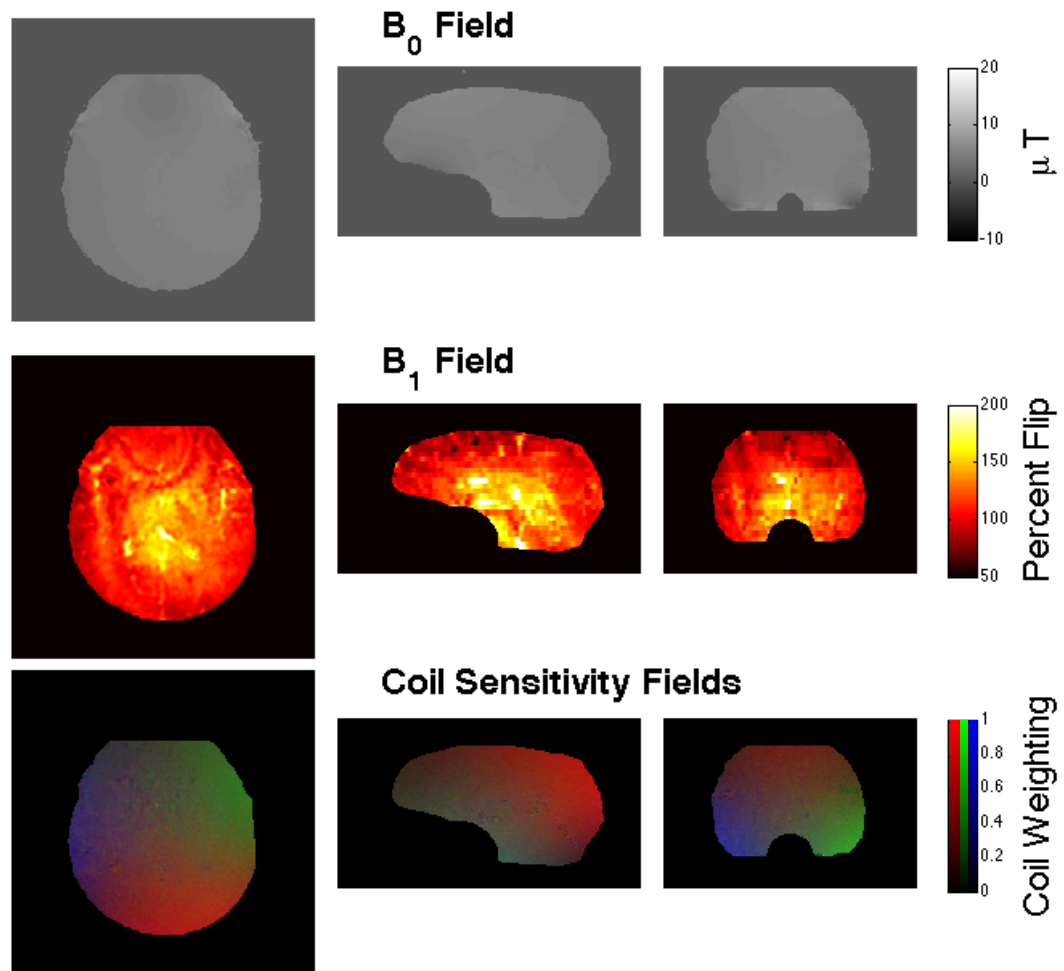


Figure 4.3: Measured B_0 field, B_1 fields, and coil sensitivity profiles. Each volume type is displayed at three orthogonal cross sections.

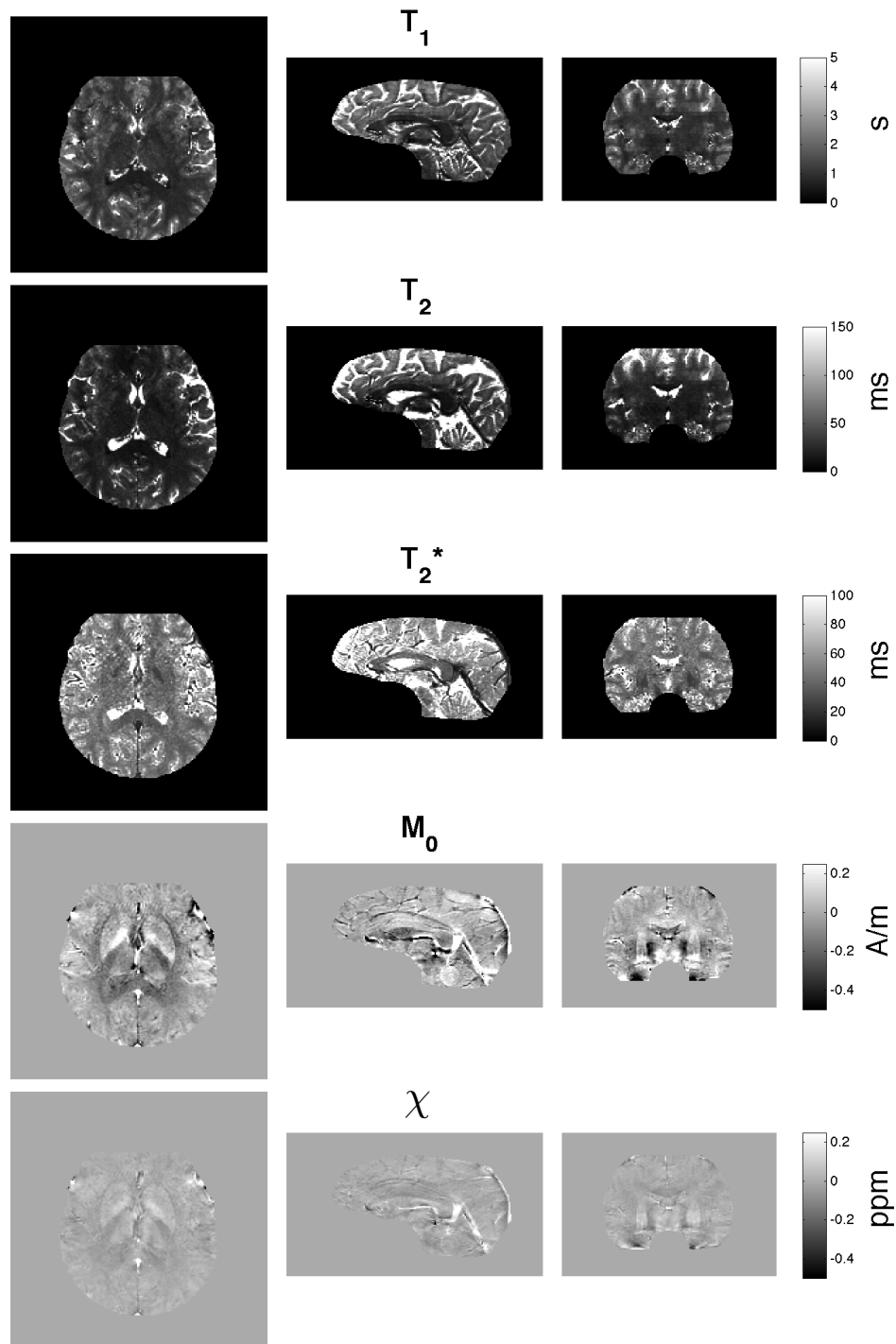


Figure 4.4: Calculated T_1 , T_2 , T_2^* , M_0 , and susceptibility maps. Estimates demonstrate accurate quantification, matching values reported in literature for different tissue types.

4.5 Results

4.5.1 Analytical Evaluation of the CRLB

Figure 4.2 shows the change of the minimum variance in both air and tissue signal. As e^{-a} increases, the minimum achievable variance is increased and the quality of the images decreases. The effect of having a lower achievable variance in the tissue is due to the chi nature of the noise in the absence of signal. In air the assumption of normally distributed noise does not hold, however in tissue the noise variance matches that found in analytic derivation based on sample resistance. This profile indicates that there is an acceptable level of correlation that can exist without significantly affecting image variance. e^{-a} is expected to range between 0.4 and 0.6 in vendor-supplied receiver coils. This degree of coil correlation could affect the SNR by up to $2\times$ to $3\times$ over that range. Full correlation between the channels might lead to a variance increase of $4\times$ to $5\times$.

4.5.2 Digital Anthropomorphic Phantom

The digital phantom was produced with expected values within reasonable tolerances. The machine distortion and physiological parameters are shown in Figure 4.3 and Figure 4.4, respectively. Measurements of distortion for the coil sensitivity, B_0 distortion, and B_1 distortion are shown in Figure 4.3. Gradient non-linear distortion (*i.e.*, geometric warping) was matched to our system and had spatial deviations of 2 mm to 3 mm towards the edge of the field of view and 1 mm to 2 mm towards the periphery of the brain, This distortion did not significantly broaden the probability density function of the noise. Example images of T_1 , T_2 , T_2^* , χ and M_0 are shown in Figure 4.4. An example of a repetition period is shown in Figure 4.5, and includes the magnetization evolution of the volume. Synthetic images generated with the Bloch equation simulator had similar characteristics compared to the empirically acquired images in Figure 4.6.

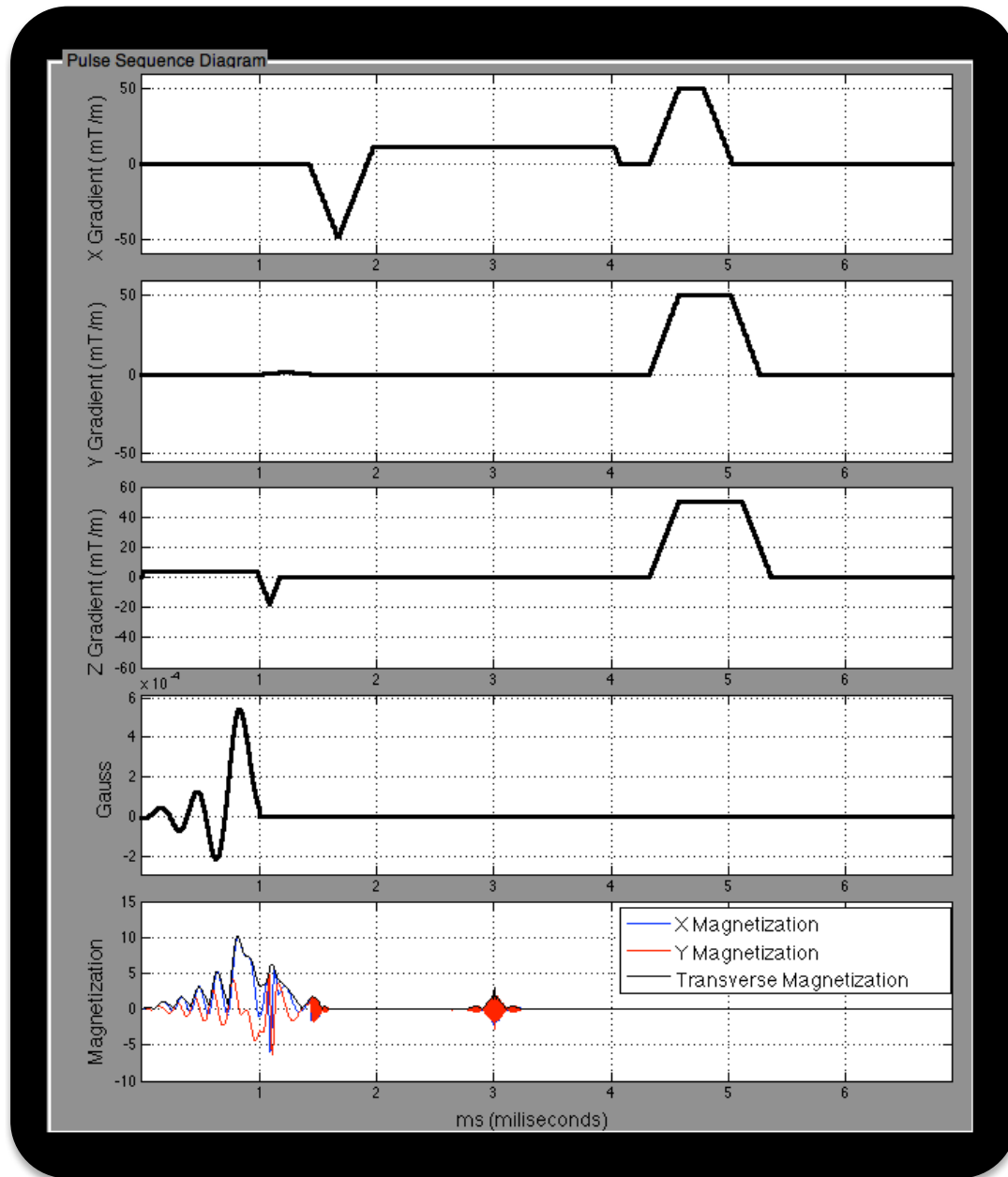


Figure 4.5: Pulse sequence used for simulation and evolving magnetization. This plot shows an echo passing near the center of k-space. The first three plots show the gradient trajectories, the fourth plot shows the excitation pulse and the fifth plot shows the evolution of the x, y and total transverse magnetization components; an echo is seen at the center of the readout gradient.

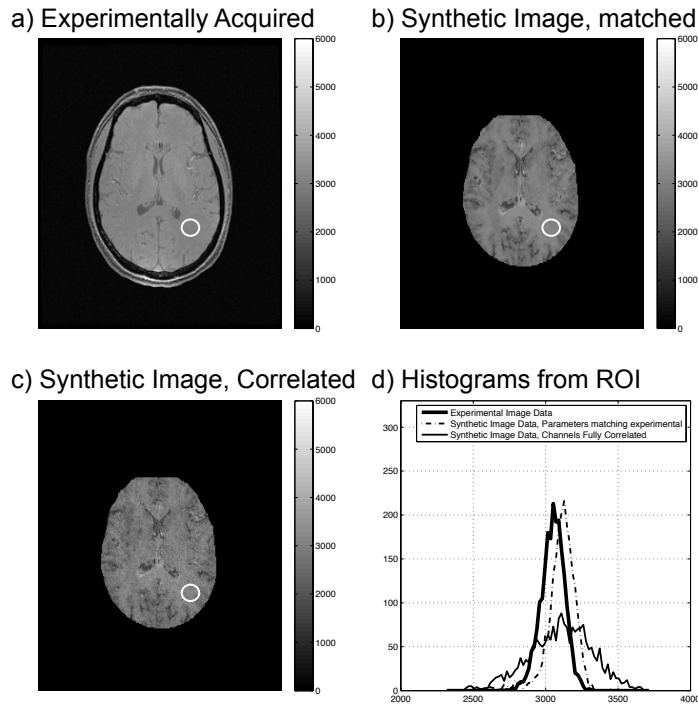


Figure 4.6: Comparison of empirical and synthetic images. Data was collected with a spoiled gradient recalled echo sequence. Parameters used to acquire the image on the scanner side (a) were matched to the parameters used in the simulation (b). An additional simulation was performed where the channels were fully correlated (c). Histograms from a region of interested (white circle) are shown (d).

4.5.3 Lower Bound

Histograms taken from the same region in the empirical and simulated SPGR images are shown overlapping in Figure 4.6d. The mean and standard deviations for these regions were found to be 3048.6 and 82.7 for the experimentally acquired image, 3106.5 and 103.5 for the simulated image with matching parameters and 3101.2 and 219.4 for the simulated image with fully correlated channels.

Plots of the signal variance are shown in Figure 4.2 and support the findings here. The variance found from the experimentally derived coils ($e^{-\alpha} \cong 0.48$), increased by $4.49\times$ when the channels were fully correlated. This is within the expected range of $4\times$ to $5\times$ increase of the CRLB based on plot in Figure 4.2. This consistency demonstrates the reliability of the simulation framework. The CRLB is found to be meaningful with respect to the experimental results.

4.6 Discussion

Estimation theory was used to examine the effect of noise propagation in the presence of correlated noise. Physiological and machine distortion parameters were quantified to create a digital brain phantom. Using the magnetic properties of this phantom, a Bloch simulation was performed to obtain magnetization. The magnetization yielded k -space data. The k -space data was then reconstructed to form synthetic MR images. The first simulated acquisition was matched to one of the experimentally acquired images. Synthetic images were also collected with fully correlated acquisition channels. Measurement of the variance of the signal was examined in the same spatial region of each image, the mean signal intensity was compared between the experimental and synthetic images and the difference was found to be less than 2%. As expected, the variance of the image data was much higher in the simulation case where the channels were fully correlated. The simulation methodology is generalizable and, for example, could be adjusted to observe the distortion effects caused by something other than just the coil correlation. For example, one could slowly adjust the magnitude of the \mathbf{B} field to see how this changes the SNR properties of the final image.

Issues of quantization are a concern due to the large number of calculations performed. Entropy enters the simulation through the parametric maps of the digital brain phantom. There may be errors due to the imprecisions in the timing of the gradients. Increasing the temporal and spatial resolution, and applying more exact knowledge of the magnetization would improve the accuracy and possibly change the observed distributions. Erosion of the brain mask was required for the reliability of some measurements, particularly the tissue susceptibility. Here, erosion was applied particularly aggressively; future iterations of the digital phantom could have less erosion applied. Motion could also be introduced to see how different acquisitions perform in its presence.

Other interesting advancements to the described brain phantom and Bloch equation simulation approach would include the ability to adjust the properties with respect to the field strength. Advancements of acquiring additional image data metrics such as velocity, diffusion and cerebral blood flow, could lead to simulated acquisition of

these effects. The result for an SPGR sequence is shown, however, the simulation could be used with other gradient and RF trajectories, such as: propeller (358), spiral (359), or cone (360), or even compare the SNR efficiency between them. Sequence trajectories such as echo planar imaging could work, but the implementation of a spectrally selective pulse would not be possible currently with this simulation, as the MR frequency spectrum was not mapped for each voxel into the digital brain phantom. Collection of the spectrum of each voxel would be an interesting advancement on the phantom to improve its use.

MR imaging is a complicated technology and, thus simulation yields to improved understanding. In this chapter, advanced simulation methodology was used to explore the effect of coil correlations on the SNR of acquired images. This simulation showed what might be considered the simplest case of acquisition, though in the future I intend to expand upon these simulations to look at the effect of various other distortions to improve the quality of acquisitions.

4.7 Chapter Summary

This chapter explores MR technology from a more philosophical point of view, to understand its limitations. The CRLB represents a limit of how good one can do with a 'linear' style of thinking. This chapter was intended to address the fundamental underlying limitations, and the effect of coil sensitivity is addressed, but there are many other available sources of distortion. The work from this chapter was continually refined during my degree. The following chapters (Chapters Five through Eight) will shift focus to the quantitative measurements of the cerebrovascular system. The next chapter will examine an illustrative case of a treated giant cerebral aneurysm.

Chapter Five:

**Pressure and Flow Alteration in a Giant Cerebral
Aneurysm Treated with a Pipeline Stent**

5.1 Chapter Overview

Cerebral aneurysms are a vascular malformation, where a bulb-like formation (*i.e.*, the fundus) projects out from the vessel lumen. The presence of an aneurysm may alter many hemodynamic parameters, including: blood velocity, volume flow rate (VFR) and intravascular pressure. It is expected that intervention on cerebral aneurysm using a pipeline stent will bring hemodynamic parameters closer to those observed on the contralateral side. A patient with a giant cerebral aneurysm was studied pre- and post-operatively using phase contrast (PC) magnetic resonance (MR) imaging. Computed tomography (CT), x-ray digital subtraction angiography (DSA), and conventional MR neuroimaging were also acquired. Non-invasive pre- and post-operative imaging was used to study the hemodynamic changes resulting from the deployment of a flow-diverting pipeline stent. PC-MR images were used to calculate intravascular pressure, which was compared to more invasive endovascular catheter-derived measurements. VFRs were compared before and after the intervention to assess the degree of flow diversion caused by the stent, and change in flow symmetry. After stent placement the measured VFRs in vessels in the treated hemisphere approached those measured on the contralateral side, flow symmetry changed from a laterality index of -0.153 to 0.116 in the middle cerebral artery. Pressure estimates derived from the PC velocity data were within 10% of the invasive catheter transducer measurements. PC-MR imaging can be used to provide non-invasive measurements of hemodynamics pre- and post-operatively. This case demonstrates how treatment with a stent can restore flow symmetry.

5.2 Objective

Cerebral aneurysms often form at high-pressure regions and at bifurcations of the cerebral arterial vasculature. They grow outward from the vessel lumen, causing damage to the brain (mass effect) and may infringe on key structures such as the optic nerve. Cerebral aneurysm carries high risk of rupture and frequently results in intra-cerebral hemorrhage (ICH). The prevalence of cerebral aneurysm is 2.3% in the adult population (52). Their etiology is unclear, but their origin and development are thought to be affected by intravascular hemodynamics (209,210,361). Wall-shear stress (WSS) (209)

and pressure normal to the vessel wall (204,362,363) have also been proposed as factors affecting aneurysm growth. Cerebral aneurysms are usually discovered incidentally with imaging examination of neurological symptoms. Standard treatments include surgical clipping, and a variety of endovascular techniques including coiling and stenting (79,364). Volume flow rates (VFR) are known to be altered near and distal to the aneurysm (365). VFR changes are associated with aneurysm growth and to disruption of the distal perfusion. Comprehensive study of hemodynamic parameters in cerebral aneurysm cases, nonetheless, is difficult in practice due to the high variability of aneurysm formation and resulting geometry. While the majority of cerebral aneurysms form near the middle cerebral or anterior cerebral artery (MCA, ACA) bifurcations or at the termination of the basilar artery, they can exist in other locations as described in this report.

Different imaging modes have been used to examine aneurysms, including: computed tomography (CT) and CT angiography (CTA), X-ray digital subtraction angiography (DSA), conventional and Doppler ultrasound (US), and MR imaging, *cf.*, (79,204,220,361,363,366). Estimation of hemodynamic parameters have been derived using many of these imaging modalities (53,209,211,361,367,368); however, there remains still much to understand with respect to 1) the relationship between hemodynamics and disease progression and 2) both planning and evaluation of interventions using these advanced parameters. Post-operatively VFR is expected to become more symmetric across the brain after aneurysm treatment with a stent, and that collateral flow will be reduced. It is also hypothesized that VFR and pressure distal to the aneurysm will increase with stent treatment. Here, a role for phase contrast (PC) MR in assessing cerebral aneurysm, pre- and post-intervention is demonstrated *via* a clinical case study. As a secondary outcome, upon successful deployment of a flow diversion stent, the VFR and pressure measurements near and distal to the aneurysm become similar to values observed on the contralateral side.

5.3 Methods

5.3.1 Patient History

A 63-year old female patient presented with a three-week history of headache without significant triggers, including trauma. They described a throbbing pain, focused behind the left eye and in the temporal region, rating the pain as an eight or nine on a scale of ten. Seizures or weakness in the face or limbs was not reported. The subject was a non-smoker and non-drinker and was not taking any medication. Other medical history was unremarkable, and vitals signs were normal. Previous CT imaging revealed a large unruptured left cavernous internal carotid artery (ICA)-segment aneurysm. The aneurysm diameter ranged between 14 mm and 23 mm, with a 6 mm-wide neck. Additional imaging revealed that the aneurysm contained thrombus, filling the inferior portion. There was no ICA stenosis found on imaging. The intervention (described below) was successful and the patient described an improvement in hearing after one week. Informed written consent was obtained prior to research imaging.

5.3.2 Imaging

The patient underwent CT and CTA examinations, DSA during intervention and three MR examinations (one prior to the intervention and two post stenting). The CT/CTA and first MR imaging exam occurred prior to the procedure. The second MR examination was part of post-operative standard care and was performed before the patient was discharged (two days after the intervention). The third MR examination occurred four days after the intervention. Non-contrast CT imaging and CTA was performed (Discovery CT750HD, General Electric Healthcare, Waukesha, WI). For CTA, 80 ml of iodine-based contrast agent (Optiray 320; Covidien, Hazelwood, MO) was injected at 5 ml/s intravenously. The CT images were reconstructed axially at a resolution of 0.625 mm in plane. The CTA was reconstructed axially at a resolution of 0.625 mm (pixel size) and reformatted to generate coronal and sagittal oriented images. The dose-length product was 933.37 mGy cm and 571.53 mGy cm, for the CT and CTA, respectively.

X-ray DSA was performed using a bi-planar angiography suite (Artis; Siemens, Forchheim, Germany) during the intervention (stent deployment). During the procedure

injection runs were collected before and after stent deployment, visualizing the passage of the contrast agent and providing 3D spin angiograms. The DSA bi-planar images were acquired at a rate of 4 Hz. An injection protocol of 10 ml injection at 5 ml/s was used in each run.

The first and third imaging examinations used a 3 T MR scanner (Discovery 750; General Electric Healthcare). The protocol included: 1) localizer and sensitivity calibration scans, 2) non-contrast enhanced time-of-flight (TOF) angiographic images and 3) several low- and moderate-resolution PC image volumes, and 4) a 4D flow imaging sequence centered on the aneurysm region. The initial strategy was to globally interrogate the larger vessels (with typical flow velocities on the order of 80 cm/s to 100 cm/s) and then to image the cerebral aneurysm (with expected flow velocities on the order of 10 cm/s to 20 cm/s). The TOF parameters were TR/TE/flip = 22 ms/2.4 ms/15°, acquired matrix and field-of-view (FOV) of 192 × 256 × 56 and 16.5 cm × 22 cm × 11.2 cm, an acceleration factor of R = 2, acquisition of two slabs with a ramped excitation pulse and eight overlapping partitions. The first 3D PC acquisition had TR/TE/flip = 8.2 ms/3.8 ms/10°, acquired matrix and FOV of 192 × 256 × 196 and 16.5 cm × 22 cm × 19.6 cm and used a PC velocity encoding (v_{enc}) = 100 cm/s. An additional reduced FOV 3D PC acquisition had TR/TE/flip = 8.2 ms/3.8 ms/10°, acquired matrix and FOV of 192 × 256 × 196 and 16.5 cm × 22 cm × 12.8 cm with v_{enc} = 30 cm/s. The 4D PC examined a region immediately surrounding the aneurysm and had TR/TE/flip = 17.0 ms/6.2 ms/15°, acquired matrix and FOV of 192 × 256 × 10 and 16.5 cm × 22 cm × 3 cm with v_{enc} = 20 cm/s. Retrospective gating was used to reconstruct 30 cardiac phases per cardiac cycle. Imaging volumes were positioned to ensure overlap so that they could easily be combined during subsequent post processing steps.

The second MR examination was performed on a 1.5-T MR scanner (Optima 450W, General Electric Healthcare) as part of standard clinical care. This imaging protocol included: 1) T₂-weighted fluid attenuated inversion recovery (FLAIR) imaging, 2) diffusion weighted imaging (DWI), 3) susceptibility-weighted angiography (SWAN; General Electric Healthcare), 4) non-contrast agent enhanced TOF imaging and 5) contrast agent enhanced TOF imaging.

5.3.3 Endovascular Intervention

The patient received antiplatelet therapy for a week prior to the operation. The intervention was performed with bi-planar angiography guidance and endovascular surgical approaches were used to place a flow diverting pipeline stent (4 mm × 20 mm; Covidien) in the left cavernous ICA segment, in order to bypass the neck of the aneurysm. The procedure was performed under general anesthesia. A puncture was made to introduce a 6 Fr shuttle catheter (Cook Medical, Bloomington, IN) over a 5 Fr VTK-selective catheter (Cook Medical) and guided to a position proximal to the aneurysm neck in the ICA. Frontal and lateral angiogram images were acquired. Pressure measurements were taken with a catheter transducer around the aneurysm, in the MCA M1, in the supraclinoid ICA and the cavernous ICA. The pipeline stent was deployed, with the distal end lying just proximal to the posterior communicating artery (PCoM) bifurcation. The stent was expanded with a balloon catheter (Hyperform; Covidien, Hazelwood, MO). Additional DSA imaging indicated that blood flow was restored to vessels distal to the stent. After the stent was deployed the catheter transducer was again used to measure the pressure at the cavernous ICA proximal to the deployed stent.

5.3.4 Analysis

PC MR image data were post-processed using a combination of custom-written programs (Matlab R2013a; The Mathworks, Natick, MA) and freely available software (Paraview v4.0; Kitware Inc., Clifton Park, NY). The hemodynamic metrics of primary interest were velocity, VFR and pressure. The PC images provided velocity measurements. VFR was calculated by placing cut planes through the vessels, then taking the surface integral of the flow velocity across the vessel lumen. Normalized VFR values were calculated by dividing the flow measured in each vessel by the total flow into the brain (summation of VFR in both ICAs and vertebral arteries) in order to observe relative changes in flow before and after the intervention. The intravascular pressure was obtained by solving the

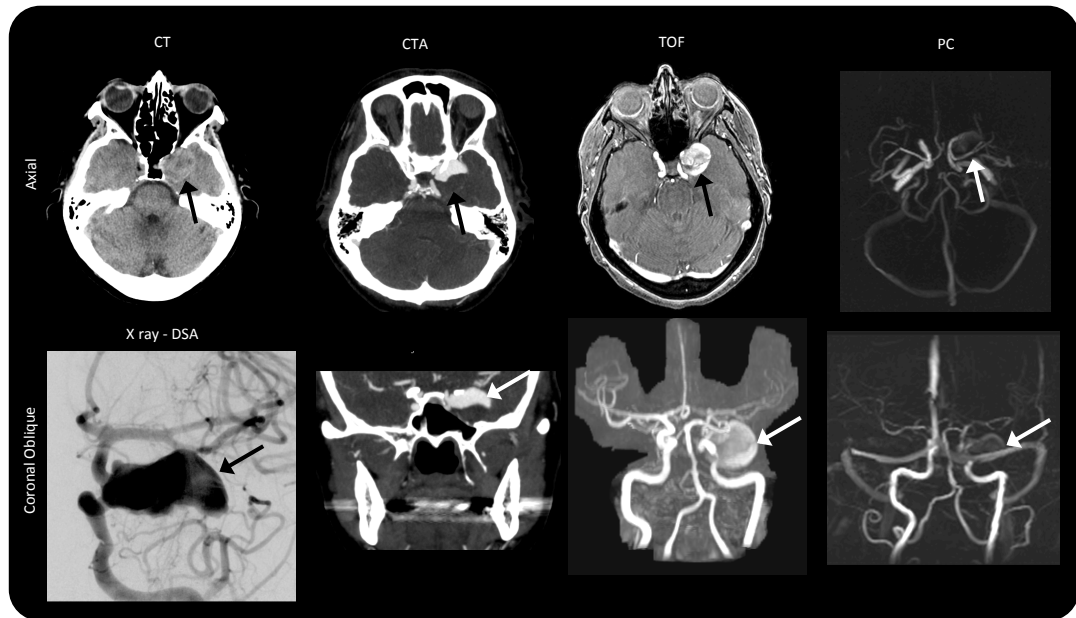


Figure 5.1: Pre-operative computed tomography (CT), CT angiography (CTA), X-ray digital subtraction angiography (DSA), non-contrast enhanced time-of-flight (TOF) imaging, and phase-contrast (PC) imaging. The aneurysm (black and white arrows) was clearly depicted on the combination of axial and coronal orientations. The coronal TOF and the PC images are maximum intensity projections.

Navier-Stokes equation (217-219) using the measured 4D velocity field (362). All post-intervention imaging was used to assess the success of the treatment. VFRs measured, before and after the intervention, were compared and the absolute difference and percent change calculated. VFRs in vessels proximal and distal to the aneurysm (with diameters >1 mm, see Table 5.1) were compared to the contralateral vessels and pre- and post-operative VFR laterality index was calculated between paired vessels. Laterality ratio was $(L-R)/(L+R)$ where R and L represent the VFR through the right and left paired vessels, respectively. Pressure estimates obtained with catheter transducer were compared to measurements derived from the 4D flow measurements.

Table 5.1: Volume flow rate (VFR) measurements in larger cerebral vessels before and after stent deployment. Vessels were measured at the cut planes shown on Fig 2. VFR is also normalized to the total flow entering the brain through the ICA and vertebral arteries (pre and post-operative 5.97 ml/s and 5.06 ml/s, respectively). VFR laterality index was calculated as $(L-R)/(L+R)$.

ICA – Internal Carotid Artery, PCA – Posterior Cerebral Artery, MCA – Middle Cerebral Artery, ACA – Anterior Cerebral Artery, Acom – Anterior communicating artery.

Blood Vessel Measured	Pre-Operative			Post-Operative			Relative Change	
	VFR (ml/s)	Normalized VFR	Laterality Index	VFR (ml/s)	Normalized VFR	Laterality Index	Absolute	Normalized
Right Above Bifurcation ICA	3.05	0.51	-0.190	2.46	0.49	-0.095	-0.19	-0.05
Left Above Bifurcation ICA	2.08	0.35		2.03	0.40		-0.02	0.15
Right Cervical ICA	3.37	0.56	-0.167	2.44	0.48	-0.048	-0.28	-0.15
Left Cervical ICA	2.40	0.40		2.22	0.44		-0.08	0.09
Right Cavernous ICA	2.97	0.50	-0.350	1.98	0.39	----	-0.33	-0.21
Left Cavernous ICA*	1.43	0.24		----	----		----	----
Right Supraclinoid ICA	1.25	0.21	-0.184	0.98	0.19	-0.116	-0.21	-0.07
Left Supraclinoid ICA	0.86	0.14		0.78	0.15		-0.10	0.07
Right Vertebral	0.40	0.07	0.057	0.25	0.05	0.127	-0.37	-0.26
Left Vertebral	0.45	0.07		0.32	0.06		-0.28	-0.15
Basilar	0.51	0.09		0.29	0.06		-0.43	-0.33
Right PCA	0.59	0.10	-0.890	0.34	0.07	-0.589	-0.43	-0.33
Left PCA	0.03	0.01		0.09	0.02		1.53	1.98
Right MCA M1	0.80	0.13	-0.153	0.47	0.09	0.116	-0.42	-0.32
Left MCA M1	0.59	0.10		0.59	0.12		0.00	0.18
Right MCA Superior M2	0.16	0.03	0.111	0.13	0.03	0.261	-0.18	-0.03
Left MCA Superior M2	0.20	0.03		0.23	0.04		0.12	0.32
Right MCA Inferior M2	0.34	0.06	-0.185	0.25	0.05	-0.158	-0.25	-0.11
Left MCA Inferior M2	0.23	0.04		0.18	0.04		-0.20	-0.06
ACA	0.09	0.02		0.11	0.02		0.21	0.42
Acom**	-0.13	-0.02		0.07	0.01		-1.52	-1.61

* - Indicates the erroneous measurements caused by artifact from the stent.

** - Negative sign indicates a flow reversal in the Acom, a change in the overall direction of the flow volume through the cut plane surface.

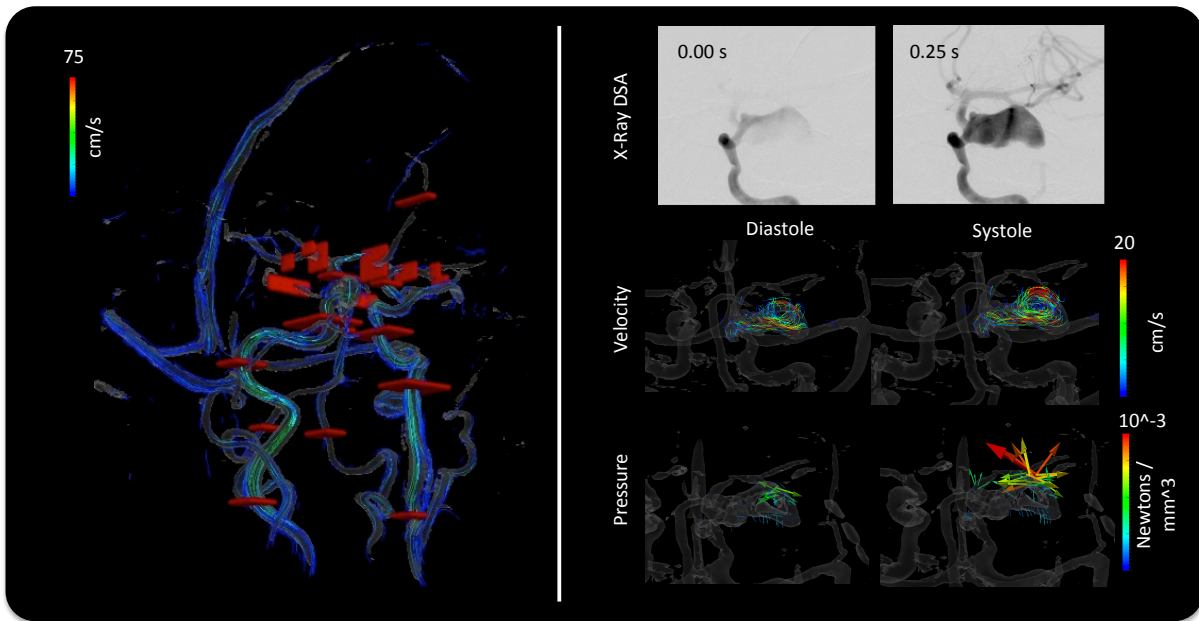


Figure 5.2: Cut planes used for flow volume calculations and temporal series of contrast inflow, and 4D flow velocity and derived fluid force. Top) The cut planes (red surfaces) are shown in red over a rendering of the vascular structure and streamlines. Bottom) The upper row shows the contrast agent filling the fundus at 4 Hz; the middle row shows 4D time frames of the flow velocity; and the lower row shows the fluid force calculated from the Navier-Stokes equation at each pixel. Flow is observed to be higher towards the outer edge the aneurysm, while forces are higher in the middle and towards the end where the flow diverts backwards.

5.4 Results

The non-contrast pre-operative CT images (Figure 5.1) showed the maximal diameter of the untreated aneurysm was 23 mm. The CTA showed filling of only the superior half of the fundus suggesting that the inferior portion of the aneurysm was filled with thrombus. The region that was filled with flowing arterial blood measured 23 mm by 14 mm. TOF images clearly depicted the entire aneurysm, including the thrombus region (due to a shorter T_1 relaxation time). The PC images highlighted only the region of flowing blood.

A temporal series of DSA images (Figure 5.2) demonstrated that the flow velocity was faster towards the periphery of the aneurysm and slower in the center. The high-resolution PC MR-derived velocity measurements confirmed this finding. Velocities toward the periphery of the aneurysm were on the order of 5 cm/s; whereas, samples in the center of the fundus were around 1.5 cm/s (Figure 5.2). Figure 5.2 also shows the force vectors generated by the blood. These vectors are analogous to the pressure, though they show the direction of the force. A higher pressure was observed in the aneurysm where the flow jet reverted or where the velocity was slow.

Post-operative imaging (Figure 5.3) confirmed patency of the stent and near complete sealing of the aneurysm. Non-contrast enhanced TOF angiography suggested no change in the size of the aneurysm, the region in the aneurysm previously filling with blood was hypo-intense due to slower blood flow or partially coagulated blood. The contrast-enhanced TOF scan, like the DSA images, showed a small amount of contrast passing through the pipeline stent into the aneurysm. PC images showed that velocity in the treated aneurysm was <0.5 cm/s. Blood velocity was observed to be higher in the arteries distal to the aneurysm, more closely matching velocity measurements from the contralateral side. As expected, MR image artifact (due to signal loss) was observed towards the outer edge of the vessel (*i.e.*, near the stent), however the velocity at the center of the lumen and within the stent matched the proximal and distal velocity measurements. The additional clinical MR images (FLAIR, DWI/ADC and SWAN) did not show any changes in the brain.

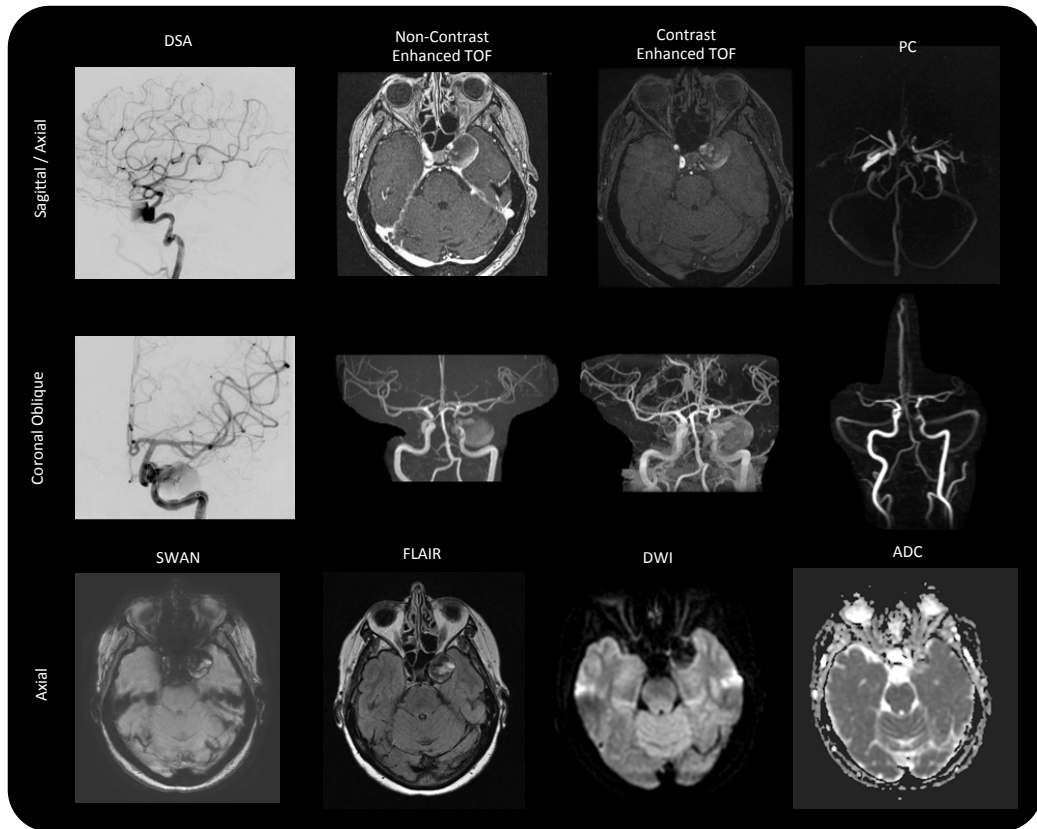


Figure 5.3: Post-operative imaging. The bi-planar x-ray digital subtraction (DSA) acquisition shows minor filling of the fundus as the contrast agent passes. This was supported by the MR imaging with non-contrast enhanced and contrast-enhanced time-of-flight (TOF) and phase contrast (PC) imaging. The aneurysm still appears large on TOF due to the short T_1 of the thrombus. The phase contrast images show near zero velocity in the aneurysm. Susceptibility-weighted angiography (SWAN), T_2 -weighted fluid attenuated inversion recovery (FLAIR) imaging, diffusion weighted imaging (DWI), and a calculated apparent diffusion coefficient (ADC) map transecting the aneurysm are also shown.

PC VFR measurements were made in locations identified by the cut planes in Figure 5.2. These planes were located on the major intra- and extra-cranial arteries in order to allow a global assessment of blood flow (Table 5.1) The total blood flow entering the brain *via* the internal carotid and vertebral arteries was 6.8 ml/s and 5.1 ml/s pre- and post-operatively, respectively. The carotid arteries and vertebral arteries also showed a reduction in VFR contributing to the total reduced flow into the brain. Flow in

Table 5.2: Comparison of measured and calculated intravascular pressures. Catheter transducer pressure measurements could not be obtained post-operatively distal to the deployed stent (i.e., supraclinoid ICA or MCA M1 segments). MR-derived pressure measurements could not be accurately measured inside the stent (near the supraclinoid ICA) due to image artifact. The average percent difference measurements was -3.1%. Data is reported as systolic/diastolic pressure pairs.

Pre-operative		pressure measured		Percent Difference
		with Catheter Transducer	with PC-MRI	
Cavernous ICA	systolic	99 mm Hg	99.6 mm Hg	0.1%
	diastolic	62 mm Hg	71.5 mm Hg	9.5%
Supraclinoid ICA	systolic	85 mm Hg	83.1 mm Hg	2.2%
	diastolic	55 mm Hg	52.2 mm Hg	5.1%
MCA-M1	systolic	76 mm Hg	72.1 mm Hg	5.1%
	diastolic	52 mm Hg	47.1 mm Hg	9.4%
Post-operative				
Cavernous ICA	systolic	89 mm Hg	84.2 mm Hg	5.4%
	diastolic	49 mm Hg	51.7 mm Hg	5.5%
Supraclinoid ICA	systolic	----	----	----
	diastolic	----	----	----
MCA-M1	systolic	----	82.1 mm Hg	----
	diastolic	----	54.6 mm Hg	----

the left ICA (where the stent was placed) increased as a percentage of total intracranial flow from 35% to 40% before and after the surgery.

Globally, a major shift in the blood flow symmetry pre- and post-operatively was observed, as can be seen by the changes to the laterality index in all paired vessels, except the MCA-superior M2 segments, cavernous ICA, and the vertebral arteries. VFR measured in ICA vessels measured distal to the bifurcation showed more symmetric flow distribution after the intervention, changing from a VFR laterality index of -0.190 to -0.095. Post-operatively, the right MCA branches all showed reductions in VFR of the same order as observed in the other right hemispheric vessels. The left MCA-M1 branches showed an increase in VFR of 72% after stent deployment. The absolute VFR through the ACom pre- and post-operatively changed from 0.13 ml/s to -0.07 ml/s (the change in sign representing a change in flow volume direction). The flow through the ACA arteries increased from 0.09 ml/s to 0.11 ml/s, due to flow being diverted past the aneurysm because of the stent. Venous flow through the sinuses also showed a large post-operative change in the left-right VFR laterality index, similar to that observed in most intracranial arteries.

The pressure in the cavernous left ICA measured with both the pressure transducer and the MR PC calculations decreased post-operatively (Table 5.2). Conversely, pressure in the MCA M1 was observed to increase after the stent was deployed, concurrent with the increased blood flow observed in that vessel (Table 5.1). A similar observation has been seen in pressure and VFR after aortic stenting (369). Overall, the PC-derived pressure measurements agreed with the catheter transducer measurements. The PC-derived pressure estimates at systole and diastole were within $\pm 10\%$ of the catheter transducer values.

5.5 Conclusions

PC-MR imaging can visualize and assess hemodynamic alterations after deployment of a pipeline stent. PC images were used to estimate velocity, VFR and pressure both before and after the intervention. In this patient, the pipeline stent achieved its intended therapeutic effect of greatly decreasing flow into the aneurysm. The treatment also increased flow distal to the aneurysm and caused a flow reversal in the ACom arterial segment. Flow in the hemisphere contralateral to the aneurysm was reduced, resulting in the VFR in major arteries across the brain being more symmetric. Flow in vessels distal to the aneurysm increased. PC data were also used to derive intravascular pressure, which was compared against catheter transducer measurements (difference of $<10\%$).

Higher signal-to-noise TOF and PC images could be achieved imaging after contrast agent injection (176). Non-contrast agent enhanced images, however, were preferred for this study as the patient was already receiving several contrast agent enhanced scans with the clinical CTA, DSA, and MR imaging. MR image quality without contrast agent was sufficient for the analyses described here. The artifact from the stent was limited to less than 2 mm and consistent with previous studies, did not prevent estimation of flow in the middle of the feeding artery (370). Deviation in the pressure estimates could arise from a host of factors, including: 1) the patient being under anesthesia, 2) the time of day and activity level, and 3) having catheters in the vessels being measured. Other reports have focused on observing the pressure gradient along a stenosis vessel in an animal model (204), providing quantitative measurements of flow is

preferred. This chapter demonstrates the ability to obtain pressure estimates with non-invasive PC MR in a clinical setting consistent with catheter transducer measurements.

The objective of presenting this case was to thoroughly analyze the hemodynamic changes caused by the treatment. This was done through a battery of imaging techniques each providing somewhat unique information; while post processing on PC MR images yielded conclusion to the hypothesis that the flow would become more symmetric. Catheter transducer measurements and pressure derived from PC MR also showed an increase distal to the aneurysm.

5.6 Chapter Summary

In this chapter the case of a giant cerebral aneurysm is examined performing flow measurements with multiple modalities. This case represented the most data collected on any one subject during the course of my degree, and is representative of a good outcome. The thoroughness of this particular evaluation and the evidence shown to support the hypothesis is why this case warranted its own chapter. Focus has particularly been on the use of phase contrast and VFR, which are key parameters for the following chapters. In the next chapter I use cohort measurements to establish what ‘normal’ flow through the brain should be.

Chapter Six:

**Phase Contrast MR Imaging Measurements
of Blood Flow in Healthy Human
Cerebral Vessel Segments**

6.1 Chapter Overview

Phase contrast (PC) magnetic resonance imaging was used to obtain velocity measurements in thirty healthy subjects to provide an assessment of hemodynamic parameters in cerebral vessels. It is expected that a lower coefficient-of-variation (COV) of the volume flow rate (VFR) compared to peak velocity (v_{peak}) measurements and the COV to increase in smaller calibre arteries compared to large arteries. PC velocity maps were processed to calculate v_{peak} and VFR in twenty-six vessel segments. The mean, standard deviation and COV of v_{peak} and VFR in each segment were calculated. A bootstrap-style analysis was used to determine the minimum number of subjects required to accurately represent the population. Significance of v_{peak} and VFR asymmetry was assessed in ten vessel pairs. The bootstrap analysis suggested that averaging more than 20 subjects would give consistent results. When averaged over the subjects, v_{peak} , VFR ranged from 5.2 ± 7.1 cm/s, 0.41 ± 0.58 ml/s (in the anterior communicating artery; mean \pm standard deviation) to 73 ± 23 cm/s, 7.6 ± 1.7 ml/s (in the left internal carotid artery). A tendency for VFR to be higher in the left hemisphere was observed in 88.8% of artery pairs, while the VFR in the right transverse sinus was larger. The VFR COV was larger than v_{peak} COV in 57.7% of segments, while smaller vessels had higher COV. VFR COV was not generally higher than v_{peak} COV. COV was higher in smaller vessels as expected. These summarized values provide a base against which v_{peak} and VFR in various disease states can be compared.

6.2 Introduction

Cardiovascular disease is the number one cause of mortality in the world (1). Cerebrovascular diseases, such as stroke and arteriovenous malformation (AVM), represent an important neurological subset of cardiovascular diseases that contribute to mortality and morbidity. Cerebral blood flow has been studied thoroughly with several technologies in animals, healthy humans and patients (226,371-373). A better understanding of healthy human blood flow is critical to advancing the knowledge of cerebrovascular disease, as these conditions commonly result in deviation from normal flow patterns. Blood flow is also known to be highly variable even in a healthy individual

(104,374-378). This study summarizes quantitative, time-averaged blood flow measurements obtained by magnetic resonance (MR) imaging from a healthy, adult human cohort and extends the flow assessment to a broader range of vessels than previous studies.

Blood flow measurements of normal subjects can be highly variable, even within the same subject (104,374-378). This underlying variability of normal flow limits the more widespread clinical application of cerebral velocity mapping techniques. In addition, stimulants including exercise and caffeine may increase blood flow to the brain by 20% to 30% (376,378). Clinically employed brain velocity mapping techniques, such as trans-cranial Doppler (TCD) ultrasound and phase contrast (PC) MR imaging, provide quantitative measurements of flow velocity. Blood velocity varies across both the vessel lumen and the cardiac cycle. The challenges of measuring a temporally and spatially varying velocity distribution (*i.e.*, over the cardiac cycle and across a vessel lumen) have resulted in researchers often just reporting the spatial peak velocity (v_{peak}) (375). Another, related and robust measurement of blood flow is the volume flow rate (VFR) (379,380), which is simply the volume of blood passing through a vessel segment in a given period of time. VFR measurements remove vessel area confounds when comparing blood supply between patients and, therefore, may provide a more robust indication of vascular function. Notably, previous studies have demonstrated that partial volume effects can impact the accuracy of the VFR measurement (205).

The calculation of VFR is difficult with ultrasound as accurate measurements of the spatially averaged velocity and vessel diameter can be hard to obtain; however, with PC-MR imaging both flow velocity and vessel diameter can be estimated accurately. Computed tomography and x-ray digital subtraction angiography, two common neuroimaging techniques, do not provide quantitative measurements of blood velocity. Imaging with PC MR has allowed for peak and spatially averaged velocity measurements, and previously has been used for the measurement of VFR in the carotid and middle cerebral artery (MCA) vessels (381-384). To date, there has been only limited MR assessment of other cerebral vessels (381,385).

Measurements of vessel diameter have been reported in the literature. The common carotid artery was found to have a mean and standard error diameters of 7.5 ± 0.04 mm (386). Another study found the internal carotid artery (ICA) diameter mean and standard deviation to be 4.66 ± 0.78 mm. Intracranial vessels including the MCA, anterior cerebral artery (ACA), basilar artery, and posterior communicating artery (PCA), have diameter mean and standard errors of 2.7 ± 0.05 mm, 2.1 ± 0.06 mm, 2.9 ± 0.09 mm and 2.1 ± 0.06 mm, respectively (387). The superior sagittal sinus diameter ranges between 3.0 mm and 7.9 mm in another study (388). The transverse sinuses are known to have different mean diameters between the left and right sides of 6.5 mm and 8.0 mm respectively (389). Like flow, these measurements of vessel diameter are highly variable between subject and change over the cardiac cycle.

PC-MR imaging can be performed in three dimensions (3D) or with time-resolved (4D) flow imaging. 4D flow imaging requires a substantially longer acquisition time to match the same spatial resolution and field-of-view (FOV) a typical 3D PC acquisition. 4D flow imaging also requires the use of cardiac gating, which can further increase the total scan time. It has also been shown that 3D measurements match the time-averaged 4D flow measurements (381). As the objective in this work is to establish measurements in smaller vessels that could be found using relatively short, clinically tractable MR methods, high-resolution 3D PC imaging was preferred. These methods provide time-averaged results with millimeter to sub-millimeter resolution, allowing for visualization over the entire brain of smaller structures, such as the MCA-M2 segment, in a clinically tractable acquisition time, *i.e.*, about ten minutes.

The purposes of this work are: 1) to establish the mean and variation of v_{peak} and VFR for major cerebral vessels (defined as having diameters >1 mm), and 2) to study left-right flow asymmetry. Thirty healthy individuals were imaged with a PC sequence and v_{peak} and VFR were calculated in twenty-six *a priori* identified cerebral arterial and venous segments. Because of implicit averaging across the vessel lumen, a lower coefficient-of-variation (COV) in the VFR measurements compared to v_{peak} is expected. It is also expected that the COV will increase in smaller caliber arteries.

6.3 Methods

6.3.1 Subjects

MR imaging was undertaken using a procedure approved by our institutional research ethics board. Thirty subjects provided written informed consent and were prospectively imaged. The cohort consisted of 17 males and 13 females, aged between 18 and 64 years of age, with at least two subjects in each decade. The majority of subjects (18/30) were between 20 and 40 years of age. All the subjects were recruited from the local community and had no known cardiovascular disease. The acquired MR angiographic images were reviewed to confirm that there was no incidental cerebrovascular disease or malformation that might impact blood flow.

6.3.2 MR Acquisition

Imaging was performed on a 3 T MR scanner (Discovery 750, General Electric Healthcare, Waukesha, WI) using a PC sequence. Velocity encoding was performed in the three orthogonal directions. A velocity encoding (v_{enc}) of 150 cm/s was used. A FOV of 22.0 cm \times 16.5 cm \times 19.2 cm was used to cover the head and upper neck with an acquisition matrix size of 256 \times 192 \times 192. Other acquisition parameters included TR/TE/ α of 8.3 ms/3.8 ms/10°. Image volumes of the velocity were encoded in each of the three orthogonal directions and velocity images were reconstructed with the vendor-supplied algorithms. Accelerated imaging techniques were not used in order to preserve high signal-to-noise and to minimize artifacts in the images. Corrections for gradient warp and Maxwell field were applied. The total scan time to acquire data using this sequence was 10 min 40 s.

6.3.3 Analysis

Cut planes were placed across twenty-six previously identified vessel segments (comprising vessels with typical diameters of >1 mm). The identified segments included twenty-one arterial locations: at four locations along each of the internal carotid arteries (ICA), the V4 segment of the vertebral arteries and basilar artery, the M1 and inferior and superior M2 segments of each MCA, the anterior communicating artery (ACom), the

anterior cerebral arteries (ACA), and the posterior cerebral arteries (PCA). Venous flow was also measured at five locations: the mid superior sagittal sinus, the posterior sagittal sinus, the vein of Galen, and along both transverse sinuses. Smaller vessels, such as the posterior communicating artery, were not routinely visible with this PC acquisition technique (as their vessel diameters were generally <0.5 mm), and were thus not assessed.

Peak velocity, v_{peak} , was calculated as the maximum flow velocity on the cut plane and within the vessel lumen. The VFR measurements were obtained by summing the velocity component that was perpendicular to the cross sectional area and then multiplying by the lumen cross sectional area (Figure 6.1). A bootstrap-style analysis was then performed to assess how the standard deviation of v_{peak} and VFR measurements changed with the number of subjects. This test was intended to determine the minimum number of subjects that would be sufficient to characterize the population by demonstrating stabilization of the average inter-subject variance. Ten thousand randomly selected permutations of the subject order were used to calculate the standard deviation as a function of the number of subjects. The mean of the standard deviations was calculated and plotted versus the number of subjects.

The mean, standard deviation, and COV in v_{peak} and VFR for each vessel segment were calculated across the thirty subjects. COV was calculated by dividing the standard deviation by the mean to provide a normalized estimate of the variability of the measurement. Flow into and out of the circle of Willis (CoW) was also assessed: the sum of VFR entering through the supraclinoid ICAs and basilar artery were compared to the total VFR leaving through the MCA, ACA and PCA vessels.

Left-right v_{peak} and VFR asymmetry was also assessed between ten paired vessels (at the four ICA segments, the MCA M1 segments, both MCA M2 segments, the vertebral arteries, the PCA segments, and the transverse sinuses). Both mean difference and laterality index were calculated for each measurement type. Laterality index was defined as $(L-R)/(L+R)$ where L and R represent the left and right segment measurements respectively. The number of subjects with higher v_{peak} and VFR in the left vessel were also recorded for each vessel pair. Normality of the data was tested with a Kolmogorov-

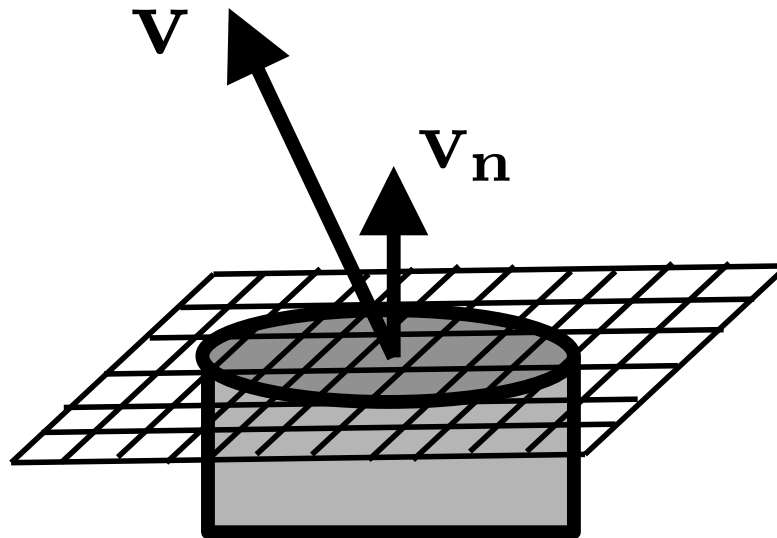


Figure 6.1: Diagram illustrating the peak velocity (v_{peak}) and volume flow rate (VFR) calculations. A cut plane (denoted by the grid) is placed across the vessel (grey). Typically the cut plane is placed nearly orthogonal to the vessel. v_{peak} is found as the max of the absolute velocity on the cross section. VFR can then be found by multiplying the average velocity by the lumen area ($VFR = A_{lumen} v_{avg}$).

Smirnov test. A two-way ANOVA test was performed on the paired v_{peak} and VFR measurements with factors left/right and vessel segment. Separate t-tests were performed on v_{peak} and VFR for each pair of vessels. A $p < 0.05$ was used to determine significance.

6.4 Results

Images of sufficient quality for subsequent analysis were acquired in all thirty subjects. All subjects tolerated the 10 min 40 s PC acquisition. There were no observed incidental findings seen on MR imaging that would warrant removal of a subject from the healthy cohort. Figure 6.2 shows the twenty-six cut planes used to measure v_{peak} and VFR in a representative subject. In this study one subject was observed to have no measurable flow in the right vertebral artery, several other right vertebral arteries and left transverse sinuses had reduced flow compared to the contralateral side. One subject exhibited a trifurcation between the M1 and M2 segments of the MCA, leading to three M2 segments

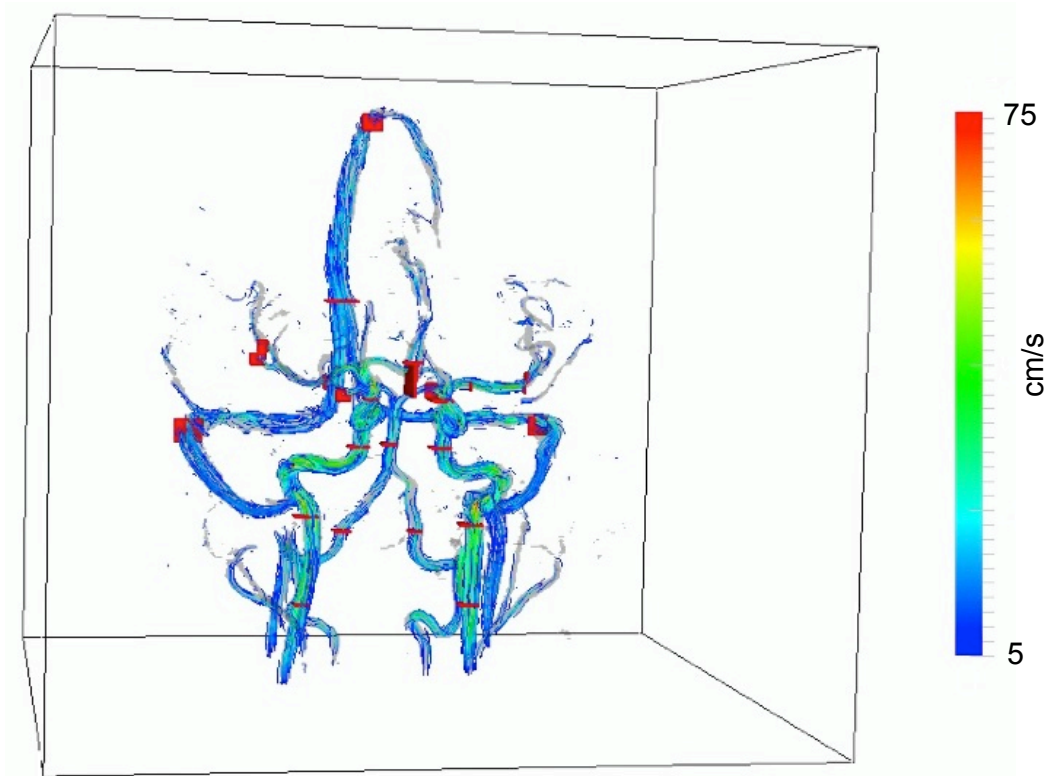


Figure 6.2: Streamline phase contrast (PC) MR angiography image and cut planes derived from one 3D data set. Angiogram is rendered with streamlines color encoded with the blood speed. The red planes are representative of the twenty-six cut planes placed in the rest of the subjects.

on the right side. The MCA-M2 segment measurements reported in this subject were taken on the two largest vessels.

The bootstrap results (Figure 6.3) plot the average standard deviation of v_{peak} and VFR as it evolves to a steady-state value with an increasing number of randomly selected subjects. The average standard deviation measured in each vessel segment converged to within 95% of the cohort overall average standard deviation after inclusion of fifteen to twenty subjects, confirming that sufficient subjects were enrolled.

Summaries of v_{peak} and VFR for the population are provided in Figure 6.4. Individual measurements can be found in the supplemental material. More distal arteries had decreased v_{peak} and VFR. The average v_{peak} and VFR in the right and left carotid

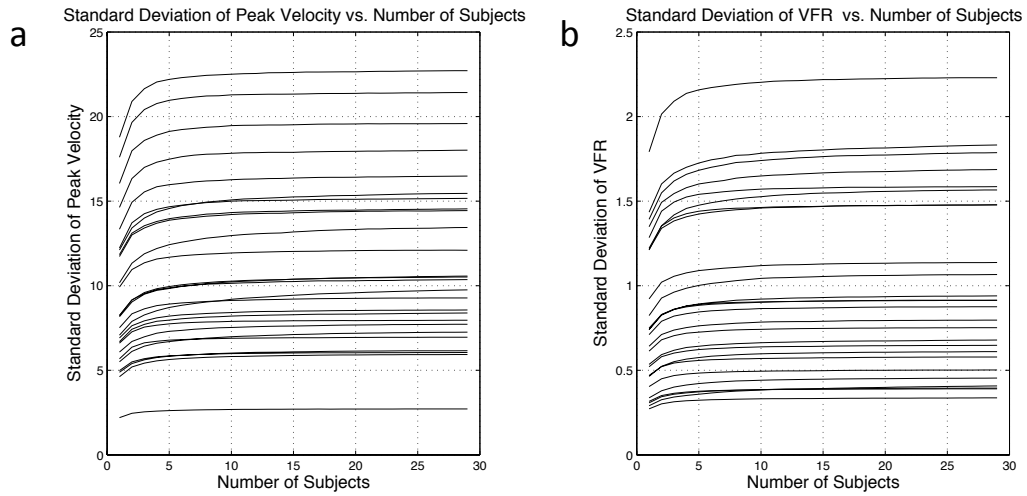


Figure 6.3: Study of the standard deviation change with subjects. For (a) peak velocity (v_{peak}) and (b) volume flow rate (VFR). Each line corresponds to a vessel segment. Data were calculated for each vessel segment (individual lines) by processing ten thousand random permutations of the order of the 30 subjects. The average standard deviation with respect to the number of subjects was plotted and demonstrated that, in each vessel, the average standard deviation converges after inclusion of fifteen to twenty subjects.

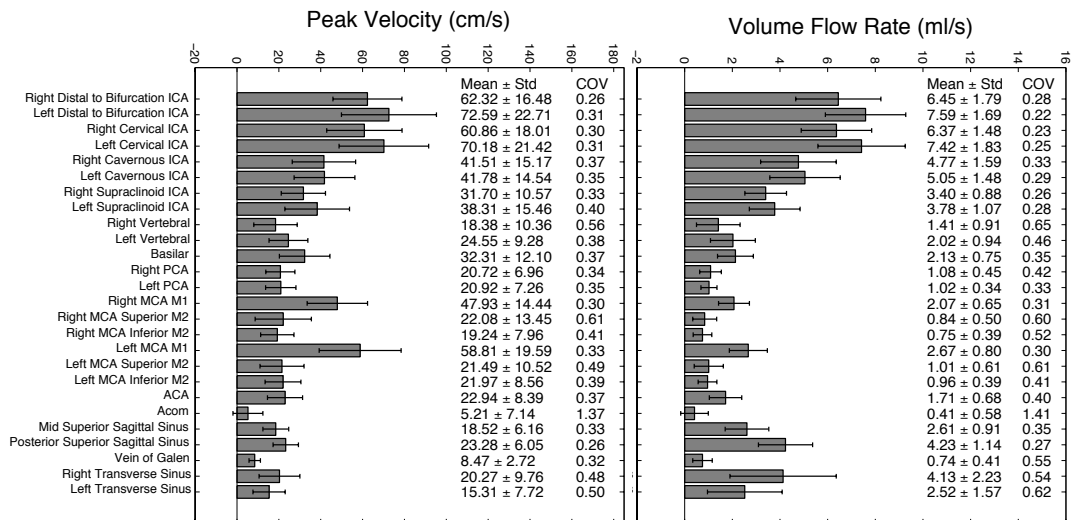


Figure 6.4: Peak velocity (v_{peak}) and volume flow rate (VFR) measured in each vessel segment. Mean and standard deviation, along with coefficient of variation (COV) are reported.

Table 6.1: Left-right asymmetry results. For peak velocity (v_{peak}), and volume flow rate (VFR). L = flow in left vessel segment, R = flow in right vessel segment. * = indicates a significant test result.

Peak Velocity	Difference in Mean (L-R), cm/s	Laterality Index (L-R)/(L+R)	Left > Right (out of 30 cases)	t-Test Outcome (p value)
Distal to Bifurcation ICA	20.5	0.08	24	0.0498 *
Cervical ICA	18.6	0.07	25	0.0733
Cavernous ICA	0.5	0.00	18	0.9441
Supraclinoid ICA	13.2	0.09	20	0.0580
Vertebral	14.2	0.16	20	0.0062 *
PCA	0.4	0.00	14	0.9134
MCA M1	21.8	0.10	25	0.0173 *
MCA Superior M2	-1.2	-0.01	14	0.8493
MCA Inferior M2	5.5	0.07	17	0.2065
Transverse Sinus	-9.9	-0.14	10	0.033 *

Volume Flow Rate	Difference in Mean (L-R), ml/s	Laterality Index (L-R)/(L+R)	Left > Right (out of 30 cases)	t-Test Outcome (p value)
Distal to Bifurcation ICA	2.28	0.08	22	0.0136 *
Cervical ICA	2.11	0.08	21	0.0171 *
Cavernous ICA	0.66	0.03	15	0.4870
Supraclinoid ICA	0.61	0.04	19	0.2391
Vertebral	1.41	0.20	21	0.0038 *
PCA	-0.13	-0.03	11	0.5331
MCA M1	1.21	0.13	27	0.0021 *
MCA Superior M2	0.34	0.09	18	0.2430
MCA Inferior M2	0.89	0.30	22	0.0028 *
Transverse Sinus	-3.21	-0.24	11	0.0020 *

arteries immediately distal to the bifurcation were: 62.3 ± 16.5 cm/s, 72.6 ± 22.7 cm/s, and 6.5 ± 1.8 ml/s, 7.6 ± 1.7 ml/s, respectively. These VFR estimates matched existing published findings (203,380,382,390). Mean v_{peak} in the right and left vertebral segments (measured along the V4 segment) were 18.4 ± 10.4 cm/s and 24 ± 9.3 cm/s, respectively, while the VFRs were 1.4 ± 0.91 ml/s and 2.0 ± 0.94 ml/s, respectively. The v_{peak} and VFR in the basilar artery were 32.3 ± 12.1 cm/s and 2.13 ± 0.75 cm/s. Of the intra-cranial vessels, the MCA-M1 segments had the highest v_{peak} and VFR. The ACom was unique in that the direction of flow changed between subjects. The ACom v_{peak} and VFR were found to be 5.2 ± 7.1 cm/s and 0.41 ± 0.58 cm/s, respectively. The v_{peak} and VFR in the posterior superior sagittal sinus was 23 ± 6.1 cm/s and 4.2 ± 1.1 ml/s. At the CoW, the total flow volume entering through the supraclinoid ICAs and basilar artery was 9.3 ± 1.9 ml/s. The total flow leaving the CoW through the MCA-M1, ACA, and PCA segments, was 8.6 ± 2.0 ml/s. The observed VFR discrepancy at the CoW was 0.7 ml/s (7.5%).

The v_{peak} COV ranged from 0.26 to 0.40 in the larger arteries (ICAs) and was higher in the smaller arteries (range 0.30 to 1.37). This range of COV was reduced to 0.30 to 0.61 if the ACom results were excluded. The v_{peak} COV of the veins ranged between 0.26 and 0.50. The VFR COV varied from 0.22 to 0.33 in the larger arteries and from 0.31 to 1.46 in the smaller vessels (0.30 to 0.60, if the ACom artery data was excluded). ACom v_{peak} and VFR had high COV due to the inter-subject left-right flow direction variability through the artery. The VFR COV in the veins ranged from 0.27 to 0.62. The VFR COV was larger than v_{peak} COV in fifteen (57.7%) of the twenty-six segments. In the larger arteries, only one (12.5%) of eight segments had VFR COV larger than v_{peak} COV. Venous v_{peak} and VFR COV were comparable to that observed in the arterial system, with the already noted exception of the ACom artery.

All vessels segments were normally distributed as indicated by the Kolmogorov-Smirnov tests. The two-way ANOVA tests were significant with respect to vessel segment for both metrics, as we would expect. The two-way ANOVA tests were not significantly different overall between the left and right sides ($p = 0.19$ for v_{peak} and $p = 0.22$ for VFR).

The left-right flow asymmetry assessment (Table 6.1) showed a tendency for higher flow in the arteries of the left hemisphere, and a tendency for higher flow in the right transverse sinus. ANOVA tests demonstrated significant asymmetries in the VFR measurements, including the MCA-M1 segment; the lower segments of the ICA, the vertebral arteries, the inferior MCA-M2 segments, and the transverse sinus. More arteries tested significant for higher left hemisphere VFR (5/9, 55.5%) than v_{peak} (4/9, 44.4%). In vessel pairs with significant VFR asymmetry, there tended to be asymmetric flow in more than two thirds of the subjects. For example, with the MCA-M1 segment: 25 (83.3%) of 30 had higher left-sided v_{peak} and 27 (90.0%) of 30 had higher left-sided VFR. Asymmetry favored flow through the left vertebral arteries and five (16.7%) of thirty subjects showed almost no flow on the right side (<0.5 ml/s).

The VFR in the veins increased as the sagittal sinus measurements became more distal, from 2.6 ± 0.91 ml/s to 4.2 ± 1.4 ml/s. The total flow through the vein of Galen and posterior sagittal sinus (5.0 ± 1.6 ml/s) was less than the total flow through the

transverse sinuses (6.7 ± 3.8 ml/s), likely due to other small and unaccounted feeding veins. Flow through the right and left transverse sinus had mean peak flow of 15 ± 7.7 cm/s to 20 ± 9.8 cm/s favoring the right hemisphere, while the VFR measured was 2.5 ± 1.6 ml/s and 4.1 ± 2.2 ml/s.

6.5 Discussion

This work was undertaken to better understand blood flow through the normal healthy human brain. Blood flow (v_{peak} and VFR) through the major cerebral vessel segments was quantified and, where possible, compared bilaterally. The COV of the VFR measurements were not lower than the COV of the v_{peak} measurements; contrary to expectations. VFR through the carotid arteries have been well documented (203,380,382,390) and range from 4.0 ml/s to 7.0 ml/s and match those reported here (7.0 ml/s \pm 1.7 ml/s, ICA just distal to the carotid bifurcation). Flow volume through the MCA-M1 (2.4 ml/s \pm 0.72 ml/s) also compare favorably to other findings (1.8 ± 0.2 ml/s) (382). Having the ICA and MCA-M1 VFR measurements agree with these published values provides confidence in the accuracy of the other measurements.

Flow asymmetry was found in the arterial system (with higher flow typically observed on the left side), and the venous system (with higher flow on the right side). The occurrence of asymmetry of the MCA-M1 was greatest, where 90.0% of subjects had higher VFR on the left side. Variability of the flow (as measured by COV) tended to increase in arteries as their cross sectional area reduced (*i.e.*, there was less variability in the flow in the carotid segments than the smaller cerebral arteries). Comparable variability was observed in the venous segments.

Partial volume effects on velocity estimates near the vessel wall present a concern, particularly in the smaller vessels (205). Previous work suggests that the VFR for some of the smaller vessels such as the MCA-M2 and PCA may be overestimated by as much as 30% (205). Small vessels may appear larger due to partial voluming effects near the vessel wall. This could be one factor contributing to the higher COV observed in the smaller and more distal vessels. Higher resolution PC imaging would help mitigate this concern, though at the cost of potentially a longer acquisition and lower acquisition

signal-to-noise ratio. Partial volume effects remain a concern for VFR analysis, but the similar trend in the COV for the v_{peak} measurements mitigates some of the worry. Normally, there are two anterior cerebral arteries, however, a combined measurement was used due to their proximity. ACom artery measurement was difficult. Measurements of flow through the ACom artery were achieved by placing the cut plane between the ACA vessels, where they appeared to join.

To speculate on the source of the asymmetry, we may do a thought experiment examining the vascular configuration proximal to the brain. From the heart stems the aortic arch, and three vessels branch from that: the brachiocephalic trunk, the left common carotid artery and the left subclavian artery. The brachiocephalic trunk branches into the right carotid and right subclavian vessels. From the left and right subclavian arteries branch the left and right vertebral arteries respectively. So we observe clearly that the left sided vessels have fewer branches proximally, which could lead to the asymmetry in flow.

Although there are only thirty subjects in this study, the bootstrapping experiment confirmed that adding subjects would not significantly change the reported values. Additional studies can therefore be powered from these data; for example, if one wished to detect a flow difference of 1.0 ml/s with a one-tail test in the right ICA (distal to the bifurcation, 7.59 ± 1.69 ml/s, see Figure 6.4) at a statistical power of 80% one would need to enroll 18 subjects. There are a host of confounds that could change the velocity measurements. Some relate to the subject (*e.g.*, mass of the subject may be positively correlated with the blood flow volume). Other factors include: age, diet, handedness, and athletic ability. An attempt to account for this variability was done by sampling of a representative healthy population.

4D flow imaging would allow for the resolution of the peak flow and VFR throughout the cardiac cycle. This would substantially limit the resolution and spatial coverage, or significantly increase the scan time. Potentially placing several 2D time resolved imaging planes where all the cut planes are located might be an option. We show time averaged peak velocity, though the true peak velocity would happen at systole and be larger than the numbers reported here.

Although VFR measurements have been demonstrated in individual vessels (principally the ICA or MCA-M1 segment), this study is novel because of the extent of the reported measurements. Measurements of v_{peak} and VFR in twenty-six major vessel segments in the brain provided an overall picture of blood flow through the healthy brain. Future studies that could improve these findings by using techniques with higher spatial resolution to establish VFR more accurately and in smaller vessel segments. Furthermore, using 4D flow imaging would allow for the study of pulsatile flow effects. Both of these suggestions, however, would either limit the coverage to a portion of the brain, or substantially increase the image acquisition time. Image acceleration (114,350) and advanced readout trajectories (391,392) might allow for faster acquisitions, higher resolution and/or improved SNR efficiency (*i.e.*, SNR per unit acquisition time). Reducing the FOV would also allow for higher resolution, but would not allow observation of all major vessels and reduce overall SNR. Minimization of total acquisition time is important. In this study few motion artifacts were observed over a 10 minute 40 sec scan, and in only one (3.3%) subject was the sequence repeated because of artifact due to subject motion.

This work can be used to compare patients with cerebrovascular disease, such as cerebral aneurysm and AVM, that potentially change flow patterns in the brain. Blood flow measures (both v_{peak} and VFR) are rarely used in the clinic, however, the hope that by establishing mean flow rates and their variability in healthy subjects using a clinically applicable approach (3D PC MR imaging), is to provide normative data to compare against diseased flow patterns.

6.6 Chapter Summary

This chapter yielded VFR measurements averaged over a sufficiently sized healthy cohort. Average and standard deviation VFR measurements for the broader population can be inferred. These measurements allowed for the assessment of asymmetry between the left and right sides, which will be explored further in Chapter Eight, where the question is posed, “Is it okay to compare blood flow on contralateral sides of the brain?”

In the following chapter these population average measurements are built upon to assess the degree to which flow is abnormal in patients with vascular malformations.

Chapter Seven:

**Flow and Pressure Measurements
in Aneurysms and Arteriovenous Malformations
with Phase Contrast MR Imaging**

7.1 Chapter Overview

Phase contrast (PC) magnetic resonance imaging is explored further in this chapter with the examination of cerebral aneurysms and arteriovenous malformations (AVM). PC imaging obtains a vector field of the blood velocity and with appropriate post-processing can yield additional information about hemodynamics including volume flow rate (VFR) and intravascular pressure. Compared to healthy subjects, lower VFR distal to aneurysms and higher VFR in feeding and draining vessels of the AVM is expected. Five cerebral aneurysm and three AVM patients were imaged with PC techniques and compared to VFR from a previously published cohort of thirty healthy subjects. Computed tomography (CT) angiography, x-ray digital subtraction angiography (DSA), and clinical MR angiography (MRA) data were also compared to the PC results. VFR was calculated in *a priori* chosen vessel segments in each patient and compared statistically to the healthy cohort by computing the z -score. In the aneurysm patients velocity was also measured in the neck, center, and towards the edge of the fundus. Intravascular pressure at these points in the aneurysms and in the nidus of each AVM was calculated from the PC data. Patients with aneurysm had $z < -0.48$ in all vessels distal to the aneurysm (reduced flow), while AVM patients had $z > 6$ in some vessels supplying and draining the nidus (increased flow). Pressure measured in the aneurysms was higher towards the wall than in the center of the aneurysm. In the nidus of the AVM patients, pressure measurements showed a trend toward higher pressure in larger AVMs. The study findings confirm the expectation of lower distal flow in aneurysm and higher arterial and venous flow in AVM patients.

7.2 Introduction

Many methods have been proposed for imaging abnormal cerebral vasculature, but few show the promise of phase contrast (PC) magnetic resonance (MR) imaging. Vascular malformations, such as cerebral aneurysm and arteriovenous malformation (AVM), have significant variation between patients and are challenging to understand from both a hemodynamic and prognostic point-of-view. PC techniques provide not only structural images of the vascular anatomy, but also direct measurement of the blood velocity. In

many cerebral vascular malformations PC imaging can be used to obtain critical information about the hemodynamic function within the brain (204,211,226,363,367,391). PC imaging can also be used to estimate pressure induced by flowing blood on the vessel wall (204,214,215,217,393). Obtaining local pressure estimates is, otherwise, an invasive process whereby endovascular catheters are typically used to obtain spot measurements. This invasive approach is undesirable due to procedural risk and because the catheters can modify the blood flow patterns around them (394,395). PC imaging can obtain pressure estimates in a minimally invasive fashion, including locations where measurements from more invasive approaches are not easily achieved (Chapter Five).

Structural images of the blood can be acquired with PC imaging, as well as several other imaging modalities, including: computed tomography angiography (CTA), x-ray digital subtraction angiography (DSA), time-of-flight (TOF) MR angiography (MRA), and contrast-enhanced (CE) MRA. Each method is commonly used clinically and provides complementary information about the cerebral vasculature. CTA, for example, quickly provides high-resolution angiographic images. There are rarely contraindications to performing a CT examination, with limitations being those associated with reactions to the x-ray contrast agent (396,397). X-ray DSA provides projection images with high temporal resolution of x-ray contrast agent passing through the brain. Modern DSA systems allow acquisitions of bi-planar projections. X-ray DSA imaging, however, is more invasive as it requires intra-arterial administration of the x-ray contrast agent. TOF imaging can provide high-resolution, 3D structural images of the arterial system in relatively short acquisition time, but like CTA and DSA, MRA does not directly yield functional information about blood velocity. Using MR contrast agents to shorten the T_1 relaxation time in the blood allows contrast-enhanced MRA to provide both structural and/or time resolved images (133). In clinical practice, multiple modalities are often used to obtain corroborating information (398-400).

The aim is to investigate PC imaging because of the information it provides about blood velocity. In addition to velocity, a number of hemodynamic metrics can be derived from PC data including volume flow rate (VFR) (205,379) and intravascular pressure

(204,214,215,217,393). As arterial blood flow is generally pulsatile and laminar, measurements of flow velocity in a blood vessel depends greatly on when (in the cardiac cycle) and where (in the vessel) the measurement is acquired. VFR is a key metric, where the volume of blood flow per unit time through a vessel is calculated. VFR is a desirable and important hemodynamic measurement that provides a functional measurement related to physiology. Intravascular pressure is another metric that can be derived from computational fluid dynamic (CFD)-based modeling of the acquired velocity field (215,217,362,368,393). Although intravascular pressure can be estimated from other modalities, such as CTA and x-ray DSA (53,368), the blood velocity in the vessels must be assumed when using these modalities. PC imaging can measure the flow velocity field directly and is thus preferable for CFD-derived estimation of pressure.

This report explores the role and highlights the advantages of using PC imaging for improving cerebral aneurysm and AVM hemodynamic characterization. A cerebral aneurysm is a bulb-like formation that protrudes outward from the normal vessel wall. The protrusion can impact other brain structures (*i.e.*, due to mass effect) and aneurysm carries the risk of rupture and, thus, increased risk of intra-cerebral hemorrhage (ICH). It is thought that the aneurysm etiology is a result of a pre-existing weakened vessel wall (401,402) or abnormally high-pressure flow impinging on the vessel wall (401-403). Typical treatments for cerebral aneurysm attempt to prevent flow from entering the fundus and include clipping or coiling/stenting (364). AVMs occur when arterial blood flow bypasses the capillary beds and instead flows directly to the veins through a shunt or nidus (a nest-like configuration of arteries and veins). AVM has a high risk of leakage, leading to ICH (69). Treatments include surgery to remove the AVM, endovascular therapy where material is injected to embolize the nidus vessels, or radiation therapy of the nidus to cause vascular necrosis (72).

The overall goal of this work is to investigate how PC imaging will provide additional information to routine clinical imaging of cerebral aneurysm and AVM. Expected findings include: 1) lower than normal VFR in aneurysm patients, particularly in the vessels distal to the aneurysm, and 2) higher than normal VFR in the feeding and draining vessels of AVM. It is also expected that intra-vascular pressure estimates in and

around the aneurysm and in the nidus of the AVM can be produced. In this chapter, the use of PC techniques are explored and compared against other structural and functional information in a cohort of aneurysm and AVM patients, and then VFR is compared to those measurements obtained in a previously described healthy cohort (Chapter Six).

7.3 Methods and Materials

7.3.1 Patient Cohort

Institutional research ethics board approval was obtained to prospectively acquire MR images in patients with untreated cerebral aneurysm and AVM. Patients were required to be over 18 years of age, free of contra-indications to MR imaging, and be able to provide written informed consent. A cohort of eight patients* were recruited into and consented to participate in this study. Five patients had cerebral aneurysm (denoted as A1 through A5) and three patients had AVM (AVM1 to AVM3). The locations and size of the vascular malformation studied in this work were heterogeneous (summarized in Table 7.1). Half of the patients (A3, A4, A5, and AVM3) were also imaged after intervention. VFR measurements obtained in these patients were compared to a previously published cohort of normal subjects described in the previous chapter.

7.3.2 Imaging Protocol

The subjects had previously undergone imaging with a combination of MR, CT, or DSA x-ray imaging of the brain following institutional protocols used for routine clinical care. Where available these images were used to complement the PC data collected in this study. Some subjects were not able to undergo all the imaging sequences (due to unease with the contrast agent or arterial injection, irregular heart rate, motion or discomfort). Table 7.2 summarizes the imaging for each patient.

The MR imaging research protocol was primarily focused on obtaining and analyzing angiographic images of the vasculature. Spatial localizer and coil sensitivity calibration acquisitions were each performed at the start of the imaging protocol. TOF

* Patient A2 (see Table 7.1) has previously been reported in Chapter Five. It was included in this chapter and analyzed in a different fashion.

Table 7.1: Patient demographics, and aneurysm and AVM size and location.

Subjects	Age	Gender	Size (mm) †	Aneurysm Location	AVM Feeding Arteries	AVM Draining veins
A1	83	F	18	right MCA M1 M2 Bifurcation	---	---
A2*	47	F	6	right ICA ACA Bifurcation	---	---
A3	63	F	23	right cavernous ICA	---	---
A4	19	M	65	left M2 bifurcation	---	---
A5	50	F	8	proximal to the ICA ACA bifurcation	---	---
AVM1	28	F	66	---	left MCA M1 and ACA	superior sagittal sinus
AVM2	60	M	70	---	left MCA M1 and ACA	superior sagittal sinus
AVM3	66	M	28	---	Right MCA-M2	Right transverse sinus

* for reasons of completeness, the subject previously described in Chapter Five is included in this summary.

† diameter of the aneurysm, diameter of the AVM nidus

images were collected, followed by several PC acquisitions with differing parameters (*i.e.*, field-of-view (FOV), velocity encoding (v_{enc}) and spatial resolution). The TOF imaging used a TR/TE/ α of 22 ms/2.5 ms/15°, a slab acquisition matrix of $256 \times 192 \times 32$ over $220 \text{ mm} \times 165 \text{ mm} \times 64 \text{ mm}$ FOV. The acquisition consisted of three axially oriented excitation slabs with a 4-slice overlap between slabs. All utilized PC techniques measured velocity in three orthogonal directions allowing the velocity vector to be calculated. The strategy with these PC acquisitions was to initially collect larger FOV and higher v_{enc} images and then to reduce the FOV and decrease v_{enc} in order to obtain higher resolution images that targeted the vascular malformation. All patients received the large FOV/high v_{enc} acquisition (TR/TE/ α of 8.3 ms/3.8 ms/10°, a matrix acquisition size of $256 \times 192 \times 192$ over $22.0 \text{ cm} \times 16.5 \text{ cm} \times 19.2 \text{ cm}$ FOV, and with a v_{enc} of 150 cm/s). This acquisition required a 10 min 40 s acquisition time. A reduced FOV/low v_{enc} scan was then obtained that limited the FOV to the vascular malformation and reduced the v_{enc} while avoiding spatial aliasing in the malformation and velocity aliasing of the flowing blood. PC images were then collected with a time-resolved, retrospective cardiac gating technique. Cardiac gated PC images typically had an in-plane FOV of $22.0 \text{ cm} \times 16.5 \text{ cm}$ over an acquisition matrix size of 256×192 and 30 cardiac phases were reconstructed.

Images were collected with an axial orientation. Cardiac gated images were collected with a slice thickness of 2 mm in the aneurysm patients and 3 mm in the AVM patients in order to obtain sufficient spatial coverage.

7.3.3 Image Processing

PC images were post-processed to obtain estimates of VFR and intravascular pressure. Instances of velocity aliasing were first corrected in the PC images, the large FOV images never had more than one aliasing wrap and this information could be used to unwrap aliasing in the lower v_{enc} acquisitions. Using the large FOV PC images, twenty-six cut planes were placed across *a priori* selected vessel segments (having diameters > 1 mm) (404). Cut planes were placed at four junctions along the internal carotid arteries (ICA), the vertebral and basilar arteries, the M1 and M2 segments of the middle cerebral arteries (MCA), the anterior communicating artery (ACom), and the posterior cerebral arteries (PCA). One cut plane was used to measure average velocity in both the anterior cerebral arteries (ACA). Cut planes were also placed across the mid superior sagittal sinus, the posterior sagittal sinus, the vein of Galen, and the transverse sinuses. Smaller vessels, such as the posterior communicating artery, were not visible on the large FOV scan and were not assessed. Placement of cut planes in a representative healthy control subject, as well as aneurysm and AVM patients, is shown in Figure 7.1. A subset of these vessel measurements (those most relevant to the particular disease state) is presented in the results.

From each cut plane VFR was calculated by integrating the flow velocity across the vessel lumen,

$$VFR = \oint_S \mathbf{v} \cdot d\mathbf{S}_{\text{cutplane}} \quad \text{Eq 7.1}$$

where \mathbf{v} is blood velocity, and $\mathbf{S}_{\text{cutplane}}$ is the cut plane surface placed across the vessel. In practice, VFR is calculated discretely on a pixel-by-pixel basis by,

$$VFR = \sum_{\mathbf{r}=1}^N \mathbf{v}(\mathbf{r}) \cdot \mathbf{s}(\mathbf{r}) \quad \text{Eq 7.2}$$

where $\mathbf{s}(\mathbf{r})$ is surface vector corresponding to the point \mathbf{r} on the cut plane, and N is the number of points on the cut plane. Mean and standard deviation of the healthy cohort

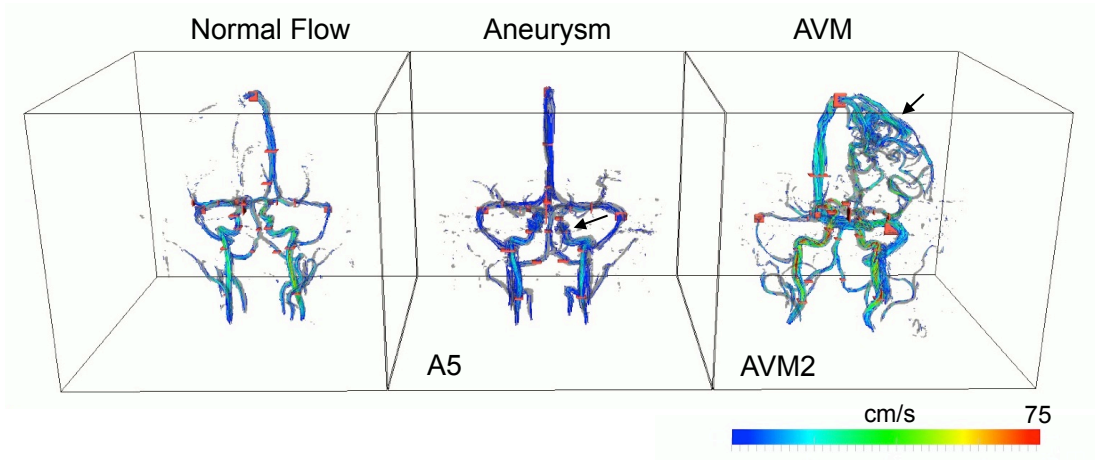


Figure 7.1: Example cut planes used for measuring volume flow rate in a representative subject with normal flow, an aneurysm patient and an AVM patient (left to right). The velocity fields are encoded as coloured streamlines. The cut planes are shown in red over the angiograms, in representative locations. Black arrows point at the aneurysm (Patient A5) and AVM (Patient AVM2), respectively.

was compared to the flow volume in each of the aneurysm and AVM patients by calculating the z -score ($z = (VFR - \mu)/\sigma$ where μ and σ are the VFR estimates of the normal population mean and standard deviation).

Intravascular pressure was calculated from the cardiac-gated PC images. The vessel wall was defined where the absolute blood velocity, $|\mathbf{v}(\mathbf{r})| < 1$ cm/s. The force of the fluid was calculated from the velocity data, and then integrated over the vessel wall to obtain the intravascular pressure. The force of the blood, $\mathbf{F}(t)$, can be estimated by,

$$\mathbf{F}(t) = \rho \left(\frac{\partial \mathbf{v}(t)}{\partial t} + \mathbf{v} \cdot \nabla \mathbf{v}(t) \right) \quad \text{Eq 7.3}$$

where ρ is the blood density (assumed 1.060 g/ml). The intravascular pressure, $P(t)$, can be found as,

$$P(t) = \oint_S \mathbf{F}(t) \cdot d\mathbf{S}_{\text{wall}} \quad \text{Eq 7.4}$$

where \mathbf{S}_{wall} is the surface vector that the force is acting on. This equation can be described discretely as,

$$P(\mathbf{r}, t) = \rho ((\mathbf{v}_i[\mathbf{r}, t] - \mathbf{v}_i[\mathbf{r}, t - 1]) + \mathbf{v}_i[\mathbf{r}, t] \cdot \nabla \mathbf{v}_i[\mathbf{r}, t]) / |\mathbf{S}_{\text{wall}}| \quad \text{Eq 7.5}$$

where $|\mathbf{S}_{\text{wall}}|$ is the surface size of the voxel upon which this force is acting .

7.4 Results

All of the patients (8/8) in the study tolerated the 10 min 40 s large FOV PC imaging acquisitions (Table 7.2). Some patients did not undergo contrast-enhanced clinical MRA (2/8 patients) or CTA (1/8 patients) due to concerns over the contrast injection. Some (2/8) patients did not undergo X-ray DSA in order to avoid the femoral puncture. CTA, DSA and clinical MRA, were compared to the PC angiograms (Figure 7.2). The structural PC images did not provide additional information with respect to the already acquired clinical imaging (detailed in Table 7.2).

The pre-operative VFRs across vessel segments in the aneurysm patients were generally reduced (Figure 7.3) and in AVM patients were generally increased (Figure 7.4), when compared to the VFRs observed in the healthy subjects (Chapter Six). The change in flow was dependent on the location of the vascular malformation.

In Patient A1, where there was an aneurysm at the right MCA-M1/M2 bifurcation, the flow distal to the aneurysm was reduced ($z_{\text{Right Superior MCA M2}} = -1.47$ and $z_{\text{Right Inferior MCA M2}} = -0.51$). The z -scores were generally lower among the twenty-six vessels, the average z -score was -1.82.

Patient A2 had an aneurysm at the left MCA/ACA bifurcation. VFR was reduced in the more distal vessels ($z_{\text{ACA}} = -0.48$), and the left MCA ($z_{\text{Left MCA-M1}} = -1.44$). Patient A2 had an average z -score of -1.29 across all vessels.

Patient A3 had an aneurysm on the right MCA-M1 segment and no flow could be measured at the MCA-M1 or -M2 vessels located distal to the aneurysm. The average pre-operative z -score for this subject was -1.33. Although this patient was treated, the approach was to maintain the M1 and M2 segment occlusions; after treatment there was no flow in the distal vessels and the average z -score was -0.54.

Patient A4 had an aneurysm located along the left cavernous ICA segment, the distal vessels included the left MCA M1 ($z_{\text{Left MCA-M1}} = -2.61$) and the ACA ($z_{\text{ACA}} = -2.39$). This subject also had collateral flow through the ACom artery ($z_{\text{ACom}} = -0.93$). This patient was treated with a pipeline stent. Post-operatively, flow in the distal vessels was unchanged ($z_{\text{Left MCA-M1}} = -2.61$ and $z_{\text{ACA}} = -2.35$), and flow through the ACom was closer

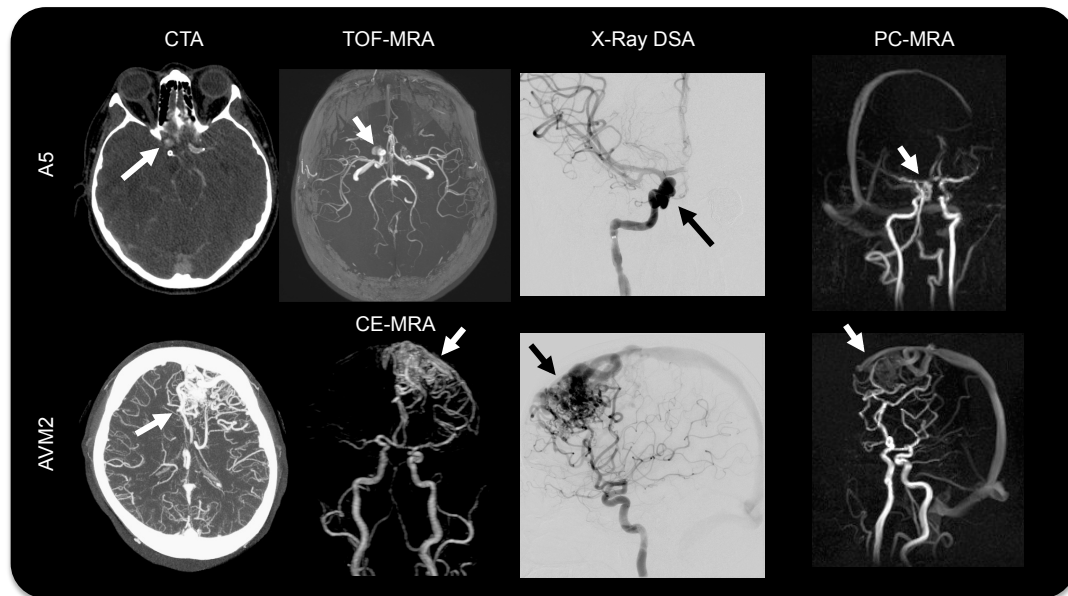


Figure 7.2: Comparison of angiography methods. Images from two subjects are shown. In the top row you can see images of the subject A5 with a cerebral aneurysm, in the bottom row are images of subject AVM2. The first column shows CTA (computed tomography angiography). The second column shows clinical MRA, on top is a non-contrast agent enhanced time-of-flight images showing the aneurysm with a similar quality to the CTA, and on the bottom is an example of a time resolved contrast enhanced MRA of the arterial phase. The third column shows x-ray DSA images of the malformations, which obtained images at the highest resolution and shows many additional vessels. The fourth column shows the PC-MRA, which illustrates the vasculature similarly to the contrast agent enhanced clinical MRA. In the case of aneurysm, it is difficult to see due to the low flow velocity, PC-MRA shows the AVM with good conspicuity and provides information about the flow velocity in the nidus.

to normal values ($z_{ACom} = -0.59$). The average z -scores for this patient were -1.87 and -2.09, pre- and post-operatively, respectively. Although there did not appear to be a change to the MCA-M1 flow, the total flow through the brain was changed and there was relatively more flow through the distal vessels after treatment.

Patient A5 had an aneurysm located on the ICA just proximal to the ICA/MCA bifurcation. The distal vessels had $z_{Left\ MCA-M1} = -2.18$ and $z_{ACA} = -1.24$. This subject also had collateral flow, and $z_{ACom} = -0.70$. Patient A5 was also treated with a pipeline stent and after treatment $z_{Left\ MCA-M1} = -1.46$, $z_{ACA} = 0.14$, and $z_{ACom} = -0.54$. The average z -score was -1.79 pre-operatively and -0.71 post operatively, suggesting that globally the

Table 7.2: Image modes acquired. Healthy cohort is from Chapter Six.

Subjects	Imaging Mode							
	TOF MRA Large FOV	Large FOV	MR-PC Small FOV	CINE	Repeated PC-MR Post-Operatively	CT/CTA	X-Ray DSA	Clinical MRI
Healthy Cohort	✓	✓						
A1	✓	✓	✓	✓		✓		
A2	✓	✓	✓	✓		✓		
A3	✓	✓	✓	✓	✓	✓	✓	✓
A4	✓	✓	✓	✓	✓	✓	✓	✓
A5	✓	✓	✓	✓	✓	✓	✓	✓
AVM1	✓	✓	✓	✓			✓	✓
AVM2	✓	✓	✓	✓		✓	✓	✓
AVM3	✓	✓	✓	✓	✓	✓	✓	✓

Table 7.3: Flow velocity and intravascular pressure in and around the aneurysm fundus for each patient.

Subject	Velocity (cm/s)			Intravascular Pressure (mm Hg)		
	At Neck	Near Edge of Fundus	Centered in Fundus	At Neck	Near Edge of Fundus	Centered in Fundus
A1	6.3	7.4	3.0	62.1	76.0	71.5
A2	8.9	13.5	2.9	169.8	188.8	110.7
A3	6.9	2.4	3.2	60.3	34.6	22.1
A4	3.7	2.7	1.9	59.4	13.8	37.2
A5	10.8	6.1	1.2	75.6	73.8	119.8

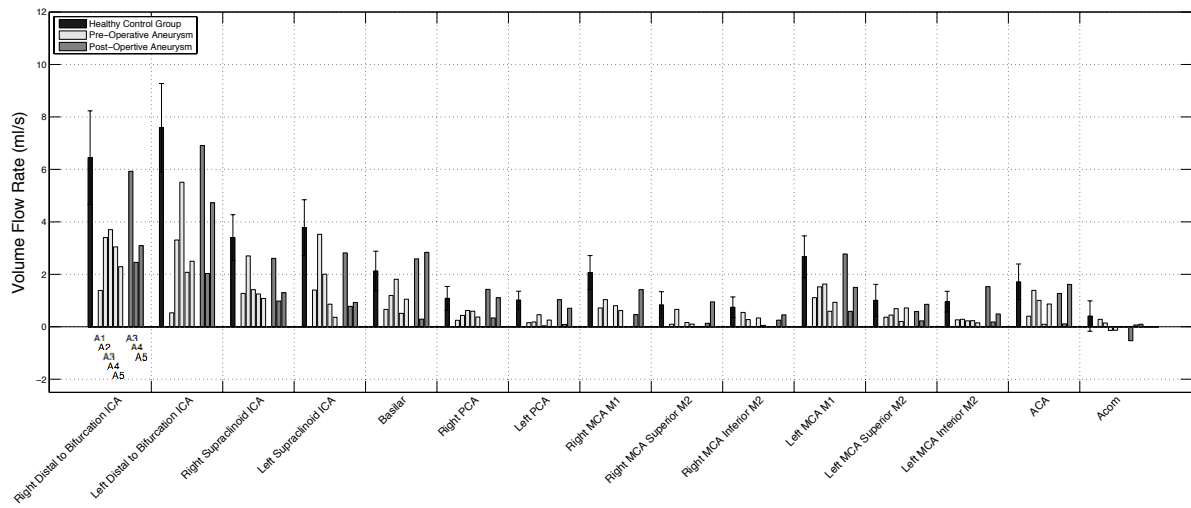


Figure 7.3: Volume flow rate measurements in aneurysm patients. Measurements from the pre- (light grey) and post-operative patients (dark grey) are shown for vessels in and around the aneurysm. Subject order is listed on the first vessel segment. The black bars indicate the flow volume from the healthy cohort and the error bar represents one standard deviation.

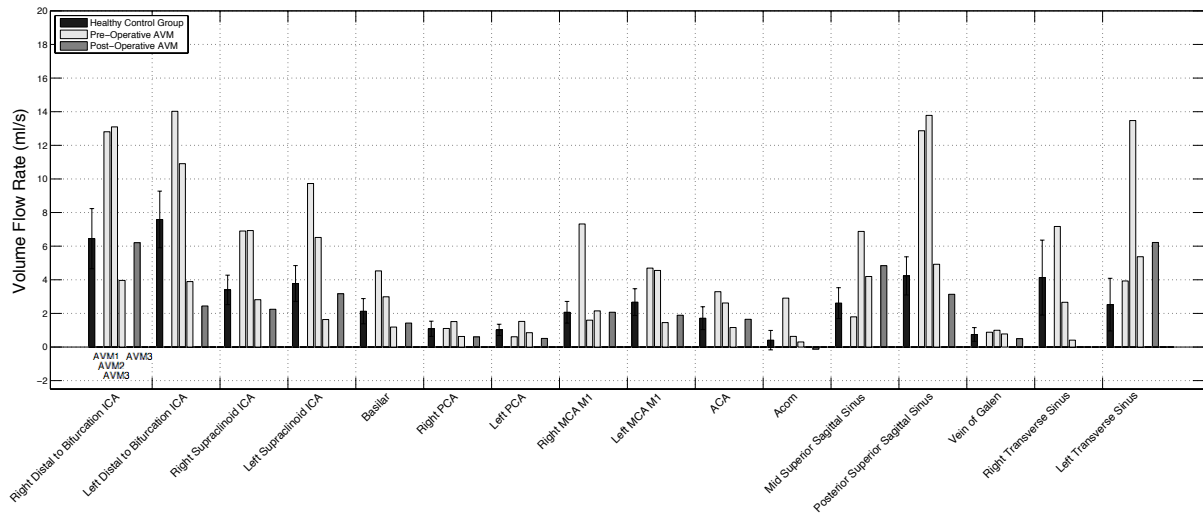


Figure 7.4: Volume flow rate measurements in the AVM patients. Grey bars indicate the pre-operative measurements and the dark-gray measurement indicates the subject that had been treated for one year with stereotactic radiosurgery. The black bars and error bar represent the mean and standard deviation for the respective vessel.

treatment made the flow return to more normal VFR values. In all the aneurysm patients lower than normal flow was observed, although not all the vessels distal to the aneurysm had significantly lower VFR.

Patient AVM1 had feeding arteries originating from the right MCA-M1 and the ACA vessels ($z_{\text{Right MCA-M1}} = 8.11$ and $z_{\text{ACA}} = 2.32$, respectively). The posterior sagittal sinus was the draining vein and also had markedly higher flow ($z_{\text{Sagittal Sinus}} = 7.59$). The ICAs distal to the bifurcation had substantially increased flows ($z_{\text{Left ICA}} = 3.82$ and $z_{\text{Right ICA}} = 3.56$). The average z -score among the vessel segments was 3.18.

Patient AVM2 had a similar-sized nidus to Patient AVM1 but located on the opposite side of the brain, with feeding arteries from the left MCA-M1 and ACA. The z -scores were again large, $z_{\text{Left MCA-M1}} = 2.36$, $z_{\text{ACA}} = 1.33$, and $z_{\text{Sagittal Sinus}} = 8.40$, for the MCA-M1, ACA, and sagittal sinus, respectively). The average z -score for subject AVM2 was 2.36.

Patient AVM3 has a smaller AVM and had a flow pattern that was closer to the normal cohort in comparison to the first two AVM patients. In this patient, there was only one feeder vessel that originated from the right inferior MCA-M2 ($z_{\text{Right Inferior MCA-M2}} = 1.11$). Interestingly, in this patient, the average of all z -scores was -0.67, indicating that subject AVM3 had lower than normal VFR with exception of the artery supplying the AVM. This subject received radiation therapy to treat the AVM and was imaged one year post-operatively, where the average z -score changed slightly to -0.58. The z -score of the right inferior MCA-M2 decreased from 1.11 to 1.06. The average VFR was reduced, but remained relatively high in the feeding artery. These VFR changes were found not to be significant.

Measurements of velocity in the aneurysm neck, in the center of the fundus and near the edge are summarized in Table 7.3. In all five aneurysm patients, velocity in the center of the fundus was observed to be less than towards the outer edge (reduced by approximately 50%). The measured velocity near the aneurysm was highly variable between patients. The intravascular pressure was also variable between aneurysm patients and was higher where the blood flow jet entered the fundus. In the AVM patients, pressures between 28.1 mm Hg and 58.7 mm Hg were measured within the nidus.

Table 7.4: Nidus size and pressure measurements in AVM patients. The pressure measurements were made towards the center of the nidus.

Subject	Nidus Size (mm)	Pressure (mm Hg)
AVM1	660	44.4
AVM2	709	58.7
AVM3	289	28.1

A positive relationship was observed between the nidus size and the intravascular pressure (Table 7.4).

7.5 Conclusions

PC imaging provided both structural and functional information in this patient cohort. The additional structural information agreed with the findings obtained by other modalities (detailed in Table 7.2). From only an anatomical point-of-view, the acquisition of PC images would be hard to justify given that CTA and x-ray DSA had higher spatial resolution and contrast-to-noise ratio between the vessel and surrounding tissues. TOF MR angiograms, generally, had superior resolution and showed additional cerebral landmarks, similar to CTA. PC images, however, did provide structural angiographic images of the blood flow comparable to those derived from time resolved CE MRA. PC imaging was preferred by patients due to its non-invasive nature – in this cohort, 3/8 patients did not receive all routine CTA, x-ray DSA and CE MRA examinations due to concerns about the contrast agent administration. PC imaging was superior with respect to flow quantification providing non-invasive estimates of velocity, VFR and intravascular pressure.

The hypotheses of reduced flow in the aneurysm subjects and increased flow in the AVM patients was confirmed by the PC data. Measurements with z -scores > 8 in some vessels, demonstrates that blood flow can be significantly altered in disease states compared to the normal brain flow patterns (404). Among the five-aneurysm patients not all distal vessels had significant flow reductions (*i.e.* $z > -1.96$). The ACA vessels tended to be not significant as flow would be compensated through the ACom artery in this

averaged measurement. A different criterion for establishing significance, such as comparing flow asymmetry may be more appropriate. In the AVM patients, specifically AVM1 and AVM2, a significant increase was observed in the feeding and draining vessels. Subject AVM3, who had a smaller AVM, had increased VFR but the changes of the feeding and draining veins were not as significant.

The consistent observation that the flow velocity is higher toward the outer edge of the aneurysm than in the center is interesting. This data contradicts the notion of using the laminar shear stress equation for estimating the wall shear stress inside the aneurysm fundus as the flow is not laminar. A similar trend in the intravascular pressure was observed, which appeared to be related more to the vascular configuration and where the jet was entering and redirecting off the vessel wall. The intravascular pressure in the AVM subjects appear to increase with nidus size, which disagrees with some previous findings (405), though with only three subjects firm statements regarding this are difficult to make.

Assessing distal flow in aneurysm and feeding/draining flow in AVMs by z -score might be used automatically to establish global impact of the malformation, or to identify individual vessels with VFR different than normal values. Automatic detection would require a more automated implementation of the cut plane measurements, as the current manual cut plane placement technique is laborious. An automated approach could register a vascular anatomy template with pre-placed cut planes.

A number of limitations are present in this study. The sources of error in the hemodynamic parameters increase with complexity of the post-processing (*i.e.*, from velocity, to VFR, then to intravascular pressure estimates). VFR measurements are limited or impacted by partial volume errors (205) caused by the finite acquired resolution – limiting this technique to larger vessels (>1 mm in diameter). Further, intravascular measurements are limited by the selection of the vessel wall, partial volume effects, and the resolution of the voxels as the velocity field gradient must be computed. The patient examples in this study at best provide limited evidence of the advantages of the PC functional imaging approach. In practice the interpretation of the functional data

must occur in concert with anatomical scanning because of the vast number of aneurysm and AVM configurations.

In this chapter the flow abnormalities in cerebral aneurysm and AVM subjects were characterized, and deviations with respect to measurements in a cohort of healthy subjects were shown (Chapter Six). I believe that the functional information in this chapter complements anatomical imaging and enhances the understanding of flow in abnormalities.

7.6 Chapter Summary

This chapter represents the main chapter examining cerebrovascular disease, building upon work in the previous chapter where the application of the techniques and normal VFR values were established. This chapter supplied evidence to support the overall hypothesis of the thesis, and meets specific aim three. The high degree of heterogeneity in the malformations made it difficult to assess, however with the normal healthy cohort data from the previous chapter, much firmer statements could be made. The next chapter represents a speculative chapter, which stemmed from findings of Chapter Six, and uses not only PC, but also ASL imaging to study flow laterality. It is the final experimental chapter before discussion.

Chapter Eight:

Is it Okay to Compare Blood Flow on Contralateral Sides of the Brain?

8.1 Chapter Overview

The appropriateness of comparing blood flow across hemispheres of the brain is questioned. Recently I have found statistically significant left-right differences in volume flow rate (VFR) measurements between vessel pairs of normal subjects (*i.e.*, flow asymmetry). Here, advanced imaging methods for measuring blood flow, specifically phase contrast (PC) and arterial spin labeling (ASL) magnetic resonance imaging, are used to further assess flow asymmetry. These techniques interrogate the macroscopic flow (blood flow velocity) and microscopic flow (tissue perfusion). Twenty-three healthy subjects were imaged with PC and ASL techniques and measurements of the VFR and cerebral blood flow (CBF) were made in five vessels and their corresponding flow territories (anterior cerebral artery (ACA), left and right middle cerebral artery (MCA), and left and right posterior cerebral artery (PCA)). A laterality index was found between the MCA territories of 0.13 ± 0.10 in the VFR measurements and 0.02 ± 0.03 (mean \pm standard deviation) in the CBF measurements. The laterality index of the PCA territories was -0.06 ± 0.18 in the VFR measurements and -0.05 ± 0.08 in the CBF measurements. From these observations, it can be concluded that a perfusion difference between hemispheres of $<42\%$ in VFR and $<21\%$ in CBF with the implemented PC and ASL methods, respectively, is undetectable.

8.2 Introduction

Over the last fifteen years there has been a substantial body of research that has used the contralateral side of the brain as a control tissue for studying blood flow changes in focal diseases, such as ischemic stroke (17,406-412). Recent evidence, however, has suggested that blood flow and perfusion differs between the left and right sides of the brain even in healthy individuals (323,413-417). A previous finding demonstrated flow asymmetry in healthy subjects: flow was higher in the left middle cerebral artery (MCA) than the right MCA, while flow through the right posterior cerebral artery (PCA) was higher than through the left (Chapter Six). Given these findings, a question naturally arises under what circumstances is it appropriate to compare blood flow between sides of the brain?

Extensive existing research generally assumes flow in each hemisphere is the same; here this assumption is assessed in a normal human cohort.

Although the four vessels appear symmetric when entering the brain, their proximal configuration and hence flow pattern is asymmetric. The concept that vascular structures superior to the aortic arch but proximal to the brain may affect flow to brain tissue can be assessed by a simple thought experiment. Consider the three vessels that branch from the aortic arch: the brachiocephalic trunk, the left carotid artery and the right subclavian artery, and then consider how they supply the four large vessels supplying the brain: the left and right common carotid arteries and left and right vertebral arteries (418). Vessels supplying the right hemisphere of the brain can be found to have more vascular branches than vessels supplying the left hemisphere. For a given pressure drop, flow is also a function of the total vascular resistance. Combined asymmetric origin configurations and resulting changes in vascular resistance suggest that asymmetric flow into the brain might be anticipated. In previous work a finding of higher VFR in the left carotid arteries (directly fed from the aortic arch) and thus higher flow in the left MCA in 90% of the subjects (Chapter Six). The finding of higher VFR on the left side was seen in many other vessel pairs (vertebral artery, and the MCA-M2 artery segments). The exception to the left-sided flow dominance, was in the PCA where 63% of subjects studied had higher flow in the right side (Chapter Six).

In this chapter further evidence is examined at both the macroscopic and microscopic flow levels to evaluate flow asymmetry in the normally healthy human brain in the MCA and PCA territories. The question is posed, “Is it okay to compare blood flow between contralateral sides of the brain?” and use magnetic resonance (MR) imaging evidence to evaluate both flow in supplying vessels and at the vascular bed. Measurements obtained with phase contrast (PC) and with arterial spin labeling (ASL) MR imaging were made in healthy human subjects and then examined for flow asymmetries at both the macroscopic (VFR in paired vessels) and microscopic (cerebral blood flow, CBF, in paired vascular territories) levels. The object of these experiments was to compare the flow in each side of the brain in order to provide estimates of the minimum flow changes that could be reliably detected between hemispheres. The VFR in

the vessels were also correlated to tissue-level CBF to assess the extent of their interdependence.

8.3 Methods and Materials

Twenty-three subjects (12 males and 11 females) with no known cerebrovascular disease were imaged prospectively using a procedure approved by our local research ethics board. The subjects varied between 18 and 64 years of age, with the majority of subjects falling within the 20 to 40 year range. The number of subjects was justified through a bootstrapping analysis, whereby the sample averages were found to converge for the number of subjects included in this analysis. Across subject analyses is used to be able to make a more generalized statement about flow through the human brain.

Two sequences were used to measure the blood flow velocity in vessels and tissue bed perfusion: PC and ASL MR imaging, respectively. The PC parameters were TR/TE/ α of 8.3 ms/3.8 ms/10°, a matrix acquisition size of $256 \times 192 \times 192$ over $22.0 \text{ cm} \times 16.5 \text{ cm} \times 19.2 \text{ cm}$ field-of-view (FOV), and with a velocity encoding of $v_{\text{enc}} = 150 \text{ cm s}^{-1}$. The PC acquisition required a 10 min 40 s acquisition time. A pseudo-continuous ASL sequence was used with a saturation time and a post-labeling delay time of 1.0 s and 2.5 s, respectively. A stack of spirals readout trajectory was used with a slice thickness of 4 mm. The spiral had a readout bandwidth of 62.5 kHz and acquired 1024 points per arm, and 4 total arms per slice. CBF was quantified using the algorithm outlined in Ref (240). The ASL sequence required an acquisition time of 4 min 21 s. Additional conventional MR sequences (time of flight, fluid attenuated inversion recovery (FLAIR), T_1 - and T_2^* -weighted imaging) were also acquired to verify that the subjects did not have brain disease.

In order to calculate the volume flow rate (VFR, in ml s^{-1}), five cut planes were placed through the PC data across the left and right MCA-M1 segments, both anterior cerebral artery (ACA), and the left and right PCA segments (Figure 8.1). Blood flow in five corresponding tissue beds of the brain were obtained (*i.e.*, in the left and right gray matter perfused by the MCAs, anterior gray matter perfused by the ACAs, and the left and right gray matter perfused by the PCAs). Regions (30 ml volume) were placed in the

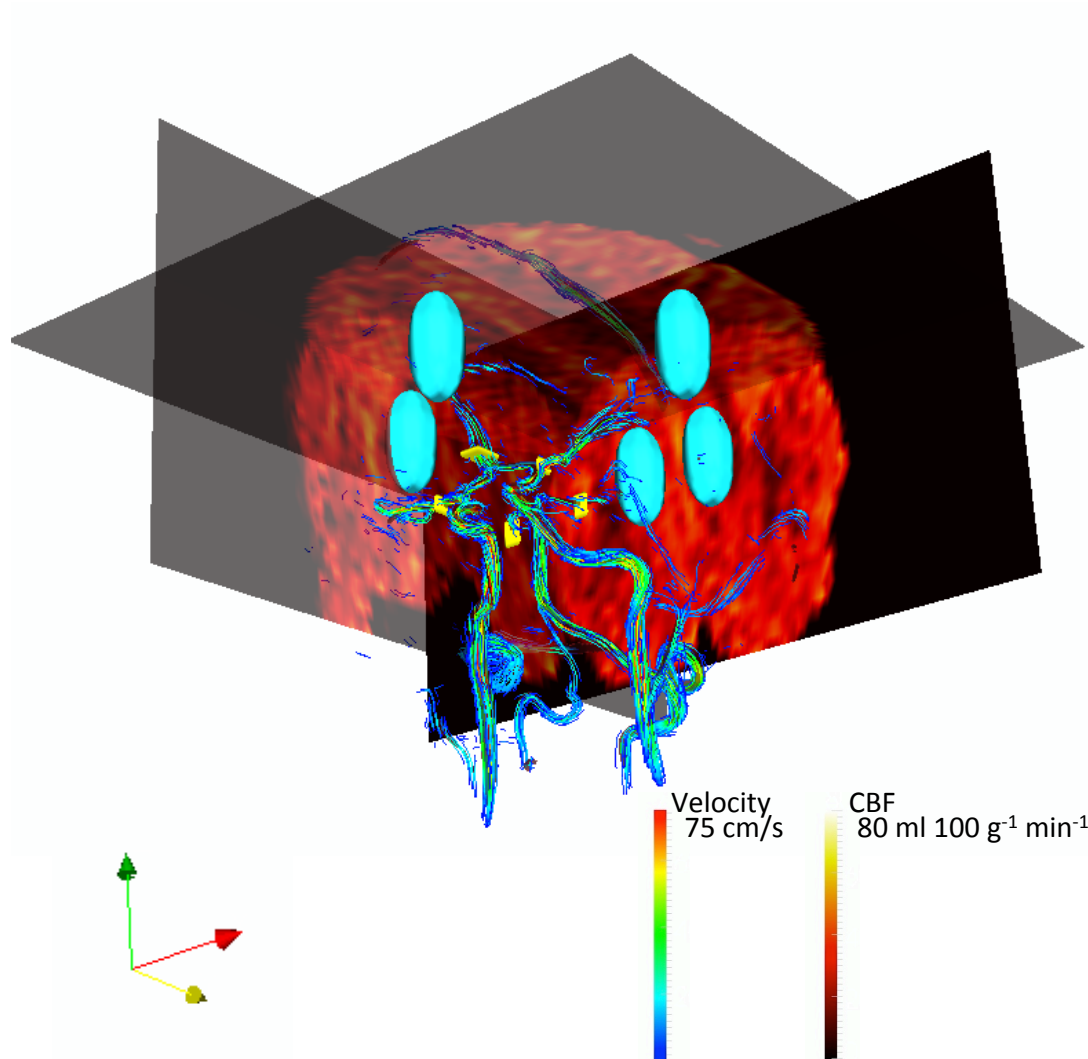


Figure 8.1: Flow measurement locations. Representative rendering of phase contrast (PC) velocity field with velocity streamlines and cut-planes (yellow boxes) used to measure the volume flow rate (VFR). Cuts through the arterial spin labeling (ASL) maps showing the regions (blue ellipsoids) where the regional cerebral blood flow (CBF) measurements were obtained. Velocity streamlines are encoded with the left color bar and CBF is encoded with the right color bar.

grey matter and CBF measurements were obtained (in $\text{ml } 100 \text{ g}^{-1} \text{ min}^{-1}$). The mean, standard deviation and coefficient-of-variation (COV) for the VFR and CBF measurements across the subjects were computed. Laterality index was calculated between the paired vessels (VFR) and paired perfusion beds (CBF). Laterality index was

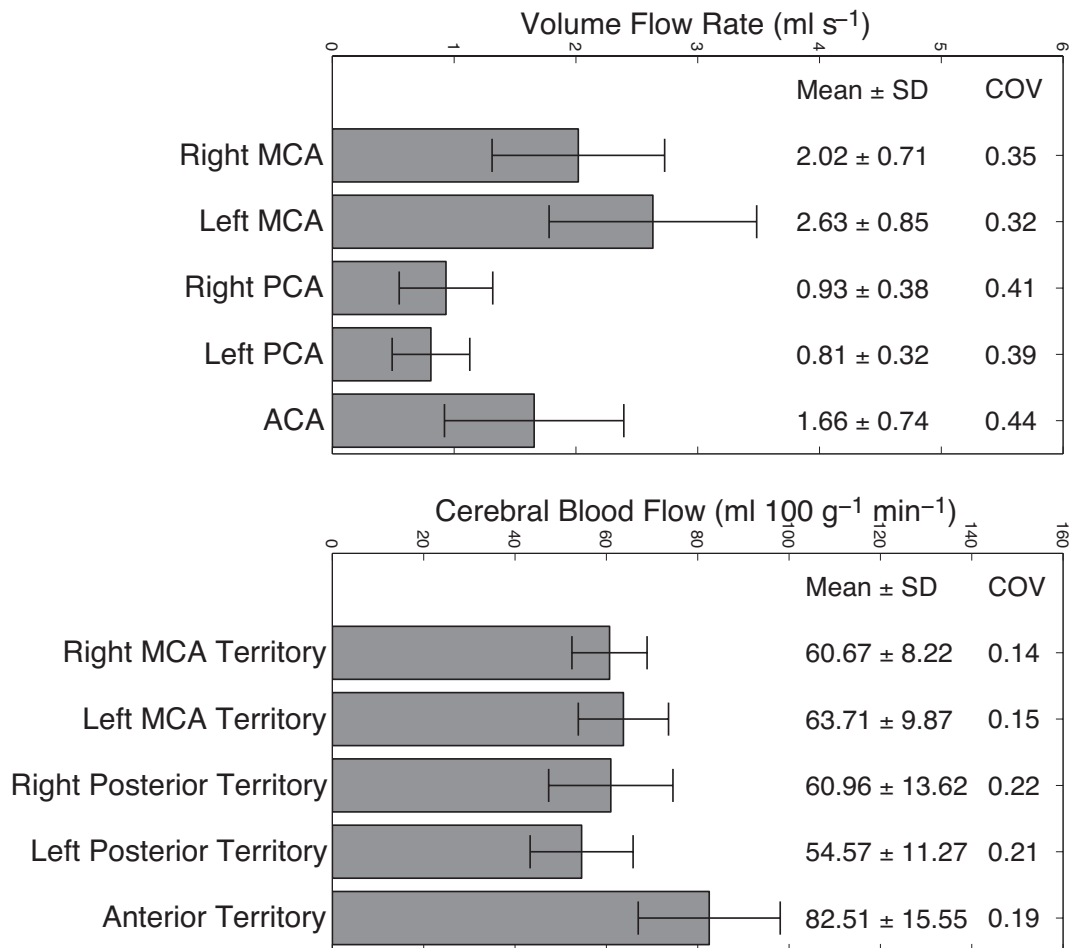


Figure 8.2: Group mean and standard deviation measurements for (top) PC VFR measurements and (bottom) ASL CBF measurements. Bars represent the group mean and the error bars represent one standard deviation (SD) over the subjects.

calculated as laterality index = $(L-R)/(L+R)$, where L and R represent the left and right measurements, respectively. Laterality index was calculated on a subject-by-subject basis and the mean and standard deviation calculated across the group. Separate ANOVA tests were applied to determine significance of VFR and CBF change between the paired vessels and vascular beds. The CBF and VFR values were fit to a line using linear regression and confidence intervals calculated. Spearman rank correlation coefficient was

calculated to examine the correlation between VFR and CBF measurements. Statistical significance was defined at the $p < 0.05$ level.

8.4 Results

VFR and CBF measurements across the subjects (Figure 8.2) showed higher values in the left MCA vessel and territory than on the right side. VFR and CBF were higher in the right PCA vessel and territory than the left side. ANOVA testing found significant differences in laterality index for the MCA VFR measurements ($p = 0.013$) and the PCA CBF measurements ($p < 0.001$, Table 1). The CBF in the anterior brain territory was the highest although the ACA VFR was lower than in the MCA, which would suggest that the anterior region volume is smaller, as would be expected (419), or that the flow in the ACA vessels perfuses other territories (collateral flow). The COV of the VFR measurements tended to be more than $2\times$ larger than the COV of CBF measurements. There was less variation between subjects in the CBF measurements, suggesting that perfusion is more tightly regulated in the micro-circulation than the respective macro-circulation.

Quantitative assessment of flow asymmetry by laterality index is summarized in Table 8.1. The MCA territories had laterality index > 0 indicating higher flow in the left hemisphere, while the PCA territories had laterality index < 0 revealing higher flow in the right hemisphere. The largest asymmetry was in the MCA VFR measurements (laterality index = 0.13 ± 0.10). The VFR laterality indices indicated greater flow asymmetry than the CBF measurements.

Table 8.1: Asymmetry between the left and right sides of the brain. Mean difference was L-R and laterality index was calculated as $(L-R)/(L+R)$, where L and R represent the left and right measurements. Mean and standard deviation (SD) were calculated across the subjects.

Vascular Territory	Mean Difference (ml/s)	VFR Laterality Index	ANOVA	Mean Difference (ml 100 g ⁻¹ min ⁻¹)	CBF Laterality Index	ANOVA
	Mean \pm SD	Mean \pm SD		Mean \pm SD	Mean \pm SD	
MCA	0.61 \pm 0.45	0.13 \pm 0.10	$p = 0.013$	3.04 \pm 4.01	0.02 \pm 0.03	$p = 0.447$
PCA	-0.12 \pm 0.32	-0.06 \pm 0.18	$p = 0.252$	-6.39 \pm 9.41	-0.05 \pm 0.08	$p < 0.001$

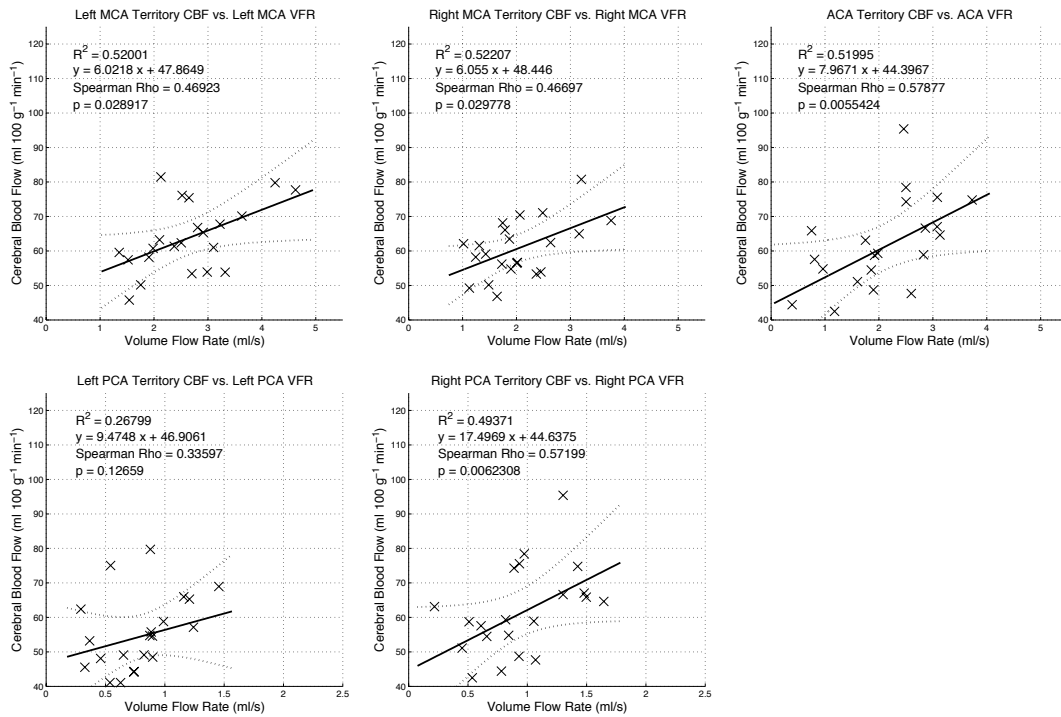


Figure 8.3: Interdependence between PC VFR and ASL CBF measurements for each vascular territory. Linear regression and R^2 coefficients for each fit line are displayed on the plots. The solid line indicates the linear fit, and the dashed line indicates the 95% confidence interval. Each plot also reports the Spearman correlation coefficient (ρ) and its level of significance.

Data were fit (Figure 8.3) and the slope of each regression line was found to vary with territory. The R^2 values ranged between 0.27 and 0.53. The VFR and CBF measurements had a positive relationship with slopes ranging from 6.0 (ml min⁻¹ 100 g⁻¹)/(ml s⁻¹) to 17.5 (ml min⁻¹ 100 g⁻¹)/(ml s⁻¹). Although a linear relationship was found for this healthy population, the non-zero intercept values (>44.4 ml/min/100 g) were unexpected. It is likely that a linear relationship between CBF and VFR would not be appropriate as flow decreases. The Spearman correlation coefficients ranged between 0.33 and 0.58, and were significant ($p < 0.05$) for all the territories except the left PCA ($p = 0.12$).

8.5 Discussion

Evidence has been presented to suggest the existence of asymmetry in the VFR and CBF measurements between hemispheres of the normal brain. These findings suggest that comparison of flow and tissue perfusion across hemispheres is acceptable only when the expected difference is sufficiently large. As a guideline, I estimate that flow changes need to be twice the standard deviation plus the mean measurement difference in order to be detectable. This recommendation would suggest that, for this PC technique, an expected VFR change of >33% for the MCA and >42% for the PCA in VFR is required for detection. For perfusion methods using this ASL approach, expected changes of >8% for the MCA territory and >21% for the PCA territory are required to ensure reliable detection. The implemented PC and ASL techniques employ fairly conventional acquisition and processing parameters.

In general, ASL-based CBF measurements had a smaller mean difference than PC-based VFR measurements, allowing them to reliably detect smaller differences. This finding is intuitive as the resistance of the vascular bed goes up as the vessel diameter becomes smaller; there is also less pulsation over the cardiac cycle in the perfusion bed than in the feeding artery; which reduces the variance of those measurements.

A linear relationship was used to understand CBF-VFR interdependence. Though due to the low R^2 values and high regression intercepts, this model should be seen as only a crude linear approximation, valid for normal blood flow. It is likely that although a reasonable linear relationship is observed, as flow through the feeding artery decreases and approaches zero flow, then the perfusion in the corresponding territory would also approach zero (*i.e.*, it is expected that the flow would taper off to zero for both metrics) plus any component of flow that is collaterally perfusing another territory (anticipated to be small in normal subjects). A more appropriate model linking the macro-vascular and micro-vascular circulation should be developed in future work and include individuals with pathological flow changes (*i.e.*, in stroke).

Most importantly, this chapter provides cautionary evidence against the use of cross-calibration approaches in, for example, dynamic susceptibility contrast (DSC)

bolus passage MR imaging. In this technique a region of normal tissue, such as normal white matter, is used to calibrate the results (*i.e.*, assumed to have a flow of $22 \text{ ml min}^{-1} 100 \text{ g}^{-1}$ (18)). Although asymmetry in the white matter perfusion was not explicitly shown, similar perfusion asymmetry as in gray matter is expected, and the accuracy of DSC CBF maps would vary depending on the side that was selected for cross calibration. For example, lower global CBF when the left MCA territory is selected for cross calibration would be anticipated. In cases of ischemic stroke where the CBF may be reduced by 80% to 90%, or in arteriovenous malformation where VFR increases by as much as 3 \times , comparison against the contralateral side may be appropriate. For conditions where the flow change is smaller relative to the observed flow asymmetry, comparison across hemispheres may yield inaccurate conclusions.

There are several limitations to this work, including: partial volume errors in the PC VFR measurements, and that the ASL CBF measurements are limited to gray matter. The number of subjects, however, is not a limitation of this study as bootstrapping analysis (not shown) confirms that the group averages have converged. VFR measurements are known to be affected by partial volume effects (205), this is further impacted by the diameters of the small intracranial vessels targeted. Repeating this experiment with a higher resolution PC acquisition would reduce this source of error, though in the current study the effect is similar for both hemispheric measurements. The across hemisphere comparison of CBF measurements is limited to gray matter where the ASL measurements were taken. Current guidelines (254) do not extend ASL measurements to white matter. To summarize, it is recommended that perfusion across the brain hemispheres be compared only if the expected difference in flow is greater than 42% in the macrovasculature VFR or greater than 21% in the microvasculature CBF.

Chapter Nine:

Discussion and Conclusions

9.1 Thesis Review

Throughout the thesis I have reviewed methods for cerebrovascular MR imaging, performed sophisticated simulations to better understand MR technology, and explored the use of PC velocity encoding in healthy humans and in patients with disease. The overall focus remained on quantification of cerebrovascular parameters, particularly velocity encoding, which had the most allure of the available methods. Initially, the potential of PC imaging was shown in the case of a single cerebral aneurysm, by mapping velocity, VFR and intravascular pressure. Next, PC images were collected in the population of healthy normal subjects and established the flow velocity and VFR for normal vessels of the human brain. Patients were recruited for imaging, specifically, cerebral aneurysm and AVM patients, and the flow was compared with the flow through normal vasculature. When studying flow in the normal case I established that there was to some degree asymmetry between left and right sides of the brain, this was explored further with arterial spin labeling perfusion imaging, comparing flow on contralateral hemispheres of the brain. We consider now the scientific approaches, reflecting upon the hypotheses that drove the experiments.

9.2 Reflection on Hypotheses

The overall hypothesis that quantifying hemodynamic parameters with MR would lead to improved knowledge about disease states has been confirmed. This is not a strictly testable hypothesis, but the experiments presented did result in new knowledge about cerebral aneurysm and AVM. This hypothesis should continue to be used as a motivation for future experiments of this nature.

The specific hypotheses, provided throughout the thesis, should also be reflected upon, these hypotheses were much more specific in nature and testable. In the simulation experiments (Chapter Four) the aim was to establish the lower bound for MR imaging, which yielded a framework for seeing how the lower bound changes with distortion. The hypothesis that the Cramer-Rao lower bound (CRLB) was obtainable, is weak, however, the expectation that the degree of receiver channel correlation would affect the CRLB was much more speculative. This hypothesis came about after examining previous

simulation. Although more difficult to test this hypothesis, the findings are much more valuable.

In the cerebral aneurysm case study (Chapter Five) it was expected that VFR would become more symmetric after treatment and that there would be a reduction of collateral flow. It was also expected that flow would increase distally to the aneurysm after stent treatment. The pre- and post-operative PC imaging confirmed these expectations. In the normal healthy flow study (Chapter Six) the level of flow asymmetry between paired vessels was assessed. It was also expected that the coefficient of variation would be higher in the v_{peak} than the VFR measurements. Significant flow asymmetry was found in several paired vessels on both metric types, confirming the first expectation. The coefficient of variation (COV) in the VFR measurements was not lower than in the v_{peak} measurements, contrary to the expectation. Though vessels with smaller diameter tended to have higher COV. In the aneurysm and AVM study (Chapter Seven) I expected to find lower flow in the aneurysm patients and higher flow in the AVM patients. This expectation was confirmed in a quantitative fashion, z-scores were calculated for vessels distal to the aneurysms confirming lower flow and global averages of the flow in all vessel segments were lower than the average. VFR in the AVM patients was significantly higher in the feeding and draining vessels, and the global average was higher than the normal case. In the final experimental chapter (Chapter Eight) the hypothesis was that flow should not be compared on contralateral sides of the brain, as there was too much asymmetry. It might be restated, depending on the flow level that one wanted to detect, it may or may not be proper to compare blood flow across hemispheres of the brain.

9.3 Conclusions

I found that MR was useful for imaging cerebrovascular hemodynamics and quantifying blood velocity. My main conclusions were directly related to the specific hypothesis of the chapters.

The lower bound of MR imaging was established and was shown to change with receiver coil coverage. A similar finding between the analytical, simulated- and empirically-derived noise as a function of receiver coil coverage helps to validate the

method. Findings regarding the change of the CRLB as a function of the receiver coil correlation is a key finding related to coil design. The lower bound of MR imaging is a function of all of the simulation parameters described in Chapter Four, and must be determined in a numerical fashion.

With respect to the chapters related to the PC measurements (Chapters Five through Eight), several conclusions can be drawn. In the case study (Chapter 5), flow became more symmetric with pipeline stent treatment and flow distal to the treatment site increased. It was speculated that this would be the case as the flow patterns were mechanically altered, and confirmed this with sophisticated empirical evidence. In Chapter Six, the analysis of healthy flow, it can be concluded that the reported measurements have converged to the population average, based on the bootstrapping evidence. I can conclude that the time averaged v_{peak} and VFR have similar COV. Additionally, it can be concluded that the flow is not symmetric between the left and right sides of the brain, and that in several paired vessel segments there was significant asymmetry present. When questioning the use of contralateral flow comparison (Chapter Eight), a conclusive, evidence-based recommendation was made about the level of contralateral flow that could be detected as abnormal (*i.e.*, the degree to which left-right flow divergence that was abnormal).

In Chapter Seven, where aneurysms and AVMs were examined, it can be concluded that there was significantly lower flow in vessels distal to aneurysms and significantly higher flow in the feeding and draining AVM vessels, though the degree to which the flow was abnormal was more than expected. In the aneurysm cases it was concluded that most distal vessels had significantly decreased flow with z -scores of $z < -1.96$, while in the AVM patients the degree to which the flow was abnormal was much greater, with $z > 5$ in the feeding vessels. This high degree of significance was an unexpected conclusion.

9.4 Significance

New knowledge was created by conducting experiments to test the aforementioned hypotheses. In the simulation chapter, I see that MR systems cannot be improved by

continuously adding coils. There is a limit to improvement, which can be described by determining the CRLB. This finding is significant, as the research field seems to propose continuously adding coils from 8 to 12 to 32 and even 128 channels (69). The CRLB analysis suggests that optimizing the coil coverage of the sample is as important as the number of coils, and proposes a way to look at the correlation with respect to the information additional coils add.

Measurement of advanced hemodynamic parameters in a single case is easily criticised, however, demonstration of such advanced metrics before and after intervention and the way that a unique case could be evaluated shows the observations that such methodology can yield; If even on a single subject. It shows how the treatment changed the flow, reducing the high degree of asymmetry that existed preoperatively. The healthy flow study (Chapter Six), supplies the research field with a superior understanding of the peak flow and VFR through a broader range of vessels than any existing studies. The analysis of the asymmetry yielded additional questions posed in Chapter Eight. The bootstrapping analysis improves the confidence in the measurements that were reported. The hemodynamics analysis of the aneurysm and AVM patients was significant; drawing hard conclusions on such heterogeneous disease states is difficult, particularly when the subjects are so few and thus hard to recruit. The measurements that were made on these patients are novel and brought a new understanding of the flow divergence from the normal case. The final chapter questioning the use of contralateral flow comparison, although short, may be the most significant work as it sets a standard for the suitability of both past and future analysis.

9.5 Future Work and Reflection on Experimental Design

There remains much future work. Imaging can play a role in the assessment of cerebrovascular disease, but it is limited by the underlying physics of acquisition.

The CRLB simulation could be advanced, as one can always seem to build more physics into their model. In that chapter the additional parameters that could be added were eluded to, such as the voxel frequency spectrum or diffusion. The CRLB simulation could be modified to assess its dependence on any of the input parameters. These

calculations took a long time to run, on the order of two weeks, reducing the simulation runtime would allow for more iterations of the simulation to explore further effects of distortion. An effort was made to reduce the number of required calculations where possible (*i.e.*, not doing the calculations in voxels containing air), but still, the required computations are vast.

There is always desire to have higher SNR and resolution, but are bound by acquisition time and field of view. The experiments with PC are no exception to this. Performing the analysis described in this thesis with superior source images (higher resolution, higher SNR) would be expected to improve the quality of the results. There are host of methods that could be explored to improve SNR efficiency. For example, multi-dimension phase encoding (420), advanced trajectories (358,392), and increased field strength: are methods expected to increase the SNR efficiency. Bootstrapping was used to show that adding additional subjects to the healthy flow cohort is not required. Assessing cofactors such as age and gender might be a worthy undertaking for future experiments. Imaging additional patients should be a future objective, ideally enough subjects with similar malformation configurations that would allow study of flow in groups would be preferred, though this would likely mean recruiting hundreds of patients.

9.6 Summary

A scientific treatment was used to arrive at conclusions; evidence from literature, simulation and empirical measurements were used to come to conclusions. The overall hypothesis drove the nature of the experiments, and then several testable hypotheses were formulated. Sophisticated experiments were undertaken to yield evidence to support the arguments. For example, a high degree of sophistication was used in simulation and experimental methodologies to arrive at a new realization about the noise encountered in MR imaging. In another example, the use of advanced PC velocity mapping was used to examine healthy and diseased flow in the brain, and extended by performing fluid simulations.

This thesis represents an original contribution to the discipline, establishing the CRLB can be done for most estimation problems like MR imaging, so it was a known

unknown. Establishing it for the purposes of MR applications is a unique contribution to the field. These experiments met specific objective 1 (described on page 6). The implications of the flow experiments can be separated into two subsets, parallel to the Specific Objectives 2&3: Firstly, advanced methodologies were used to better characterize the flow through the brain, by establishing flow measurements and degree of asymmetry in cerebrovascular segments in a broad range of vessels, with conclusive evidence supporting these measurements; Secondly, velocity and pressure were measured in aneurysm and AVM patients. PC MR was used to obtain hemodynamic measurements to examine the flow volume in vascular malformations among this expanded vessel set yielding new knowledge about the degree to which flow may diverge in different types of vascular malformations.

Chapter Ten: References

1. World Health Organization. Global burden of disease: 2004 Update. Geneva, Switzerland: WHO Press: 2004.
2. Pendlebury ST. Worldwide under-funding of stroke research. *International Journal of Stroke* 2007;2(2):80-84.
3. Nichols WW, O'Rourke MF. McDonald's Blood Flow in Arteries: Theoretical, experimental and clinical principles: Co-published by Arnold and the Oxford University Press: 1960.
4. Willis T, Weber JC. *Cerebri Anatomie: cui accessit nervorum*: Jo. Martyn, London: 1664.
5. Knott J. On The Cerebral Sinuses and Their Variations. *Journal of Anatomical Physiology* 1881;16(1):27-42.
6. Marty AT. Arterial Variations in Man: Classification and Frequency. *JAMA: The Journal of the American Medical Association* 1986;255(20):2821.
7. Puchades-Orts A, Nombela-Gomez M, Ortuño-Pacheco G. Variation in form of circle of willis: Some anatomical and embryological considerations. *The Anatomical Record* 1976;185(1):119-123.
8. Henderson RD, Eliasziw M, Fox AJ, Rothwell PM, Barnett HJM. Angiographically Defined Collateral Circulation and Risk of Stroke in Patients With Severe Carotid Artery Stenosis. *Stroke* 2000;31(1):128-132.
9. Hoksbergen A, Legemate D, Csiba L, Csáti G, Síró P, Fülesdi B. Absent Collateral Function of the Circle of Willis as Risk Factor for Ischemic Stroke. *Cerebrovasc Dis* 2003;16(3):191-198.
10. Nonaka H, Akima M, Nagayama T, Hatori T, Zhang Z, Ihara F. Microvasculature of the human cerebral meninges. *Neuropathology* 2003;23(2):129-135.
11. Pardridge WM. *Introduction to the blood-brain barrier: methodology, biology and pathology*: Cambridge University Press: 1998.
12. Witt KA, Gillespie TJ, Huber JD, Egleton RD, Davis TP. Peptide drug modifications to enhance bioavailability and blood-brain barrier permeability. *Peptides* 2001;22(12):2329-2343.
13. Crivori P, Cruciani G, Carrupt P-A, Testa B. Predicting Blood-Brain Barrier Permeation from Three-Dimensional Molecular Structure. *J Med Chem* 2000;43(11):2204-2216.
14. Sourbron S, Ingrisch M, Siefert A, Reiser M, Herrmann K. Quantification of cerebral blood flow, cerebral blood volume, and blood-brain-barrier leakage with DCE-MRI. *Magn Reson Med* 2009;62(1):205-217.
15. Calamante F, Gadian DG, Connelly A. Delay and dispersion effects in dynamic susceptibility contrast MRI: Simulations using singular value decomposition. *Magn Reson Med* 2000;44(3):466-473.
16. Roberts HC, Roberts TPL, Lee TY, Dillon WP. Dynamic, Contrast-Enhanced CT of Human Brain Tumors: Quantitative Assessment of Blood Volume, Blood Flow, and Microvascular Permeability: Report of Two Cases. *American Journal of Neuroradiology* 2002;23(5):828-832.

17. MacDonald ME, Smith MR, Frayne R. Deconvolution with simple extrapolation for improved cerebral blood flow measurement in dynamic susceptibility contrast magnetic resonance imaging during acute ischemic stroke. *Magn Reson Imaging* 2011;29(5):620-629.
18. Østergaard L, Sorensen AG, Kwong KK, Weisskoff RM, Gyldensted C, Rosen BR. High resolution measurement of cerebral blood flow using intravascular tracer bolus passages. Part II: Experimental comparison and preliminary results. *Magn Reson Med* 1996;36(5):726-736.
19. Østergaard L, Weisskoff RM, Chesler DA, Gyldensted C, Rosen BR. High resolution measurement of cerebral blood flow using intravascular tracer bolus passages. Part I: Mathematical approach and statistical analysis. *Magn Reson Med* 1996;36(5):715-725.
20. Nabavi DG, Cenic A, Craen RA, et al. CT Assessment of Cerebral Perfusion: Experimental Validation and Initial Clinical Experience. *Radiology* 1999;213(1):141-149.
21. Lee TY. Functional CT: physiological models. *Trends Biotechnol* 2002;20(8):S3-S10.
22. Pantano P, Baron JC, Lebrun-Grandie P, Duquesnoy N, Bousser MG, Comar D. Regional cerebral blood flow and oxygen consumption in human aging. *Stroke* 1984;15(4):635-641.
23. Hatazawa J, Fujita H, Kanno I, et al. Regional cerebral blood flow, blood volume, oxygen extraction fraction, and oxygen utilization rate in normal volunteers measured by the autoradiographic technique and the single breath inhalation method. *Ann Nucl Med* 1995;9(1):15-21.
24. Groves W, Brandt J, Steinberg M, et al. Vascular Dementia and Alzheimer's Disease: Is There a Difference?: A Comparison of Symptoms and Disease Duration. *The Journal of Neuropsychiatry and Clinical Neurosciences* 2000;12(3):305-315.
25. Farkas E, Luiten PGM. Cerebral microvascular pathology in aging and Alzheimer's disease. *Prog Neurobiol* 2001;64(6):575-611.
26. Cheng A-L, Batool S, McCreary CR, et al. Susceptibility-Weighted Imaging is More Reliable Than T2*-Weighted Gradient-Recalled Echo MRI for Detecting Microbleeds. *Stroke* 2013;44(10):2782-2786.
27. Fisher M, French S, Ji P, Kim RC. Cerebral Microbleeds in the Elderly. *Stroke* 2010;41(12):2782-2785.
28. Prati P, Vanuzzo D, Casaroli M, et al. Prevalence and determinants of carotid atherosclerosis in a general population. *Stroke* 1992;23(12):1705-1711.
29. Lorenz MW, von Kegler S, Steinmetz H, Markus HS, Sitzer M. Carotid Intima-Media Thickening Indicates a Higher Vascular Risk Across a Wide Age Range. *Stroke* 2006;37(1):87-92.
30. Chambless LE, Folsom AR, Davis V, et al. Risk Factors for Progression of Common Carotid Atherosclerosis: The Atherosclerosis Risk in Communities Study, 1987-1998. *Am J Epidemiol* 2002;155(1):38-47.
31. Smith SC, Jr, Allen J, Blair SN, et al. AHA/ACC Guidelines for Secondary Prevention for Patients With Coronary and Other Atherosclerotic Vascular

- Disease: 2006 Update: Endorsed by the National Heart, Lung, and Blood Institute. *J Am Coll Cardiol* 2006;47(10):2130-2139.
32. Amarenco P, Labreuche J, Lavallée P, Touboul P-J. Statins in Stroke Prevention and Carotid Atherosclerosis: Systematic Review and Up-to-Date Meta-Analysis. *Stroke* 2004;35(12):2902-2909.
 33. Nissen Se NSJSI, et al. Effect of very high-intensity statin therapy on regression of coronary atherosclerosis: The asteroid trial. *JAMA* 2006;295(13):1556-1565.
 34. Ferguson GG, Eliasziw M, Barr HWK, et al. The North American Symptomatic Carotid Endarterectomy Trial : Surgical Results in 1415 Patients. *Stroke* 1999;30(9):1751-1758.
 35. Mas JL, Trinquart L, Leys D, et al. Endarterectomy Versus Angioplasty in Patients with Symptomatic Severe Carotid Stenosis (EVA-3S) trial: results up to 4 years from a randomised, multicentre trial. *Lancet Neurology* 2008;7:885-892.
 36. Brott TG, Hobson RW, Howard G, et al. Stenting versus Endarterectomy for Treatment of Carotid-Artery Stenosis. *N Engl J Med* 2010;363(1):11-23.
 37. Henkes H, Miloslavski E, Lowens S, Reinartz J, Liebig T, Kühne D. Treatment of intracranial atherosclerotic stenoses with balloon dilatation and self-expanding stent deployment (WingSpan). *Neuroradiology* 2005;47(3):222-228.
 38. Chimowitz MI, Lynn MJ, Derdeyn CP, et al. Stenting versus Aggressive Medical Therapy for Intracranial Arterial Stenosis. *N Engl J Med* 2011;365(11):993-1003.
 39. Lloyd-Jones D, Adams R, Carnethon M, et al. Heart Disease and Stroke Statistics-2009 Update. *Circulation* 2009;119(3):480-486.
 40. Sacco RL. Risk factors, outcomes, and stroke subtypes for ischemic stroke. *Neurology* 1997;49(5 Suppl 4):S39-S44.
 41. Strbian D, Soenne L, Sairanen T, et al. Ultraearly Thrombolysis in Acute Ischemic Stroke Is Associated With Better Outcome and Lower Mortality. *Stroke* 2010;41(4):712-716.
 42. Soares BP, Chien JD, Wintermark M. MR and CT Monitoring of Recanalization, Reperfusion, and Penumbra Salvage: Everything That Recanalizes Does Not Necessarily Reperfuse! *Stroke* 2009;40(3 suppl 1):S24-S27.
 43. Eilaghi A, Brooks J, d'Esterre C, et al. Reperfusion Is a Stronger Predictor of Good Clinical Outcome than Recanalization in Ischemic Stroke. *Radiology* 2013.
 44. Sacco RL, Adams R, Albers G, et al. Guidelines for Prevention of Stroke in Patients With Ischemic Stroke or Transient Ischemic Attack: A Statement for Healthcare Professionals From the American Heart Association/American Stroke Association Council on Stroke: Co-Sponsored by the Council on Cardiovascular Radiology and Intervention: The American Academy of Neurology affirms the value of this guideline. *Circulation* 2006;113(10):e409-449.
 45. Smith WS, Sung G, Saver J, et al. Mechanical Thrombectomy for Acute Ischemic Stroke: Final Results of the Multi MERCI Trial. *Stroke* 2008;39(4):1205-1212.
 46. Liebeskind DS, Cotsonis GA, Saver JL, et al. Collaterals dramatically alter stroke risk in intracranial atherosclerosis. *Ann Neurol* 2011;69(6):963-974.
 47. Lansberg MG, Bluhmki E, Thijs VN. Efficacy and Safety of Tissue Plasminogen Activator 3 to 4.5 Hours After Acute Ischemic Stroke: A Metaanalysis. *Stroke* 2009;40(7):2438-2441.

48. Tuhim S, Horowitz DR, Sacher M, Godbold JH. Validation and comparison of models predicting survival following intracerebral hemorrhage. *Crit Care Med* 1995;23(5):950-954.
49. Mendelow AD, Unterberg A. Surgical treatment of intracerebral haemorrhage. *Current Opinion in Critical Care* 2007;13(2):169-174.
50. Mayer SA. Recombinant Activated Factor VII for Acute Intracerebral Hemorrhage. *Stroke* 2007;38(2):763-767.
51. Schulman S, Beyth RJ, Kearon C, Levine MN. Hemorrhagic Complications of Anticoagulant and Thrombolytic Treatment. *Chest* 2008;133(6 suppl):257S-298S.
52. Rinkel GJE, Djibuti M, Algra A, van Gijn J. Prevalence and Risk of Rupture of Intracranial Aneurysms : A Systematic Review. *Stroke* 1998;29(1):251-256.
53. Valencia A, Morales H, Rivera R, Bravo E, Galvez M. Blood flow dynamics in patient-specific cerebral aneurysm models: The relationship between wall shear stress and aneurysm area index. *Med Eng Phys* 2008;30(3):329-340.
54. Wermer MJH, van der Schaaf IC, Algra A, Rinkel GJE. Risk of Rupture of Unruptured Intracranial Aneurysms in Relation to Patient and Aneurysm Characteristics. *Stroke* 2007;38(4):1404-1410.
55. David CA, Vishteh AG, Spetzler RF, Lemole M, Lawton MT, Partovi S. Late angiographic follow-up review of surgically treated aneurysms. *J Neurosurg* 1999;91(3):396-401.
56. Brilstra EH, Rinkel GJE, van der Graaf Y, van Rooij WJJ, Algra A. Treatment of Intracranial Aneurysms by Embolization with Coils : A Systematic Review. *Stroke* 1999;30(2):470-476.
57. Piotin M, Blanc R, Spelle L, et al. Stent-Assisted Coiling of Intracranial Aneurysms: Clinical and Angiographic Results in 216 Consecutive Aneurysms. *Stroke* 2010;41(1):110-115.
58. Wardlaw JM, Smith EE, Biessels GJ, et al. Neuroimaging standards for research into small vessel disease and its contribution to ageing and neurodegeneration. *The Lancet Neurology* 2013;12(8):822-838.
59. Ferri CP, Prince M, Brayne C, et al. Global prevalence of dementia: a Delphi consensus study. *The Lancet* 2005;366(9503):2112-2117.
60. Jellinger KA, Attems J. Is there pure vascular dementia in old age? *J Neurol Sci* 2010;299(1, 2):150-154.
61. Rastas S, Pirttilä T, Mattila K, et al. Vascular risk factors and dementia in the general population aged >85 years: Prospective population-based study. *Neurobiol Aging* 2010;31(1):1-7.
62. Kalaria RN, Maestre GE, Arizaga R, et al. Alzheimer's disease and vascular dementia in developing countries: prevalence, management, and risk factors. *The Lancet Neurology* 2008;7(9):812-826.
63. Schuff N, Matsumoto S, Kmiecik J, et al. Cerebral blood flow in ischemic vascular dementia and Alzheimer's disease, measured by arterial spin-labeling magnetic resonance imaging. *Alzheimer's and Dementia* 2009;5(6):454-462.
64. Viswanathan A, Rocca WA, Tzourio C. Vascular risk factors and dementia. *Neurology* 2009;72(4):368-374.

65. Deschaintre Y, Richard F, Leys D, Pasquier F. Treatment of vascular risk factors is associated with slower decline in Alzheimer disease. *Neurology* 2009;73(9):674-680.
66. Schuur M, van Swieten JC, Schol-Gelok S, et al. Genetic risk factors for cerebral small-vessel disease in hypertensive patients from a genetically isolated population. *J Neurol Neurosurg Psychiatry* 2011;82(1):41-44.
67. Alessandro B, Steven M G. Cerebral Amyloid Angiopathy: A Systematic Review. *Journal of Clinical Neurology* 2011;7(1):1-9.
68. McCarron MO, Nicoll JAR. Cerebral amyloid angiopathy and thrombolysis-related intracerebral haemorrhage. *The Lancet Neurology* 2004;3(8):484-492.
69. Hofmeister C, Stapf C, Hartmann A, et al. Demographic, Morphological, and Clinical Characteristics of 1289 Patients With Brain Arteriovenous Malformation. *Stroke* 2000;31(6):1307-1310.
70. Al-Shahi R, Warlow C. A systematic review of the frequency and prognosis of arteriovenous malformations of the brain in adults. *Brain* 2001;124(10):1900-1926.
71. Walker EJ, Su H, Shen F, et al. Arteriovenous malformation in the adult mouse brain resembling the human disease. *Ann Neurol* 2011;69(6):954-962.
72. Gobin YP, Laurent A, Merienne L, et al. Treatment of brain arteriovenous malformations by embolization and radiosurgery. *J Neurosurg* 1996;85(1):19-28.
73. Jain RK. Determinants of Tumor Blood Flow: A Review. *Cancer Res* 1988;48(10):2641-2658.
74. Jain RK, di Tomaso E, Duda DG, Loeffler JS, Sorensen AG, Batchelor TT. Angiogenesis in brain tumours. *Nat Rev Neurosci* 2007;8(8):610-622.
75. Dewhirst MW, Tso CY, Oliver R, Gustafson CS, Secomb TW, Gross JF. Morphologic and hemodynamic comparison of tumor and healing normal tissue microvasculature. *International Journal of Radiation Oncology*Biophysics* 1989;17(1):91-99.
76. Mäntylä MJ, Toivanen JT, Pitkänen MA, Rekonen AH. Radiation-induced changes in regional blood flow in human tumors. *International Journal of Radiation Oncology*Biophysics* 1982;8(10):1711-1717.
77. Ma J, Waxman DJ. Combination of antiangiogenesis with chemotherapy for more effective cancer treatment. *Molecular Cancer Therapeutics* 2008;7(12):3670-3684.
78. Crummy AB, Mistretta CA. Digital Subtraction Arteriography (DSA). In: Baert A, Boijesen E, Fuchs W, Heuck FW, editors. *Frontiers in European Radiology. Volume 2, Frontiers in European Radiology: Springer Berlin Heidelberg; 1982. p. 73-90.*
79. Anxionnat R, Bracard S, Ducrocq X, et al. Intracranial Aneurysms: Clinical Value of 3D Digital Subtraction Angiography in the Therapeutic Decision and Endovascular Treatment. *Radiology* 2001;218(3):799-808.
80. Crummy A, Strother C, Sackett J, et al. Computerized fluoroscopy: digital subtraction for intravenous angiocardiology and arteriography. *Am J Roentgenol* 1980;135(6):1131-1140.

81. Achenbach S, Marwan M, Ropers D, et al. Coronary computed tomography angiography with a consistent dose below 1 mSv using prospectively electrocardiogram-triggered high-pitch spiral acquisition. *Eur Heart J* 2010;31(3):340-346.
82. Mollet NR, Cademartiri F, van Mieghem CAG, et al. High-Resolution Spiral Computed Tomography Coronary Angiography in Patients Referred for Diagnostic Conventional Coronary Angiography. *Circulation* 2005;112(15):2318-2323.
83. Kidwell CS, Chalela JA, Saver JL, et al. Comparison of MRI and CT for Detection of Acute Intracerebral Hemorrhage. *JAMA: The Journal of the American Medical Association* 2004;292(15):1823-1830.
84. Yonas H, Good WF, Gur D, et al. Mapping cerebral blood flow by xenon-enhanced computed tomography: clinical experience. *Radiology* 1984;152(2):435-442.
85. Wintermark M, Thiran J-P, Maeder P, Schnyder P, Meuli R. Simultaneous Measurement of Regional Cerebral Blood Flow by Perfusion CT and Stable Xenon CT: A Validation Study. *American Journal of Neuroradiology* 2001;22(5):905-914.
86. Jordan BD, Elizabeth L. Xenon as an Anesthetic Agent. *AANA J* 2010;78(5):387-392.
87. Tofts PS, Brix G, Buckley DL, et al. Estimating kinetic parameters from dynamic contrast-enhanced t1-weighted MRI of a diffusable tracer: Standardized quantities and symbols. *J Magn Reson Imaging* 1999;10(3):223-232.
88. Axel L. Cerebral blood flow determination by rapid-sequence computed tomography: theoretical analysis. *Radiology* 1980;137(3):679-686.
89. St. Lawrence KS, Lee T-Y. An Adiabatic Approximation to the Tissue Homogeneity Model for Water Exchange in the Brain: I. Theoretical Derivation. *J Cereb Blood Flow Metab* 1998;18(12):1365-1377.
90. Cohnen M, Wittsack H-J, Assadi S, et al. Radiation Exposure of Patients in Comprehensive Computed Tomography of the Head in Acute Stroke. *American Journal of Neuroradiology* 2006;27(8):1741-1745.
91. Smith-Bindman R. Is Computed Tomography Safe? *N Engl J Med* 2010;363(1):1-4.
92. Aaslid R, Markwalder T-M, Nornes H. Noninvasive transcranial Doppler ultrasound recording of flow velocity in basal cerebral arteries. *J Neurosurg* 1982;57(6):769-774.
93. O'Leary DH, Bots ML. Imaging of atherosclerosis: carotid intima-media thickness. *Eur Heart J* 2010;31(14):1682-1689.
94. Crouse JR, Harpold GH, Kahl FR, Toole JF, McKinney WM. Evaluation of a scoring system for extracranial carotid atherosclerosis extent with B-mode ultrasound. *Stroke* 1986;17(2):270-275.
95. Parraga G, Fenster A, Krasinski A, Chiu B, Egger M, Spence JD. 3D Carotid Ultrasound Imaging. In: Suri JS, Kathuria C, Molinari F, editors. *Atherosclerosis Disease Management*: Springer New York; 2011. p. 325-350.

96. Coli S, Magnoni M, Sangiorgi G, et al. Contrast-Enhanced Ultrasound Imaging of Intraplaque Neovascularization in Carotid Arteries Correlation With Histology and Plaque Echogenicity. *J Am Coll Cardiol* 2008;52(3):223-230.
97. Harer C, von Kummer R. Cerebrovascular CO₂ reactivity in migraine: assessment by transcranial Doppler ultrasound. *J Neurol* 1991;238(1):23-26.
98. De Salles AAF, Manchola I. CO₂ reactivity in arteriovenous malformations of the brain: a transcranial Doppler ultrasound study. *J Neurosurg* 1994;80(4):624-630.
99. Mettler FA, Guiberteau MJ. *Essentials of Nuclear Medicine Imaging*, 6th Edition: Elsevier Saunders: 2012.
100. Ye FQ, Berman KF, Ellmore T, et al. H₂¹⁵O PET validation of steady-state arterial spin tagging cerebral blood flow measurements in humans. *Magn Reson Med* 2000;44(3):450-456.
101. Bremmer J, Berckel BM, Persoon S, et al. Day-to-Day Test-Retest Variability of CBF, CMRO₂, and OEF Measurements Using Dynamic ¹⁵O PET Studies. *Molecular Imaging and Biology* 2011;13(4):759-768.
102. Joshi F, Rosenbaum D, Bordes S, Rudd JHF. Vascular imaging with positron emission tomography. *J Intern Med* 2011;270(2):99-109.
103. Rudd JHF, Warburton EA, Fryer TD, et al. Imaging Atherosclerotic Plaque Inflammation With [¹⁸F]-Fluorodeoxyglucose Positron Emission Tomography. *Circulation* 2002;105(23):2708-2711.
104. Bremmer J, van Berckel B, Persoon S, et al. Day-to-Day Test-Retest Variability of CBF, CMRO₂, and OEF Measurements Using Dynamic ¹⁵O PET Studies. *Molecular Imaging and Biology* 2011;13(4):759-768.
105. Zaro-Weber O, Moeller-Hartmann W, Heiss W-D, Sobesky J. The Performance of MRI-Based Cerebral Blood Flow Measurements in Acute and Subacute Stroke Compared With ¹⁵O-Water Positron Emission Tomography. *Stroke* 2009;40(7):2413-2421.
106. Bloch F. Dynamic Theory of Nuclear Induction Part 2. *Physical Review* 1956;102(1):104-135.
107. Wangsness R, Bloch F. The Dynamic Theory of Nuclear Induction. *Physical Review* 1953;89(4):728-739.
108. Bloch F, Hansen W, Packard M. The Nuclear Induction Experiment. *Physical Review* 1946;70(7):474-485.
109. Bloch F. Nuclear Induction. *Physical Review* 1946;70(7):460-474.
110. Yi S, Parker DL. Performance analysis of maximum intensity projection algorithm for display of MRA images. *Medical Imaging, IEEE Transactions on* 1999;18(12):1154-1169.
111. Brown DG, Riederer SJ. Contrast-to-noise ratios in maximum intensity projection images. *Magn Reson Med* 1992;23(1):130-137.
112. Korosec FR, Frayne R, Grist TM, Mistretta CA. Time-resolved contrast-enhanced 3D MR angiography. *Magn Reson Med* 1996;36(3):345-351.
113. Sodickson D, Manning W. Simultaneous Acquisition of Spatial Harmonics (SMASH): Fast Imaging with Radiofrequency Coil Arrays. *Magn Reson Med* 1997;38:591-603.

114. Pruessmann K, Weiger M, Scheidegger M, Boesiger P. SENSE: Sensitivity Encoding for Fast MRI. *Magn Reson Med* 1999;42:952-962.
115. Griswold MA, Jakob PM, Nittka M, Goldfarb JW, Haase A. Partially parallel imaging with localized sensitivities (PILS). *Magn Reson Med* 2000;44(4):602-609.
116. Griswold MA, Jakob PM, Heidemann RM, et al. Generalized autocalibrating partially parallel acquisitions (GRAPPA). *Magn Reson Med* 2002;47(6):1202-1210.
117. Lustig M, Donoho D, Pauly JM. Sparse MRI: The application of compressed sensing for rapid MR imaging. *Magn Reson Med* 2007;58(6):1182-1195.
118. Lustig M, Pauly JM. SPIRiT: Iterative self-consistent parallel imaging reconstruction from arbitrary k-space. *Magn Reson Med* 2010;64(2):457-471.
119. Liang Z-P, Lauterbur PC. *Principles of Magnetic Resonance Imaging: IEEE Press Series in Biomedical Engineering*: 1999.
120. Haacke EM, Brown RW, Thompson MR, Venkatesan R. *Magnetic Resonance Imaging: Physical Principles and Sequence Design*: Wiley-Liss: 1999.
121. Dowsett DJ, Kenny PA, Johnston RE. *The Principles of Diagnostic Imaging*: Hodder Arnold: 1998.
122. Nishimura D. *Principles of Magnetic Resonance Imaging*: Nishimura, Printed by LuLu: 1996.
123. Eiichi F, Stephen B W R. *Experimental Pulse NMR: Nuts and Bolts Approach*: Addison-Wesley Publishing Company: 1981.
124. Malcom H L. *Spin dynamics: Basics of Nuclear Magnetic Resonance*: John Wiley and Sons: 2001.
125. Matt A B, Kevin F K, Xiaohong Joe Z. *Handbook of MRI Pulse Sequences*: Elsevier Academic Press: 2004.
126. Jerrold T B, J Anthony S, Edwin M LJ, John M B. *The Essential Physics of Medical Imaging*: Williams & Wilkins: 1994.
127. Frias JC, Williams KJ, Fisher EA, Fayad ZA. Recombinant HDL-Like Nanoparticles: A Specific Contrast Agent for MRI of Atherosclerotic Plaques. *J Am Chem Soc* 2004;126(50):16316-16317.
128. Artemov D. Molecular magnetic resonance imaging with targeted contrast agents. *J Cell Biochem* 2003;90(3):518-524.
129. Winter PM, Morawski AM, Caruthers SD, et al. Molecular Imaging of Angiogenesis in Early-Stage Atherosclerosis With $\alpha\beta 3$ -Integrin-Targeted Nanoparticles. *Circulation* 2003;108(18):2270-2274.
130. Venditto VJ, Regino CAS, Brechbiel MW. PAMAM Dendrimer Based Macromolecules as Improved Contrast Agents. *Molecular Pharmaceutics* 2005;2(4):302-311.
131. Flacke S, Fischer S, Scott MJ, et al. Novel MRI Contrast Agent for Molecular Imaging of Fibrin. *Circulation* 2001;104(11):1280-1285.
132. Noebauer-Huhmann IM, Szomolanyi P, Juras V, Kraff O, Ladd ME, Trattnig S. Gadolinium-Based Magnetic Resonance Contrast Agents at 7 Tesla: In Vitro T1 Relaxivities in Human Blood Plasma. *Invest Radiol* 2010;45(9):554-558
510.1097/RLI.1090b1013e3181ebd1094e1093.

133. Frayne R, Omary RA, Unal O, Strother CM. Determination of Optimal Injection Parameters for Intraarterial Gadolinium-enhanced MR Angiography. *J Vasc Interv Radiol* 2000;11(10):1277-1284.
134. Kuperman VY, Alley MT. Differentiation between the effects of T1 and T2* shortening in contrast-enhanced MRI of the breast. *J Magn Reson Imaging* 1999;9(2):172-176.
135. Parker DL, Goodrich KC, Alexander AL, Buswell HR, Blatter DD, Tsuruda JS. Optimized visualization of vessels in contrast enhanced intracranial MR angiography. *Magn Reson Med* 1998;40(6):873-882.
136. Caravan P, Farrar CT, Frullano L, Uppal R. Influence of molecular parameters and increasing magnetic field strength on relaxivity of gadolinium- and manganese-based T1 contrast agents. *Contrast Media & Molecular Imaging* 2009;4(2):89-100.
137. Jung J-W, Kang H-R, Kim M-H, et al. Immediate Hypersensitivity Reaction to Gadolinium-based MR Contrast Media. *Radiology* 2012;264(2):414-422.
138. Rydahl C, Thomsen HS, Marckmann P. High Prevalence of Nephrogenic Systemic Fibrosis in Chronic Renal Failure Patients Exposed to Gadodiamide, a Gadolinium-Containing Magnetic Resonance Contrast Agent. *Invest Radiol* 2008;43(2):141-144 110.1097/RLI.1090b1013e31815a33407.
139. Kuo PH, Kanal E, Abu-Alfa AK, Cowper SE. Gadolinium-based MR Contrast Agents and Nephrogenic Systemic Fibrosis. *Radiology* 2007;242(3):647-649.
140. Prince MR, Zhang H, Newhouse JH. Science to Practice: A New Insight into Nephrotoxicity after Contrast Medium Administration. *Radiology* 2012;265(3):651-653.
141. Perez-Rodriguez J, Lai S, Ehst BD, Fine DM, Bluemke DA. Nephrogenic Systemic Fibrosis: Incidence, Associations, and Effect of Risk Factor Assessment—Report of 33 Cases. *Radiology* 2009;250(2):371-377.
142. Weinreb JC. Impact on Hospital Policy: Yale Experience. *Journal of the American College of Radiology* 2008;5(1):53-56.
143. Pavone P, Patrizio G, Buoni C, et al. Comparison of Gd-BOPTA with Gd-DTPA in MR imaging of rat liver. *Radiology* 1990;176(1):61-64.
144. Vittadini G, Felder E, Musu C, Tirone P. Preclinical Profile of Gd-BOPTA A Liver-Specific MRI Contrast Agent. *Invest Radiol* 1990;25:S59-S60.
145. Spinazzi A, Lorusso V, Pirovano G, Kirchin M. Safety, tolerance, biodistribution, and MR imaging enhancement of the liver with gadobenate dimeglumine: Results of clinical pharmacologic and pilot imaging studies in nonpatient and patient volunteers. *Acad Radiol* 1999;6(5):282-291.
146. Kirchin MA, Pirovano GP, Spinazzi A. Gadobenate Dimeglumine (Gd-BOPTA): An Overview. *Invest Radiol* 1998;33(11):798-809.
147. Staks T, Schuhmann-Giampieri G, Frenzel T, Weinmann HJ, Lange L, Platzek J. Pharmacokinetics, Dose Proportionality, and Tolerability of Gadobutrol after Single Intravenous Injection in Healthy Volunteers. *Invest Radiol* 1994;29(7):709-715.

148. Vogler H, Platzek J, Schuhmann-Giampieri G, et al. Pre-clinical evaluation of gadobutrol: a new, neutral, extracellular contrast agent for magnetic resonance imaging. *Eur J Radiol* 1995;21(1):1-10.
149. Mühler A. Assessment of myocardial perfusion using contrast-enhanced MR imaging: Current status and future developments. *Magnetic Resonance Materials in Physics, Biology and Medicine* 1995;3(1):21-33.
150. Wagoner MV, Worah D. Gadodiamide Injection: First Human Experience with the Nonionic Magnetic Resonance Imaging Enhancement Agent. *Invest Radiol* 1993;28:S44-S48.
151. Harpur ES, Worah D, Hals PA, Holtz E, Furuham K, Nomura H. Preclinical Safety Assessment and Pharmacokinetics of Gadodiamide Injection, a New Magnetic Resonance Imaging Contrast Agent. *Invest Radiol* 1993;28:S28-S43.
152. Joffe P, Thomsen HS, Meusel M. Pharmacokinetics of gadodiamide injection in patients with severe renal insufficiency and patients undergoing hemodialysis or continuous ambulatory peritoneal dialysis. *Acad Radiol* 1998;5(7):491-502.
153. Parmelee DJ, Walovitch RC, Ouellet HS, Lauffer RB. Preclinical Evaluation of the Pharmacokinetics, Biodistribution, and Elimination of MS-325, a Blood Pool Agent for Magnetic Resonance Imaging. *Invest Radiol* 1997;32(12):741-747.
154. Caravan P, Cloutier NJ, Greenfield MT, et al. The Interaction of MS-325 with Human Serum Albumin and Its Effect on Proton Relaxation Rates. *J Am Chem Soc* 2002;124(12):3152-3162.
155. Lauffer RB, Parmelee DJ, Dunham SU, et al. MS-325: albumin-targeted contrast agent for MR angiography. *Radiology* 1998;207(2):529-538.
156. Grist TM, Korosec FR, Peters DC, et al. Steady-state and dynamic MR angiography with MS-325: initial experience in humans. *Radiology* 1998;207(2):539-544.
157. Claussen C, Laniado M, Schörner W, et al. Gadolinium-DTPA in MR imaging of glioblastomas and intracranial metastases. *American Journal of Neuroradiology* 1985;6(5):669-674.
158. Magerstädt M, Gansow OA, Brechbiel MW, et al. Gd(DOTA): An alternative to Gd(DTPA) as a T1,2 relaxation agent for NMR imaging or spectroscopy. *Magn Reson Med* 1986;3(5):808-812.
159. Oudkerk M, Sijens PE, Van Beek EJR, Kuijpers TJA. Safety and Efficacy of Dotarem (Gd-DOTA) versus Magnevist (Gd-DTPA) in Magnetic Resonance Imaging of the Central Nervous System. *Invest Radiol* 1995;30(2):75-78.
160. Weinmann H, Brasch R, Press W, Wesbey G. Characteristics of gadolinium-DTPA complex: a potential NMR contrast agent. *Am J Roentgenol* 1984;142(3):619-624.
161. Carr D, Brown J, Bydder G, et al. Gadolinium-DTPA as a contrast agent in MRI: initial clinical experience in 20 patients. *Am J Roentgenol* 1984;143(2):215-224.
162. Brugiores P, Gaston A, Degryse HR, et al. Randomised double blind trial of the safety and efficacy of two gadolinium complexes (Gd-DTPA and Gd-DOTA). *Neuroradiology* 1994;36(1):27-30.

163. Herborn CU, Honold E, Wolf M, et al. Clinical Safety and Diagnostic Value of the Gadolinium Chelate Gadoterate Meglumine (Gd-DOTA). *Invest Radiol* 2007;42(1):58-62.
164. Bousquet JC, Saini S, Stark DD, et al. Gd-DOTA: characterization of a new paramagnetic complex. *Radiology* 1988;166(3):693-698.
165. Runge VM, Kaufman DM, Wood ML, Adelman LS, Jacobson S. Experimental trials with Gd(DO3A)-a nonionic magnetic resonance contrast agent. *International Journal of Radiation Applications and Instrumentation Part B Nuclear Medicine and Biology* 1989;16(6):561-567.
166. Runge VM, Gelblum DY, Pacetti ML, Carolan F, Heard G. Gd-HP-DO3A in clinical MR imaging of the brain. *Radiology* 1990;177(2):393-400.
167. Desimone D, Morris M, Rhoda C, et al. Evaluation of the Safety and Efficacy of Gadoteridol Injection (a low osmolal magnetic resonance contrast agent): Clinical Trials Report. *Invest Radiol* 1991;26:S212-S216.
168. Runge VM, Dean B, Lee C, Carolan F, Heard G. Phase III clinical evaluation of Gd-HP-DO3A in head and spine disease. *J Magn Reson Imaging* 1991;1(1):47-56.
169. Rubin DL, Desser TS, Semelka R, et al. A multicenter, randomized, double-blind study to evaluate the safety, tolerability, and efficacy of OptiMARK (gadoversetamide injection) compared with Magnevist (gadopentetate dimeglumine) in patients with liver pathology: Results of a phase III clinical trial. *J Magn Reson Imaging* 1999;9(2):240-250.
170. Swan SK, Baker JF, Free R, et al. Pharmacokinetics, safety, and tolerability of gadoversetamide injection (OptiMARK) in subjects with central nervous system or liver pathology and varying degrees of renal function. *J Magn Reson Imaging* 1999;9(2):317-321.
171. Grossman RI, Rubin DL, Hunter G, et al. Magnetic Resonance Imaging in Patients with Central Nervous System Pathology: A Comparison of OptiMARK (Gd-DTPA-BMEA) and Magnevist (Gd-DTPA). *Invest Radiol* 2000;35(7):412-419.
172. Schuhmann-Giampieri G, Mahler M, Roll G, Maibauer R, Schmitz S. Pharmacokinetics of the liver-specific contrast agent Gd-EOB-DTPA in relation to contrast-enhanced liver imaging in humans. *The Journal of Clinical Pharmacology* 1997;37(7):587-596.
173. Weinmann HJ, Schuhmann-Giampieri G, Schmitt-Willich H, Vogler H, Frenzel T, Gries H. A new lipophilic gadolinium chelate as a tissue-specific contrast medium for MRI. *Magn Reson Med* 1991;22(2):233-237.
174. Laub G. Time-of-Flight Method of MRA. *Encyclopedia of Magnetic Resonance*: John Wiley & Sons, Ltd; 2007.
175. Bosmans H, Marchal G, Lukito G, et al. Time-of-flight MR angiography of the brain: comparison of acquisition techniques in healthy volunteers. *Am J Roentgenol* 1995;164(1):161-167.
176. Yang JJ, Hill MD, Morrish WF, et al. Comparison of Pre- and Postcontrast 3D Time-of-Flight MR Angiography for the Evaluation of Distal Intracranial Branch

- Occlusions in Acute Ischemic Stroke. *American Journal of Neuroradiology* 2002;23(4):557-567.
177. Al-Kwif O, Emery DJ, Wilman AH. Vessel contrast at three Tesla in time-of-flight magnetic resonance angiography of the intracranial and carotid arteries. *Magn Reson Imaging* 2002;20(2):181-187.
 178. Rofsky NM, Purdy DE, Johnson G, et al. Suppression of venous signal in time-of-flight MR angiography of the lower extremities after administration of gadopentetate dimeglumine. *Radiology* 1997;202(1):177-182.
 179. Nishimura DG. Time-of-flight MR angiography. *Magn Reson Med* 1990;14(2):194-201.
 180. Wehrli FW. Time-of-flight effects in MR imaging of flow. *Magn Reson Med* 1990;14(2):187-193.
 181. A E, AH W. Ramped RF Excitation in 3DTOF MR Angiography at High Magnetic Field. *Proceedings of International Society of Magnetic Resonance in Medicine*. Kyoto, Japan; 2004. p. 369.
 182. Heverhagen JT, Bourekas E, Sammet S, Knopp MV, Schmalbrock P. Time-of-Flight Magnetic Resonance Angiography at 7 Tesla. *Invest Radiol* 2008;43(8):568-573.
 183. Kang C-K, Park C-W, Han J-Y, et al. Imaging and analysis of lenticulostriate arteries using 7.0-Tesla magnetic resonance angiography. *Magn Reson Med* 2009;61(1):136-144.
 184. Martin-Vaquero P, da Costa RC, Echandi RL, Tosti CL, Knopp MV, Sammet S. Time-of-flight magnetic resonance angiography of the canine brain at 3.0 Tesla and 7.0 Tesla. *Am J Vet Res* 2011;72(3):350-356.
 185. Kim S-E, Parker DL. Time-of-Flight Angiography Magnetic Resonance Angiography. In: Carr JC, Carroll TJ, editors: Springer New York; 2012. p. 39-50.
 186. von Morze C, Xu D, Purcell DD, et al. Intracranial time-of-flight MR angiography at 7T with comparison to 3T. *J Magn Reson Imaging* 2007;26(4):900-904.
 187. Steinman DA, Rutt BK. On the nature and reduction of plaque-mimicking flow artifacts in black blood MRI of the carotid bifurcation. *Magn Reson Med* 1998;39(4):635-641.
 188. Fayad ZA, Fuster V, Fallon JT, et al. Noninvasive In Vivo Human Coronary Artery Lumen and Wall Imaging Using Black-Blood Magnetic Resonance Imaging. *Circulation* 2000;102(5):506-510.
 189. Balu N, Chu B, Hatsukami TS, Yuan C, Yarnykh VL. Comparison between 2D and 3D high-resolution black-blood techniques for carotid artery wall imaging in clinically significant atherosclerosis. *J Magn Reson Imaging* 2008;27(4):918-924.
 190. Antiga L, Wasserman BA, Steinman DA. On the overestimation of early wall thickening at the carotid bulb by black blood MRI, with implications for coronary and vulnerable plaque imaging. *Magn Reson Med* 2008;60(5):1020-1028.
 191. Balu N, Yarnykh VL, Chu B, Wang J, Hatsukami T, Yuan C. Carotid plaque assessment using fast 3D isotropic resolution black-blood MRI. *Magn Reson Med* 2011;65(3):627-637.

192. Qiao Y, Steinman DA, Qin Q, et al. Intracranial arterial wall imaging using three-dimensional high isotropic resolution black blood MRI at 3.0 Tesla. *J Magn Reson Imaging* 2011;34(1):22-30.
193. Harloff A, Zech T, Frydrychowicz A, et al. Carotid intima-media thickness and distensibility measured by MRI at 3 T versus high-resolution ultrasound. *Eur Radiol* 2009;19(6):1470-1479.
194. Crowe LA, Gatehouse P, Yang GZ, et al. Volume-selective 3D turbo spin echo imaging for vascular wall imaging and distensibility measurement. *J Magn Reson Imaging* 2003;17(5):572-580.
195. Lotz J, Meier C, Leppert A, Galanski M. Cardiovascular Flow Measurement with Phase-Contrast MR Imaging: Basic Facts and Implementation. *Radiographics* 2002;22(3):651-671.
196. Frayne R, Steinman DA, Rutt BK, Ethier CR. Accuracy of MR phase contrast velocity measurements for unsteady flow. *J Magn Reson Imaging* 1995;5(4):428-431.
197. Pelc NJ, Bernstein MA, Shimakawa A, Glover GH. Encoding strategies for three-direction phase-contrast MR imaging of flow. *J Magn Reson Imaging* 1991;1(4):405-413.
198. Markl M, Bammer R, Alley MT, et al. Generalized reconstruction of phase contrast MRI: Analysis and correction of the effect of gradient field distortions. *Magn Reson Med* 2003;50(4):791-801.
199. Polzin JA, Frayne R, Grist TM, Mistretta CA. Frequency response of multi-phase segmented k-space phase-contrast. *Magn Reson Med* 1996;35(5):755-762.
200. Frayne R, Rutt BK. Frequency response of retrospectively gated phase-contrast MR imaging: Effect of interpolation. *J Magn Reson Imaging* 1993;3(6):907-917.
201. Middione MJ, Ennis DB. Chemical shift-induced phase errors in phase-contrast MRI. *Magn Reson Med* 2012;69(2):391-401.
202. MacDonald ME, Dolati P, Wong J, Leung T, Nielsen J, Frayne R. Sensitivity of Phase Contrast Derived Velocity and Stress Fields to Receiver Bandwidth at the Circle of Willis. *International Magnetic Resonance Angiography Club*. Utrecht, NL; 2012.
203. Steinman DA, Thomas JB, Ladak HM, Milner JS, Rutt BK, Spence JD. Reconstruction of carotid bifurcation hemodynamics and wall thickness using computational fluid dynamics and MRI. *Magn Reson Med* 2002;47(1):149-159.
204. Moftakhar R, Aagaard-Kienitz B, Johnson K, et al. Noninvasive Measurement of Intra-Aneurysmal Pressure and Flow Pattern Using Phase Contrast with Vastly Undersampled Isotropic Projection Imaging. *American Journal of Neuroradiology* 2007;28(9):1710-1714.
205. Tang C, Blatter DD, Parker DL. Accuracy of phase-contrast flow measurements in the presence of partial-volume effects. *J Magn Reson Imaging* 1993;3(2):377-385.
206. Gibson CM, Diaz L, Kandarpa K, et al. Relation of vessel wall shear stress to atherosclerosis progression in human coronary arteries. *Arterioscler Thromb Vac Biol* 1993;13(2):310-315.

207. Malek Am ASLIS. HEodynamic shear stress and its role in atherosclerosis. *JAMA* 1999;282(21):2035-2042.
208. Frayne R, Rutt BK. Measurement of fluid-shear rate by fourier-encoded velocity imaging. *Magn Reson Med* 1995;34(3):378-387.
209. Bousset L, Rayz V, Martin A, et al. Phase-contrast magnetic resonance imaging measurements in intracranial aneurysms in vivo of flow patterns, velocity fields, and wall shear stress: Comparison with computational fluid dynamics. *Magn Reson Med* 2009;61(2):409-417.
210. Cebal J, Putman C, Alley M, Hope T, Bammer R, Calamante F. Hemodynamics in normal cerebral arteries: qualitative comparison of 4D phase-contrast magnetic resonance and image-based computational fluid dynamics. *Journal of Engineering Mathematics* 2009;64(4):367-378.
211. Frydrychowicz A, François CJ, Turski PA. Four-dimensional phase contrast magnetic resonance angiography: Potential clinical applications. *Eur J Radiol* 2011;80(1):24-35.
212. Markl M, Wallis W, Harloff A. Reproducibility of flow and wall shear stress analysis using flow-sensitive four-dimensional MRI. *J Magn Reson Imaging* 2011;33(4):988-994.
213. Steinman DA, Ethier CR, Rutt BK. Combined analysis of spatial and velocity displacement artifacts in phase contrast measurements of complex flows. *J Magn Reson Imaging* 1997;7(2):339-346.
214. Ebbers T, Wigström L, Bolger AF, Engvall J, Karlsson M. Estimation of relative cardiovascular pressures using time-resolved three-dimensional phase contrast MRI. *Magn Reson Med* 2001;45(5):872-879.
215. Lum DP, Johnson KM, Paul RK, et al. Transstenotic Pressure Gradients: Measurement in Swine-Retrospectively ECG-gated 3D Phase-Contrast MR Angiography versus Endovascular Pressure-sensing Guidewires. *Radiology* 2007;245(3):751-760.
216. Tyszka JM, Laidlaw DH, Asa JW, Silverman JM. Three-dimensional, time-resolved (4D) relative pressure mapping using magnetic resonance imaging. *J Magn Reson Imaging* 2000;12(2):321-329.
217. Thompson RB, McVeigh ER. Fast measurement of intracardiac pressure differences with 2D breath-hold phase-contrast MRI. *Magn Reson Med* 2003;49(6):1056-1066.
218. Navier C. Memoire sur les Lois du Mouvement des Fluides. *French Academy of Sciences* 1827;6(2):389.
219. Stokes GH. On the Theories of the Internal Friction of Fluids in Motion. *Transactions of the Cambridge Philosophical Society* 1845;8:287.
220. Dempere-Marco L, Oubel E, Castro M, Putman C, Frangi A, Cebal J. CFD Analysis Incorporating the Influence of Wall Motion: Application to Intracranial Aneurysms. In: Larsen R, Nielsen M, Sporning J, editors. *Medical Image Computing and Computer-Assisted Intervention*. Volume 4191, *Lecture Notes in Computer Science*: Springer Berlin Heidelberg; 2006. p. 438-445.
221. Mistretta CA. Sub-Nyquist acquisition and constrained reconstruction in time resolved angiography. *Med Phys* 2011;38(6):2975-2985.

222. Swan JS, Carroll TJ, Kennell TW, et al. Time-resolved Three-dimensional Contrast-enhanced MR Angiography of the Peripheral Vessels. *Radiology* 2002;225(1):43-52.
223. Fink C, Ley S, Kroeker R, Requardt M, Kauczor H-U, Bock M. Time-Resolved Contrast-Enhanced Three-Dimensional Magnetic Resonance Angiography of the Chest: Combination of Parallel Imaging With View Sharing (TREAT). *Invest Radiol* 2005;40(1):40-48.
224. Van Vaals JJ, Brummer ME, Thomas Dixon W, et al. "Keyhole" method for accelerating imaging of contrast agent uptake. *J Magn Reson Imaging* 1993;3(4):671-675.
225. Otazo R, Kim D, Axel L, Sodickson DK. Combination of compressed sensing and parallel imaging for highly accelerated first-pass cardiac perfusion MRI. *Magn Reson Med* 2010;64(3):767-776.
226. Velikina JV, Johnson KM, Wu Y, Samsonov AA, Turski P, Mistretta CA. PC HYPR flow: A technique for rapid imaging of contrast dynamics. *J Magn Reson Imaging* 2010;31(2):447-456.
227. Wang K, Busse RF, Holmes JH, et al. Interleaved variable density sampling with a constrained parallel imaging reconstruction for dynamic contrast-enhanced MR angiography. *Magn Reson Med* 2011;66(2):428-436.
228. Haider CR, Borisch EA, Glockner JF, et al. Max CAPR: High-resolution 3D contrast-enhanced MR angiography with acquisition times under 5 seconds. *Magn Reson Med* 2010;64(4):1171-1181.
229. Nikolaou K, Kramer H, Grosse C, et al. High-Spatial-Resolution Multistation MR Angiography with Parallel Imaging and Blood Pool Contrast Agent: Initial Experience. *Radiology* 2006;241(3):861-872.
230. Lebel RM, Jones J, Ferre J-C, Law M, Nayak KS. Highly accelerated dynamic contrast enhanced imaging. *Magn Reson Med* 2014;71(2):635-644.
231. Harris AD, Kosior JC, Ryder RC, et al. MRI of ischemic stroke in canines: Applications for monitoring intraarterial thrombolysis. *J Magn Reson Imaging* 2007;26(6):1421-1428.
232. Quick HH, Kuehl H, Kaiser G, et al. Interventional MRA using actively visualized catheters, TrueFISP, and real-time image fusion. *Magn Reson Med* 2003;49(1):129-137.
233. Quick H, Zenge M, Kuehl H, et al. Interventional Magnetic Resonance Angiography with No Strings Attached: Wireless Active Catheter Visualization. *Magn Reson Med* 2005;53:446-455.
234. Paetzel C, Zorger N, Bachthaler M, et al. Magnetic Resonance-Guided Percutaneous Angioplasty of Femoral and Popliteal Artery Stenoses Using Real-Time Imaging and Intra-arterial Contrast-Enhanced Magnetic Resonance Angiography. *Invest Radiol* 2005;40(5):257-262.
235. Bos C, Smits HFM, Bakker CJG, Viergever MA. Selective contrast-enhanced MR angiography. *Magn Reson Med* 2000;44(4):575-582.
236. Williams DS, Detre JA, Leigh JS, Koretsky AP. Magnetic resonance imaging of perfusion using spin inversion of arterial water. *Proc Natl Acad Sci U S A* 1992;89(1):212-216.

237. Detre JA, Leigh JS, Williams DS, Koretsky AP. Perfusion imaging. *Magn Reson Med* 1992;23(1):37-45.
238. Robson PM, Dai W, Shankaranarayanan A, Rofsky NM, Alsop DC. Time-resolved Vessel-selective Digital Subtraction MR Angiography of the Cerebral Vasculature with Arterial Spin Labeling. *Radiology* 2010;257(2):507-515.
239. Okell TW, Chappell MA, Woolrich MW, Günther M, Feinberg DA, Jezzard P. Vessel-encoded dynamic magnetic resonance angiography using arterial spin labeling. *Magn Reson Med* 2010;64(2):430-438.
240. MacDonald ME, Menon B, Dolati P, Goyal M, Frayne R. Arterial Spin Labelling Applications of Ischemic Stroke. Canadian Stroke Congress, Published in Stroke. Calgary, AB, Canada; 2012. p. 128.
241. Wang J, Alsop DC, Li L, et al. Comparison of quantitative perfusion imaging using arterial spin labeling at 1.5 and 4.0 Tesla. *Magn Reson Med* 2002;48(2):242-254.
242. Gardener AG, Gowland PA, Francis ST. Implementation of quantitative perfusion imaging using pulsed arterial spin labeling at ultra-high field. *Magn Reson Med* 2009;61(4):874-882.
243. Nöth U, Meadows GE, Kotajima F, Deichmann R, Corfield DR, Turner R. Cerebral vascular response to hypercapnia: Determination with perfusion MRI at 1.5 and 3.0 Tesla using a pulsed arterial spin labeling technique. *J Magn Reson Imaging* 2006;24(6):1229-1235.
244. Wu H, Block WF, Turski PA, Mistretta CA, Johnson KM. Noncontrast-enhanced three-dimensional (3D) intracranial MR angiography using pseudocontinuous arterial spin labeling and accelerated 3D radial acquisition. *Magn Reson Med* 2013;69(3):708-715.
245. Shin DD, Liu TT, Wong EC, Shankaranarayanan A, Jung Y. Pseudocontinuous arterial spin labeling with optimized tagging efficiency. *Magn Reson Med* 2012;68(4):1135-1144.
246. Fan AP, Benner T, Bolar DS, Rosen BR, Adalsteinsson E. Phase-based regional oxygen metabolism (PROM) using MRI. *Magn Reson Med* 2012;67(3):669-678.
247. Tan H, Hoge WS, Hamilton CA, Günther M, Kraft RA. 3D GRASE PROPELLER: Improved image acquisition technique for arterial spin labeling perfusion imaging. *Magn Reson Med* 2011;66(1):168-173.
248. Ouyang C, Sutton BP. Pseudo-continuous transfer insensitive labeling technique. *Magn Reson Med* 2011:768-776.
249. Wells JA, Thomas DL, King MD, Connelly A, Lythgoe MF, Calamante F. Reduction of errors in ASL cerebral perfusion and arterial transit time maps using image de-noising. *Magn Reson Med* 2010;64(3):715-724.
250. Dai W, Robson PM, Shankaranarayanan A, Alsop DC. Modified pulsed continuous arterial spin labeling for labeling of a single artery. *Magn Reson Med* 2010;64(4):975-982.
251. Wong EC. Vessel-encoded arterial spin-labeling using pseudocontinuous tagging. *Magn Reson Med* 2007;58(6):1086-1091.
252. Wong EC, Cronin M, Wu W-C, Inglis B, Frank LR, Liu TT. Velocity-selective arterial spin labeling. *Magn Reson Med* 2006;55(6):1334-1341.

253. Wang Z, Wang J, Connick TJ, Wetmore GS, Detre JA. Continuous ASL (CASL) perfusion MRI with an array coil and parallel imaging at 3T. *Magn Reson Med* 2005;54(3):732-737.
254. Alsop DC, Detre JA, Golay X, et al. Recommended implementation of arterial spin-labeled perfusion MRI for clinical applications: A consensus of the ISMRM perfusion study group and the European consortium for ASL in dementia. *Magn Reson Med* 2013.
255. Chappell MA, Okell TW, Jezzard P, Woolrich MW. A general framework for the analysis of vessel encoded arterial spin labeling for vascular territory mapping. *Magn Reson Med* 2010;64(5):1529-1539.
256. Perthen JE, Bydder M, Restom K, Liu TT. SNR and functional sensitivity of BOLD and perfusion-based fMRI using arterial spin labeling with spiral SENSE at 3 T. *Magn Reson Imaging* 2008;26(4):513-522.
257. St. Lawrence KS, Frank JA, Bandettini PA, Ye FQ. Noise reduction in multi-slice arterial spin tagging imaging. *Magn Reson Med* 2005;53(3):735-738.
258. Buxton RB, Frank LR, Wong EC, Siewert B, Warach S, Edelman RR. A general kinetic model for quantitative perfusion imaging with arterial spin labeling. *Magn Reson Med* 1998;40(3):383-396.
259. Wong EC, Buxton RB, Frank LR. A theoretical and experimental comparison of continuous and pulsed arterial spin labeling techniques for quantitative perfusion imaging. *Magn Reson Med* 1998;40(3):348-355.
260. Zhang W, Silva AC, Williams DS, Koretsky AP. NMR Measurement of Perfusion Using Arterial Spin Labeling Without Saturation of Macromolecular Spins. *Magn Reson Med* 1995;33(3):370-376.
261. Wu W-C, St Lawrence KS, Licht DJ, Wang DJJ. Quantification Issues in Arterial Spin Labeling Perfusion Magnetic Resonance Imaging. *Top Magn Reson Imaging* 2010;21(2):65-73 10.1097/RMR.1090b1013e31821e31570a.
262. Kansagra AP, Wong EC. Improved estimation of cerebral artery branch territories using cluster-based segmentation of vessel-encoded pseudocontinuous ASL data. 20th International Society of Magnetic Resonance in Medicine Scientific Meeting. Melbourne, Australia; 2012. p. 581.
263. Okell TW, Chappell MA, Jezzard P. A theoretical framework for quantifying blood volume flow rate from dynamic angiographic data and application to vessel-encoded arterial spin labeling MRI. *Med Image Anal* 2013;17(8):1025-1036.
264. Chng SM, Petersen ET, Zimine I, Sitoh Y-Y, Lim CCT, Golay X. Territorial Arterial Spin Labeling in the Assessment of Collateral Circulation. *Stroke* 2008;39(12):3248-3254.
265. Helle M, Norris DG, Rüfer S, Alfke K, Jansen O, van Osch MJP. Superselective pseudocontinuous arterial spin labeling. *Magn Reson Med* 2010;64(3):777-786.
266. Wen-Chau W, Edlow BL, Elliot MA, Jiongjiong W, Detre JA. Physiological Modulations in Arterial Spin Labeling Perfusion Magnetic Resonance Imaging. *Medical Imaging, IEEE Transactions on* 2009;28(5):703-709.

267. Chalela JA, Alsop DC, Gonzalez-Atavales JB, Maldjian JA, Kasner SE, Detre JA. Magnetic Resonance Perfusion Imaging in Acute Ischemic Stroke Using Continuous Arterial Spin Labeling. *Stroke* 2000;31(3):680-687.
268. Wang DJJ, Alger JR, Qiao JX, et al. The Value of Arterial Spin-Labeled Perfusion Imaging in Acute Ischemic Stroke. *Stroke* 2012.
269. Johnson NA, Jahng G-H, Weiner MW, et al. Pattern of Cerebral Hypoperfusion in Alzheimer Disease and Mild Cognitive Impairment Measured with Arterial Spin-labeling MR Imaging: Initial Experience. *Radiology* 2005;234(3):851-859.
270. Du AT, Jahng GH, Hayasaka S, et al. Hypoperfusion in frontotemporal dementia and Alzheimer disease by arterial spin labeling MRI. *Neurology* 2006;67(7):1215-1220.
271. Biagi L, Abbruzzese A, Bianchi MC, Alsop DC, Del Guerra A, Tosetti M. Age dependence of cerebral perfusion assessed by magnetic resonance continuous arterial spin labeling. *J Magn Reson Imaging* 2007;25(4):696-702.
272. Okell TW, Chappell MA, Jezzard P. Visualizing Artery-specific Blood Flow Patterns Above the Circle of Willis with Vessel-Encoded Arterial Spin Labeling. 20th International Society of Magnetic Resonance in Medicine Scientific Meeting. Melbourne, Australia; 2012. p. 581.
273. Matthias CS, Dennis LP. Uncertainty and bias in contrast concentration measurements using spoiled gradient echo pulse sequences. *Phys Med Biol* 2008;53(9):2345.
274. Gauderon P. Whole-brain Perfusion Imaging using Dynamic Contrast-Enhanced Magnetic Resonance. Department of Biomedical Engineering. Volume MSc: University of Calgary; 2011.
275. Tofts PS. Modeling tracer kinetics in dynamic Gd-DTPA MR imaging. *J Magn Reson Imaging* 1997;7(1):91-101.
276. Ewing JR, Brown SL, Lu M, et al. Model selection in magnetic resonance imaging measurements of vascular permeability: Gadomer in a 9L model of rat cerebral tumor. *J Cereb Blood Flow Metab* 2005;26(3):310-320.
277. Benjaminsen IC, Brurberg KG, Ruud E-BM, Rofstad EK. Assessment of extravascular extracellular space fraction in human melanoma xenografts by DCE-MRI and kinetic modeling. *Magn Reson Imaging* 2008;26(2):160-170.
278. Sourbron SP, Buckley DL. On the scope and interpretation of the Tofts models for DCE-MRI. *Magn Reson Med* 2011;66(3):735-745.
279. Li K-L, Buonaccorsi G, Thompson G, et al. An improved coverage and spatial resolution—using dual injection dynamic contrast-enhanced (ICE-DICE) MRI: A novel dynamic contrast-enhanced technique for cerebral tumors. *Magn Reson Med* 2012;68(2):452-462.
280. Duhamel G, Schlaug G, Alsop DC. Measurement of arterial input functions for dynamic susceptibility contrast magnetic resonance imaging using echoplanar images: Comparison of physical simulations with in vivo results. *Magn Reson Med* 2006;55(3):514-523.
281. Mouridsen K, Christensen S, Gyldensted L, Østergaard L. Automatic selection of arterial input function using cluster analysis. *Magn Reson Med* 2006;55(3):524-531.

282. Sourbron S, Luypaert R, Van Schuerbeek P, Dujardin M, Stadnik T, Osteaux M. Deconvolution of dynamic contrast-enhanced MRI data by linear inversion: Choice of the regularization parameter. *Magn Reson Med* 2004;52(1):209-213.
283. Sourbron S, Dujardin M, Makkat S, Luypaert R. Pixel-by-pixel deconvolution of bolus-tracking data: optimization and implementation. *Phys Med Biol* 2007;52(2):429.
284. Salluzzi M, Frayne R, Smith MR. An alternative viewpoint of the similarities and differences of SVD and FT deconvolution algorithms used for quantitative MR perfusion studies. *Magn Reson Imaging* 2005;23(3):481-492.
285. Smith MR, Lu H, Trochet S, Frayne R. Removing the effect of SVD algorithmic artifacts present in quantitative MR perfusion studies. *Magn Reson Med* 2004;51(3):631-634.
286. Wu O, Østergaard L, Weisskoff RM, Benner T, Rosen BR, Sorensen AG. Tracer arrival timing-insensitive technique for estimating flow in MR perfusion-weighted imaging using singular value decomposition with a block-circulant deconvolution matrix. *Magn Reson Med* 2003;50(1):164-174.
287. Chen JJ, Smith MR, Frayne R. The impact of partial-volume effects in dynamic susceptibility contrast magnetic resonance perfusion imaging. *J Magn Reson Imaging* 2005;22(3):390-399.
288. Zaharchuk G, Bammer R, Straka M, et al. Improving dynamic susceptibility contrast MRI measurement of quantitative cerebral blood flow using corrections for partial volume and nonlinear contrast relaxivity: A xenon computed tomographic comparative study. *J Magn Reson Imaging* 2009;30(4):743-752.
289. van Osch MJP, Vonken E-jPA, Bakker CJG, Viergever MA. Correcting partial volume artifacts of the arterial input function in quantitative cerebral perfusion MRI. *Magn Reson Med* 2001;45(3):477-485.
290. Jezzard P, Balaban RS. Correction for geometric distortion in echo planar images from B0 field variations. *Magn Reson Med* 1995;34(1):65-73.
291. Newbould RD, Skare ST, Jochimsen TH, et al. Perfusion mapping with multiecho multishot parallel imaging EPI. *Magn Reson Med* 2007;58(1):70-81.
292. Gauderon P, Salluzzi M, Lauzon ML, Smith MR, Frayne R. High SNR DCE Imaging for Whole-Brain Perfusion Assessment. 20th International Society of Magnetic Resonance in Medicine Scientific Meeting. Melbourne, Australia; 2012. p. 581.
293. Duyn JH, van Gelderen P, Talagala L, Koretsky A, de Zwart JA. Technological advances in MRI measurement of brain perfusion. *J Magn Reson Imaging* 2005;22(6):751-753.
294. Takasawa M, Jones PS, Guadagno JV, et al. How Reliable Is Perfusion MR in Acute Stroke? *Stroke* 2008;39(3):870-877.
295. Lüdemann L, Warmuth C, Plotkin M, et al. Brain tumor perfusion: Comparison of dynamic contrast enhanced magnetic resonance imaging using T1, T2, and contrast, pulsed arterial spin labeling, and H215O positron emission tomography. *Eur J Radiol* 2009;70(3):465-474.

296. Quarles CC, Gore JC, Xu L, Yankeelov TE. Comparison of dual-echo DSC-MRI- and DCE-MRI-derived contrast agent kinetic parameters. *Magn Reson Imaging* 2012;30(7):944-953.
297. Schenck JF. The role of magnetic susceptibility in magnetic resonance imaging: MRI magnetic compatibility of the first and second kinds. *Med Phys* 1996;23:815-850.
298. Farahani K, Sinha U, Sinha S, Chiu LCL, Lufkin RB. Effect of field strength on susceptibility artifacts in magnetic resonance imaging. *Comput Med Imaging Graph* 1990;14(6):409-413.
299. Haacke EM, Xu Y, Cheng Y-CN, Reichenbach JR. Susceptibility weighted imaging (SWI). *Magn Reson Med* 2004;52(3):612-618.
300. Liu T, Surapaneni K, Lou M, Cheng L, Spincemaille P, Wang Y. Cerebral Microbleeds: Burden Assessment by Using Quantitative Susceptibility Mapping. *Radiology* 2012;262(1):269-278.
301. Liu J, Liu T, de Rochefort L, et al. Morphology enabled dipole inversion for quantitative susceptibility mapping using structural consistency between the magnitude image and the susceptibility map. *Neuroimage* 2012;59(3):2560-2568.
302. Greenberg SM, Vernooij MW, Cordonnier C, et al. Cerebral microbleeds: a guide to detection and interpretation. *The Lancet Neurology* 2009;8(2):165-174.
303. Wycliffe ND, Choe J, Holshouser B, Oyoyo UE, Haacke EM, Kido DK. Reliability in detection of hemorrhage in acute stroke by a new three-dimensional gradient recalled echo susceptibility-weighted imaging technique compared to computed tomography: A retrospective study. *J Magn Reson Imaging* 2004;20(3):372-377.
304. Li D, Wang Y, Waight DJ. Blood oxygen saturation assessment in vivo using T2* estimation. *Magn Reson Med* 1998;39(5):685-690.
305. Ogawa S, Lee TM, Barrere B. The sensitivity of magnetic resonance image signals of a rat brain to changes in the cerebral venous blood oxygenation. *Magn Reson Med* 1993;29(2):205-210.
306. Denk C, Rauscher A. Susceptibility weighted imaging with multiple echoes. *J Magn Reson Imaging* 2010;31(1):185-191.
307. Haacke EM, DelProposto ZS, Chaturvedi S, et al. Imaging Cerebral Amyloid Angiopathy with Susceptibility-Weighted Imaging. *American Journal of Neuroradiology* 2007;28(2):316-317.
308. Tian L, Weiyu X, Spincemaille P, Avestimehr AS, Yi W. Accuracy of the Morphology Enabled Dipole Inversion (MEDDI) Algorithm for Quantitative Susceptibility Mapping in MRI. *Medical Imaging, IEEE Transactions on* 2012;31(3):816-824.
309. Schweser F, Deistung A, Lehr BW, Reichenbach JR. Quantitative imaging of intrinsic magnetic tissue properties using MRI signal phase: An approach to in vivo brain iron metabolism? *Neuroimage* 2011;54(4):2789-2807.
310. Shmueli K, de Zwart JA, van Gelderen P, Li T-Q, Dodd SJ, Duyn JH. Magnetic susceptibility mapping of brain tissue in vivo using MRI phase data. *Magn Reson Med* 2009;62(6):1510-1522.

311. de Rochefort L, Liu T, Kressler B, et al. Quantitative susceptibility map reconstruction from MR phase data using bayesian regularization: Validation and application to brain imaging. *Magn Reson Med* 2010;63(1):194-206.
312. Bilgic B, Pfefferbaum A, Rohlfing T, Sullivan EV, Adalsteinsson E. MRI estimates of brain iron concentration in normal aging using quantitative susceptibility mapping. *Neuroimage* 2012;59(3):2625-2635.
313. Jackson JD. *Classical Electrodynamics*: Wiley: 1998.
314. Jenkinson M. Fast, automated, N-dimensional phase-unwrapping algorithm. *Magn Reson Med* 2003;49(1):193-197.
315. Liu T, Khalidov I, de Rochefort L, et al. A novel background field removal method for MRI using projection onto dipole fields (PDF). *NMR Biomed* 2011;24(9):1129-1136.
316. Liu T, Spincemaille P, de Rochefort L, Kressler B, Wang Y. Calculation of susceptibility through multiple orientation sampling (COSMOS): A method for conditioning the inverse problem from measured magnetic field map to susceptibility source image in MRI. *Magn Reson Med* 2009;61(1):196-204.
317. Liu C. Susceptibility tensor imaging. *Magn Reson Med* 2010;63(6):1471-1477.
318. Liu C, Li W, Wu B, Jiang Y, Johnson GA. 3D fiber tractography with susceptibility tensor imaging. *Neuroimage* 2012;59(2):1290-1298.
319. Tang J, Neelavalli J, Liu S, Norman Cheng YC, Haacke EM. *SWIM: Susceptibility Mapping as a Means to Visualize Veins and Quantify Oxygen Saturation*: Wiley: 2011.
320. Haacke EM, Ye Y. The role of susceptibility weighted imaging in functional MRI. *Neuroimage* 2012;62(2):923-929.
321. Zaharchuk G, Do HM, Marks MP, Rosenberg J, Moseley ME, Steinberg GK. Arterial Spin-Labeling MRI Can Identify the Presence and Intensity of Collateral Perfusion in Patients With Moyamoya Disease. *Stroke* 2011;42(9):2485-2491.
322. Okell TW, Chappell MA, Schulz UG, Jezzard P. A kinetic model for vessel-encoded dynamic angiography with arterial spin labeling. *Magn Reson Med* 2012;68(3):969-979.
323. Bokkers RPH, van Osch MJP, Klijn CJM, Kappelle LJ, Hendrikse J. Cerebrovascular reactivity within perfusion territories in patients with an internal carotid artery occlusion. *J Neurol Neurosurg Psychiatry* 2011;82(9):1011-1016.
324. Kim SJ, Son JP, Ryoo S, et al. A novel magnetic resonance imaging approach to collateral flow imaging in ischemic stroke. *Ann Neurol* 2014:n/a-n/a.
325. Calamante F, Gadian DG, Connelly A. Quantification of Perfusion Using Bolus Tracking Magnetic Resonance Imaging in Stroke: Assumptions, Limitations, and Potential Implications for Clinical Use. *Stroke* 2002;33(4):1146-1151.
326. Henderson E, Sykes J, Drost D, Weinmann H-J, Rutt BK, Lee T-Y. Simultaneous MRI measurement of blood flow, blood volume, and capillary permeability in mammary tumors using two different contrast agents. *J Magn Reson Imaging* 2000;12(6):991-1003.
327. Daly B, Templeton PA. Real-time CT Fluoroscopy: Evolution of an Interventional Tool. *Radiology* 1999;211(2):309-315.

328. Kay SM. Fundamentals of Statistical Signal Processing: Estimation Theory: Prentice Hall Signal Processing Series: 1993.
329. Geise R. Fluoroscopy: Recording of Fluoroscopic Images and Automatic Exposure Control. *Radiographics* 2001;21:227-236.
330. Alexander DC. A general framework for experiment design in diffusion MRI and its application in measuring direct tissue-microstructure features. *Magn Reson Med* 2008;60(2):439-448.
331. Li C, Pan X, Ying K, et al. An internal reference model-based PRF temperature mapping method with Cramer-Rao lower bound noise performance analysis. *Magn Reson Med* 2009;62(5):1251-1260.
332. Naeyer DD, Ceelen WP, Verdonck P. In vivo validation of Cramer-Rao lower bounds for evaluating the reproducibility of Tofts kinetic modeling of DCE-MRI data. *AACR Meeting Abstracts (Molecular Diagnostics Meeting) 2010*;2010:B7.
333. Vonken E-jPA, Beekman FJ, Bakker CJG, Viergever MA. Maximum likelihood estimation of cerebral blood flow in dynamic susceptibility contrast MRI. *Magn Reson Med* 1999;41(2):343-350.
334. Ardekani BA, Kershaw J, Kashikura K, Kanno I. Activation detection in functional MRI using subspace modeling and maximum likelihood estimation. *Medical Imaging, IEEE Transactions on* 1999;18(2):101-114.
335. Sijbers J, den Dekker AJ. Maximum likelihood estimation of signal amplitude and noise variance from MR data. *Magn Reson Med* 2004;51(3):586-594.
336. Basser PJ, Pajevic S. Statistical artifacts in diffusion tensor MRI (DT-MRI) caused by background noise. *Magn Reson Med* 2000;44(1):41-50.
337. Liu C-Y, McKenzie CA, Yu H, Brittain JH, Reeder SB. Fat quantification with IDEAL gradient echo imaging: Correction of bias from T1 and noise. *Magn Reson Med* 2007;58(2):354-364.
338. Hoult DI, Richards RE. The signal-to-noise ratio of the nuclear magnetic resonance experiment. *J Magn Reson* 1976;24(1):71-85.
339. Edelstein WA, Glover GH, Hardy CJ, Redington RW. The intrinsic signal-to-noise ratio in NMR imaging. *Magn Reson Med* 1986;3(4):604-618.
340. Roemer PB, Edelstein WA, Hayes CE, Souza SP, Mueller OM. The NMR phased array. *Magn Reson Med* 1990;16(2):192-225.
341. Gudbjartsson H, Patz S. The rician distribution of noisy mri data. *Magn Reson Med* 1995;34(6):910-914.
342. A O, R S. *Discrete-Time Signal Processing: Prentice Hall Signal Processing: 1989.*
343. Kay SM. *Fundamentals of Statistical Signal Processing: Detection Theory: Prentice Hall Signal Processing Series: 1998.*
344. Walsh DO, Gmitro AF, Marcellin MW. Adaptive reconstruction of phased array MR imagery. *Magn Reson Med* 2000;43(5):682-690.
345. Stafford RB, Lauzon ML, Sabati M, Frayne R, Thompson RI. A tutorial on the precessional behaviour of hydrogen nuclei in external magnetic fields. *Canadian Journal of Physics* 2010;88(7):465-477.

346. Kwan RKS, Evans AC, Pike GB. MRI simulation-based evaluation of image-processing and classification methods. *Medical Imaging, IEEE Transactions on* 1999;18(11):1085-1097.
347. Hahn EL. Spin Echoes. *Physical Review* 1950;80(4):580.
348. Chang H, Fitzpatrick JM. A technique for accurate magnetic resonance imaging in the presence of field inhomogeneities. *Medical Imaging, IEEE Transactions on* 1992;11(3):319-329.
349. Voigt T, Nehrke K, Doessel O, Katscher U. T1 corrected B1 mapping using multi-TR gradient echo sequences. *Magn Reson Med* 2010;64(3):725-733.
350. Pruessmann KP, Weiger M, Börner P, Boesiger P. Advances in sensitivity encoding with arbitrary k-space trajectories. *Magn Reson Med* 2001;46(4):638-651.
351. Van Vaals JJ, Bergman AH. Optimization of eddy-current compensation. *J Magn Reson* 1990;90(1):52-70.
352. Turner R. Gradient coil design: A review of methods. *Magn Reson Imaging* 1993;11(7):903-920.
353. Janke A, Zhao H, Cowin GJ, Galloway GJ, Doddrell DM. Use of spherical harmonic deconvolution methods to compensate for nonlinear gradient effects on MRI images. *Magn Reson Med* 2004;52(1):115-122.
354. Doran SJ, et al. A complete distortion correction for MR images: I. Gradient warp correction. *Phys Med Biol* 2005;50(7):1343.
355. Eccles CD, Crozier S, Westphal M, Doddrell DM. Temporal Spherical-Harmonic Expansion and Compensation of Eddy-Current Fields Produced by Gradient Pulses. *Journal of Magnetic Resonance, Series A* 1993;103(2):135-141.
356. Deoni SCL, Peters TM, Rutt BK. Quantitative diffusion imaging with steady-state free precession. *Magn Reson Med* 2004;51(2):428-433.
357. Deoni SCL, Rutt BK, Peters TM. Rapid combined T1 and T2 mapping using gradient recalled acquisition in the steady state. *Magn Reson Med* 2003;49(3):515-526.
358. Pipe JG. Motion correction with PROPELLER MRI: Application to head motion and free-breathing cardiac imaging. *Magn Reson Med* 1999;42(5):963-969.
359. Glover GH. Simple analytic spiral K-space algorithm. *Magn Reson Med* 1999;42(2):412-415.
360. Gurney PT, Hargreaves BA, Nishimura DG. Design and analysis of a practical 3D cones trajectory. *Magn Reson Med* 2006;55(3):575-582.
361. Jou L-D, Lee DH, Mawad ME. Cross-flow at the anterior communicating artery and its implication in cerebral aneurysm formation. *J Biomech* 2010;43(11):2189-2195.
362. MacDonald ME, Dolati P, Mitha A, Wong JH, Frayne R. Phase Contrast Magnetic Resonance Imaging in Cerebrovascular Malformations: Towards Pressure Estimation. *International Magnetic Resonance Angiography Club* 2013.
363. Kecskemeti S, Johnson K, Wu Y, Mistretta C, Turski P, Wieben O. High resolution three-dimensional cine phase contrast MRI of small intracranial aneurysms using a stack of stars k-space trajectory. *J Magn Reson Imaging* 2012;35(3):518-527.

364. Claiborne Johnston S, Wilson CB, Halbach VV, et al. Endovascular and surgical treatment of unruptured cerebral aneurysms: Comparison of risks. *Ann Neurol* 2000;48(1):11-19.
365. Aenis M, Wakhloo AK, Lieber BB, Stancampiano AP. Modeling of Flow in a Straight Stented and Nonstented Side Wall Aneurysm Model. *J Biomech Eng* 1997;119(2):206-212.
366. Baert A, Knauth M, Sartor K. *Intracranial Vascular Malformations and Aneurysms*: Springer: 2008.
367. Schuster L, Schenk E, Giesel F, et al. Changes in AVM angio-architecture and hemodynamics after stereotactic radiosurgery assessed by dynamic MRA and phase contrast flow assessments. *Eur Radiol* 2011;21(6):1267-1276.
368. Alnæs MS, Isaksen J, Mardal K-A, Romner B, Morgan MK, Ingebrigtsen T. Computation of Hemodynamics in the Circle of Willis. *Stroke* 2007;38(9):2500-2505.
369. Wendell DC, Samyn MM, Cava JR, et al. Including aortic valve morphology in computational fluid dynamics simulations: Initial findings and application to aortic coarctation. *Med Eng Phys* 2013;35(6):723-735.
370. Masaryk AM, Frayne R, Unal O, Krupinski E, Strother CM. In Vitro and In Vivo Comparison of Three MR Measurement Methods for Calculating Vascular Shear Stress in the Internal Carotid Artery. *American Journal of Neuroradiology* 1999;20(2):237-245.
371. Willats L, Calamante F. The 39 steps: evading error and deciphering the secrets for accurate dynamic susceptibility contrast MRI. *NMR Biomed* 2012:913-931.
372. Zaharchuk G, Straka M, Marks MP, Albers GW, Moseley ME, Bammer R. Combined arterial spin label and dynamic susceptibility contrast measurement of cerebral blood flow. *Magn Reson Med* 2010;63(6):1548-1556.
373. Harloff A, Zech T, Wegent F, Strecker C, Weiller C, Markl M. Comparison of Blood Flow Velocity Quantification by 4D Flow MR Imaging with Ultrasound at the Carotid Bifurcation. *American Journal of Neuroradiology* 2013:1407-1413.
374. Sorond FA, Hollenberg NK, Panych LP, Fisher NDL. Brain Blood Flow and Velocity: Correlations Between Magnetic Resonance Imaging and Transcranial Doppler Sonography. *J Ultrasound Med* 2010;29(7):1017-1022.
375. Bishop CC, Powell S, Rutt D, Browse NL. Transcranial Doppler measurement of middle cerebral artery blood flow velocity: a validation study. *Stroke* 1986;17(5):913-915.
376. Cameron OG, Modell JG, Hariharan M. Caffeine and human cerebral blood flow: A positron emission tomography study. *Life Sci* 1990;47(13):1141-1146.
377. Henriksen OM, Larsson HBW, Hansen AE, Grüner JM, Law I, Rostrup E. Estimation of intersubject variability of cerebral blood flow measurements using MRI and positron emission tomography. *J Magn Reson Imaging* 2012;35(6):1290-1299.
378. Jorgensen LG, Perko G, Secher NH. Regional cerebral artery mean flow velocity and blood flow during dynamic exercise in humans. *J Appl Physiol* 1992;73(5):1825-1830.

379. Frayne R, Polzin JA, Mazaheri Y, Grist TM, Mistretta CA. Effect of and correction for in-plane myocardial motion on estimates of coronary-volume flow rates. *J Magn Reson Imaging* 1997;7(5):815-828.
380. Yiemeng H, Bruce AW, Yuanyuan JX, et al. Characterization of volumetric flow rate waveforms at the carotid bifurcations of older adults. *Physiol Meas* 2010;31(3):291.
381. Enzmann DR, Marks MP, Pelc NJ. Comparison of cerebral artery blood flow measurements with gated cine and ungated phase-contrast techniques. *J Magn Reson Imaging* 1993;3(5):705-712.
382. Enzmann DR, Ross MR, Marks MP, Pelc NJ. Blood flow in major cerebral arteries measured by phase-contrast cine MR. *American Journal of Neuroradiology* 1994;15(1):123-129.
383. Harloff A, Albrecht F, Spreer J, et al. 3D blood flow characteristics in the carotid artery bifurcation assessed by flow-sensitive 4D MRI at 3T. *Magn Reson Med* 2009;61(1):65-74.
384. Zhao M, Charbel FT, Alperin N, Loth F, Clark ME. Improved phase-contrast flow quantification by three-dimensional vessel localization. *Magn Reson Imaging* 2000;18(6):697-706.
385. Gu T, Korosec FR, Block WF, et al. PC VIPR: A High-Speed 3D Phase-Contrast Method for Flow Quantification and High-Resolution Angiography. *American Journal of Neuroradiology* 2005;26(4):743-749.
386. Hansen F, Mangell P, Sonesson B, Länne T. Diameter and compliance in the human common carotid artery — variations with age and sex. *Ultrasound Med Biol* 1995;21(1):1-9.
387. Stefani MA, Schneider FL, Marrone ACH, Severino AG. Influence of the gender on cerebral vascular diameters observed during the magnetic resonance angiographic examination of willis circle. *Brazilian Archives of Biology and Technology* 2013;56:45-52.
388. Andrews BT, Dujovny M, Mirchandani HG, Ausman JI. Microsurgical anatomy of the venous drainage into the superior sagittal sinus. *Neurosurgery* 1989;24(4):514-520.
389. Gejrot T, Laurén T. Retrograde Venography of the Internal Jugular Veins and Transverse Sinuses: Technique and roentgen anatomy. *Acta Otolaryngol (Stockh)* 1964;57(3-6):556-570.
390. Bogren HG, Buonocore MH, Gu W-Z. Carotid and vertebral artery blood flow in left- and right-handed healthy subjects measured with MR velocity mapping. *J Magn Reson Imaging* 1994;4(1):37-42.
391. Johnson KM, Lum DP, Turski PA, Block WF, Mistretta CA, Wieben O. Improved 3D phase contrast MRI with off-resonance corrected dual echo VIPR. *Magn Reson Med* 2008;60(6):1329-1336.
392. Block W, Barger A, Mistretta C. Vastly Undersampled Isotropic Projection Imaging. *International Society of Magnetic Resonance in Medicine*. Denver, Colorado, USA; 2000. p. 161.

393. Yang G-Z, Kilner PJ, Wood NB, Underwood SR, Firmin DN. Computation of flow pressure fields from magnetic resonance velocity mapping. *Magn Reson Med* 1996;36(4):520-526.
394. Gabe IT, Gault JH, Ross J, et al. Measurement of Instantaneous Blood Flow Velocity and Pressure in Conscious Man with a Catheter-Tip Velocity Probe. *Circulation* 1969;40(5):603-614.
395. Millar HD, Baker LE. A stable ultraminiature catheter-tip pressure transducer. *Med Biol Eng* 1973;11(1):86-89.
396. Morcos S, Thomsen H. Adverse reactions to iodinated contrast media. *Eur Radiol* 2001;11(7):1267-1275.
397. Farkas J, Liebling MS, Pritzker HA. Reactions to Iodinated Contrast Media. *Pediatr Rev* 1996;17(11):385-386.
398. Goddard AJP, Tan G, Becker J. Computed tomography angiography for the detection and characterization of intra-cranial aneurysms: Current status. *Clin Radiol* 2005;60(12):1221-1236.
399. Sugahara T, Korogi Y, Nakashima K, Hamatake S, Honda S, Takahashi M. Comparison of 2D and 3D Digital Subtraction Angiography in Evaluation of Intracranial Aneurysms. *American Journal of Neuroradiology* 2002;23(9):1545-1552.
400. Piotin M, Gailloud P, Bidaut L, et al. CT angiography, MR angiography and rotational digital subtraction angiography for volumetric assessment of intracranial aneurysms. An experimental study. *Neuroradiology* 2003;45(6):404-409.
401. Stehbens WE. Etiology of intracranial berry aneurysms. *J Neurosurg* 1989;70(6):823-831.
402. Sekhar LN, Heros RC. Origin, Growth, and Rupture of Saccular Aneurysms: A Review. *Neurosurgery* 1981;8(2):248-260.
403. Cebal JR, Mut F, Weir J, Putman CM. Association of Hemodynamic Characteristics and Cerebral Aneurysm Rupture. *American Journal of Neuroradiology* 2011;32(2):264-270.
404. MacDonald ME, Dolati P, Wong JH, Frayne R. Blood Volume Flow Rates of Vessels in Healthy Human Cerebral Vasculature. *Proc Intl Soc Mag Reson Med* 22. Milan, Italy; 2014. p. 1829.
405. Spetzler RF, Hargraves RW, McCormick PW, Zabramski JM, Flom RA, Zimmerman RS. Relationship of perfusion pressure and size to risk of hemorrhage from arteriovenous malformations. *J Neurosurg* 1992;76(6):918-923.
406. Dahl A, Russell D, Nyberg-Hansen R, Rootwelt K, Bakke SJ. Cerebral vasoreactivity in unilateral carotid artery disease. A comparison of blood flow velocity and regional cerebral blood flow measurements. *Stroke* 1994;25(3):621-626.
407. Tan JC, Dillon WP, Liu S, Adler F, Smith WS, Wintermark M. Systematic comparison of perfusion-CT and CT-angiography in acute stroke patients. *Ann Neurol* 2007;61(6):533-543.
408. Peyron R, Faillenot I, Mertens P, Laurent B, Garcia-Larrea L. Motor cortex stimulation in neuropathic pain. Correlations between analgesic effect and

- hemodynamic changes in the brain. A PET study. *Neuroimage* 2007;34(1):310-321.
409. Kim S-G, Tsekos NV, Ashe J. Multi-slice perfusion-based functional MRI using the FAIR technique: comparison of CBF and BOLD effects. *NMR Biomed* 1997;10(4-5):191-196.
410. Hartkamp MJ, van der Grond J, van Everdingen KJ, Hillen B, Mali WPTM. Circle of Willis Collateral Flow Investigated by Magnetic Resonance Angiography. *Stroke* 1999;30(12):2671-2678.
411. Lin W, Celik A, Derdeyn C, et al. Quantitative measurements of cerebral blood flow in patients with unilateral carotid artery occlusion: A PET and MR study. *J Magn Reson Imaging* 2001;14(6):659-667.
412. Chuang YM, Chang YJ, Chang CH, et al. Correlation between the flow pattern of the circle of Willis and segmental perfusion asymmetry after carotid artery revascularization. *Eur J Neurol* 2011;18(9):1132-1138.
413. Moore S, David T, Chase JG, Arnold J, Fink J. 3D models of blood flow in the cerebral vasculature. *J Biomech* 2006;39(8):1454-1463.
414. Divani AA, Qureshi AI, Hoffman KR, Suri MFK, Kirmani JF. Comparison of Asymmetry in Cerebral Blood Flow Between Brain Hemispheres Using Digital Subtraction Angiography. *J Neuroimaging* 2006;16(2):139-145.
415. Hendrikse J, van der Grond J, Lu H, van Zijl PCM, Golay X. Flow Territory Mapping of the Cerebral Arteries With Regional Perfusion MRI. *Stroke* 2004;35(4):882-887.
416. Kansagra AP, Wong EC. Mapping of vertebral artery perfusion territories using arterial spin labeling MRI. *J Magn Reson Imaging* 2008;28(3):762-766.
417. van Laar PJ, Hendrikse J, Golay X, Lu H, van Osch MJP, van der Grond J. In vivo flow territory mapping of major brain feeding arteries. *Neuroimage* 2006;29(1):136-144.
418. MacDonald M. Catheter Tracking with Accelerated MRI. Department of Biomedical Engineering. Volume M.Sc.: University of Calgary; 2010.
419. Ouyang C, Sutton BP. Regional perfusion imaging using pTILT. *J Magn Reson Imaging* 2014;40(1):192-199.
420. Zwart NR, Pipe JG. Multidirectional high-moment encoding in phase contrast MRI. *Magn Reson Med* 2013;69(6):1553-1563.

Appendix Ethics Approvals



July 3, 2008

Dr. Richard Frayne,
Clinical Neurosciences
FMC
Calgary
Alberta

OFFICE OF MEDICAL BIOETHICS
Room 93A, Heritage Medical Research Bldg
3330 Hospital Drive NW
Calgary, AB, Canada T2N 4N1
T (403) 210-9757
F (403) 283-8524
E ggodlovi@ucalgary.ca

Dear Dr. Frayne:

Re: Your application to CHREB entitled "Collection and storage of MRI images with a view to future research"

Ethics ID: 21866

Thank you for your application and your supporting documentation including the consent form and project description for image banking. As Chair of the Conjoint Health Research Ethics Board I have reviewed your documentation and have met with you and your team to discuss your work. My understanding confirmed by you is that at this stage you are collecting images with a view to designing research projects which you will submit individually as they arise to the Conjoint Health Research Ethics Board.

As Chair of the Board and with delegated power to review expedited applications, this letter confirms that you have approval to collect, store and save MRIs based on the informed consent documents which you have provided to the Board.

You are required to request renewal of this project on or before July 3, 2009

Kindly note that when you design any specific projects for investigation with the collected data you will at that time need to submit a full application to the Conjoint Health Research Ethics Board. This letter constitutes sufficient authority from the Conjoint Health Research Ethics Board for you to continue in the meantime with your data collection.

Please quote the above noted tracking number in any future correspondence. Best wishes.

Yours sincerely,

A handwritten signature in black ink, appearing to read "G. Godlovitch".

Glenys Godlovitch, BA(Hons) LLB, PhD.
Chair, Conjoint Health Research Ethics Board
Director, Office of Medical Bioethics
GG/eb

c.c. Ms. Sharon Van Oort, Manager, Research Compliance, Research Services, University of Calgary



Conjoint Health Research Ethics Board (CHREB)
 Research Services, University of Calgary
 Main Floor, Energy Resources Research Building
 3512 - 33 Street NW Calgary, AB T2L 2A6
 resethic@ucalgary.ca | (403) 220-7990

FORM 6: ANNUAL REPORT AND RENEWAL FORM

Instructions:

1. Provide information only for the 12 months immediately prior to current anniversary date.
2. Do not aggregate data since start of study unless specifically requested
3. Do not include copy/copies of current consent forms
4. Submit electronically to Annrept@ucalgary.ca
5. Subject line to read: <Ethics ID #> Annual Report
6. Annrept@ucalgary.ca will generate an automatic response for your records
7. Annrept@ucalgary.ca will contact you for follow up if required within 5 working days.

Ethics ID #: 21942

Anniversary Date: Aug 11, 2013

Submission Date: Aug 15, 2013

Complete Research Protocol Title: Advanced Signal Processing for Rapid Imaging	
Principal Investigator: Dr. Richard Frayne	Signature: Date:
Coordinator: Dr. Linda Andersen	Signature: Date:
Telephone: 403-944-8076	Email: lbanders@ucalgary.ca

Within the current reporting period:

1. Has the research protocol closed to accrual? Yes No
 If yes, when was it closed to accrual? Date (DD/MM/YY): _____
2. Has the research protocol closed to follow-up? Yes No
 If yes, when was it closed to follow-up? Date (DD/MM/YY): _____
 Total number of subjects on follow-up: Number: _____
3. Has this study completely closed to all research activity? Yes No
4. If so, when was the study completely closed? Date (DD/MM/YY): _____
5. If the study is continuing, what is the expected end date: Date (MM/YY): _____/16
6. How many subjects did you expect to accrue? Number: _____
7. Have all modifications been reported? Yes No N/A
(If no, contact the office immediately)
8. Have all complications been reported? Yes No N/A
(If no, contact the office immediately)
9. Have all adverse events been reported? Yes No N/A
(If no, contact the office immediately)
10. Have any subject withdrawn? Yes No
 If yes, how many? Number: _____

11. Number of subjects in last 12 months accrued by age and gender:

Age years	0-<1	1-<4	4-<12	12-<18	18-<65	>65
Number of Male						
Number of Female						

ANONYMOUS DATA COLLECTION

If your research method required anonymity, so that study subjects cannot be categorized by gender or age, check appropriate box: Anonymous: Yes No

AND

provide a total count of the number of subjects accrued into the study in the reporting period.

Total Summaries

12. Total number of subjects accrued since start of study: Number: n/a

13. Total number of subjects withdrawn since start of study: Number: 0

14. Have there been any complaints? Yes No

(If yes, please provide details)

15. Have the results been published/presented? Yes No

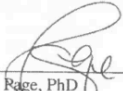
(If yes, please provide details)

Thank you very much for the **progress report** on this protocol. As Chair of the Conjoint Health Research Ethics Board, University of Calgary, and the Affiliated Teaching institutions, I am pleased to advise you that ethical approval for this proposal has been extended to Aug 11, 2014. Please note that this approval is contingent upon strict adherence to the original protocol. Prior permission must be obtained from the Board for any contemplated modification(s) of the original protocol.

A **progress report** concerning this study will be required by Aug 11, 2014.

This request received full Board approval on Sept 5, 2013.

Please accept the Board's best wishes for continued success in your research.


Stacey Page, PhD
Chair, Conjoint Health Research Ethics Board

date

Sept 5, 2013

cc: Research Coordinator • Research Services



2008-08-11

Dr. Richard Frayne
Clinical Neurosciences
FMC
Calgary
Alberta

OFFICE OF MEDICAL BIOETHICS
Room 93, Heritage Medical Research Bldg
3330 Hospital Drive NW
Calgary, AB, Canada T2N 4N1
Telephone: (403) 220-7990
Fax: (403) 283-8524
Email: omb@ucalgary.ca

Dear Dr. Frayne:

RE: Advanced Signal Processing for Rapid Imaging

Ethics ID: E-21942

The above-named research, including the Form (NSERC Application Form; NSERC Form 101, System ID 90341595) has been granted ethical approval by the Conjoint Health Research Ethics Board of the Faculties of Medicine, Nursing and Kinesiology, University of Calgary, and the Affiliated Teaching Institutions. The Board conforms to the Tri-Council Guidelines, ICH Guidelines and amendments to regulations of the Food and Drugs Act re clinical trials, including membership and requirements for a quorum.

You and your co-investigators are not members of the CHREB and did not participate in review or voting on this study.

Please note that this approval is subject to the following conditions:

- (1) access to personal identifiable health information was not requested in this submission;
- (2) a copy of the informed consent form must have been given to each research subject, if required for this study;
- (3) a Progress Report must be submitted by **August 11, 2009**, containing the following information:
 - i) the number of subjects recruited;
 - ii) a description of any protocol modification;
 - iii) any unusual and/or severe complications, adverse events or unanticipated problems involving risks to subjects or others, withdrawal of subjects from the research, or complaints about the research;
 - iv) a summary of any recent literature, finding, or other relevant information, especially information about risks associated with the research;
 - v) a copy of the current informed consent form;
 - vi) the expected date of termination of this project.
- 4) a Final Report must be submitted at the termination of the project.

Please accept the Board's best wishes for success in your research.

Yours sincerely,



Gladys Glowacki, BA(Hons), LLB, PhD
Chair, Conjoint Health Research Ethics Board

GG/emcg
c.c. Ms. Gladys Glowacki (Health Records) Ms. Donna McDonald (RTA) Dr. J. Gregory Cairncross (information)
Research Services Dr. Linda Andersen (Research Coordinator)
Office of Information & Privacy

CREATING THE FUTURE OF HEALTH *An innovative medical school committed to excellence and leadership in education, research and service to society.*

11. Number of subjects in last 12 months accrued by age and gender:

Age years	0-<1	1-<4	4-<12	12-<18	18-<65	>65
Number of Male						
Number of Female						

ANONYMOUS DATA COLLECTION

If your research method required anonymity, so that study subjects cannot be categorized by gender or age, check appropriate box: Anonymous: Yes No

AND

provide a total count of the number of subjects accrued into the study in the reporting period.

Total Summaries

12. Total number of subjects accrued since start of study: Number: n/a

13. Total number of subjects withdrawn since start of study: Number: n/a

14. Have there been any complaints? Yes No

(If yes, please provide details)

15. Have the results been published/presented? Yes No

(If yes, please provide details)

Thank you very much for the **progress report** on this protocol. As Chair of the Conjoint Health Research Ethics Board, University of Calgary, and the Affiliated Teaching institutions, I am pleased to advise you that ethical approval for this proposal has been extended to July 3, 2014. Please note that this approval is contingent upon strict adherence to the original protocol. Prior permission must be obtained from the Board for any contemplated modification(s) of the original protocol.

A **progress report** concerning this study will be required by July 3, 2014.

This request received full Board approval on June 20, 2013.

Please accept the Board's best wishes for continued success in your research.


 Stacey Page, PhD date 20 June 2013
 Chair, Conjoint Health Research Ethics Board

cc: Research Coordinator • Research Services



FACULTY OF UNIVERSITY OF
MEDICINE | CALGARY

2012-07-23

Dr. John H. Wong
Division of Neurosurgery
Foothills Medical Centre
1403 - 29th Street NW
Calgary Alberta T2N 2T9

OFFICE OF MEDICAL BIOETHICS
Room 93, Heritage Medical Research Bldg
3330 Hospital Drive NW
Calgary, AB, Canada T2N 4N1
Telephone: (403) 220-7990
Fax: (403) 283-8524
Email: omb@ucalgary.ca

Dear Dr. Wong:

RE: Hemodynamic Analysis of Arteriovenous Malformations and Cerebral Aneurysms with 4D Phase Contrast Magnetic Resonance Imaging

Ethics ID: E-24627

The above-named research, including the Consent Form (version 1.0, April 2012), Letters (AHS, April 10, 2012), Protocol (version 1.0, December 2011), Funding Confirmation Letter (Heart and Stroke Program, March 27, 2012) has been granted ethical approval by the Conjoint Health Research Ethics Board of the Faculties of Medicine, Nursing and Kinesiology, University of Calgary, and the Affiliated Teaching Institutions. The Board conforms to the Tri-Council Guidelines, ICH Guidelines and amendments to regulations of the Food and Drugs Act re clinical trials, including membership and requirements for a quorum.

You and your co-investigators are not members of the CHREB and did not participate in review or voting on this study. Please note that this approval is subject to the following conditions:

- (1) appropriate procedures for consent for access to identified health information have been approved;
- (2) a copy of the informed consent form must have been given to each research subject, if required for this study;
- (3) a Progress Report must be submitted by **July 23, 2013**, containing the following information:
 - i) the number of subjects recruited;
 - ii) a description of any protocol modification;
 - iii) any unusual and/or severe complications, adverse events or unanticipated problems involving risks to subjects or others, withdrawal of subjects from the research, or complaints about the research;
 - iv) a summary of any recent literature, finding, or other relevant information, especially information about risks associated with the research;
 - v) a copy of the current informed consent form;
 - vi) the expected date of termination of this project.
- 4) a Final Report must be submitted at the termination of the project.

Please accept the Board's best wishes for success in your research.

Yours sincerely,

Stacey Page, PhD
Chair, Conjoint Health Research Ethics Board

SP/emcg

c.c. Dr. J. Gregory Cairncross (information) Ms. Sharon Van Oort, Research Services - Main Campus Dr. Linda Anderson
(Research Coordinator) Mr. Matthew Ethan MacDonald, Dr. Richard Frayne, Dr. Parviz Dolati (Co-Investigators)
Office of Information & Privacy

CREATING THE FUTURE OF HEALTH *An innovative medical school committed to excellence and leadership in education, research and service to society.*